STAR FORMATION IN GIANT EXTRAGALACTIC H II REGIONS

A Thesis

Submitted for the Degree of

Doctor of Philosophy

in the Faculty of Science

by

Y. DIVAKARA MAYYA

DEPARTMENT OF PHYSICS

INDIAN INSTITUTE OF SCIENCE
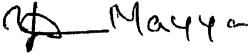
BANGALORE – 560 012 (INDIA)

FEBRUARY 1993

Declaration

I hereby declare that the work presented in this thesis is entirely original and did not form the subject matter for any other thesis submitted by me for any outside degree. The thesis has been carried out at the Indian Institute of Astrophysics under the auspices of Dept. of Physics, Indian Institute of Science, Bangalore.
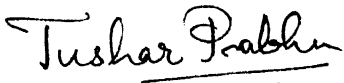
22 February 1993

Bangalore

Y.D. Mayya,

Candidate

T. P. PRABHU

Acknowledgement

SUMMARY

Giant Extragalactic H II Regions (GEHRs) are the primary sites of star formation in external galaxies. A star forming complex is characterised by the initial mass function (IMF) and the star formation rate (SFR). The IMF is believed to have a power-law form with an index, known as IMF slope, close to 2.35 and lower and upper cut-off masses in the range 0.08–$3.0 M_\odot$ and 30–$120 M_\odot$ respectively. The universality of the slope has to be confirmed under different environments. The studies in our galaxy are based on direct star counts while indirect methods are used to infer about IMF in other galaxies. The derived SFR in galaxies are currently uncertain due to our insufficient knowledge of the above parameters. The studies aimed at investigating the mass function parameters are mainly based on global properties of galaxies, which are evolved systems and hence the results are heavily dependent on the history of star formation and the adopted stellar evolutionary models. In comparison Giant H II complexes are young and much simpler systems. The present study is an attempt in understanding these using optically derived quantities. Being young, these systems are not much affected by the uncertainties in the history of star formation and the adopted stellar evolutionary models. The major sources of errors in modelling these regions are (a) the amount of interstellar extinction, (b) the distance estimate to the galaxies, and (c) the uncertainties due to small apertures often used in spectroscopic observations. We have tried to minimize these errors in the present study.

We use aperture photometric data in emission lines and continua derived from CCD images of galaxies to investigate the IMF and SF properties in individual complexes in galaxies. The H II regions are chosen to have published spectroscopic data, giving information on gaseous parameters such as Balmer decrement and oxygen abundance. $BVR H\alpha$ photometry of individual H II regions is carried out on our

image data. The observed values are corrected for interstellar extinction using the reddening obtained from Balmer decrement and galactic extinction curve, assuming uniform distribution of dust clouds following normal conventions. The amount of gaseous emission within each of the BVR bands is estimated and subtracted from the band, and continuum magnitudes are obtained for the young star cluster. The $H\alpha$ flux is a measure of ionizing radiation from the cluster. These data are used to form a dimensionless quantity $\frac{\phi}{L_B}$, which is the ratio of equivalent $H\beta$ luminosity to blue band luminosity. The expected values of this quantity and $B - V$ and $V - R$ colours are computed using Evolutionary Population Synthesis Model, for a range of IMF parameters, age and metallicities. The extinction corrected pure stellar quantities are then compared with the models in an attempt to understand the IMF parameters and star formation. Following is a summary of the contents of the thesis.

Details of instruments, observations, reductions and calibration of the instruments are described in detail in Chapter II. Atmospheric extinction coefficients are reported for twelve photometric nights. Methods used for the photometric calibration of broadband and narrowband filters are also described and the resulting transformation coefficients are presented. Synthetic aperture photometric techniques for stars and H II regions, developed during the course of this study, are described.

A catalogue of photometry of H II regions in $BVRH\alpha$ and in some cases in $BVRIH\alpha H\beta$ [O III] λ 5007 is presented in Chapter III. The chapter contains identification charts for H II regions as well. Aperture growth curves and radial surface brightness profiles are constructed around the nucleus of the programme galaxies. These results are compared with the existing BV photoelectric photometry.

Chapter IV describes the model developed as a part of the present work for synthesizing the observational properties of Giant H II complexes. The basics

of modelling star clusters are given along with the sources of input stellar data. Some of the basic quantities of stars, used as inputs to the cluster model, are presented in tabular form in Table IV.1. The observational parameters, namely, the ratio of equivalent Hβ luminosity to B band luminosity, denoted as $\frac{\phi}{L_B}$, and $B - V$ and $V - R$ colours are synthesized in the models and diagnostic diagrams are constructed using these parameters. The results are shown graphically as well as in tabular format.

Observational data are compared with the models in Chapter V. Regions having spectroscopic data giving information at least on Balmer decrement and oxygen abundance are selected from our photometric catalogue. Broad band continuum fluxes are corrected for nebular contribution to extract continuum from the cluster. It is shown that dereddening using Balmer decrement overcorrects the cluster continuum. An alternate prescription is given, where a fraction of stellar light escapes without attenuation. This fraction is found to be close to be 50%. It is shown that a similar fraction of ionizing radiation either escapes the H II region or escapes detection through absorption of Balmer radiation by dense clouds. The colours of embedded clusters show evidence of red supergiants which belong to an earlier burst of age greater than 6 Myr. Three colour images of some galaxies in BVHα bands are presented. From these images we infer the presence of two clusters of differing age situated at separations 40–100 pc. If the younger burst has occurred due to a trigger from the older one the inferred speed of propagation of the trigger is 4–10 km s^{-1}. The average mass of each cluster is $\sim 10^5$ M$_\odot$.

Chapter VI summarizes the major results of this study. Scope for future multiwavelength and high spatial resolution studies is discussed.

Contents

I. INTRODUCTION

Stars are the most dominant constituents of galaxies, at visible wavelengths. Galaxies contain stars of a variety of ages, suggesting that star formation is an ongoing process. Gas containing mainly hydrogen in its atomic and molecular forms is the raw material from which stars form. The rate at which stars form is controlled by the amount of gas present. The Star Formation Rate (SFR) in the past and the present determines the current physical appearance of galaxies. Accordingly galaxies take either elliptical, spiral or irregular morphology. Elliptical galaxies had a violent beginning, in which most of the gas was converted into stars and hence they do not contain a significant component of young stars. The gas left in other systems after the initial star formation event settled into a disk structure. Young stars are currently forming out of this gas in the disk, often tracing spiral structures in Spiral galaxies, or in a chaotic manner in Irregular galaxies. Stars form either in associations, groups or clusters and have a mass distribution. The ultraviolet photons radiated by massive stars, which are hot when young ionize the surrounding gas giving rise to H II regions or H II complexes. H II regions have a characteristic spectrum, rich with emission lines of hydrogen, oxygen, nitrogen and sulphur, spread throughout the electromagnetic spectrum. The presence of emission lines and their high intensity makes it possible to use H II regions as a tool to study a variety of properties in galaxies. Temperature, density, and chemical abundances of metals in the gas can be probed using emission line ratios sensitive to the corresponding physical quantity. The Doppler shifts of the lines are used to map the velocity fields in galaxies.

For any quantitative estimation of SFRs in galaxies, it is important to know the mass spectrum of newly formed stars. The long lifetimes ($> 10^9$ yr) of low mass stars lock up the matter in galaxies, while high mass stars return most of their

gas, enriched with heavy elements from nucleosynthesis, back into the interstellar medium in a few million years. Thus the evolution of galaxies depends not only on the number but also on the mass spectrum of newly formed stars. The mass spectrum of stars at birth, known as the Initial Mass Function (IMF), is canonically represented as a power-law distribution. An IMF is completely represented by the lowest and highest masses of the stars formed, in addition to the coefficient (slope in logarithmic representation) of the power-law. It is theoretically not known whether there should be a universal value for the slope. Direct observational investigation of the slope involves counting all stars in a region of space, over various luminosity bins, and converting the bins into mass bins using luminosity-mass relation for stars. Such studies done so far do not fully agree with a universal slope, but at the same time are not decisive enough to rule out universality. However for purposes of SFR estimates an average value of this slope is generally assumed.

Except in a few nearby galaxies it is not possible to resolve, count and observe individual stars and hence the IMF cannot be determined by the direct method. However the combined effect of a stellar aggregate can be modelled, from which IMF parameters can be investigated, provided the aggregate contains statistically large number of stars. From the amount of ionization required to ionize H II complexes seen in external galaxies, it is often inferred that they contain several hundreds of massive stars. Accompanying these massive stars will be a much higher number of lower mass stars, which are incapable of producing any ionizing flux, but contribute substantially to the visible light. The bulk of the total mass of the cluster is contained in these lower mass stars. The presence of a large number of young stars qualifies them as one of the ideal sites for the investigation of mass spectrum in star forming regions. Most important for this study is a theoretical model, that can predict the expected luminosity in selected bands from an H II complex. The IMF parameters are derived by comparing the observed quantities with models.

The present study is an attempt in understanding the physical properties of H II complexes so that some constraints can be placed on the IMF using the methods outlined above. Considerable attention is given to other factors influencing the observational data.

1. History of Star Formation in Galaxies

The history of star formation in galaxies can be completely represented by two functions, one based on the relative distribution of various stellar masses at the birth time of stars and the second based on the time dependence of the rate at which gas is converted to stars. The two functions are known as the Initial Mass Function (IMF) $\psi(m)$, and the Birth Rate Function $B(t)$. The SFR per unit mass interval at a time t over the volume considered is then given by $\psi(m)B(t)$. Any time dependence of $\psi(m)$ is neglected in the above definition. The observational method of obtaining the form of $B(t)$ is summarized below.

1. Select a set of observables, each one being sensitive to a specific stellar population. Such quantities in the optical band are, $B-V$, $V-R$ colours; $H\alpha$ or $H\beta$ luminosities or their equivalent widths, which are defined as the ratio of the line intensities to the underlying continuum.

2. Synthesize the above parameters using theoretical models for an assumed IMF for various forms of $B(t)$.

3. The form of $B(t)$ which consistently matches the selected observables represents the star formation history for the region under consideration.

For elliptical galaxies an exponentially decreasing form $(B(t) \propto \exp(-t/\tau)$ was found to produce the observables (Huchra 1977). Forms such as $B(t) = $ constant throughout the age T also yield good agreement for some systems, particularly for the disks of spirals and the irregulars (Kennicutt 1983; Gallagher, Hunter and Tutukov 1984). Both these formulations suggest that stars form continuously over

3

the period T. Stars may form in some cases over a short time interval with little or no star formation outside the interval. The birth rate in this case is suitably represented by a delta function. The name "starburst" suggests such a kind of star formation history. It is possible that more than one kind of formulation is required for many cases.

$B(t)$ thus determined is sensitive to the assumed IMF and other basic data on stars used in the theoretical models. Following the pioneering work of Salpeter (1955), the IMF of stars is assumed to follow a power-law distribution with a slope $\alpha = 2.35$. The lower and upper cutoff masses, denoted as m_l and m_u respectively are uncertain because of the observational difficulties in estimating these parameters. It is generally believed that $m_l \approx 0.05 - 0.1$ and $m_u \approx 100$ in units of solar mass. However there are suggestions that m_l can be as high as 2–3 in some violently star forming regions, known as starburst galaxies (Rieke et al. 1980; Jensen, Talbot and Dufour 1981). The upper mass limit is related to the effectiveness of radiation pressure relative to gravity, while the lower mass is dictated by the inability of collapsing objects to heat the core to temperatures where nuclear reactions can commence. Cooling due to electron conduction plays a major part in deciding the lowest mass.

The IMF slope and its possible dependence on physical conditions of star forming regions is poorly understood. Most of our knowledge regarding IMF comes from the study of field stars and cluster stars in our Galaxy. Star forming regions in the Galaxy differ in a variety of ways from those in other galaxies. For example the population of giant H II regions, so commonly found in external galaxies is totally absent in the Galaxy. The metallicity spread in different star forming regions in other galaxies is much more than that in the Galaxy. Scalo (1986) reviews the attempts made so far in investigating IMF in Milky Way and other galaxies. There is no compelling evidence at present for an IMF slope different from Salpeter's solar

neighbourhood value of 2.35, though there are hints that it may not be universal. The major problems encountered in estimating IMF in extragalactic star-forming regions are listed below.

1) Extinction due to dust : The derived values of IMF slopes are very sensitive to the correction for interstellar extinction. It is known from studies of H II regions that, the extinction varies from region to region. The problem will be more severe, when global properties of galaxies are used. Common methods used for extinction correction are discussed in Appendix A.

2) Stellar Evolutionary Model : In estimating IMF from the integrated properties of galaxies, the stellar models have to be followed to several billion years. Thus the derived values are highly sensitive to the assumptions in the stellar evolutionary models. The problems are highly reduced for the young systems such as H II regions.

3) Hβ equivalent widths derived from conventional slit spectrographs are used for deriving IMF by several groups. Slits usually do not enclose the full emitting region and hence the derived equivalent widths may not be representative of the entire region.

4) The integrated properties of the galaxies are affected heavily by the inhomogenous distribution of emitting regions having different elemental abundances.

2. IMF in Giant H II Complexes

Most of the problems encountered in obtaining IMF parameters from global data on galaxies can be tackled better in the case of Giant Extragalatic H II Regions (GEHRs). The most commonly used tracer of H II regions is the Hα flux, which indicates the presence of massive ionizing stars. These stars live for less than 5 Myr and hence the brightest H II regions in galaxies must be younger than 5 Myr. It is often a good approximation to assume the embedded stars to be coeval. Thus the

problems involving the nature of birth rate function is eliminated. GEHRs are relatively simpler systems, and can be considered chemically homogenous. Extinction in these regions can be corrected better. In the rest of this section the observational methods normally followed in the investigation of IMF are summarized along with the past results.

2.1 Observational Methods for IMF Determination

Methods used to investigate the IMF parameters can be broadly classified as Direct and Indirect methods. In the direct method individual stars are resolved and stellar photometry and spectroscopy is used to infer about IMF. Since individual stars are not resolved in galaxies other than our own and some nearby galaxies, this method cannot be applied to star forming complexes in a majority of galaxies. It is in these regions that the IMF parameters are inferred by indirect means. In this method, which is used in this study, the global properties of star forming regions are compared with the model-derived values. The entire galaxy or an individual H II complex is treated as a star forming unit. It is necessary to observe the regions in bands sensitive to both ends of the mass spectrum. In the following, the physical processes describing H II regions are summarized, with emphasis on observables in the optical band.

The ultraviolet photons from massive stars ionize the surrounding gas, which is predominantly hydrogen. These are followed by recombinations to different bound levels of hydrogen atom. Equilibrium is established in a short time scale relative to the lifetime of the ionizing stars, when the number of ionizations are balanced by the number of recombinations. The electron gas also attains an equilibrium temperature, at which the relative intensities of recombination lines and gaseous continua are fixed. These ionized regions, known as H II regions, are assumed to be ionization bounded, i.e., the extent of ionization is limited by the availability

6

of ionizing photons, rather than the extent and density of the neutral gas. In such an event the number of photons emitted in a recombination line or in the nebular continuum is proportional to the number of Lyman continuum (ionizing) photons. Thus the total number of Lyman continuum photons can be inferred by observations in one of the Balmer, Brackett or Paschen lines or in the free-free continuum. The most commonly used tracer is the Hα line, the brightest line in the optical region. Estimation of the number of massive ionizing stars based either on recombination lines or thermal radio continuum are generally referred to as Lyman continuum photon counting method. While Lyman continuum luminosity is very sensitive to high mass stars, it is relatively insensitive to the presence of low mass stars. Non-ionizing stars contribute to the continuum at ultraviolet, optical and infrared wavelengths. Hence the ratio of the recombination line intensity to the continuum intensity, encompasses a wide mass range and can be used for determining the IMF.

Hα luminosity

The main advantages of Hα as a star formation tracer are its sensitivity — for every 2.22 ionizing photons there is one Hα photon — and the relative ease with which observations can be obtained. Being strong, this line can be used even in far off galaxies. Lyman continuum photon luminosity (N_L) can be derived from Hα luminosity ($L_{H\alpha}$) using the following simple equation (Osterbrock 1989), which neglects a weak temperature dependence, and is applicable at densities that are not high.

$$\frac{N_L}{\text{ph s}^{-1}} = 7.32 \times 10^{11} \frac{L_{H\alpha}}{\text{erg s}^{-1}}. \tag{I.1}$$

N_L can also be obtained from Hβ using equation A10 in Appendix A along with the above equation. 8.61 ionizing photons are required to produce one Hβ photon.

The primary limitation of the technique is interstellar extinction internal to the galaxies, which can average from a few tenths of a magnitude in irregular galaxies

such a Magellanic Clouds (Caplan and Deharveng 1986), to 1–3 magnitudes in normal spirals (Israel and Kennicutt 1980; Kennicutt 1983) and much more in highly obscured infrared-luminous galaxies. However, extinction towards optically emitting regions can be estimated by observing the regions both in Hα and Hβ line and using the relations given in Appendix A. While it is one of the most widely used methods for extinction correction, there are problems with this method. These are discussed in the following.

Colours and Equivalent Widths

Optical continuum emission has the largest contribution from intermediate mass stars and hence gives complimentary information to Lyman continuum photon counting. Early understanding of the SFRs and evolutionary properties of disks was reached mainly from modelling the colours (Searle, Sargent and Bagnuolo 1973; Huchra 1977; Larson and Tinsley 1978). Using $U - B$ and $B - V$ colours integrated over galaxies, Larson and Tinsley (1978) inferred enhanced current star formation in a sample of peculiar galaxies compared to normal galaxies. In the case of H II regions, the colour-colour diagrams can be used to constrain IMF parameters.

The ratio of emission line intensity to the underlying continuum, known as equivalent width is independent of extinction and serves as a very good diagnostic ratio for IMF in GEHRs. Equivalent widths at Hα and Hβ are observationally easy to obtain and have been used by several workers to investigate IMF and estimate SFRs (Kennicutt 1983, De Gioia-Eastwood 1985). The Balmer line emission is a measure of massive ionizing stars, whereas the continuum at optical wavelengths is dominated by intermediate mass main sequence stars ($M \sim 5 - 10\ M_\odot$) and disk giants ($M \sim 0.7 - 3\ M_\odot$), the ratio is very sensitive to the IMF slope. Combining the equivalent widths with colours helps to constrain lower and upper cutoff masses of IMF for regions with moderate evolution. Using Hα equivalent widths and $B - V$

colours of galaxies, Kennicutt (1983) found the data to be in good agreement with Salpeter's slope for a sample of normal galaxies. Similar conclusions were drawn by Baut, Donas and Deharveng (1987) from a comparison of total $H\alpha$ and ultraviolet fluxes in a sample of spiral and irregular galaxies. There are other studies which find a different value from that of Salpeter's (Jensen, Talbot and Dufour 1981). The derived values are heavily dependent on the adopted extinction model.

2.3 Summary of Previous Studies

From the studies done so far it is clear that it is not yet possible to derive the absolute value of IMF slope from the observed data. Most of the problems involving IMF determinations can be isolated if one chooses individual H II complexes as star forming units instead of entire galaxies. Surprisingly, very little study has been carried out on star formation in individual regions after the work of De Gioia-Eastwood (1985), who investigated IMF in three H II regions in NGC 6946, a late type Sd spiral. The IMF in 30 Doradus in Large Magellinic Cloud (LMC), which is the nearest giant H II complex, is studied by the direct method itself. Melnick (1985) suggests that the IMF in this region might be considerably flatter. In addition, Massey *et al.* (1989) have studied three H II regions in LMC and SMC and all are consistent with a power-law slope of 2.8 over a mass range 10–85 $M_\odot$. There has been some study of star formation in slightly bigger systems, collectively known as H II galaxies (also referred to as the blue compact dwarf galaxies, BCDGs, extragalactic isolated H II regions, *etc.*) (Terlevich and Melnick 1981; Terlevich 1985; Campbell, Terlevich and Melnick, 1986; Melnick, Moles and Terlevich, 1987; Viallefond 1985). From the study of H II galaxies and giant H II complexes, the above authors conclude that the observations cannot be explained by a single IMF for all regions. In fact they argue that the slope of the IMF in these objects must decrease with metallicity. However the results are controversial as of now, and need

further investigation.

3. Outline of Present Work

The present work is an attempt in investigating IMF, by reducing the errors due to extinction, age, apertures *etc.* discussed above. GEHRs in external galaxies are studied for this purpose. Most of the past conclusions drawn regarding IMF in individual H II regions were based on observations with narrow slit or small apertures. Thus in a majority of cases, the H II complexes are not fully sampled. It is very common to centre the slits on Hα bright regions, which need not enclose the associated cluster, thus resulting in equivalent widths that are not representative of the entire cluster. Imaging spectroscopic studies by Roy and Walsh (see Roy, Belly and Walsh 1989 and references therein) have shown significant pixel-to-pixel fluctuations of emission line ratios and Hβ equivalent widths in giant complexes. This work highlights the danger of using slit spectroscopic results as typical values for the entire complex. We use aperture photometric data in emission lines and continua derived from CCD images of galaxies to investigate the IMF and SF properties in individual complexes in galaxies. The H II regions are chosen to have published spectroscopic data, giving information on gaseous parameters such as Balmer decrement and oxygen abundance. $BVR H\alpha$ photometry of individual H II regions is carried out on our image data. The observed values are corrected for interstellar extinction using the reddening obtained from Balmer decrement and galactic extinction curve, for uniform distribution of dust clouds following normal conventions. The amount of gaseous emission within each of the BVR bands is estimated and subtracted from the band. These data are used to form a dimensionless quantity $\frac{\phi}{L_B}$, which is the ratio of equivalent Hβ luminosity to B band luminosity. The expected values of this quantity and $B - V$ and $V - R$ colours are computed using Evolutionary Population Synthesis Model, for a range of IMF

parameters, age and metallicities. The extinction corrected pure stellar quantities are then compared with the models to get a handle on the IMF parameters and star formation.

Chapter II describes instrumentation, observations, reductions and calibration details. The instrument used for observations in this study is calibrated in the course of this work and hence some of the basic details about the instrument are also included in this chapter. The methods followed for the gain calibration of the CCD detector are described in the context of one of the CCDs used in the present observations. Atmospheric extinction coefficients are reported for all the photometric nights (Table II.3). Methods used for the photometric calibration of broadband and narrowband filters are also described. The resulting transformation coefficients are presented in Table II.4. BVR photometry of one of the routinely observed standard fields in the star cluster M 67, is presented in Table II.5. Synthetic aperture photometric techniques for stars and H II regions, developed during the course of this study, are described. H II region magnitudes are highly affected by systematic errors introduced by the uncertainties in the "true" background values. A method parametrizing the errors on the measured magnitudes as a function of uncertainties in the background is suggested and implimented.

Chapter III contains the catalogue of GEHR photometry, along with identification charts (Fig. III.1–9). First, the criteria for selecting the sample of H II regions are described. The galaxies in the sample are described briefly and the calibration details for each galaxy are discussed. The photometric catalogue containing results in $BVRH\alpha$ bands is presented in Table III.4. The table also contains results on $BVRIH\alpha H\beta$ [O III] λ 5007 photometry for two galaxies in the sample. Aperture growth curves around the nucleus of the programme galaxies are represented graphically in Figures III.11-18 and are presented in Table III.5. These results are compared with the existing BV photoelectric photometry.

Chapter IV describes the model developed as a part of the present work for synthesizing the observational properties of GEHRs. The basics of modelling star clusters are given along with the sources of input stellar data. Some of the basic quantities of stars, used as inputs to the cluster model, are presented in Table IV.1. The observational parameters, namely, the ratio of equivalent Hβ luminosity to B band luminosity, denoted as $\frac{\phi}{L_B}$, and $B-V$ and $V-R$ colours are synthesized in the models and their sensitivity to the input parameters is studied. The most important results are shown graphically. Table IV.2 contains results of this study for selected models. The effect of statistical variations in stellar mass and numbers on the derived properties is also studied (Table IV.3). Gaseous contribution to the broad bands are estimated using Hβ luminosity and temperature of the nebula. The model results are compared with that of Mas-Hesse and Kunth (1991) and the agreement is found to be good.

In **Chapter V** observational data are compared with the model and useful parameters are derived. Regions having spectroscopic data giving information at least on Balmer decrement and oxygen abundance are selected from our photometric catalogue. Broadband continuum fluxes are corrected for nebular contribution. The resulting quantities are dereddened using Balmer decrement and galactic extinction curve. The errors on the derived quantities are discussed and the observed values of $\log(\frac{\phi}{L_B})$ and $B-V$ are compared with the models. The dereddened colours are shown to be too blue. A dereddening prescription is evolved, which brings the observations in agreement with theory. It is shown that the corrected colours show a strong evidence for multiple star bursts in most GEHRs. Composite colour photographs of four of the programme galaxies are reproduced. Emission line and continuum structure of GEHRs are studied based on these images.

Chapter VI summarizes the major results of this study. Scope for future studies are discussed in the end. The main results are that (1) about 50% of the stellar

photons do not experience any extinction; (2) about 50% of ionizing photons are not detected either because they escape from the densest regions of the nebula or because some Hα photons are totally absorbed by intervening clouds; (3) most of the regions show evidence for the presence of red supergiants indicating that the regions have experienced at least two bursts of star formation during the last 10 Myr; spiral arms in NGC 2997 and 4303 show complexes, in which an older population is spatially separated from the younger population; (4) masses of the order of 10^5 M$_\odot$ are converted into stars in each burst. The scope of future multiwavelength and high spatial resolution observations useful towards more accurate modelling of these regions is also discussed.

II. INSTRUMENT CALIBRATION AND REDUCTION SOFTWARE

Telescope, instrument and detector form important components of any astronomical observation. The telescope does the job of collecting the photons, while the instrument analyses them, and the detector registers and stores them in a format convenient for future analysis. In the case of imaging in a selected band of electromagnetic radiation, the speed and the image scale are decided by the focal ratio F/D of the telescope, F being the effective focal length of the telescope and D the diameter of the primary mirror. Modern electronic detectors known as Charge Coupled Devices (CCDs) serve as ideal detectors for most astronomical applications and have replaced photographic plates in almost all observatories.

The observational data required for the present work were obtained with the 1-m and 2.34-m telescopes of Vainu Bappu Observatory (VBO), during the observing seasons 1989–92. The 1-m telescope is a Carl Zeiss reflector, with its $F/13$ Cassegrain focus used for imaging purposes. The CCD chip is a Thomson CSF TH 7882 type obtained from the Photometrics Ltd, USA, with pixel size of 23 μm on each side and a format 384×576. The 15.6 arcsec mm^{-1} image scale corresponds to an image scale of 0.357 arcsec pixel^{-1} and a total field of view of 137 $\times$ 206 arcsec^2. The controller and the data acquisition system have also been procured from the Photometrics Ltd. The 2.34-m Vainu Bappu Telescope (VBT) is equipped with a CCD dewar containing a GEC P8603 chip obtained from the Astromed Inc. U. K. The pixel size in this chip is also 23 μm on each side. The 385×578 pixel format at the $F/3$ prime focus of VBT, gives a total field of view of 3.56×5.35 arcmin^2 with an image scale of 0.555 arcsec pixel^{-1}. The performance of both these systems were closely monitored during the course of observations. The details of calibration and the results form a major part of this chapter. Most of the observations were obtained with 1-m telescope and hence the calibration

procedures adopted for this system are described in greater detail in this chapter. The Photometrics CCD system at the 1-m telescope will be referred to as PCCD and the Astromed system at the VBT as ACCD, throughout this thesis. In the last section of this chapter, the software developed for the aperture photometry of stellar and extended objects on CCD images is briefly described.

1. CCDs as Detectors

CCDs are 2-dimensional detectors made up of semiconductors and work on the principle of creation of a hole-electron pair by an incident photon. The elctronic charge so generated is measured and stored, wherever photons are incident by applying suitable electrostatic voltages. Each detector element or *pixel* is *read out* after the exposure is over and the resulting analog signal is amplified and converted into digital counts. Being digital in nature, the resulting images can be displayed and assessed immediately after each exposure. Compared to photographic plates, which were the only 2-dimensional detectors available for most part of this century, CCDs have several advantages. They have a higher sensitivity and and they are linear over a wide range of signal levels. Because of their re-usability, CCDs can be accurately calibrated. Presently, the only limitations of CCDs are their small size and hence they cannot be used in applications which demand high spatial coverage. CCDs are good detectors of cosmic ray particles producing high counts over the pixel that intercepts a particle as also one or more adjacent pixels. For exposures longer than 30 mins, too many pixels will be affected by cosmic ray events.

The thermal agitation of electrons within the simiconductor gives rise to lot of electrons within a CCD at room temperatures. Thermal charge, also known as *dark signal* decreases rapidly with decreasing temperature and hence for astronomical applications the CCDs are operated at liquid nitrogen temperatures. Temperatures around $-120°$ C are preferred for most CCDs. Spectral response of CCDs also

peaks at these temperatures. Intrinsically, the sensitivity of a CCD peaks in the red falling very steeply for blue photons. The CCD surface is hence coated with a suitable dye to convert the blue photon into a red one and thereby enhance the sensitivity in the blue and ultraviolet parts of the spectrum. Both the CCDs in use are coated.

1.1 Basic Properties and Reduction Methods

The detection mechanism in CCDs can be summarized by the following equation. In a unit integration period, N_e electrons are accumulated on a typical pixel as given by

$$N_e = b_e + d_e + f S_e, \qquad (\text{II.1})$$

where b_e is the DC offset ('bias') applied (in units of electronic charge) to avoid negative signal caused by fluctuations due to noise, d_e is the number of thermal electrons generated, referred to as 'dark' and S_e is the number of electrons generated due to signal photons. The factor f varies from pixel to pixel, and denotes the relative quantum efficiency. The process of correcting for this is known as 'flat fielding'. If G denotes counts in Analog to Digital Units (ADUs) or Data Number (DN) corresponding to one electron (and hence one photon), the equation can be rewritten as

$$N_c = N_e G = b_c + d_c + f S_c, \qquad (\text{II.2})$$

where N_c, b_c, d_c, and S_c are in units of DN. The preliminary reduction of a CCD image involves correcting for different terms in the above equation, which are explained in detail below, in the context of CCDs that were used for observations in this work.

Bias

The quantity b_c appearing in the above equations is the bias value on a single pixel.
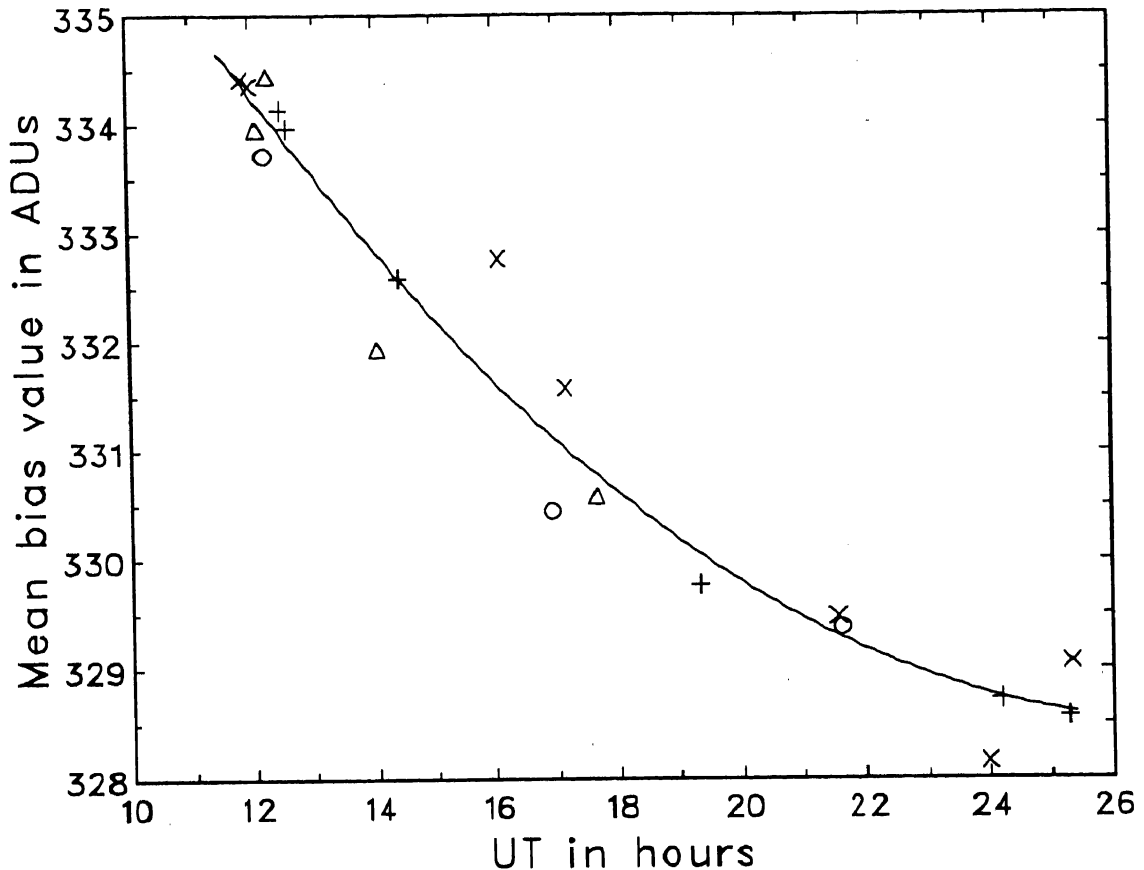
Figure II.1 Variation of mean bias level of CCD over four different nights. The continuous line corresponds to a quadratic fit to the data. The first bias frame is obtained about 30 min after switching on the system. The CCD display temperatute was stable at -120.2^0 C throughout the nights.

In principle, the bias value over the entire frame need not be the same and hence has to be estimated for every pixel in the array. This is done by reading the charges, over the smallest possible integration time, without allowing any light to fall on the CCD. The acquisition software allows obtaining such a frame, known as the bias frame. The first step in the reduction involves subtraction of a good estimate of b_c from the object frame.

An inspection of many bias frames over several nights in 1991 with PCCD showed that the first 2–3 rows have lower counts and first 2–3 columns have higher

counts compared to the mean value in the frame. Hence the first four rows and columns were trimmed out from each frame, bringing the frame size to 380×572 format. The mean counts in the trimmed bias frames varied by less than a count over the entire frame and hence mean values can be used as good estimates. This mean value is found to decrease over a night by about 5–6 counts, in spite of a stable CCD temperature. This is depicted in Fig. II.1 for four nights in February and March in 1991, when the system was continuously on throughout the night (12–14 hours). Such an effect can be explained if some of the components in the controller are sensitive to ambient temperature, which is found to decrease steadily over a night. In subtracting bias levels from all object frames, this variation is taken into consideration. As can be seen in the figure, the decrease is more rapid in the early part compared to the later part.

From the observations carried out with the ACCD system on 5 nights during 1992 March–April, the variations over bias frames are found to be negligible as with PCCD. From the limited data on these nights no significant variation of the mean value could be inferred. First 5 rows and columns are trimmed in these frames to get a final format of 380×574.

Dark

Counts registered on the CCD with the shutter of the CCD closed are due to thermal currents in the semiconductor and are referred to as dark counts (d_c). At the operating temperatures of $-120°C$, the dark counts are less than a few counts even for exposure times of 30 min. Hence no correction is applied to account for dark counts.

Flat Fielding

The quantum efficiency of CCD pixels differs from pixel to pixel. It is very important to estimate the relative efficiency of different pixels accurately before correcting

18

the object frames. An exposure indicating the relative response of different pixels can be obtained by exposing the CCD to a uniform field (flat field). Efficiency is also dependant on wavelength and hence the spectrum of the spatially uniform source should match that of the object of interest as closely as possible. The relative counts in a flat field exposure represent pixel properties only if the counts are high enough to reduce the photon noise relative to the signal. Blank regions in the night sky serve as good flat source, both in terms of uniformity and spectrum, but require enormously long exposure times to build up a good signal. Thus in normal practice, either twilight skies or illuminated dome or white board are used as flat field sources. Flatfield frames also help in estimating the relative efficiency of the telescope and optics as a function of position known as 'vignetting'. This information can be obtained only from sky frames, since the dome is a nearby object.

Twilight sky flats exposed to a level of 10000–15000 counts in each filter are used in flat fielding all the images with the PCCD. These count levels correspond to 2.7–4.1 $\times 10^5$ electrons pixel^{-1} or signal-to-noise (S/N) ratios of 500–600. In order to achieve 1% accuracy of f, the flat field frames should have exposure levels exceeding 10^5 electrons (Prabhu, Mayya and Anupama 1992). Normally 2 or more flat exposures taken just after sunset and before sunrise are stacked together, normalized to the mean of a 10×10 box near the centre of the chip, and used for flat fielding the object frames taken during that night. When more than three flat field frames are available, stacking is done with the median option. Main features noticeable on all flat fields are :

i) A slow gradient from row number 200 to 1, with the efficiency of pixels in the first row being around $80 - 90\%$ of those in the 200th row. The gradient is as a result of vignetting caused by the insufficient hole size in the field-viewing flipping mirror. It is also noticed that the steepness of the gradient mentioned above depends on the inclination of the telescope during flat field exposures, causing flat field errors

of $\sim 10\%$ in some cases. These errors are due to the scattered light entering the CCD directly and are found to reduce if precaution is taken to avoid direct entry of light, through the offset mirror assembly.

ii) Dark rings of diameter 30–50 pixels. The annular portion of the ring is around 7 pixels wide with the darkest regions having efficiencies in the range 96–97%. Such rings are reported in a similar system at University of Toronto Southern Observatory (UTSO), and are possibly due to the dust settled on the window of the CCD dewar (McCall, English and Shelton 1989). Generally rings are well-corrected in the process of flat fielding.

In addition there are about 10 highly inefficient pixels which are not well-corrected even after flat fielding. Over the years there has been a constant increase in both the number of rings as well the number of inefficient pixels.

The methods followed for flat fielding with the ACCD system are very similar to those described above. Total variation of the flat field is around 4%, without showing any signs of vignetting. Dust rings are not prominent for this CCD.

The final equation used to obtain object counts (s) from the observed counts (n) is as follows.

$$s_{ij} = \frac{n_{ij} - \langle b \rangle}{\langle f_{ij} \rangle}, \tag{II.3}$$

where the suffixes i, j indicate a particular pixel in the CCD array. $\langle b \rangle$ is the bias value averaged over a frame, and $\langle f_{i,j} \rangle$ denotes the stacked and normalized flat field frame.

The software packages presently available have routines to do the above operations of division and subtraction on images. *STARLINK* is one of the major software packages used today by many optical astronomers. This package is available on the VAX 11/780 computor at VBO. *EDRS* is one of the subpackages of *STARLINK*, which has routines suitable for operations on images. *STARLINK* is supplimented by many locally written programmes incorporating *COMTAL* as the

display device. This was necessitated by the absence at VBO of *ARGS* display system which *STARLINK* uses. Operations on images such as subtraction, division, stacking *etc.* are performed using the *EDRS* routines such as *ARITH, IMGARITH, NSTACK*. These routines work on integers and hence after every arithmatic operation, some noise is introduced due to truncation. However care is taken to reduce truncation errors by proper choice of image headers namely BZERO (additive) and BSCALE (multiplier).

1.2 CCD Gain and its Calibration

The charge (q) accumulated in a CCD pixel is converted to voltage $V_0 = \frac{qA}{C}$, where C is the output node capacitance and A, voltage gain of the analog amplifier. An analog-to-digital converter (ADC) digitizes the voltage such that a specific voltage (V_m) is converted to a specific number of bits. The full-well capacity of some CCD chips exceeds 500,000 electrons (McLean 1989). It is easier to use an ADC with 14–16 bits, which, at 1 electron per count will utilize only $3 - 13$ per cent of the dynamic range. For applications demanding higher dynamic range one count or Data Number (DN) should correspond to more than one electron.

The system gain can be computed if the capacitance at the output node, the voltage gain of the amplifier, and the conversion factor at the ADC are known. On the other hand, it can easily be determined experimentally (*cf.,* Djorgovski 1984; Mackay 1986; Horne 1988; McLean 1989; McCall, English and Shelton 1989). Prabhu, Mayya and Anupama (1992) have examined the experimental methods of calibrating the gain and readout noise of a CCD system, and have evolved a simple and accurate method using flats obtained routinely during spectroscopic observations. Here we describe the experiments carried out for determining the values of gain and readout noise using imaging observations, with PCCD.

1.2.1 The Methodology

The gain calibration of a CCD system can be effected by studying its noise characteristics. The mean and variance of observed counts for a uniform illumination can be written as

$$\langle N_c \rangle = b_c + d_c + \langle S_c \rangle, \tag{II.4}$$

$$\sigma^2 = G^2 B_e^2 + G(d_c + S_c) + \sigma_f^2 S_c^2, \tag{II.5}$$

where B_e is the base-level noise in electrons and equals the sum in quadrature of the readout noise (R_e) and noise from other signal-independent sources (Newberry 1991). We have assumed in deriving Equation (II.5) that the noise in electrons generated thermally as well as due to signal is Poissonian. The noise in signal electrons equals $\sqrt{S_e}$ electrons (*cf.*, Newberry 1991), and hence the noise in the signal counts is $G\sqrt{S_e} = \sqrt{GS_c}$ counts. We also assume that the mean value of f is unity (definition). In the following, we drop the angular brackets for simplicity. We will also assume that the mean thermal counts and bias have been subtracted from the data and the rms thermal noise has been subtracted from the derived noise. Most CCD chips currently available have very low thermal charge, and hence also its variance, at liquid nitrogen temperatures. Equation (5) can thus be written as

$$\sigma^2 = G^2 B_e^2 + GS_c + \sigma_f^2 S_c^2. \tag{II.6}$$

It is clear from Equation (II.6) that it is possible to determine G and B_e using a set of observed, bias- and dark-subtracted, signal counts (S_c) and their rms scatter (σ), sometimes referred to as the variance diagram. A set of flatfield images obtained at a range of illumination levels (or equivalently exposure times) can be used to this end. A quadratic fit to the data yields all the constants in Equation (II.6). In practice, the use of graded exposures spanning a sufficiently broad range of signal levels results in the propagation of errors downwards, *i.e.*, $\epsilon(\sigma_f^2 G^2) \ll \epsilon(G) \ll \epsilon(G^2 B_e^2)$. This problem can be alleviated by the procedures described below.

22

The accuracy of determination of G in Equation (II.6) can be enhanced by reducing the magnitude of the third term in the equation. The quadratic term arises due to pixel-to-pixel sensitivity variations as also on the non-uniformity of illumination in the flatfield. The most accurate way of reducing the flatfield variations is to correct for them by using an accurate flatfield frame. The alternative approach of reducing the effect of flatfield noise by division or subtraction of two flats is described in detail in Prabhu, Mayya and Anupama (1992). In practice, it is not possible to correct for pixel-to-pixel variations exactly, but only to a desired accuracy. If one desires that the third term in Equation (II.6) should not be larger than the second term even at the largest values of S_c, one obtains the condition that $\sigma_f \lesssim [G/S_c(\text{max})]^{\frac{1}{2}} = S_e(\text{max})^{-\frac{1}{2}}$, where σ_f is the residual flat-field variation. For a signal reaching the full-well capacity of 10^5 electrons, this implies that the flatfield corrections should be carried out to an accuracy of 0.3% in order to achieve 1% accuracy in σ_f. Many flats need to be stacked to obtain a master flat accurate to this level. It should be noted that the individual images used for obtaining the master flat cannot be used to study the noise statistics since the master contains the memory of the noise in individual flats. The corrected flats would, in such a case, show a lower-than-real noise. An independent set of flats, corrected using the master flat, should be used to determine the noise statistics. A quadratic fit of Equation II.6 would still be necessary for the determination of G, though the constant σ_f^2 would now be very small. An example of this procedure is given by Horne (1988). Having reduced the quadratic term in Equation II.6, the values of G and B are determined using a fit based on the Marquardt alogorithm. The results are presented below.

For PCCD system the electronic gain can be selected through software using the command "n   cgain" where the parameter n can take any integral value between 0 and 4095. The R band, twilight sky flat images obtained using this system during the imaging observations of 1991 April 16 and May 16 were used in the analysis. In addition to well-exposed flats obtained routinely during observations, additional graded flats were obtained to uniformly cover lower signal levels. The gain setting 'cgain' = 0 was used in April, whereas a value of 33 was used in May. A set of flats were stacked to obtain a master flat accurate to $\sim 0.1\%$. The remaining flats were corrected for pixel-to-pixel sensitivity variations, as also for the vignetting in the system, using the master flat. An area of the corrected flat enclosed by the rows (201, 500) and columns (101, 300) was used for determining the statistics, since this area was less affected by vignetting. The mean signal counts were determined from the flats before correction, in order to represent the signal accurately before correction for vignetting. The rms noise was estimated over contiguous boxes of 5×5 pixels after rejection of deviants over three iterations. This procedure determines the local variance and should be relatively free of errors due to incomplete flatfield corrections.

The initial estimates of G and B were obtained by a linear regression analysis, and were improved iteratively using the Marquardt algorithm. Equation II.6 was fit both in the linear domain and in the logarithmic domain. Fits were attempted by including as well as neglecting the quadratic term. In general, the logarithmic fit was better as it passed through the bias values closely. It was noticed that whenever the quadratic term was negligible the fit tended to yield a negative value for the last coefficient. In such cases, as also whenever the value of the coefficient was less than its formal error, it was decided to use the fit that neglects the quadratic term.

The final results are presented in Table II.1. and the statistical data and the
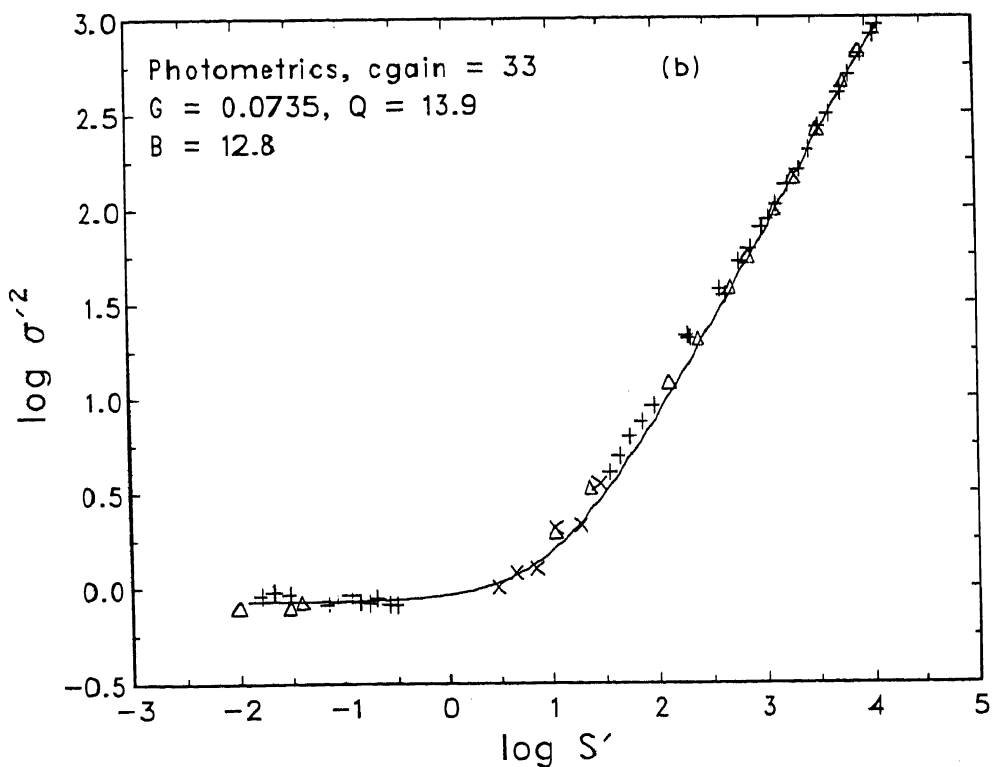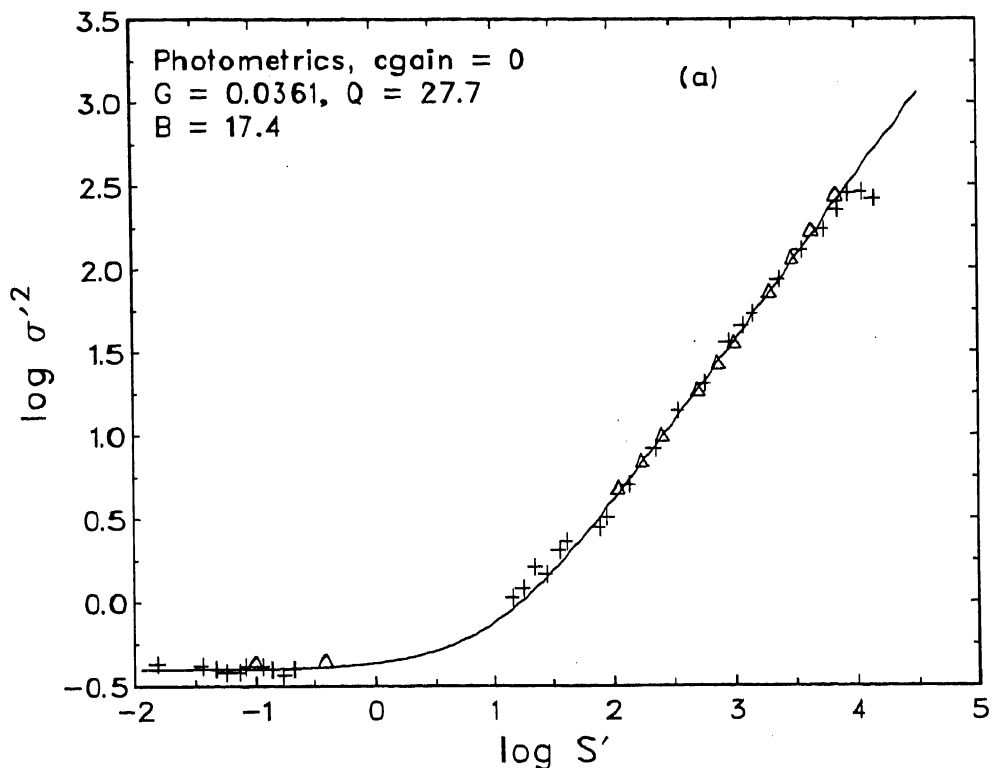
Figure II.2(a). The logarithmic plot of variance versus signal together with the theoretical fit for the Photometrics CCD system at cgain = 0. A larger number of points from spectroscopic data were used in deriving the fit, especially in the range $150 \leq S \leq 5000$; also the variance of bias counts is shown as $\log S < 0$. **(b)** Same as (a), but with cgain = 33. The fit is based on spectroscopic data in the range $300 \leq S \leq 10000$, and the bias statistics.

Table II.1 System gain and readout noise.

cgain	B	G	Q
	electrons	DN electron^{-1}	electrons DN^{-1}
0	17.90	0.0367	27.26
	0.10	0.0001	0.09
33	11.85	0.0761	13.15
	0.10	0.0004	0.07

Notes:

Formal errors of the fit appear below the values.

adopted fits are shown in Figs II.2(a)-(b) for cgain=0 and 33 respectively. The formal errors of G and B are $< 1\%$. It is apparent that even though flatfielding is done to an accuracy of $\lesssim 1\%$, the variance contains the effect of flatfield to the level of $\sim 1\%$. Prabhu, Mayya and Anupama (1992) showed that the fits to the spectroscopic data give better results and hence those results are used in further applications. The curves shown in Figs II.2(a)-(b) are the results of fits to spectroscopic data. The resulting values of Q are 27.7 electrons DN^{-1} for cgain $=$ 0 and 13.7 electrons DN^{-1} for cgain $=$ 33, which differ from the values given in Table II.1 by < 5 per cent.

1.3 S/N of CCD Observations

The signal-to-noise ratio of a CCD observation is given by (Newberry 1991),

$$S/N = \frac{C_0}{[G + n\sigma_{bg}^2 C_0^{-1}]^{1/2}}, \qquad (\text{II.7})$$

where C_0 denotes the observed counts from an object integrated over n pixels, and

$$\sigma_{bg}^2 = C_{sky} + B^2$$

is the net noise squared, which includes noise due to sky counts and base level variations. Limiting case of base level noise is the readout noise but substantial

contribution can come from truncation due to digitization, patterns due to mains pickup *etc.* A detailed analysis of the base level noise for the systems used here is given in Prabhu, Mayya, Anupama (1992). It can be seen that, when the counts from the object are much larger than the noise counts $[n\sigma_{bg}^2 \ll C_0^{-1}]$, the S/N ratio approches the value expected from photon noise alone.

2. Photometry with CCDs

Photometric observations are often classified between broadband, intermediate band, narrowband and spectrophotometry, depending on the bandwidth of observations. It is important to transform each observation into some standard system or units, so that data collected by different observers at different telescopes can be directly compared. The most common broadband system in use is due to Johnson. Although the filter system was originally designed to suit photoelectric tubes as detectors, suitable combination filters have been designed to match the net filter responses with CCDs as well (see Bessell 1990). These bands have bandwidths ~ 1000 Å, and are defined such that for Vega (α Lyrae, a star of spectral type A0), the V magnitude and all colours (the magnitude difference between two bands) have values identical to zero. Among the intermediate band systems, the one which is commonly used is due to Stromgren (see Stromgren 1966). In Narrowband photometry, one uses filters enclosing a particular line of interest. Line fluxes (in the case of emission lines) and flux deficits (in the case of absorption lines) are estimated after subtracting continuum in an equivalent band at a nearby continuum. It is conventional to express the resulting fluxes directly in flux units *e.g.* erg cm^{-2}s^{-1}. The term spectrophotometry is used when the fluxes are determined over a large number of adjacent wavelength bands at resolutions $\ll 100$ Å, which can be achieved through spectroscopic means.

The data obtained for this work are based on broad and narrowband photometry.

In the remaining part of this section, the methods generally followed for accurate photometry are described in detail, with special emphasis on CCD photometry with the systems we have used.

2.1 Description of the Filter Systems used

Results presented in this thesis are based on observations made during the observing seasons of 1990, 1991 and 1992, both with 1-m and 2.34-m telescopes at VBO. The observational programme involved obtaining calibrated images of galaxies in $BVRH\alpha$ bands. As part of development, the filters had to be changed every season during this period. Glass filter combinations suitable for BVR photometry were designed and used with the CCD in 1991 along with an interference filter of bandwidth 160Å, centred around 6563 Å. Table II.2(a) lists the combinations used.

The combined thickness of different sets of filters was maintained the same (4mm) to avoid focus differences. The filters were circular in shape with outer diameters of 25mm. The glass combinations used for B and V are identical to those of Bessell (1976), while for R, RG 610 was used instead of OG 570 for lower wavelength cut-off following Schild (1983), since this was readily available. Our combination results in shifting of the effective wavelength for R band slightly towards red, bringing it closer to Hα . This is advantageous when one wishes to estimate in-band continuum at Hα from R band images. Filters coated to produce the net response of BVR bands are used in 1992 at the 1-m telescope. These had outer diameters of 50 mm. The filters used with the VBT were similar to the above set. Details of these filter systems are given in Table II.2 (b). The narrowband filters used for the emission line photometry are interference filters.

Most of the observations were obtained with 1-m telescope in 1991 and hence the calibration procedures adopted for this filter system is described in greater detail below. The filter systems available before 1990 at 1-m telescope has been described

28

Table II.2(a) Glass filter combinations used with PCCD in 1991

Band   Components (thickness in mm)

B	GG 13 (2) + BG 12 (1) + BG 18 (1)
V	GG 14 (2) + BG 18 (2)
R	RG 610 (2) + KG 3 (2)
Hα	6563/160

Table II.2(b) Details of coated filters

Band	$\lambda_0/\Delta\lambda$	
	PCCD-1992	ACCD
B	4400/1050	4400/1050
V	5425/1050	5425/1050
R	6550/1300	6550/1300
I	8150/1700	8150/1700
Hα	6563/100	6563/50
Hβ	4862/73	4861/50
[O III]	5008/75	5007/50

by Sagar and Pati (1989). Calibration of filter sets available at 1-m telescope in 1992 and those at VBT are done in a similar way, and the results are described briefly in section 2.4.

2.2 Atmospheric Extinction

Earth's atmosphere affects the amount of light reaching the telescope from a source. The molecules in the earth's atmosphere absorb as well as scatter the incoming light. The absorbtion and scattering are dependant on the thickness of the atmosphere and hence on the altitude of the site. The absorption, which is independent of

wavelength (neutral absorption), has a scale height of 1.5 km. Rayleigh scattering is the main scattering process, which has a strong wavelength dependence, and a scale height of 8 km. In addition, ozone molecules in the upper atmosphere present a wavelength dependence predominantly in the blue, whereas the oxygen and water vapour give rise to absorption bands at characteristic wavelengths (see Bessell 1990). The combined process of absorption and scattering is known as extinction and can be determined from observations of stars. The dependence of the extinction values on the spectrum (or colour) of the star, known as the second order extinction can also be investigated by observing two stars of extreme colours.

The brightest two stars in the dipper asterism field in M 67 (Schild 1983) were used for atmospheric extinction determinations. The observations were mostly done at five equal intervals of airmass in the range 1–2. These stars have a large colour difference($\Delta(B - V) = 1.4$ mag) and hence are useful in determining colour dependence of extinction coefficients. The equations discussed by Hardie (1977) are used in the determination of extinction coefficient and are as follows:

$$v = v_0 + k_{\mathrm{v}}\, X \ ,$$

$$b - v = (b - v)_0 + k_{\mathrm{b\text{-}v}}\, X \ , \qquad\qquad\text{(II.8)}$$

$$v - r = (v - r)_0 + k_{\mathrm{v\text{-}r}}\, X \ ,$$

$$k_{\mathrm{v}} = k'_v - k''_v\, (b - v) \ ,$$

$$k_{\mathrm{b\text{-}v}} = k'_{\mathrm{b\text{-}v}} - k''_{\mathrm{b\text{-}v}}\, (b - v) \ , \qquad\qquad\text{(II.9)}$$

$$k_{\mathrm{v\text{-}r}} = k'_{\mathrm{v\text{-}r}} - k''_{\mathrm{v\text{-}r}}\, (v - r) \ ,$$

where lower case letters b, v and r stand for instrumental magnitudes in B, V and R filters respectively and suffix 0 denotes the 'above atmosphere' instrumental magnitudes. k' and k'' with suffixes represent first-order and second-order extinction coefficients respectively.

Table II.3 First-order atmospheric extinction coefficients .

Date	k'_b	k'_v	k'_r
1991			
Jan 13	0.341 ± 0.023	0.166 ± 0.015	0.090 ± 0.013
Feb 13	0.407 ± 0.003	0.214 ± 0.006	0.113 ± 0.002
Feb 14	0.385 ± 0.002	0.206 ± 0.001	0.119 ± 0.002
Feb 15	0.472 ± 0.011	0.295 ± 0.012	0.212 ± 0.016
Mar 16	0.397 ± 0.006	0.187 ± 0.002	0.102 ± 0.002
Mar 17	0.430 ± 0.003	0.224 ± 0.003	0.133 ± 0.007
Mar 18	0.478 ± 0.005	0.259 ± 0.003	0.145 ± 0.002
Apr 14	0.418 ± 0.008	0.237 ± 0.007	0.153 ± 0.006
Mean	0.416 ± 0.045	0.224 ± 0.041	0.133 ± 0.038
1992			
Feb 4	0.527 ± 0.005	0.374 ± 0.009	0.295 ± 0.007
Mar 6	0.753 ± 0.017	0.541 ± 0.012	0.426 ± 0.016
Mar 7	0.702 ± 0.010	0.527 ± 0.013	0.421 ± 0.010
Apr 3	0.631 ± 0.078	0.460 ± 0.038	0.368 ± 0.027

Equations II.8 and II.9 were solved to determine k'' first and then k' values. The second-order extinction coefficients obtained on different nights were found to be similar. The mean values of these coefficients are 0.010 in V, 0.026 in $b-v$ and 0.010 in $v-r$. These mean values are used in the determination of first-order coefficients. The values of first-order coefficients for eight photometric nights in 1991 and four in 1992 appear in Table II.3 together with their errors. The table also contains the mean values for 1991, with the errors representing the nightly variations of the coefficients. The corresponding values for the colours are 0.193 ± 0.017 in $b-v$ and 0.090 ± 0.012 in $v-r$. Allowing for the fact that we have used instrumental colours in our extinction equations, the $B - V$ coefficient reduces to 0.167. Theoretical values for the site calculated using the equations of Bessell (1990) are 0.213, 0.135

and 0.093 for V, $B - V$ and $V - R$ respectively. The relatively higher values for the extinction are because of the lower altitude of the site (725 m). Thus the agreement between the observed and theoretical values are good for V and $V - R$ while the observed coefficients are ~ 0.03 mag higher for $B - V$. It would thus appear that the extrapolation of Bessell's empirical fit is not valid for B band at low altitude sites. It can be seen from the table that the colour coefficients do not change as much as the coefficients in any particular band. The night-to-night variations of extinction values indicate that the scale height of aerosols, which cause neutral extinction, varies from night to night. The extinction coefficients derived on nights in 1992 are systematically higher than the mean values in 1991 (probably due to the increased density of dust as a result of volcanic activity in Philippines !).

2.3 Photometric Calibration of PCCD using 1991 Data

Calibration involves obtaining coefficients to transform instrumental magnitudes to one of the standard systems. This is best done by observing stars of known magnitudes and colours, covering a good range of colours. The usefulness of 'dipper asterism' field in M 67 (NGC 2682) in calibrating CCDs for photometric purposes is discussed by several authors (Schild 1983; Sagar and Pati 1989; Joner and Tayler 1990; Chevalier and Ilovaisky 1991). We have carried out photometry of 16 stars in this field. Ten of these were used to calibrate the system using standard magnitudes of Chevalier and Ilovaisky (1991).

The observations were carried out during 1991 January – April, during the course of observations of programme objects. The dipper asterism field in M 67 was observed regularly in order to obtain accurate transformation coefficients and also the extinction coefficients on each night. The observations were mostly done at five equal intervals of airmass in the range 1–2. Typical integration times were around 5 minutes each in B and Hα, 2 minutes in V and 1 minute in R band. The images

obtained using the Hα filter are intended for studying the colour dependence of Hα to R band flux ratios, of objects without line emission at Hα. All the observations were done at the default gain (parameter cgain = 0).

2.3.1 Photometric Transformations

The 'above atmosphere' magnitudes and colours v_0, $(b - v)_0$ and $(v - r)_0$ are transformed into Johnson-Cousins BVR system by fitting the equations of the following form to our data.

$$B - V = \alpha_{\text{b-v}} + \beta_{\text{b-v}} \, (b - v)_0 \; ,$$

$$V - R = \alpha_{\text{v-r}} + \beta_{\text{v-r}} \, (v - r)_0 \; , \qquad\qquad \text{(II.10)}$$

$$V - v_0 = \alpha_{\text{v}} + \beta_{\text{v}} \, (b - v)_0 \; ,$$

$$B - b_0 = \alpha_{\text{b}} + \beta_{\text{b}} \, (b - v)_0 \; , \qquad\qquad \text{(II.11)}$$

$$R - r_0 = \alpha_{\text{r}} + \beta_{\text{r}} \, (v - r)_0 \; ,$$

where the upper-case letters B, V and R are standard magnitudes in the corresponding filters, taken from Chevalier and Ilovaisky (1991). The fit to the first three equations are shown in Figs II.3(a)–(c), with the ordinates representing colour and magnitude differences. Similar transformations were tried with Schild's (1983) data and we confirm the finding of Chevalier and Ilovaisky that the zero points for the brightest 2 stars are different from the rest in Schild's data. The transformation coefficients are derived for all the nights. Colour coefficients (β) obtained on different nights agree well while the zero points (α) differ by as much as 0.1 mag on different nights. Table II.4, lists the transformation coefficients obtained for 1991 April 14, together with the standard errors of coefficients and the standard error of the fit. The transformations involving R are more colour-dependant than the rest, which

Table II.4 Transformation coefficients to Johnson-Cousins system.

Quantity	α	β	Std. error
PCCD-1991			
$B - V$	-1.037 ± 0.006	1.056 ± 0.004	0.006
$V - R$	0.094 ± 0.003	0.868 ± 0.007	0.007
V	18.292 ± 0.004	0.018 ± 0.003	0.004
B	17.256 ± 0.007	0.073 ± 0.005	0.007
R	18.217 ± 0.003	0.160 ± 0.007	0.007
$(r - h)^\dagger$	-2.114 ± 0.004	0.023 ± 0.011	0.011
PCCD-1992			
$B - V$	-0.433 ± 0.009	1.348 ± 0.010	0.013
$V - R$	-0.096 ± 0.007	0.973 ± 0.015	0.012
V	19.498 ± 0.008	0.010 ± 0.010	0.011
B	19.065 ± 0.008	0.358 ± 0.010	0.012
R	19.596 ± 0.006	0.040 ± 0.014	0.011
$(r - h\alpha)^\dagger$	-2.989 ± 0.006	0.199 ± 0.010	0.010
$(v - o3)^\dagger$	-3.161 ± 0.014	-0.469 ± 0.018	0.021
$(b - h\beta)^\dagger$	-3.665 ± 0.031	0.553 ± 0.040	0.046
ACCD-1992			
$B - V$	-1.222 ± 0.015	1.267 ± 0.010	0.013
$V - I$	-0.630 ± 0.017	1.063 ± 0.014	0.019
V	21.150 ± 0.015	0.098 ± 0.010	0.012
B	19.928 ± 0.026	0.365 ± 0.018	0.022
I	21.821 ± 0.017	0.019 ± 0.014	0.019
$(i - h\alpha)^\dagger$	-3.429 ± 0.021	-0.351 ± 0.017	0.024
$(v - o3)^\dagger$	-3.170 ± 0.053	-0.548 ± 0.037	0.045
$(b - h\beta)^\dagger$	-3.846 ± 0.046	0.496 ± 0.032	0.039

$\dagger$ see text for definitions.

is expected because the effective wavelength of our R band is $\sim$ 300 Å redder than the standard.
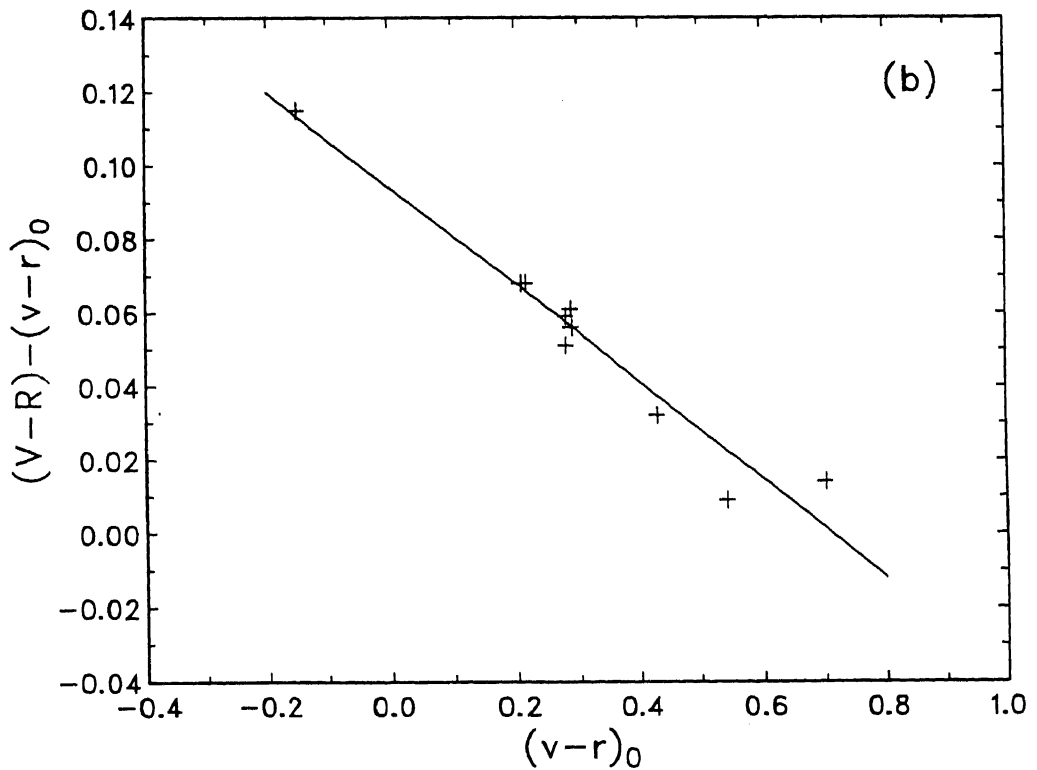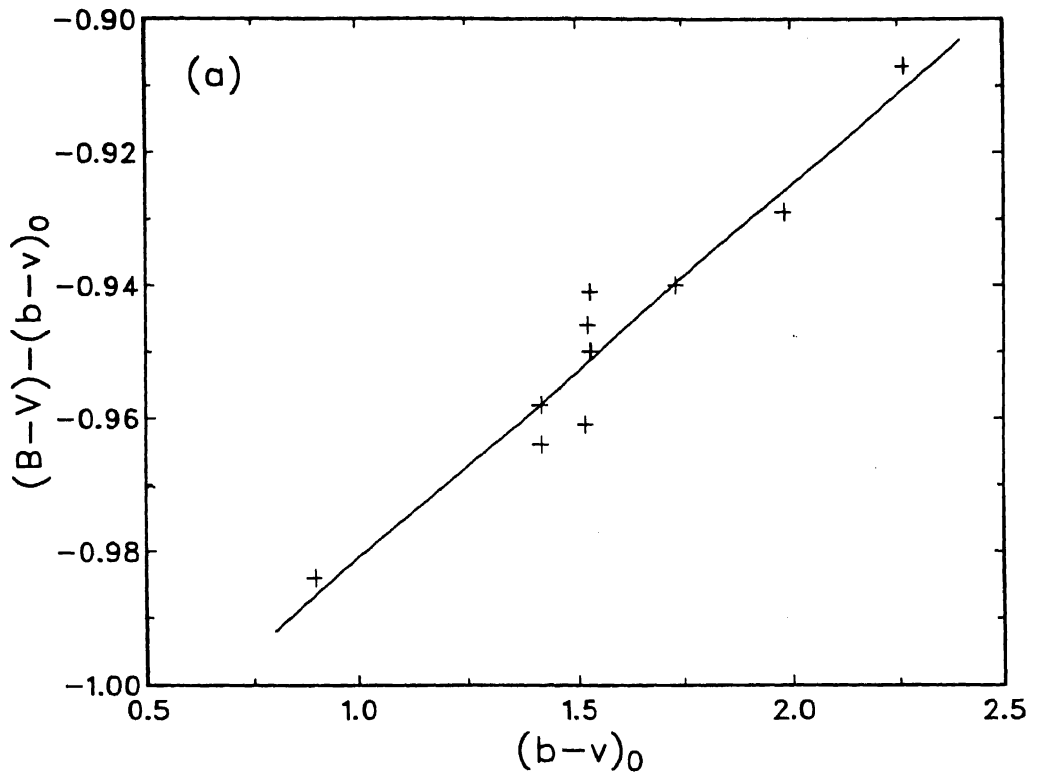
Figure II.3 Standard − instrumental colours (**a**) $B − V$, and (**b**) $V − R$, and magnitude differences (**c**) $(V − v_0)$, and (**d**) $(r − h)_0$ plotted against the extinction-corrected instrumental colours. The least squares fit to the data is represented by the line.
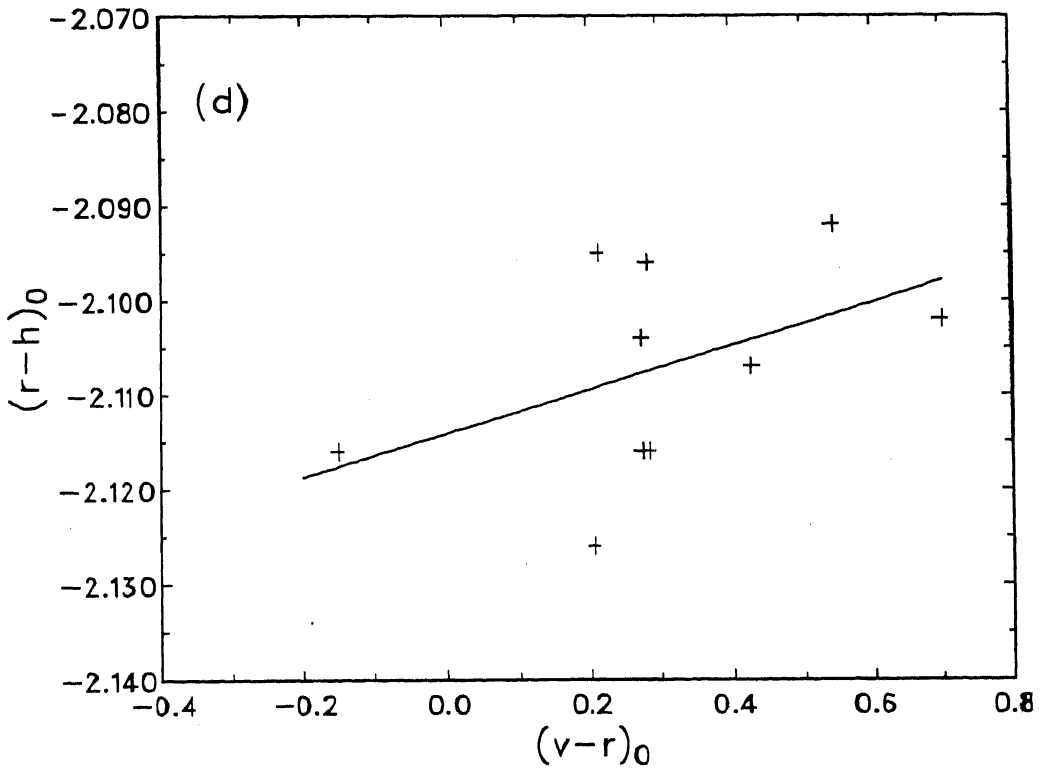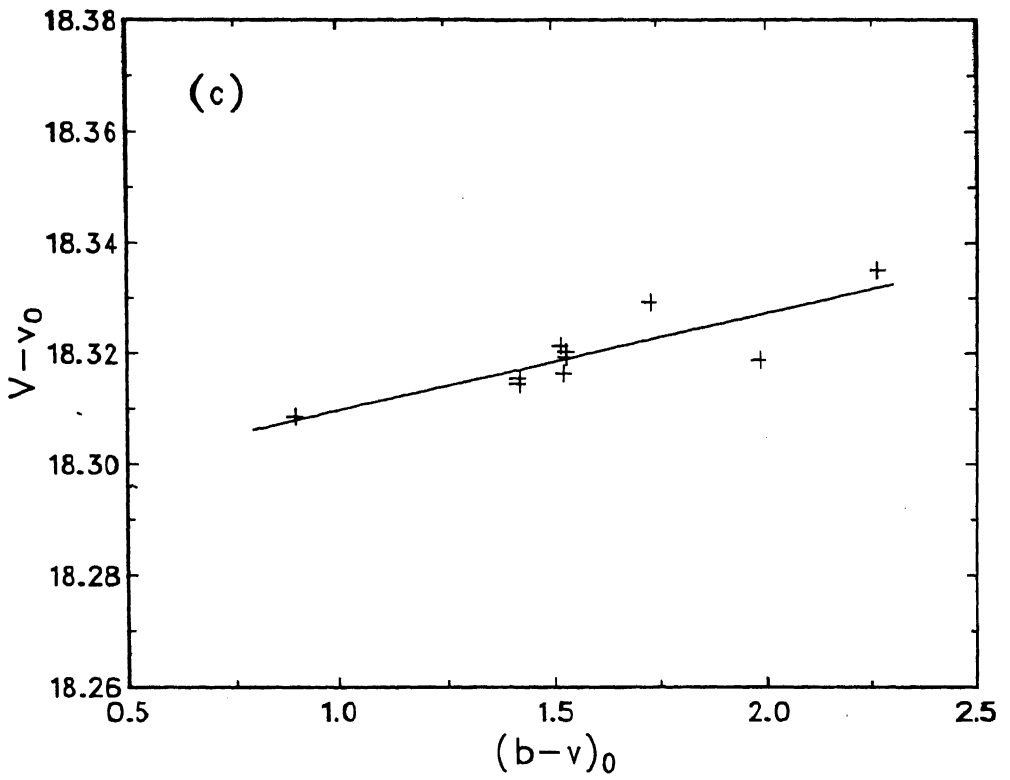
Figure II.3 cont.

The availability of a large number of frames allowed us to estimate the internal consistency of our magnitude measurements. All the stars in a given frame are first transformed into the standard system using the zero points derived from one of the stars in the field (star F 81). All such measurements on a single night (1991 March 17) were used to obtain the average magnitude and rms error for each star given in Table II.5.

Table II.5 Derived magnitudes and colours of M 67 stars.

Id	V	$\Delta^\dagger$	$B - V$	$\Delta^\dagger$	$V - R$	$\Delta^\dagger$	N
F 81	10.022 ± 0.000	0.000	-0.086 ± 0.000	0.000	-0.034 ± 0.000	0.000	5
F 108	9.713 ± 0.005	-0.011	1.353 ± 0.005	0.006	0.734 ± 0.004	-0.020	5
F 117	12.602 ± 0.004	0.034	0.790 ± 0.013	0.004	0.479 ± 0.003	-0.018	5
F 124	12.121 ± 0.002	0.003	0.464 ± 0.008	-0.006	0.294 ± 0.005	-0.011	5
F 127	12.764 ± 0.004	0.001	0.555 ± 0.009	0.002	0.349 ± 0.005	-0.020	5
F 134	12.209 ± 0.023	0.038	0.580 ± 0.009	-0.001	0.357 ± 0.003	-0.010	5
F 135	11.383 ± 0.025	0.049	1.066 ± 0.011	-0.009	0.595 ± 0.005	-0.022	5
F 130	12.874 ± 0.011	0.010	0.453 ± 0.012	0.000	0.286 ± 0.006	-0.010	5
F 128	13.132 ± 0.008	0.015	0.594 ± 0.021	-0.014	0.345 ± 0.012	-0.008	5
F 129	13.166 ± 0.014	0.007	0.600 ± 0.014	-0.011	0.359 ± 0.002	-0.016	5
I-228	12.400 ± 0.002	-0.003	0.744 ± 0.004	0.000	0.434 ± 0.000	-0.008	2
F 111	12.733 ± 0.002	0.009	0.564 ± 0.010	0.004	0.350 ± 0.004	-0.014	2
I-9	13.144 ± 0.041	0.048	0.591 ± 0.010	-0.007	0.351 ± 0.006	-0.016	2
F 83	13.212 ± 0.003	-0.013	0.586 ± 0.018	0.012	0.358 ± 0.003	-0.007	2
I-227	14.158 ± 0.003	-0.026	0.764 ± 0.001	-0.057	0.414 ± 0.008	0.002	2
I-226	13.940 ± 0.004	-0.007	0.623 ± 0.007	-0.031	0.356 ± 0.009	-0.004	2

†The differences in magnitudes and colours in the sense

Chevalier and Ilovaisky (1991) $-$ present work.

An identification chart of this field is reproduced in Fig. II.4 from one of our observations. The rms errors on magnitude and colour determination are ∼ 0.01 mag for majority of stars in the field. The derived magnitudes and colours themselves agree well with the standard values within 0.01 mag. On the other hand, the zero points on different nights vary by as much as 0.1 mag and hence by obtaining zero points for each night, it is possible to reach an overall photometric accuracy of 0.01 mag. The variation of the zero points can be understood as due to the variations in the thickness of the neutral absorption layer.

Five of the 16 stars observed exhibited an appreciable departure (∼0.03–0.05 mag) from Chevalier and Ilovaisky (1991) — F 117, F 134, F 135, I-9 and I-227. Of these, F 134, F 135 and I-9 have higher rms errors and are spatially together on the CCD frame, occupying the first 100 rows. I-227 is the faintest in our list. Hence the observed differences may not be significant for these stars. On the other hand F 117 was consistently brighter by 0.03 mag on all the three nights in March. The magnitude of this star on other nights are 12.645 (13 Jan), 12.631 (13 Feb), 12.626 (14 Feb), 12.608 (16 Mar), 12.606 (18 Mar) and 12.636 (14 Apr). This star is possibly a small amplitude variable and more observations are required to determine its light curve.

The overall efficiency of the system in $BVRH\alpha$ bands is estimated by comparing the zero points in the transformation equations with the expected values. The expected counts for a star of magnitude m using a telescope of diameter D is given by McLean (1989),

$$\frac{S_0}{1 \text{ count s}^{-1}} = \frac{3.95 \times 10^{11}}{Q} \left(\frac{D}{1\text{m}}\right)^2 \left(\frac{\lambda}{\text{Å}}\right) \left(\frac{\Delta\lambda}{\text{Å}}\right) \text{F}_\lambda(0) 10^{-0.4m} \epsilon\eta(\lambda) \text{ ,(II.12)}$$

where Q in electrons count^{-1} is the system gain (27.7 in the present case), $\lambda, \Delta\lambda$ are the effective wavelength and bandwidth of the filters, computed based on transmission curves for Schott glass filters. $\text{F}_\lambda(0)$ is the flux density in erg cm^{-2}s^{-1}Å^{-1}

38
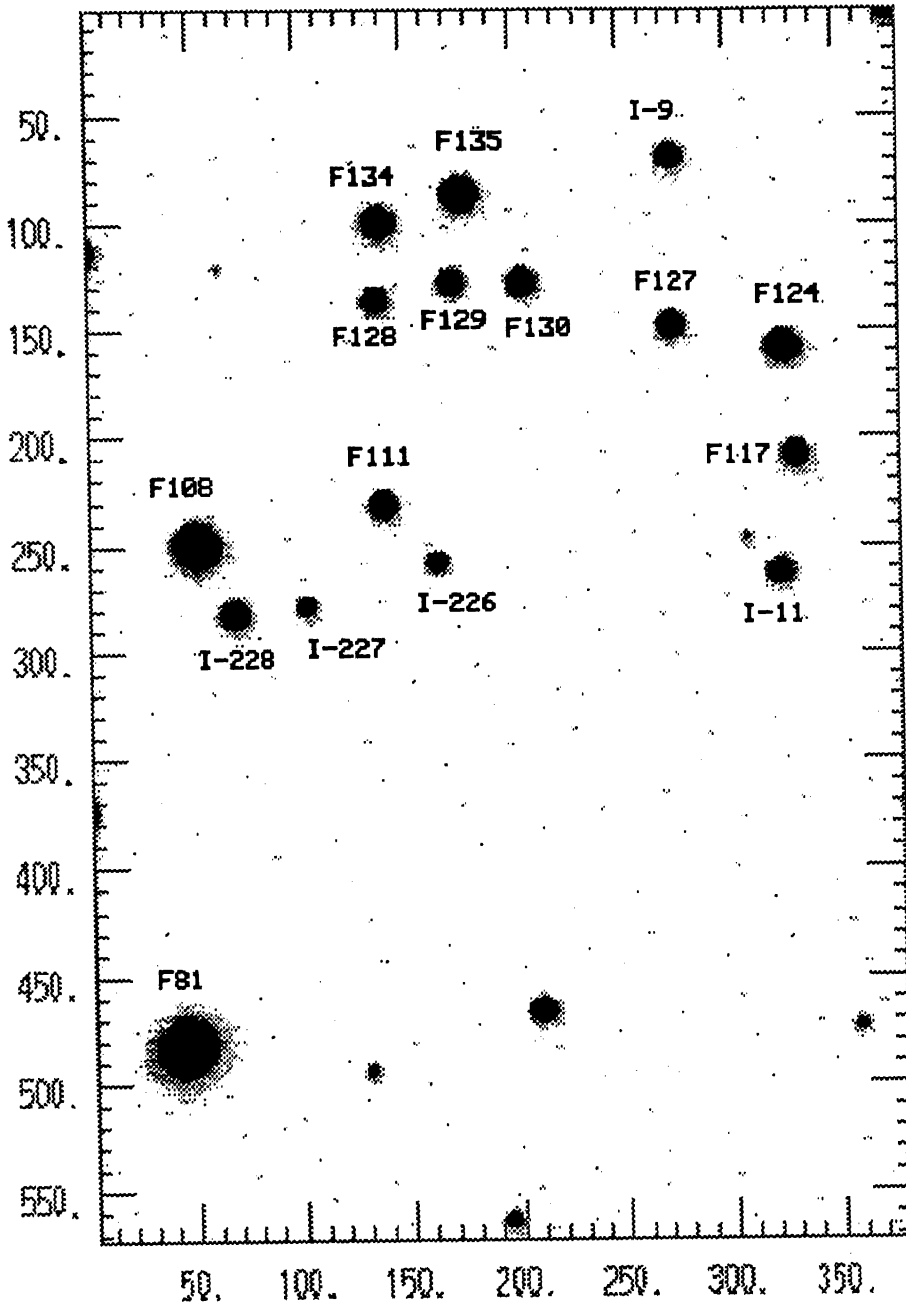
Figure II.4 An Identification chart for dipper asterism field in M 67 cluster from one of our observations with 1-m telescope. North is to the right and East is to the top.

from a star of magnitude 0 at wavelength λ above earth's atmosphere, ϵ is the fractional reflecting area of the mirror surface ($\sim$ 0.85) and η is the efficiency of the system (mirrors + filter + CCD). The resulting values of η are given in Table II.6. The peak efficiency is around 10% and lies in the red region. In the blue region the efficiency drops to just 2%.

Table II.6 Filter properties and the sensitivity of the system (PCCD-1991).

Sl. No.	Quantity	B	V	R	H_α	Units
1	λ_0	4351	5419	6713	6567	Å
2	$\Delta\lambda$	965	920	975	160	Å
3	$F_\lambda(0)$	6.90	3.83	1.81	2.04	10^{-9}erg cm^{-2}s^{-1}Å^{-1}
4	$-m_{th} = 2.5\log S_0$	21.36	20.96	20.72	18.61	mag
5	$-m_i$	17.22	18.29	18.22	16.11	mag
6	η	2.04	8.33	9.68	10.18	%
7	$S_0(\lambda)(m = 15)$ X=0	7.73	20.70	19.41	2.78	count s^{-1}
	estimate X=1	5.60	17.22	17.54	2.51	count s^{-1}
8	μ_i	14.98	16.05	15.98		mag arcsec^{-2}
9	μ_{sky}	21.43	20.62	19.62		mag arcsec^{-2}
10	Flux				1.00	10^{-13} erg cm^{-2}s^{-1}
11	Sky brightness				2.02	10^{-15} erg cm^{-2}s^{-1} arcsec^{-2}

Notes to **Table II.6 :**

See text following Equation (II.12) for the explanation of quantities in row numbers 1-3. S_0 appearing in row 4 is calculated using Equation (II.12) with $\eta = 1$ and $m = 0$. In row 5 zero points of the transformation equations are given, which indicate the magnitude which would produce a count rate of 1 count s^{-1}. η values given in row 6 are the derived efficiencies for the telescope+ filter+CCD combination. In row 7 estimated count rates for a star of magnitude 15 are given at airmasses 0 and 1. Row 8 lists the surface brightness required to produce a count rate of 1 count s^{-1} pixel^{-1} and row 9 gives the surface brightness of the sky close to the zenith as observed on 16 Mar 1991 which was a moon−less night. Hα line flux required to produce 1 count s^{-1} is given in row 10. Row 11 contains the sky surface brightness in flux units within Hα filter for the same night as for other filters.

2.3.3 Hα Photometry

The accuracy of emission-line photometry largely depends on the estimation of the contribution of the in-band continuum. Obtaining well-exposed continuum (off-

band) images with filters of bandwidth < 200Å, using telescopes of 1-m class, is difficult and costly in terms of telescope time. Saving the telescope time leads to subtraction of poorly exposed continuum images from well-exposed line images, when continuum filters of similar width as that of line filters are used. Most of the uncertainties involved in continuum subtraction can be eliminated if in-band continuum can be estimated from an image taken with a broader filter. However, this might lead to additional errors depending on the shape of the spectrum of the emitting object near the line of interest. In order to study these errors, we observed the dipper asterism field also with the Hα filter on most of the nights.

The Hα filter images of stars without strong Hα emission or absorption line will have contribution mainly from the continuum. The relative bandwidth of Hα filter with respect to R band can hence be obtained by transforming the data obtained through the Hα and R filters over a wide range of colours. For this purpose we define an 'instrumental Hα magnitude' h_0 in anology with broad continuum bands. The magnitude differences $(r - h)_0$ for stars are fitted against their $(v - r)_0$ colour with an equation of the form

$$(r - h)_0 = \alpha_{\text{r-h}} + \beta_{\text{r-h}} \, (v - r)_0 \; . \tag{II.13}$$

The resulting coefficients $\alpha_{\text{r-h}}$ and $\beta_{\text{r-h}}$ are given in Table II.4 for one of the nights, and the fit is shown in Fig. II.3(d). Neglecting the small colour term, the zero point $\alpha_{\text{r-h}}$ corresponds to a factor of 7.09 between the broadband R filter and the narrowband Hα filter. Variation of this ratio remained within 3% on all the nights. Scaling the R band fluxes with this ratio would thus give a good estimate of in-band continuum in Hα over a wide range of colours. Waller (1990) has demonstrated this by obtaining continuum-subtracted Hα images and line-subtracted continuum images of Orion nebula, from observations in Hα and R bands.

The overall process of continuum subtraction can be summarized by the follow-

41

ing equations,

$$\frac{f_\alpha}{\text{count s}^{-1}} = \left(\frac{f_\alpha^{\text{obs}}}{t_\alpha} - \frac{f_R^{\text{obs}}}{t_R a}\right) / \left(1 - \frac{1}{a}\right) , \qquad \text{(II.14)}$$

where f_α^{obs} and f_R^{obs} are observed counts for Hα and R filters in t_α and t_R sec respectively. The quantity $a = 10^{-0.4\alpha_{r-h}}$ is the ratio of effective bandwidths of R and Hα bands. The fraction in the denominator accounts for the line emission within the R band. The observed counts are converted into flux units using the following equations,

$$\frac{F_\alpha}{\text{erg cm}^{-2}\text{s}^{-1}} = C_\alpha \frac{f_\alpha}{\text{count s}^{-1}} \qquad \text{(II.15)}$$

$$\text{or } \log F_\alpha = \log C_\alpha + \log f_\alpha . \qquad \text{(II.16)}$$

Thus, calibrating Hα images involves obtaining the value of C_α. This is done using two methods. In the first method, the zero point for the Hα filter is evaluated using α_r and α_{r-h}. This zero point is in effect the R magnitude required to produce a count rate of 1 count s^{-1} within the Hα filter. This leads to a value of $10^{-12.99}$ erg cm^{-2}s^{-1} of incident flux for 1 count s^{-1} detected in Hα filter (with $Q = 27.7$ electron count^{-1}). In the other method observed counts for the spectrophotometric standard stars EG 99 and HD 60778 are compared with the expected flux within the band as computed by integrating the stellar spectrum within the bandpass. The conversion factors derived from these two stars are $10^{-13.02}$ and $10^{-13.01}$ erg cm^{-2}s^{-1} for 1 count s^{-1} respectively. Hα equivalent widths are computed as,

$$W(\text{H}\alpha)(\text{Å}) = \frac{F_\alpha(\text{ erg cm}^{-2}\text{s}^{-1})}{10^{-0.4R}} \left(\frac{\lambda^2}{c}\right) . \qquad \text{(II.17)}$$

R appearing in the above equation is the R magnitude, which also includes the Hα line. λ corresponds to Hα line wavelength and c is the speed of light. Errors in the equivalent width measurements as estimated from dipper asterism stars are $\pm 15 - 20$ Å.

The filter wheel at the 1-m telescope is changed in 1992 to accomodate 50 mm filters. New set of coated filters were used for BVR bands, whereas an interference filter of 100 Å bandwidth replaced the older Hα filter. Two more interference filters corresponding to Hβ and [O III]λ 5007 Å were also in use during this season. Details of these filters appear in Table II.2(b). The broadband filters in use at VBT have the same specifications as the above-mentioned coated filters. Details of these filters and the interference filters used at VBT are also given in Table II.2(b). A cgain value of 33 corresponding to 13.7 electron count^{-1} was opted in all the observations in 1992 at the 1-m telescope. VBT observations were carried out with the dip switch position corresponding to 4 electron count^{-1} (Prabhu, Mayya and Anupama 1992). Calibration procedures very similar to the methods described in section 2.3 are followed for both these systems. Encouraged by the small colour term in Hα calibration (Equation II.13 above) and suggestions by Waller (1990), the approach of using broad bands for continuum subtraction was extended to Hβ and [O III]λ 5007Å lines also. To improve the calibration, the suspected variable (F 117) was not used in calibration and star F 111 was included instead. The resulting transformation coefficients are given in Table II.4 under the headings PCCD-1992 and ACCD-1992. Conversion factors $\log C_\beta$ and $\log C_{OIII}$ are also given in the tables. It can be seen that the broadband colour coefficients generally agree in both the systems, in spite of using different CCDs at the two telescopes. However B band colour terms are not negligible. Also transformation coefficients $\beta_{b-H\beta}$ and β_{v-oIII} involving narrow and broad bands are substantial and hence cannot be neglected. This is because of large mismatch between the central wavelengths of narrow and broadband filters. Thus in scaling the broadband continuum to the narrow bands, the colour terms cannot be neglected.

3. Synthetic Aperture Photometry

CCD imaging allows the extraction of magnitudes using software techniques. This can be done either by fitting 2-d profiles to stellar images or by simply summing all the counts within a reasonable software aperture centred around the object of interest. The main basis on which the profile fitting technique works is the existence of standard profiles for all the stars in a frame. Thus for non-stellar objects for which no standard profile exists, one has to use the second technique namely synthetic aperture photometry. While doing stellar photometry, both the techniques can be used with similar results in most cases. However profile fitting techique gives better results in crowded fields, whereas aperture photometry is preferred when the object of interest does not have a regular shape. In the following sections, implementation of aperture photometry for stars and H II regions are described.

3.1 Stellar Photometry with Howell's Algorithm

Howell (1989) describes an optimal extraction algorithm which improves the magnitudes obtained with simple aperture photometry. This method considers the magnitude and S/N profiles, within a series of concentric apertures around stars. S/N increases first because of increasing signal but begins to drop beyond certain radius, where sky counts start dominating the weak wings of the stellar profiles. Magnitudes are extracted only upto a radius where S/N peaks, and to account for the flux contained beyond this radius, a correction factor is applied based on well-exposed stars in the frame. This method reduces the errors introduced by inaccurate sky subtraction. Accurate magnitudes of stars can be extracted even in cases where the separation between the stars is only a few pixels. A computer programme based on this method is developed locally under STARLINK environment and is used for the extraction of all stellar magnitudes discussed in the previous section. The programme in the present format asks the user to select one star in

44

the frame, which is well exposed and as isolated as possible. The growth profile of this star is used to correct the magnitudes of other stars, beyond the radius of maximum S/N. Magnitudes are computed both for an average sky value chosen from an isolated region in the frame and sky value chosen from an annulus around the star. In all our frames of dipper asterism in M 67, stars brighter than 13 mag are well exposed with S/N peaking between 5–15 pixels and hence 'aperture magnitudes' at fixed apertures (say 20 pixel = 7 arcsec radius), give values within 0.01 magnitudes of those derived from optimal extraction method. The improvements are easily realized for fainter stars. Growth curves and S/N plots for some of the stars in one of the frames are shown in Figs II.5(a) and II.5(b) respectively.

3.2 HII Region Photometry

H II complexes in nearby galaxies have angular sizes of several arcsec and hence are resolved by optical telescopes. Their structure differs from region to region and hence methods based on the uniformity of profiles cannot be used in H II region photometry. Simple aperture photometry with carefully chosen sky values is the only way of getting H II region fluxes. The largest source of uncertainty in this method is in the 'true' estimation of galaxy background + sky for subtraction. This is because the average surface brightness of H II regions is of the same order or less than the surface brightness of sky + background. Thus the extracted magnitudes are very sensitive to the estimated background. Normally giant H II complexes are found in spiral arms where background is not only strong but also varying. Thus the estimation of background is subjective to some extent, adding errors to photometry. Methods followed in this study are described below.

Programmes are developed locally to extract total fluxes from H II regions with special care taken for estimating the background for subtraction for every region. For convenience we use circular apertures for flux measurements, which is normally
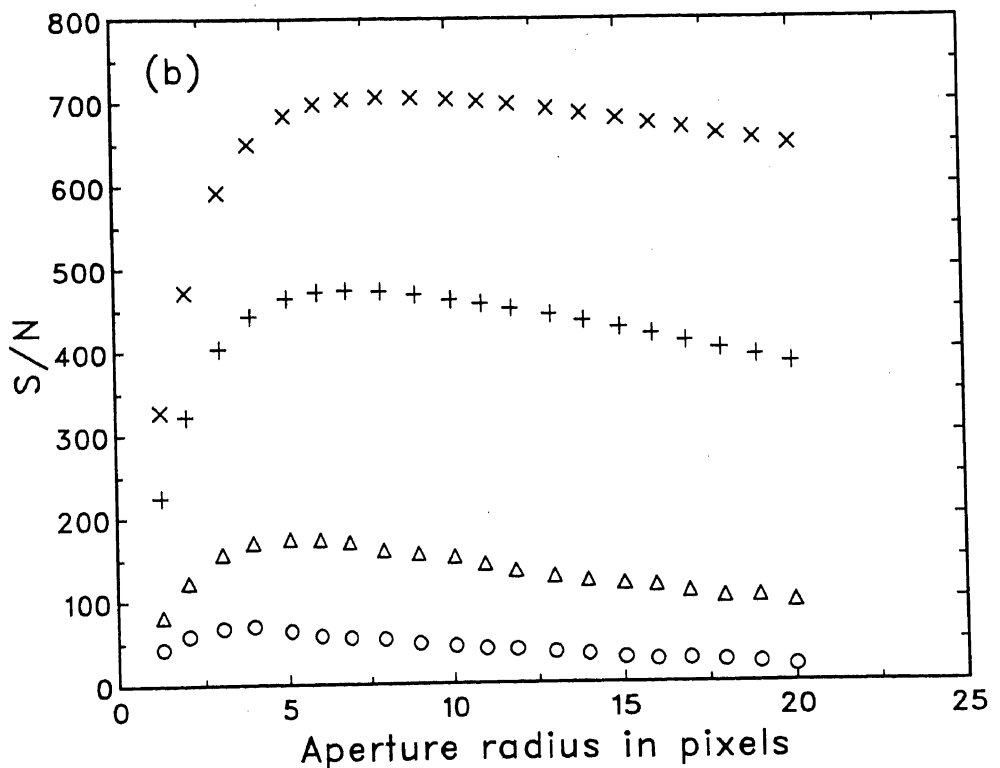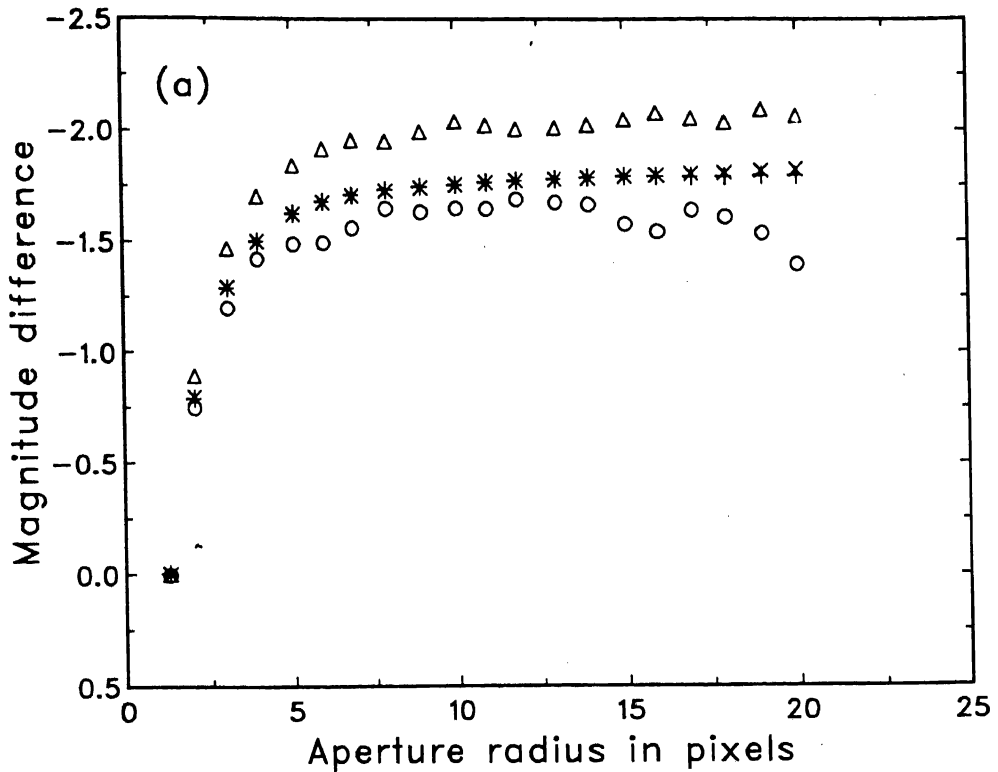
Figure II.5 **(a)** CCD aperture growth curves, and **(b)** S/N ratio, for four stars in a single CCD frame. The magnitudes of these stars as estimated from optimal extraction method are 12.37($\times$), 13.20($+$), 15.04($\triangle$) and 16.33($\circ$) in V band. For the sake of display, magnitude within an aperture of 1 pixel radius is subtracted from all concentric apertures for all the stars. Note that the growth curves for the fainter two stars deviate from the others due to an underestimation ($\triangle$) or overestimation ($\circ$) of sky. The S/N peaks at a smaller radius for fainter stars.
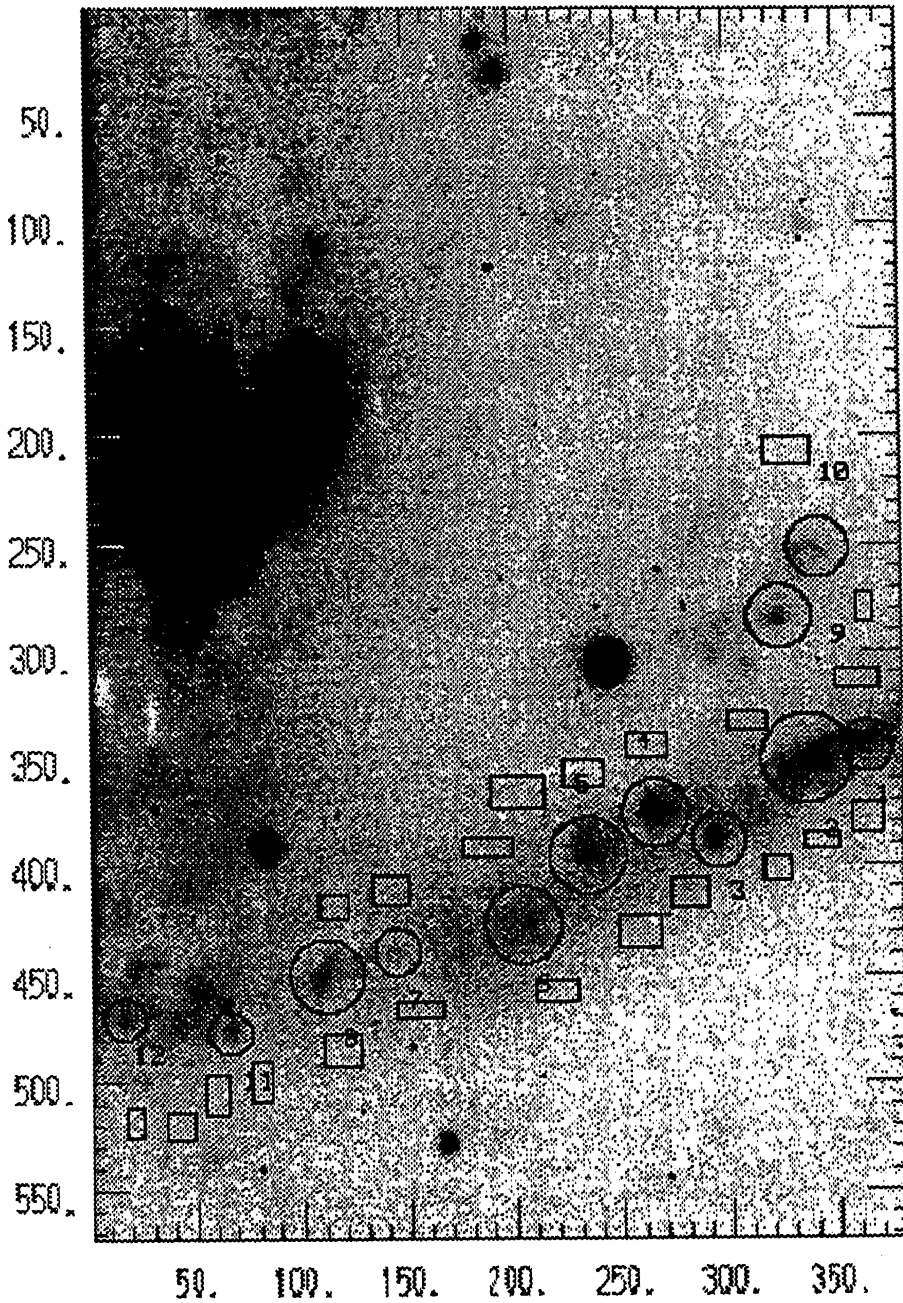
Figure II.6 A chart of nucleus and north-west arm of NGC 1365 illustrating the synthetic aperture photometry for HII regions. Circular apertures centred on emitting knots are used for flux measurements. The rectangular apertures flanking the circles are the regions chosen for sky+background measurements.

preferred by other investigators also (*e.g.* Kennicutt 1979). HII regions are mostly selected based on their brightness on Hα images. Some fainter regions are included if they are found to have a very strong continuum. The aperture centre and radius are chosen interactively on a colour composite image formed by the superimposition of Hα, *B* and *V* band images, displayed on COMTAL display unit. It is noticed that the centres of HII regions in Hα frames do not always coincide with the continuum images, which necessitated the usage of both line and continuum images for choosing the centre and radius. This problem is addressed separately in Chapter V. While choosing the radius, care is taken to enclose most of the emission from a region, minimising the contamination from a neighbouring region.

It is necessary to have a model for the galaxian background before one subtracts it to get pure HII region contribution. The working assumption in this study is that HII regions are fully transparent to disk/arm background light. Based on this assumption, rectangular regions for sky + background measurements are chosen interactively around each HII region and an average value (count per pixel) is taken to represent sky + background for that region. Once the centre and radius of apertures for HII regions and positions for background measurements are decided, these parameters are used for flux measurements on all aligned frames. This procedure ensures that fluxes measured on different frames using different filters correspond to the same region in the galaxy. An example of this can be found in Fig. II.6. The fluxes are measured as the sums of pixel counts enclosed by the circles. The rectangular areas represent the regions for sky + background measurements. There is around 5–10% variation of the background from region to region in the example shown.

3.3 Error Estimation under Non-uniform Background

It was noticed often that growth curves continue to rise beyond the aperture used for

magnitude extraction. This will be so if there is enough emission beyond the apertures used for measurements. Since it is expected that the gas extends more than the stellar component, growth rate should be more in Hα compared to broadbands, which are continuum dominated. While this is true for some regions, there are many regions for which the growth rates in BVR bands match or even exceed the Hα growth rates. Since growth rates are very sensitive to the selected background value, we did some experiments to assess the errors on the derived magnitudes. We selected a few isolated H II regions and constructed growth profiles by selecting background values very close to the regions. Growth curves show a tendency to flatten off suggesting that growth rate of aperture magnitudes is dominated by background underestimation in our measurements. However it is not possible to choose background regions very close to all H II regions because of 'crowding'. At the same time, one can estimate the errors on the magnitudes for any chosen background on the assumption that true background is that which flattens the growth profiles. The approach we follow in estimating these errors are described below.

Magnitudes are defined as,

$$m_h = -2.5 \log(C_{h+b} - C_b n), \tag{II.18}$$

where C_b is the background + sky estimate per pixel in units of count s^{-1}, C_{h+b}, total count s^{-1} over n pixels enclosing the H II regions and include background also. Let $C_b = C_{b-}$ be the background value used in the measurements, which normally shows increasing growth profile, and $C_b = C_{b+}$ be the actual background value needed to flatten off the growth profiles.

$$m_{h-} = -2.5 \log(C_{h+b} - C_{b+} n), \tag{II.19}$$

$$m_{h+} = -2.5 \log(C_{h+b} - C_{b-} n). \tag{II.20}$$

m_{h+} is the magnitude with the lower value of background (C_{b-}) and hence an overestimate in brightness, while m_{h-} is the magnitude with (C_{b+}) as the background
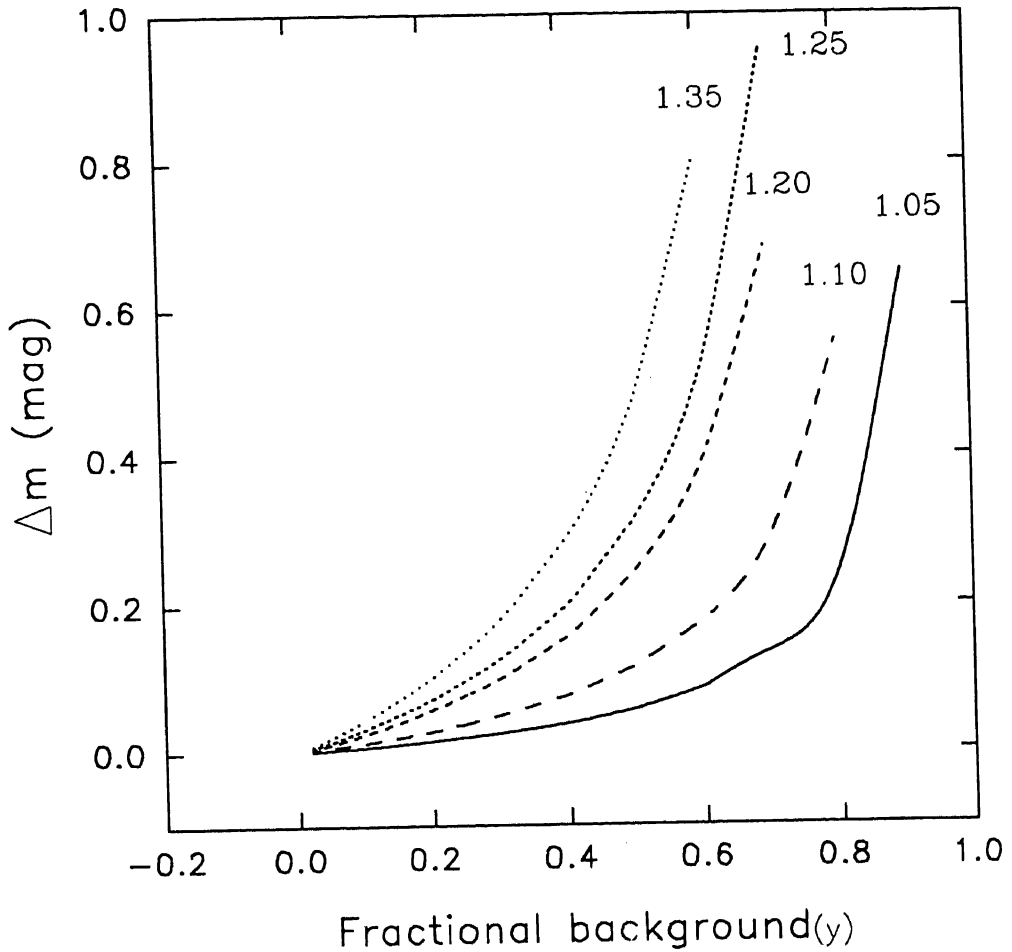
Figure II.7 Estimation of errors in the magnitude measurements of H II regions as a function of fractional background contribution(y), in the presence of a non-uniform background. x is the ratio of the actual background to the assumed background and is constant along a curve. For most of the H II regions x lies between 1.05–1.10 and y lies between 0.50–0.90.

and hence close to the asymptotic value. The quantity $\Delta m = m_{h-} - m_{h+}$ is the maximum amount by which the present measurements might be overestimated. Let us define x and y as,

$$x = \frac{C_{b+}}{C_{b-}}, \tag{II.21}$$

$$y = \frac{C_{b-}n}{C_{h+b}}. \tag{II.22}$$

Thus by definition x is a positive quantity greater than or equal to 1, whereas y is

the fraction of the assumed background within the aperture and hence always less than 1.

Substituting the values of x and y we get,

$$m_{h-} = -2.5\log(C_{h+b}(1 - xy)), \qquad\qquad (II.23)$$

$$m_{h+} = -2.5\log(C_{h+b}(1 - y)), \qquad\qquad (II.24)$$

$$\Delta m = -2.5(\log(1 - xy) - \log(1 - y)). \qquad\qquad (II.25)$$

Thus Δm can be parametrized by x and y alone. This is shown in Fig. II.7. In general the errors on individual magnitudes are less than Δm. In our measurements the background counts contribute between 50–90% to the total counts and hence the measured magnitudes are very sensitive to the assumed background values. V and R measuements are affected more than others. x is usually less than 1.1 in our measurements. For regions with background contribution not exceeding 80%, errors lie below 0.50 mag. In our method, the background values are measured at the same location for all the bands, and hence the errors are correlated. Thus in general errors on colours are likely to be less than that on the magnitudes.

In Chapter III, we estimate the photometric quality of each region based on Δm derived by the methods discussed above.

III. PHOTOMETRIC OBSERVATIONS AND DATA

Giant Extragalactic H II Regions (GEHRs) are ionized regions embedding clusters of young and massive stars. They trace the spiral arms in spiral galaxies. Compared to most familiar galactic H II regions, GEHRs are larger, brighter, less dense (O'Dell and Castaneda 1984a,b, Kennicutt 1984) and more turbulent (Melnick 1977, Roy, Arsenault and Joncas 1986, Hippelein 1986). The properties of these regions have been recently summarized by Shields (1990). Their high Balmer luminosities indicate that they harbour hundreds or thousands of solar mass in OB stars, emitting copious amounts of ionizing photons ($\log N_L$ ph $s^{-1} = 50 - 53$) equivalent to tens or even thousands of O5 V stars Kennicutt and Chu (1988). The nearest GEHR, namely 30 Dor lies in the nearby Irregular galaxy Large Magellenic Cloud (LMC) requires around 200 O5 V stars to explain the observed ionization. Spectroscopic classification of the embedded cluster stars in this nebula shows the presence of at least 60 stars of spectral type earlier than B (Melnick 1985). The strength of ionization helps these regions to be traced at farther distances. GEHRs are used for a variety of studies in galaxies. The brightest regions in galaxies are used to find galaxian distances either by using them as standard candles or standard scales (Sandage and Tammann 1974, Kennicutt 1979). Almost the entire information regarding the abundances in galaxies is based on emission lines arising in the nebulae (See the review by Dinerstein 1990). The velocity profiles of individual GEHRs are used to investigate the energetic phenomenon going on in massive star-forming regions (Roy *et al.* 1991, Roy, Arsenault and Joncas 1986).

Most of the early studies of GEHRs are based on photographic images of galaxies in Hα emission line. Because of difficulties of flux calibration of photographic images, these images are mostly used only to catalogue the position and approximate diameters of individual H II regions. Calibrated Hα images of galaxies started

becoming available in early eighties, mainly due to the work of Hodge and Kennicutt (1983). In their work photographic images were calibrated using photoelectric photometry of selected regions. These studies were used to derive the luminosity function of H II regions for different Hubble types (Kennicutt, Edgar and Hodge 1989). Most important of the calibrated Hα surveys of spirals are due to Kennicutt (1983b) and Kennicutt and Kent (1983), which are based on large aperture photoelectric photometry. Irregulars are surveyed by Hunter, Gallagher and Rautenkranz (1982) using video camera images. Global SFRs in spirals and irregulars are derived based on these studies. With the advent of CCDs, calibrated Hα fluxes of H II regions have become available for many galaxies, with the aim of extending the earlier studies to fainter levels (*cf.*, Cepa and Beckman 1989, 1990). Multi-band photometry of individual H II regions barely exists in the literature as of now. On the other hand, several bright H II regions have attracted spectroscopic observers, mainly for abundance studies. Most extensive of these studies is due to McCall, Rybsky and Shields (1985). GEHRs can be studied at other wavelengths as well. Radio continuum studies of bright H II regions were done by Israel (1980). Along with one of the Balmer lines these fluxes were used to study the extinction properties of H II regions (Israel and Kennicutt 1980, Caplan and Deharveng 1986). Spectroscopy of some of the H II regions in the ultraviolet is available from *International Ultraviolet Explorer* (IUE) (Rosa, Joubert and Benvenuti 1984). Total molecular mass associated with star forming complexes based on millimetre wave observations are available only for a few giant H II complexes in nearby galaxies (M 101: Blitz *et al.* 1981; M 51 Vogel, Kulkarni and Scoville 1988).

Investigation of star formation properties of individual H II regions calls for multi-wavelength-band observations. Mas-Hesse and Kunth (1991) have shown the power of such studies for a sample of starburst and H II galaxies. However, GEHRs in nearby galaxies presently lack such extensive data. The main purpose of our

study is to supply multi-band photometric data in optical region, with a view to investigate the star formation parameters such as Inital Mass Function (IMF) of individual regions. We make use of the available spectroscopic data on the observed regions to derive the physical conditions such as abundance, temperature *etc.* The sample of galaxies chosen for this study along with their observations and reductions are given in the next section. A brief description of the individual galaxies are given in the section following that. This section also contains identification chart for H II regions. The results on the photometry of H II regions are presented in the form of a catalogue in section 3. Aperture growth and surface brightness profiles centred around the nuclei of galaxies are presented graphically in section 4. These results are also compared with multi-aperture photoelectric photometry. We use the compilations in *UBV galaxy catalogue* by Longo and de Vaucouleurs (1983) for this purpose. The structural properties of H II regions in nebular and pure cluster light are briefly discussed in section 5 with the help of 'three-colour' photographs.

1. The Sample, Observations and Reductions

Galaxies are primarily chosen based on the availability of spectroscopic data on atleast a few regions in them. Roy and Walsh (see Table III.1 for references) have provided uniform spectroscopic data for a sample of H II regions in four southern galaxies, namely NGC 1365, 1566, 2997 and 5253. We have included all these galaxies for our photometry. Another source of extensive spectroscopy is due to McCall, Rybsky and Shields (1985). Galaxies NGC 2903, 3351, 4303, 4449 are selected based on these and other studies. NGC 2366 has a Giant H II complex, which has been studied spectroscopically by many groups (Kennicutt, Balick and Heckman 1980; Peimbert, Peña and Torres-Peimbert 1986). An attempt was made to obtain the relevent spectroscopic quantities such as abundance and extinction using imaging observations in $H\alpha, H\beta$ and [O III] λ 5007 bands. Three late type

galaxies NGC 2366, NGC 4449 and NGC 4656 are chosen for this purpose. NGC 4656 does not have any published spectroscopic data available. Basic properties of the galaxies are summarised in Table III.1, along with the references to earlier spectroscopic studies. Sources from which the distances are taken are also given in the table. The galactocentric velocities of the above galaxies are not high enough to shift the emission lines much away from the filter band-widths. $\mathcal{N}$(H II) refers to the number of H II regions on which good published spectroscopic data is available. Photometry is done for many regions, including most of these. Because of the large angular sizes of the galaxies compared to the CCD size (137×207 arcsec^2) only selected regions in the galaxies could be observed. The regions selected are given in the last column in the table. The estimated visual extinction to the galaxy (de Vaucouleurs, de Vaucouleurs and Corwin 1976, RC2 here onwards) is also given in the table.

Emission line and broad-band photometry of the ten sample galaxies were carried out with the help of CCD imaging. Most of these observations were done with the 1-m telescope in 1991–1992 observing seasons, using BVRHα bands. Some of the images, mainly Hα, obtained during 1990 season are also made use of in this study. 2.34-m VBT was used to obtain $BVRI$ broadband and Hα, Hβ and [O III] λ 5007 narrowband images of three late type galaxies NGC 2366, 4449, 4656. As with the previous chapter, the systems at 1-m and 2.34-m telescopes are refered as PCCD and ACCD respectively. Section II.2.1 and the tables II.2(a) and (b) give the details of CCD and filter systems available during various observing runs. All observations in emission lines were of 30 min duration. For $BVRI$ filters it ranged from 10–30 minutes with the 1-m telescope and 5–15 minutes with VBT. A brief log of observations of each galaxy is given in Table III.2. All the frames used in obtaining the final photometric data are included in this table. Airmass and seeing ranges of these observations are also given. Seeing measurements are

Table III.1 Sample of galaxies.

Galaxy NGC	deV. Type	A_v(gal)	Incl. ($°$)	Velocity km s^{-1}	Distance (Mpc)	Reference dist	Reference spect	$\mathcal{N}$(H II)	Region
1365	SB(s)b	0.159	56	1502	10.0	1	11,12	5	NW arm
1566	SAB(s)bc	0.212	36	1178	13.0	2	13,14	5	NW arm
2366	SBm	0.303	62	252	3.6	3	15,16	1	NGC 2363
2903	SAB(rs)bc	0.166	58	467	10.0	4	17	8	N+S
2997	S(s)c	0.408	37	805	10.0	5	18,19	49	NE+SW arm
3351	SB(r)b	0.144	46	673	8.5	6	17	4	Centre
4303	SAB(rs)bc	0.151	24	1483	19.0	7	20	10	Centre
4449	IBm	0.151	44	262	5.0	8	17,21	3	Centre
4656	SB(s)mP	0.144	76	662	5.2	3			NE part
5253	Irr IIp	0.144	64	209	2.0	9	22	1	Nucleus

References :

(1) Jones and Jones (1980)

(2) Pence, Taylor and Atherton (1990)

(3) Sandage and Tammann (1976)

(4) Sandage and Tammann (1981)

(5) Peterson (1978)

(6) Bottinelli *et al.* (1984)

(7) Kennicutt (1981)

(8) Sandage and Tammann (1975)

(9) de Vaucouleurs (1979)

(11) Roy and Walsh (1988)

(12) Alloin *et al.* (1981)

(13) Roy and Walsh (1986)

(14) Hawley and Phillips (1980)

(15) Peimbert, Peña, and Torres-Peimbert (1986)

(16) Kennicutt, Balick and Heckman (1980)

(17) McCall, Rybsky and Shields (1985)

(18) Walsh and Roy (1989b)

(19) Roy and Walsh (1987)

(20) Shields, Skillman and Kennicutt (1991)

(21) Lequeux *et al.* (1979)

(22) Walsh and Roy (1989a)

Table III.2 Observational log.

NGC	Date	Frames	Airmass	Seeing($''$)
1365	1990 Jan 23	$R(10)$	2.88	3.9
	1990 Jan 24	$H\alpha(30)$	1.77	2.6
	1991 Jan 14	$2B(30), V(20)$	1.52–1.67	2.4
	1991 Feb 15	$B(10), V(5), R(3), H\alpha(10)$	2.16–2.17	2.1–2.6
1566	1990 Jan 24	$H\alpha(30)$	3.59	3.74
	1991 Feb 14	$B(30), V(30), R(15)$	2.71–3.49	2.1–3.6
	1992 Mar 7	$V(30), H\alpha(30)$	3.64–4.56	3.6
2366	1990 Feb 1[†]	$3H\alpha(20)$	1.88–1.99	3.8
	1990 Feb 2[†]	$2R(15), R(5)$	1.88–2.01	3.8
	1991 Mar 17	$B(30), V(30)$	1.82–1.84	
	1992 Mar 8[†]	$I(10), H\beta(30), [OIII](30)$	1.82–1.90	2.6–3.2
	1992 Mar 9[†]	$B(15), V(10), H\beta(30)$	1.82–1.87	3.1–3.8
2903 South	1991 Feb 13	$B(30), V(30), R(15), H\alpha(30)$	1.02–1.24	2.6–3.6
North	1991 Feb 14	$B(30), V(30), R(15), H\alpha(30)$	1.01–1.08	2.2–2.6
2997-NE	1990 Jan 24	$H\alpha(30)$	1.39	2.0
	1991 Mar 16	$V(30), R(15)$	1.43–1.62	2.7
	1991 Apr 14	$V(30)$	1.42	1.7
	1992 Apr 1	$B(30)$	1.47	1.7
	1992 Apr 2	$B(30)$	1.41	2.7
	1992 Apr 3	$B(30), V(20), R(20), H\alpha(30)$	1.39–1.70	1.5–3.0
-SW	1990 Feb 25	$H\alpha(30)$	1.44	2.3
	1991 Mar 18	$B(30), V(30), R(15)$	1.43–1.72	1.9–2.2
	1991 Apr 15	$H\alpha(30)$	1.39	2.9
	1991 Apr 16	$B(30), V(30)$	1.38–1.41	2.1
3351	1991 Jan 13	$B(30), V(15)$	1.03–1.06	2.6–3.0
	1991 Jan 14	$H\alpha(30)$	1.05	2.9
	1991 Feb 14	$B(20), V(15)$	1.02–1.05	1.9–2.6
	1991 Feb 15	$R(15), H\alpha(30)$	1.00–1.01	2.3–2.7
4303	1991 Feb 15	$B(30), V(20), R(15), H\alpha(30)$	1.01–1.10	1.6–2.5
	1992 Feb 3	$I(10), H\alpha(30)$	1.02	2.5
	1992 Feb 5	$B(30), V(15), R(10)$	1.05–1.12	2.4–2.7
	1992 Apr 1	$B(30)$	1.02	3.4
	1992 Apr 2	$B(30), H\alpha(30)$	1.01–1.06	3.0
	1992 Apr 3	$V(30), H\alpha(30)$	1.10–1.19	1.8–2.1

Table III.2 Continued.

NGC	Date	Frames	Airmass	Seeing($''$)
4449	1990 Feb 1[†]	Hα(30), Hα(20)	1.17–1.18	
	1990 Feb 2[†]	R(10), R(5), R(2)	1.18–1.21	
	1991 Mar 17	B(30), V(30)	1.22–1.28	2.8–3.4
	1991 Apr 15	R(15), Hα(30)	1.19–1.22	2.5–2.9
	1992 Mar 9[†]	B(15), V(10), Hβ(30), [$OIII$](30)	1.18–1.33	2.4–3.5
	1992 Apr 7[†]	Hβ(30), [$OIII$](30)	1.18–1.21	2.7
	1992 Apr 29[†]	B(15), V(10), Hβ(30), [$OIII$](30)	1.17–1.24	3.2–3.7
	1992 May 1[†]	R(5), I(5), Hα(20)	1.18	3.4–3.5
4656	1992 Mar 8[†]	I(10), I(5), Hα(20), Hβ(30), [$OIII$](30)	1.06–1.20	2.7
	1992 Mar 9[†]	B(15), V(10)	1.26–1.32	2.9–3.8
	1992 Apr 6[†]	2Hβ(30), [$OIII$](30)	1.05–1.09	2.5–2.8
	1992 Apr 7[†]	2Hβ(30)	1.06	2.6–3.0
	1992 Apr 30[†]	B(20), V(15)	1.13–1.18	3.1
	1992 May 1[†]	R(10), I(10), Hα(20)	1.06–1.10	3.3–4.4
5253	1991 Feb 14	B(30), V(30), R(15), Hα(30)	1.40–1.43	

[†] Observations are carried out with VBT.

Notes :

The numbers inside brackets in the third column denote the exposure time in minutes.
A number preceding the filter type indicates number of exposures. *e.g.* 2B(30) .

based on fitting the profiles on the stars within the frames. For two of the galaxies (NGC 2903 and 2997) we had two settings so as to cover the main optical disk of the galaxies. Only Noth-East part could be observed for galaxies NGC 1365 and 4656. For the remaining galaxies, observations are done keeping the nucleus at the centre of the CCD. The longer axis of the CCD was maintained along East-West within the errors of few degrees ($\leq 5°$) in all nights in 1991–92. The angle was more than 5° on some of the nights in 1990. With VBT, CCD longer axis was aligned roughly North-South. All observations are done with the default gain (cgain= 0 or 27.7 electron count^{-1}) in 1991 and earlier and with cgain= 33 (13.7 electron count^{-1}) in 1992 at the 1-m telescope. All the observing runs at VBT used a gain corresponding to around 4 electron count^{-1}, except for the run in 1990 (~ 1 electron count^{-1}).

As this is the first attempt in carrying out photometry of non-stellar objects like H II regions with the CCD systems in the observatory, much attention was given for calibration (see Chapter II for details). For the southern galaxies in the sample, $UBVRI$ photometric standards drawn from the list of Hamuy and Maza (1989) were observed, whenever the sky seemed to be photometric. Extinction values were obtained on all photometric nights at 1-m telescope, and are as given in Table II.3. For VBT observations, either the extinction obtained with other telescopes or an average value for the site is assumed. Spectrophotometric standard star EG 99 (Oke 1974), which is also a $UBVRI$ photometric standard (Kilkenny and Menzies 1989), was observed on alomost every photometric night. Another standard field which was routinely observed is the dipper asterism in M 67 (Schild 1983). These observations help us to check the emission line calibration and scaling factors between the narrow bands and broad bands in addition to providing the broadband calibration. Tables III.3(a) and (b) contain the resulting zeropoints for each galaxy observation. The objects on which the zeropoints are based are also

given in the table along with the references to the sources. Equations defining the zeropoints in Table III.3(a) (PCCD observations except for NGC 2366 R and Hα frames) are the same as eqns. II.11 described in Chapter II, while they are as follows for Table III.3(b) (ACCD observations).

$$V - v_i = \alpha_{\text{v}} + \beta_{\text{v}} (b - v)_i \ ,$$

$$B - V = \alpha_{\text{b-v}} + \beta_{\text{b-v}} (b - v)_i \ ,$$

$$V - R = \alpha_{\text{v-r}} + \beta_{\text{v-r}} (v - r)_i \ ,$$

$$V - I = \alpha_{\text{v-i}} + \beta_{\text{v-i}} (v - i)_i \qquad\qquad \text{(III.1.)}$$

Suffix 'i' indicates that the magnitudes and colours are not corrected for atmospheric extinction, and have been absorbed into the zeropoint. The differences in the definitions arise mainly due to the smaller airmass range with VBT observations, which enabled us to treat $BVRI$ photometry as $V, B - V, V - R$ and $V - I$ photometry, neglecting the airmass differences. On the otherhand, BVR magnitudes are individually transformed with the PCCD data, while combining data from different nights.

Corrections for bias, dark and flat fielding non-uniformities of the chip in the image plane are done similar to the methods described in Section II.1.1. After these primary reductions the images of a particular field (a galaxy or a part of it) are brought into a common coordinate system. This is done using the routines XYFIT, RESAMPLE *etc.* in the EDRS subpackage of *STARLINK*. The process involved can be summarized as follows. The common stars in frames to be aligned are identified first. Taking one of the frames as reference the coefficients for transfoming other frames are computed using XYFIT, allowing a shift of the centres and rotation. The resultant coefficients are applied to the frame to be aligned using RE-SAMPLE, interpolating linearly between pixels, when necessary. The coefficients suggest negligible rotational term. It was possible to obtain more than three stars

Table III.3(a) Zeropoints of BVRHα photometry[†]

NGC	α_B	α_V	α_R	$\log C_\alpha$	Dates	Std star	Reference
1365	17.389	18.359	18.390	-13.00	15Feb91/24Jan90	NGC 1097 field	1
1566	17.282	18.214	18.255	-13.00	14Feb91/24Jan90	NGC 1672 field	1
2366	17.300	18.332	22.960	-14.73	17Mar91/1Feb90	M 67	2
2903-N	17.320	18.262	18.259	-13.00	14Feb91	M 67	2
2903-S	17.288	18.229	18.221	-13.00	13Feb91	M 67	2
2997-NE	19.101	19.516	19.713	-13.00	3Apr92/24Jan90	MCG 5-16-23	1
2997-SW	17.268	18.279	18.196	-13.00	18Mar91/25Feb90	MCG 5-16-23	1
3351	17.313	18.258	18.017	-13.00	14/15Feb91	M 67	2
4303	17.144	17.981	17.981	-13.00	15Feb91	EG 99	3
4449	17.220	18.261	18.131	-13.00	17Mar/15Apr91	EG 99	3
5253	17.289	18.233	18.218	-13.00	14Feb91	EG 99	3

[†] R and Hα zeropoints for NGC 2366 correspond to VBT observations.
Remaining zeropoints correspond to 1-m observations.
Zeropoints for NGC 2997-NE is from 1992 with a different filter set.

References

(1) Hamuy and Maza (1989)

(2) Chevalier and Ilovaisky (1991)

(3) Kilkenny and Menzies (1990)

Table III.3(b) Zeropoints for BVRI$H\alpha H\beta$[OIII] photometry[†]

NGC	α_V	α_{B-V}	α_{V-R}	α_{V-I}	$\log C_\alpha$	$\log C_{\alpha-\beta}$	$\log C_{[OIII]-\beta}$	Dates
4449	20.62	-0.94	0.61	0.77	-14.29	-0.55	0.29	8/9 Mar92
4656	20.62	-0.94	0.61	0.77	-14.29	-0.55	0.29	8/9 Mar92

[†] All the data are from VBT observations. See text for calibration details.

for alignment in all cases except NGC 2903 and NGC 3351. For these galaxies carefully selected H II knots are taken as references. Rms alignment errors were less than 0.5 pixel for majority of frames, with the errors not exceeding a pixel even for extreme cases. The magnitude measurements of H II regions on the aligned frames are done using aperture photometry as described in Section II.3. Centres and aperture sizes are chosen so as to enclose most of the emission in Hα and broad bands. Regions for sky+background are chosen flanking the H II regions.

2. Individual Galaxies — Brief Description and H II Region Identification

We summarize here, previous studies on individual objects. Identification charts for selected GEHRs are presented in the form of grey scale maps. The apertures chosen for flux measurements are represented by circles, with identification numbers. Cross identifications, when available, are given in the catalogue in the next section. Charts are represented in pixel coordinates, with North to the right and east to the top for all galaxies except for NGC 4449 and 4656, which are observed with VBT, for which north is to the top and east to the left. We generally preferred R frames for grey scale representation, as they contain contributions from both nebula and cluster. The regions in NGC 2366 and 5253 can be easily identified even without charts and hence identification charts are not reproduced. The adopted calibration methods are described for individual galaxies.

NGC 1365

This barred galaxy in the southern hemisphere has got two well defined spiral arms containing chains of H II regions. The nuclear region stands out with "hot spots" (Sérsic and Pastoriza 1965). The galaxy has been the subject of many spectroscopic studies (Pagel *et al.* 1979; Alloin *et al.* 1981; Roy and Walsh 1988) mainly giving information on the abundances in H II regions. The galaxy is a member of Fornax

group at a distance of 10 Mpc (Jones and Jones 1980).

We have observed the North-Western arm of the galaxy in BVRHα bands. The frame includes the nuclear hot spots apart from 5 out of 6 H II regions mapped spectroscopically by Roy and Walsh (1988). A total of 16 regions are selected for photometry, of which three are nuclear hot spots. The nucleus is also identified for photometry. The selected regions are identified in Fig. III.1. The inset contains the nuclear region with a different grey scale mapping. BVR calibration is based on the frames taken on 1991 Feb 15. A field containing two standard stars is observed in the vicinity of NGC 1097 Hamuy and Maza (1989) twice, at similar airmasses as of NGC 1365 observations. The zero points derived from these stars (see Table III.3(a)) agree well with the values found from M 67 observations near zenith. Observations done on other nights are shifted to match the 1991 Feb 15 frames and transformed using the above zero points. The Hα frame calibrations are based on the frames obtained on 1990 Jan 24.

NGC 1566

This is a weakly barred galaxy with two strong arms containing chains of H II regions. Hackwell and Schweizer (1983), from their $UBVRIJHK$ band observations, have found the bar to be more prominent in the infrared. The galaxy has been the subject of many previous studies, including a detailed BVR photometric and gas kinematic study by Pence, Taylor and Atherton (1990). Roy and Walsh (1986) have spectroscopically mapped the northern arm of the galaxy.

In the present study, the galaxy nucleus is centred on the CCD, enclosing the bright H II complexes of both the arms. Twelve regions are selected for photometry, which are identified in Fig. III.2. Five regions, surrounding the central part of the galaxy, have lot of disk light contamination, and hence are left out of our catalogue. BVR calibration is based on the frames on 1991 Feb 14. Because of the

large airmasses (> 2.7) at which the galaxy is available for observations, standard stars close to the object are observed at similar airmasses as that of the galaxy. SAO 233486 (HD 27713), whose $UBVRI$ photometry is available due to Winkler, Van Wyk and Glass (1990), is observed twice and star number 1 in the field of NGC 1672 (Hamuy and Maza 1989) is observed once. The zeropoints derived independently from these stars (see Table III.3(a)), are compared with those from M 67 frames, which are found to agree within 0.05 mag of each other. The Hα frame calibrations are based on the frames obtained on 1990 Jan 24.

NGC 2366

This is a late type dwarf irregular of Magellanic type. The galaxy is dominated by the giant H II complex NGC 2363, situated at one end of the galaxy. The brightness of this object has enabled several groups to study this region in great detail spectroscopically (Kennicutt, Balick and Heckman 1980; Gondhalekar 1983, Peimbert, Peña and Torres-Peimbert 1986). This region is one of the examples of low abundance, high excitation H II regions.

The part of galaxy enclosing the giant H II complex NGC 2363 was observed in B and V filters on 1991 Mar 17, with the PCCD system. Hα and R observations were carried out on 1990 Feb 1 and 2 with VBT. The region south-west of this complex was also included for photometry. A bigger aperture enclosing both these regions is also used. The image scale for R and Hα images are different from B and V and hence aperture centre and radii were chosen separately, matching as closely as possible. BV calibration is done using the average zeropoints for 1991 Mar 17 for PCCD. The calibration of Hα frame observed with VBT is based on the spectrophotometric standard EG 99. The calibration yields 1.865×10^{-15} erg s^{-1}count^{-1}. The R magnitude could not be accurately transformed. A rough estimate is given based on the calibration by Bhat *et al.* (1992).

This galaxy is well known for the bright "hot spots" in its nuclear region (Sérsic and Pastoriza 1967). Many of the studies of the galaxy are centred around these hot spots (Oka *et al.* 1974; Beck, Beckwith and Gatley 1984, Wynn-Williams and Becklin 1985, Simons *et al.* 1988, Prabhu 1980a,b). The spectroscopic work on the galaxy is carried out by Simkin *et al.* (1975) and McCall, Rybsky and Shields (1985).

The main optical extent of the galaxy could be covered in two settings, both enclosing nuclear regions. A total of eighteen regions are identified for photometry, including the 6 hot spots. These include 5 of the regions spectroscopically studied by McCall, Rybsky and Shields (1985). The background contamination is slightly more in the galaxy, probably due to the large inclination to the line of sight. Fig. III.3 contains the identifications of individual regions on a chart obtained by the mosaic of north and south frames. Nuclear hot spots are scaled separately in the inset. The $BVR H\alpha$ observations of the northern side were carried out on 1991 Feb 13, and the southern side on the following night. Magnitude measurements were done on the north and south regions separately, using the zeropoints derived from M 67 frames, on the two nights. Transformed magnitudes for the objects in common agree well.

NGC 2997

This spiral galaxy has two bright and symmetrical arms, with chains of H II regions. A large fraction of the published work on this galaxy is concentrated on the nuclear region, which contains "hot spots" (Sérsic and Pastoriza 1965; Prabhu 1980a; Milliard and Marcelin 1981). The north-east arm has been spectroscopically mapped by Roy and Walsh (1987). Spectra of 49 H II regions were obtained by Walsh and Roy (1989b) using multi-object fibre optics fed spectrograph. These studies have mainly concentrated on the abundance analysis.

Considering the large number of H II regions for which spectroscopic information is available, we devoted considerable observing time on this galaxy. It was possible to cover both the arms in two settings, both containing the central hotspots. From these, a total of 36 regions are selected on the frame containing the N-E arm and 23 regions on the other frame. Photometry of nine complexes in the N-E is done with bigger apertures. Typically the HII regions have slightly smaller sizes in this galaxy compared to other galaxies in the sample such as NGC 1365, 1566. Also there are many regions, which have hardly any continuum detectable above the background. Identification of the regions in the N-E frame are given in Fig. III.4(a) and (b), containing respectively smaller and bigger apertures. Both these are based on Hα images. Regions in the S-W arm are identified in Fig. III.5. Some of the regions in this galaxy are dropped after identification and are missing in the chart. The BVR observations of the galaxy are done both in 1991 and 1992. These observations are accompanied by observations of the standard stars in the field of MCG - 5 - 16 23 (Hamuy and Maza 1989), at similar airmasses. For the nuclear region the aperture growth curves for 3 BVR sets of observations are independently transformed using the standards observed on the corresponding nights. The agreement is found to be satisfactory ($\sim$ 0.1 mag). All Hα observations are tied to the 1990 Jan 24 set of observations.

NGC 3351

This is a barred galaxy having a nuclear ring of "hot spots" and an outer ring. The galaxy has been well studied both photometrically and dynamically (Buta 1988). The morphology of the hot spots has been studied by Alloin and Nieto (1982), Prabhu (1980a). Two of the regions in the galaxy have been studied spectroscopically by McCall, Rybsky and Shields (1985).

The main optical extent of the galaxy could be fitted well within the CCD. The

nucleus of the galaxy is centred on the CCD. Seven regions including nucleus are identified for photometry. Region 1 is the giant H II region which McCall, Rybsky and Shields (1985) regard as the most important H II region on the sky, based on its high metallic abundance. Rest of the regions are nuclear hot spots. The regions are identified in Fig. III.6, with the inset showing the nuclear hot spots on a different grey scale. Magnitudes were measured on two frames each in $H\alpha, B$ and V, which were then averaged after correcting for zeropoint differences. BV calibration is based on 1991 Feb 14 observations, while Feb 15 frames are used for $H\alpha$ and R calibration.

NGC 4303

This Sérsic Pastoriza galaxy is a face-on spiral, belonging to the Virgo cluster. The galaxy does not lie near the centre of the cluster and hence not much affected due to the cluster environment. Morphologically the galaxy has two well defined spiral arms, both containing chains of giant H II regions. The galaxy is studied mostly because of its membership to the Virgo cluster.

The galaxy was observed by centering the nucleus on the CCD. This setting includes most of both the arms. Based on $H\alpha$ and V band images, we have identified 40 regions for photometry. Additional photometry is done using bigger apertures for 16 regions, each of which includes more than one emitting knot identified with smaller apertures. Figs III.7(a) and (b) contain the identification for smaller and larger apertures respectively. The galaxy was observed on 1991 Feb 15, in all the $BVRH\alpha$ bands. During Feb and April observing runs in 1992, additional frames were obtained. Magnitude measurements were done on all the frames and the 1991 and 1992 data were transformed independently. This gives a check on the reliability of the observed magnitudes and colours. Comparing the growth profiles around the nucleus, the V measurements agree within 0.03 mag, which is around 0.1 mag fainter

than Tifft (1969). The 1992 $B - V$ colours are bluer by around 0.1 mag, with the Tifft (1969) colours midway between our two measurements (see Table III.6). 1991 calibration is more reliable of the two and hence is used in this study.

NGC 4449

This is an Irregular galaxy rich in H II regions (Crillon and Monnet 1969; Hodge 1969; Sabbadin and Bianchini, 1979) and blue supergiants. The galaxy is most interesting for the presence of filamentary and bubble like structures (Sabbadin and Bianchini 1979; Hunter 1982; Hunter and Gallagher 1990, 1992). Hunter (1982) found evidence for star induced star formation from the spatial sequence of blue stars, Hα emitting regions and dust. The optical size of 4.7×3.0 arcmin^2 is about 13 times smaller compared to the neutral Hydrogen extent (van Woerden, Bosma and Mebold 1975). The brightest of the H II complexes in this galaxy, namely CM 39, is investigated for star formation properties using multiwavelength observations (Lequeux *et al.* 1979, 1981).

$BVRH\alpha$ observations of this galaxy were carried out with 1-m telescope in 1991 season. The galaxy is imaged in emission lines of Hα, Hβ and [O III] λ 5007 in addition to broad bands $BVRI$ with the VBT. Because of the larger field, the VBT images cover all the H II regions in the galaxy. Twelve regions including the nucleus were selected for photometry on 1-m images. In addition to these, eight more regions are selected on VBT images. Measurements were made around seven regions using bigger apertures. The identification of all H II regions are done on an Hα frame taken with VBT. Fig. III.8(a) and (b) respectively correspond to small and large apertures. North is to the top and east is to the left in these diagrams. The image scale is 0.64 arcsec pixel^{-1} on these plots. 1-m observations are calibrated using the EG 99 standard star frames (see Table III.3(a)). Calibration of the frames obtained with VBT are done using the photometry of H II regions

common with the 1-m frames, along with data taken from literature for some other regions. The BVR transformation coefficients are re-determined for H II region data from PCCD as standard data. The resulting coefficients are given in Table III.3(b). $V - I$ transformation is based on Hunter's (1982) photometry around the nucleus ($V - I = 0.84$ in an $8''$ aperture). Hα calibration is based on Kennicutt's (1988) photometry of region HK 27 ($\log$ H$\alpha = -11.70$ erg cm^{-2} s^{-1}). [O III] λ 5007 and Hβ calibrations are based on the spectroscopic data on the nucleus by McCall, Rybsky and Shields (1985). In all these transormations care is taken to see that the apertures are matched as closely as possible.

NGC 4656

This is a Magellanic type Irregular having an $\int$ shaped morphology, with highly asymmetric light distribution. Little is known about this galaxy inspite of its peculiar morphology and bright nuclear region. The optical surface photometry is carried out by Stayton, Angione, Talbert (1983). Other studies are mainly concentrated on the H I bridge connecting this galaxy with NGC 4631 (Winter 1975; Weliachew, Sancisi and Guelin 1978).

Only the brighter North-East part of the galaxy is observed for the study. $BVRI$HαHβ [O III] λ 5007 observations were carried out with VBT on the same nights and at very similar airmasses as of NGC 4449. Thus the coefficients used for transformations are the same as that for NGC 4449. A total of nine regions are chosen for the photometry. Published spectrophotometric data are not available for any of these regions. The chosen regions are identified on the Hα image from VBT in Fig. III.9. The orientation and the image scale is same as for NGC 4449.

NGC 5253

The southern galaxy NGC 5253 has been the object of many studies due to the
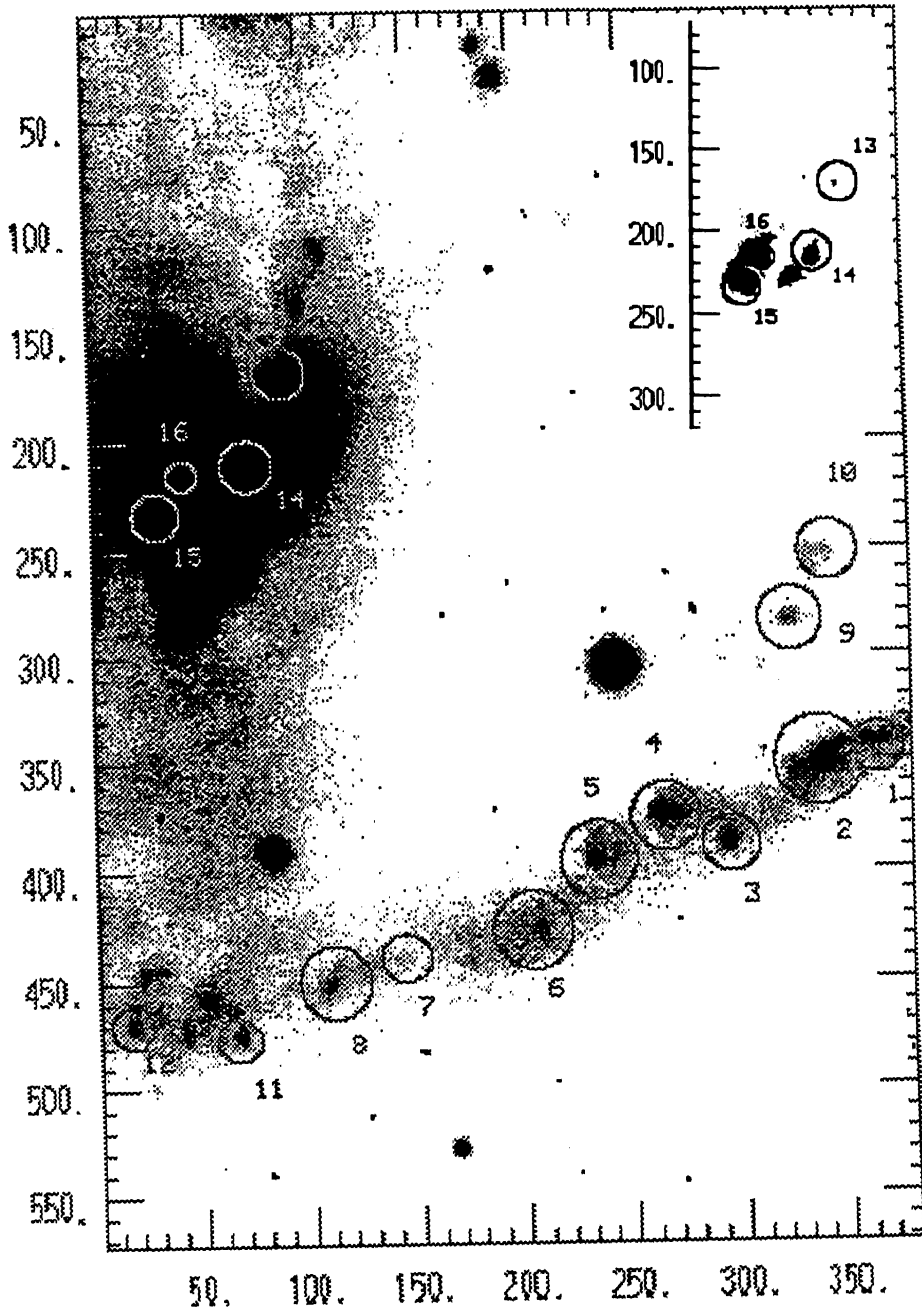
Figure III.1 NGC 1365 A chart identifying the HII regions selected for this study. Circular apertures denote the area used for flux measurements. Axes are in pixel coordinates. North is to the right and East to the top. Inset shows the nuclear region with a different grey scale.
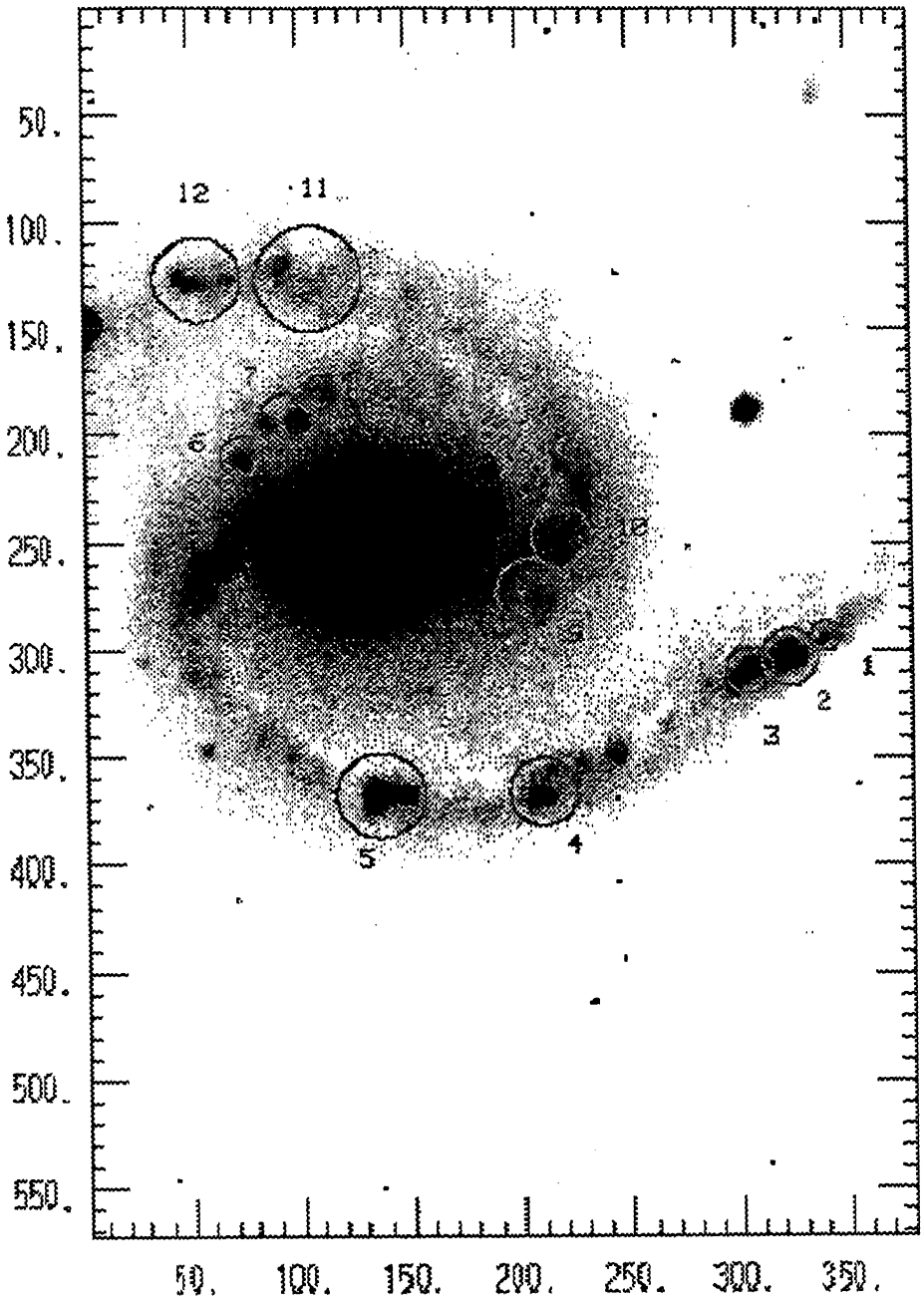
Figure III.2   NGC 1566.
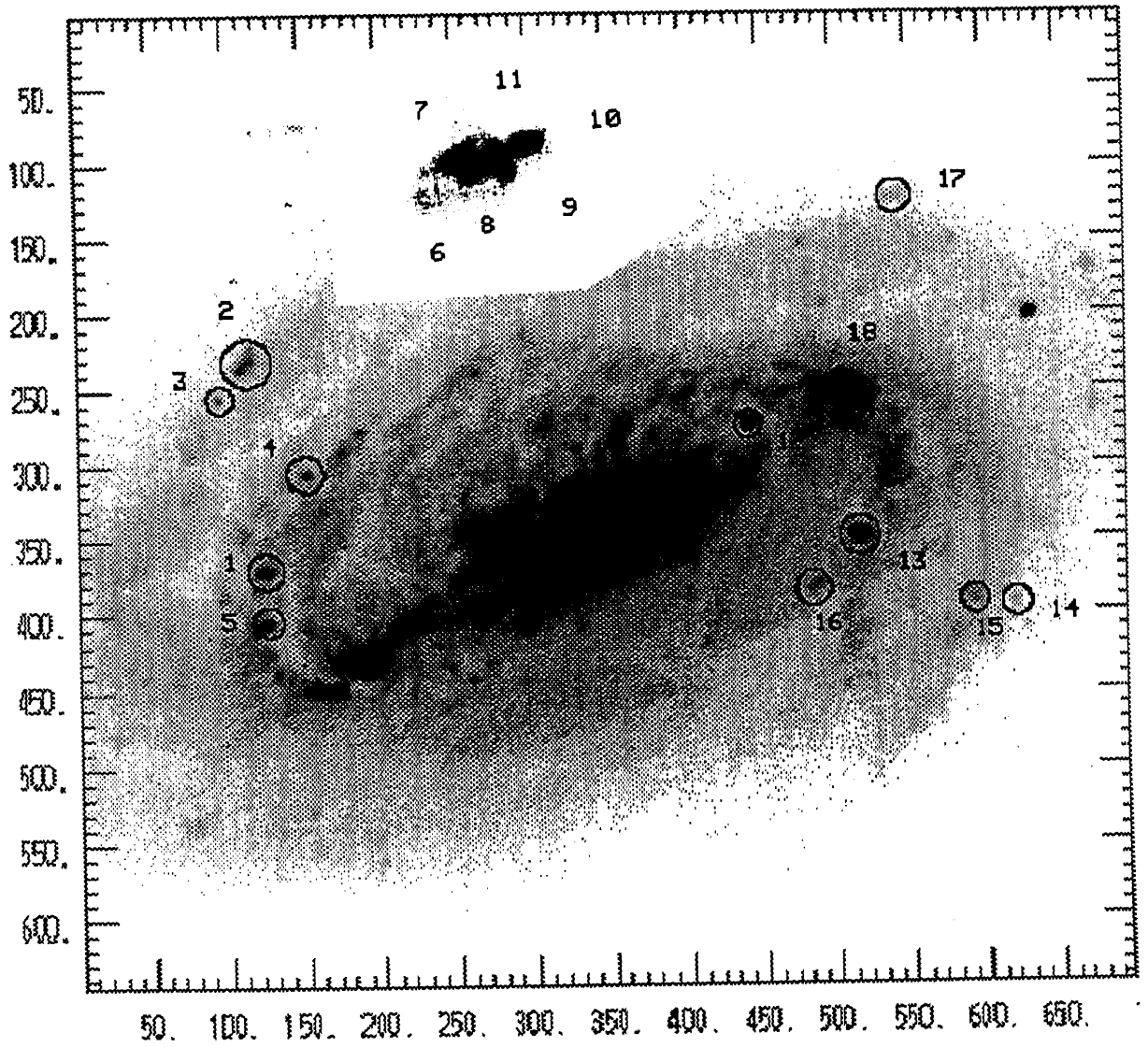
Figure III.3   NGC 2903.

Inset shows the nuclear hotspots with a different grey scale.
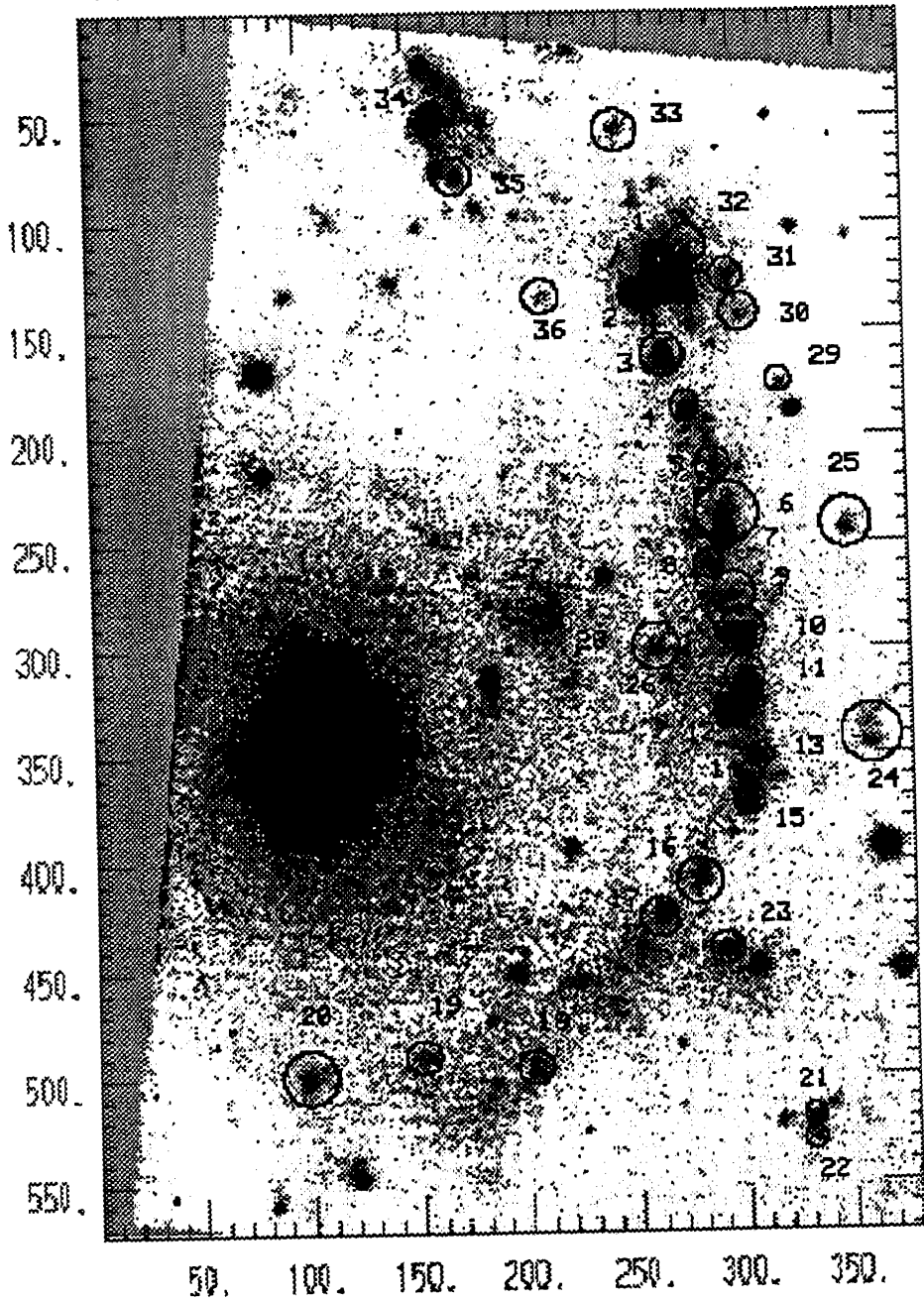
Figure III.4(a)   NGC 2997 North-East arm.
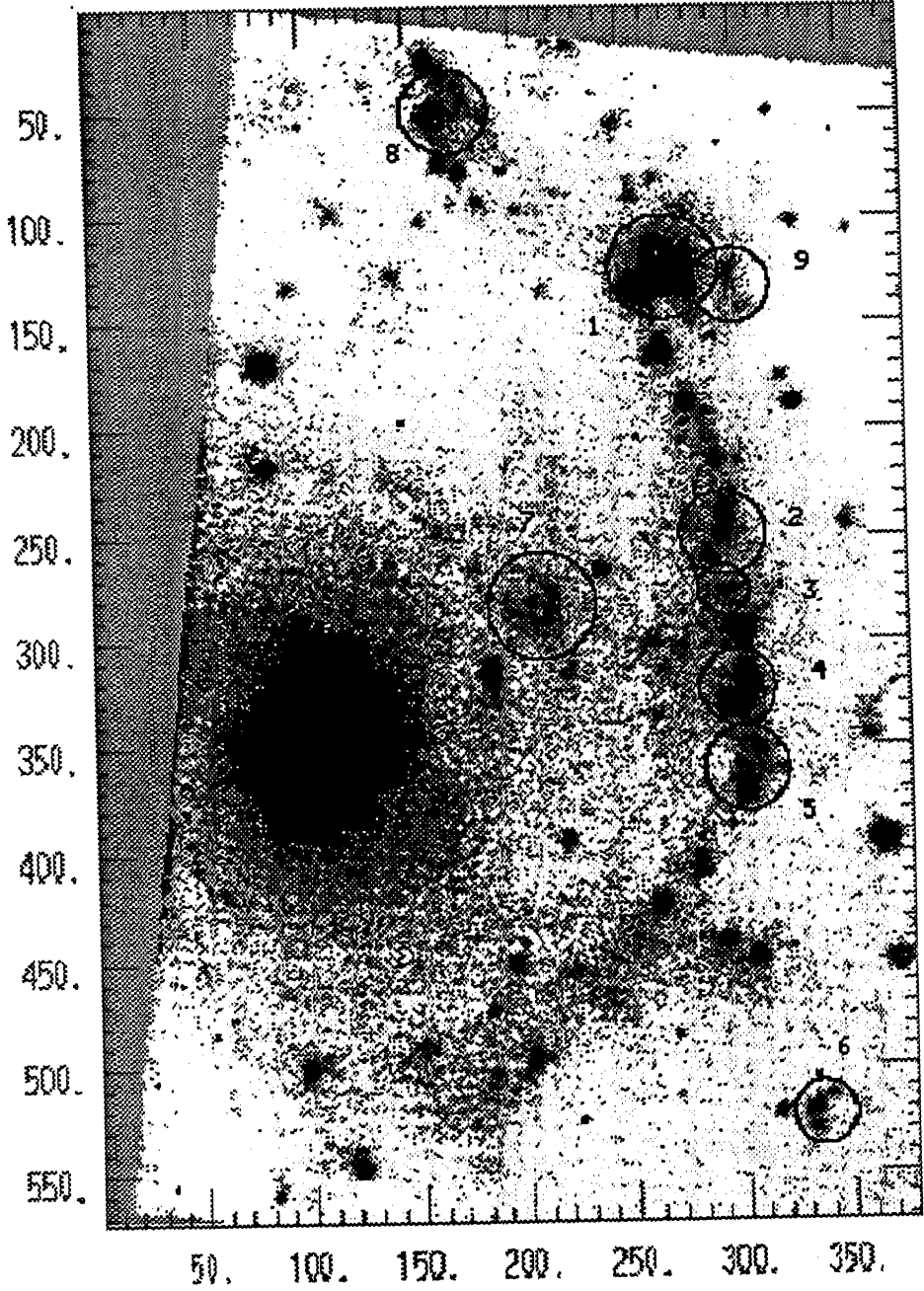
Figure III.4(b) NGC 2997 North-East arm.

H II complexes with photometry using bigger apertures are identified.
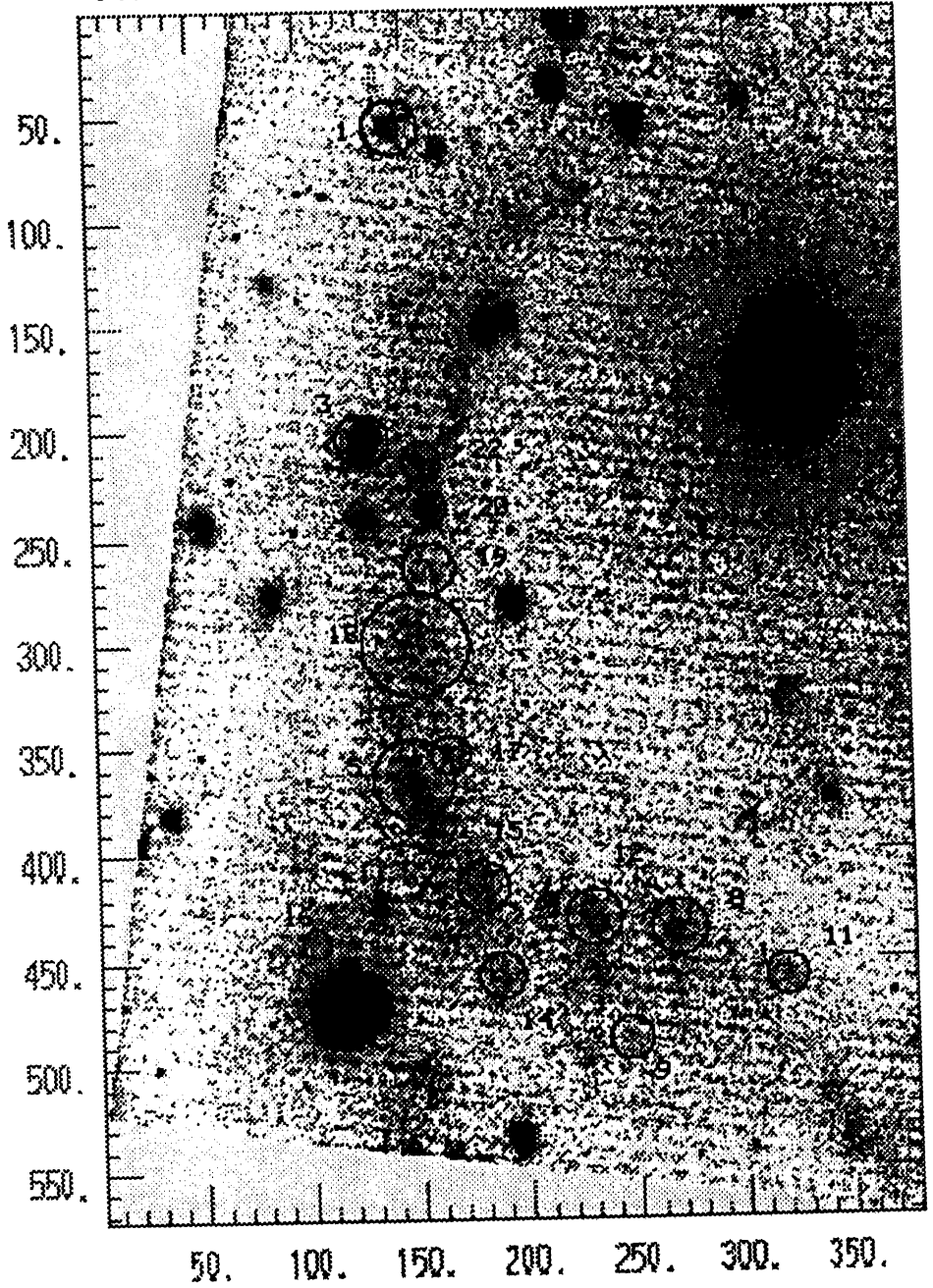
Figure III.5   NGC 2997 South-West arm.
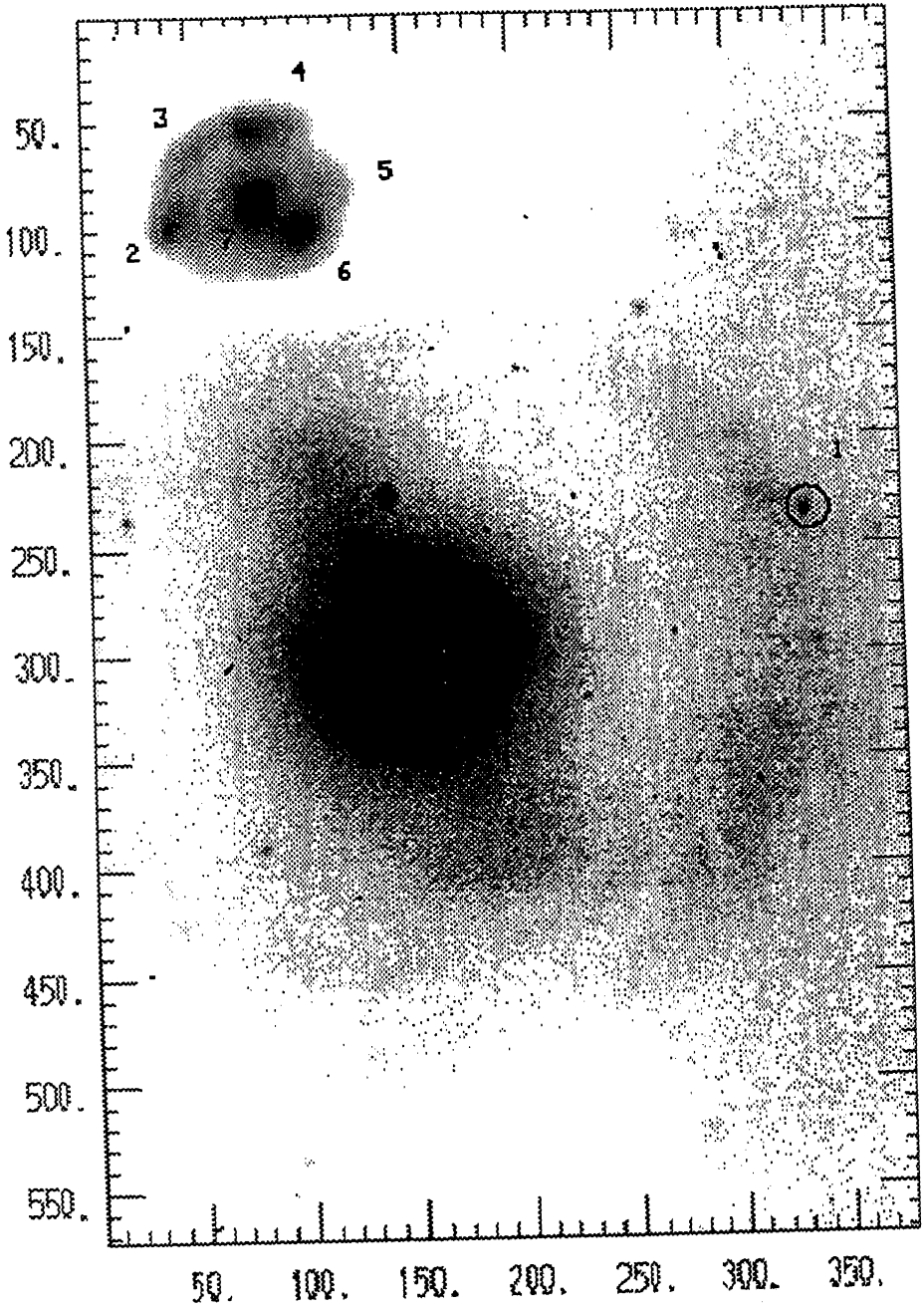
Figure III.6   NGC 3351.

Inset shows the nuclear hot spots with a different grey scale
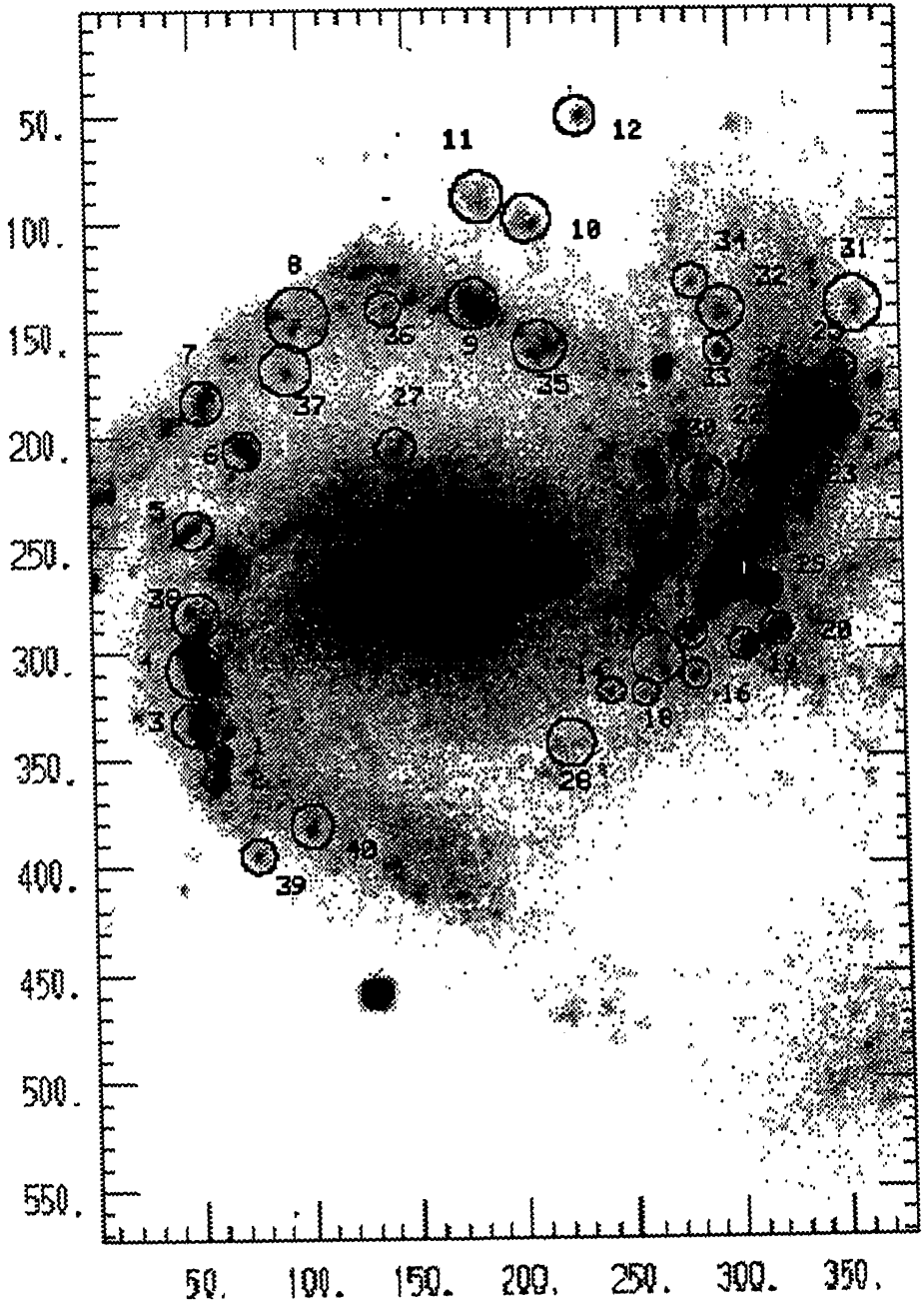
Figure III.7(a)   NGC 4303.
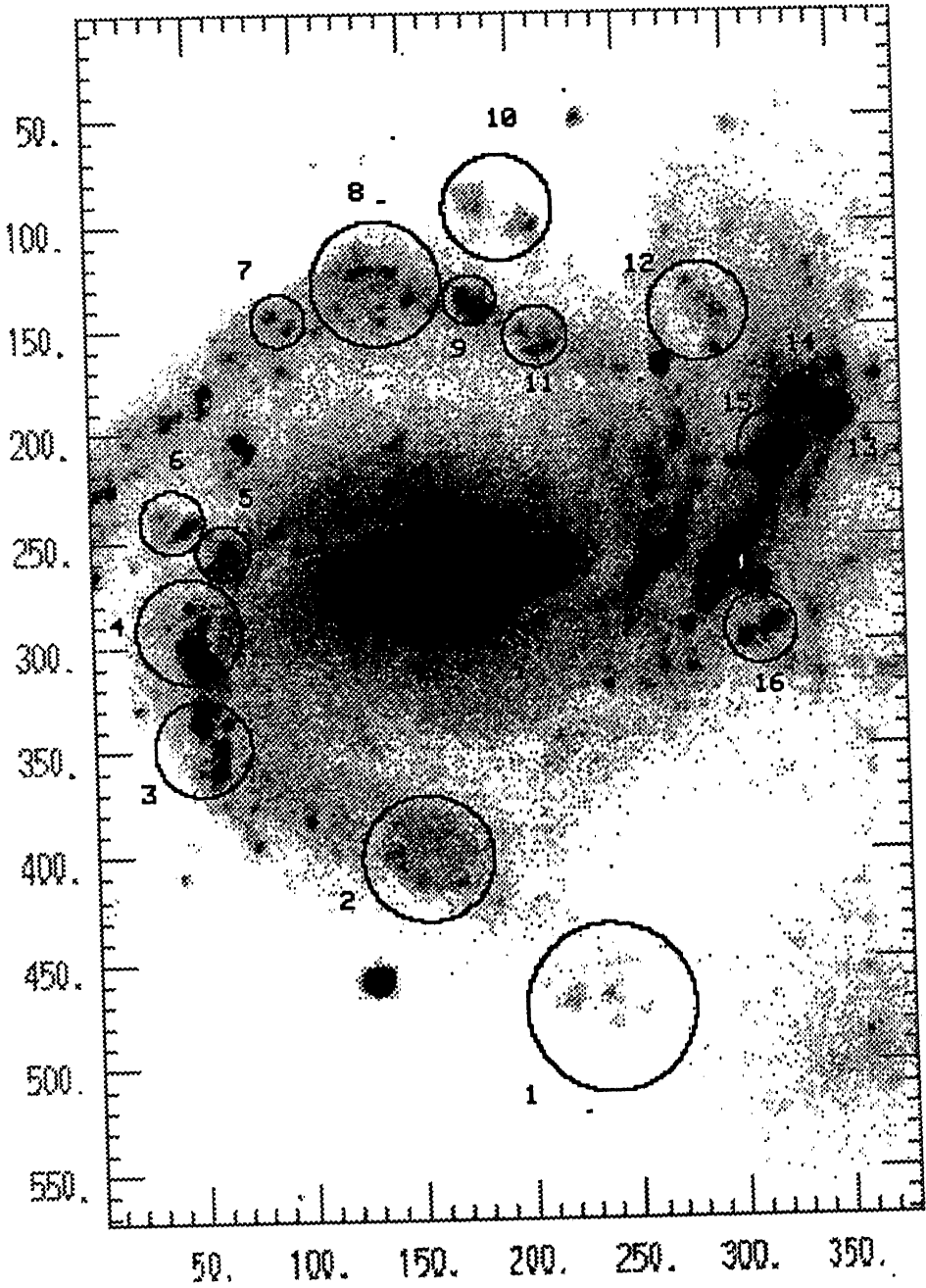
Figure III.7(b) NGC 4303.

H II complexes with photometry using bigger apertures are identified.
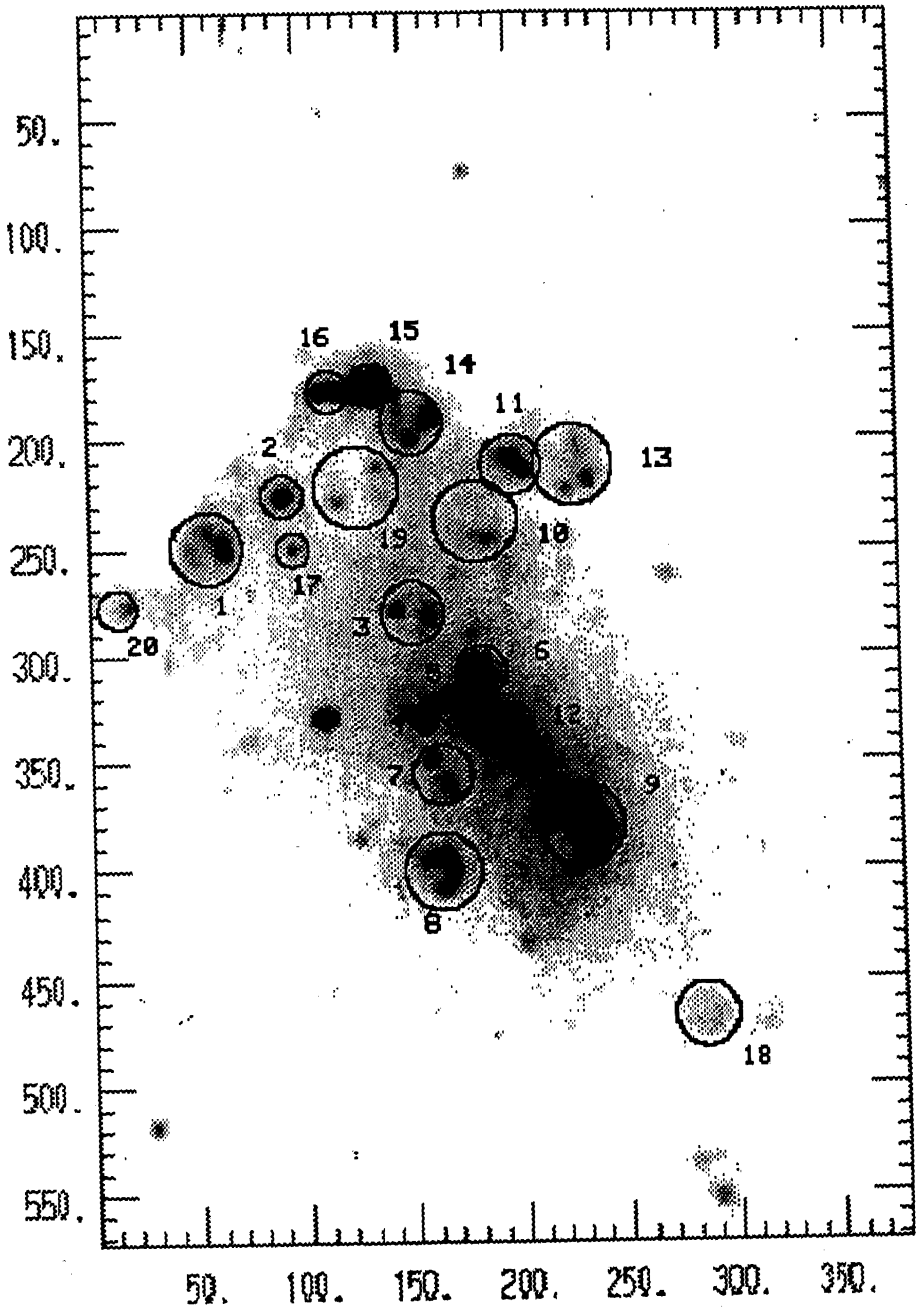
Figure III.8(a)   NGC 4449.

North is up and East to the right. See text for the image scale.

NGC 4449 H_ALPHA
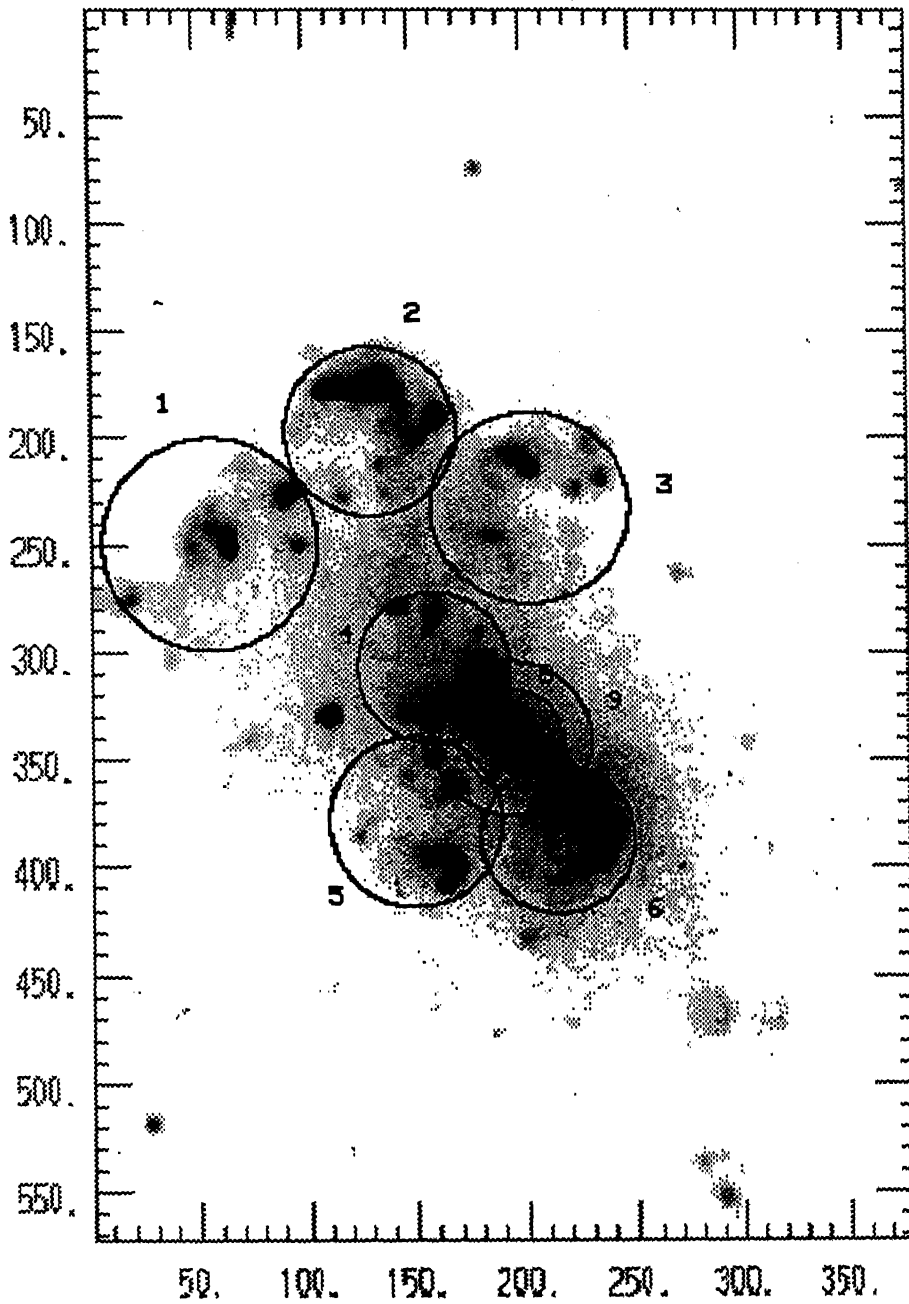
Figure III.8(b)   NGC 4449.

H II complexes with photometry using bigger apertures are identified.
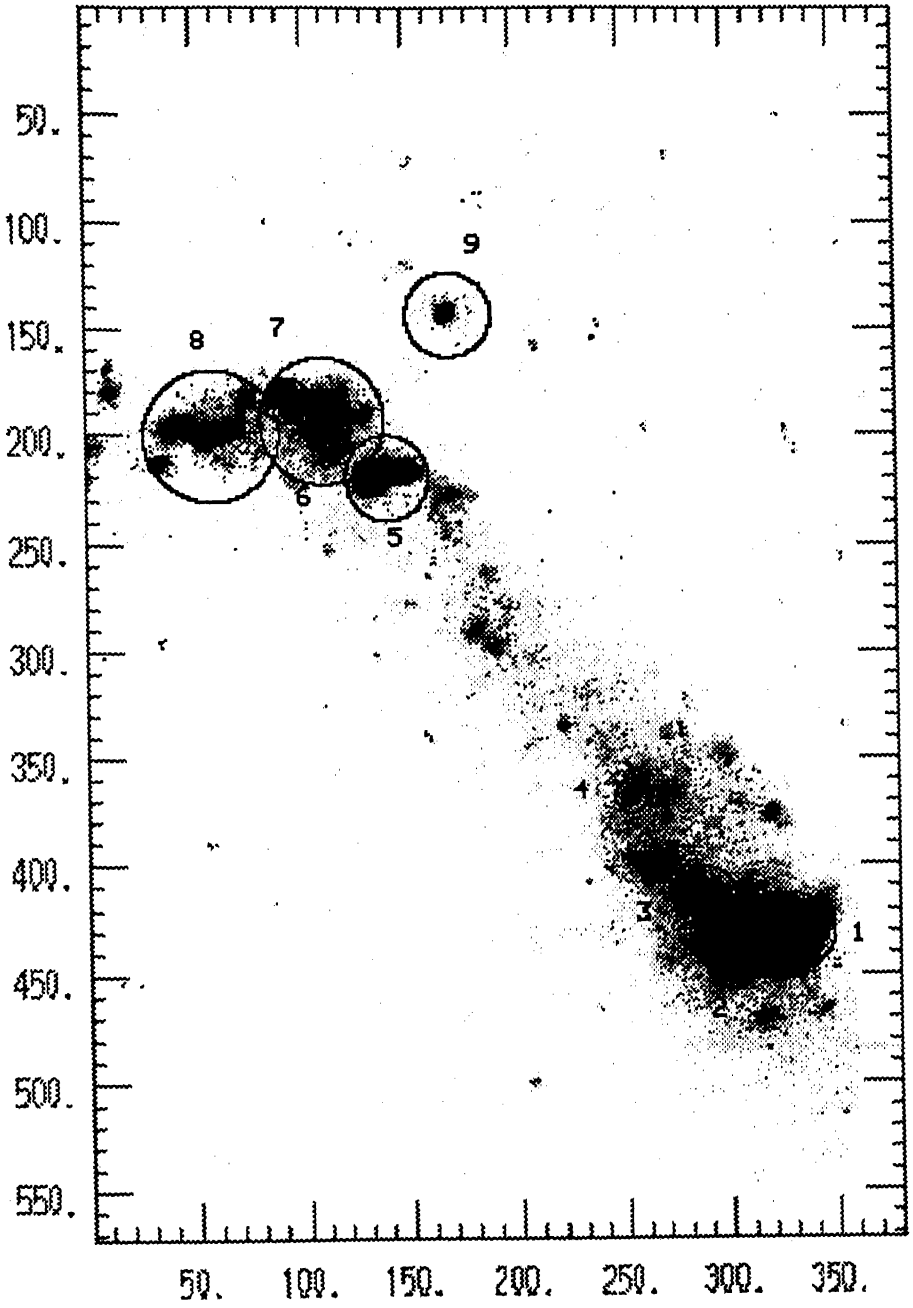
Figure III.9   NGC 4656.

North is up and East to the right. See text for the image scale.

noticeable characteristics of its nucleus. This has been classified as Irr II p (Irregular non-magellanic and peculiar). The outer isophotes resemble elliptical galaxies, while the inner nuclear region shows characteristics of young star forming regions. The ionized gas in the central region has been studied spectroscopically by Webster and Smith (1983), Campbell, Terlevich and Melnick (1986), Walsh and Roy (1989a) among others. The nuclear structure is clearly seen in the broad band photograph of Campbell and Terlevich (1984).

The galaxy is observed in $BVRH\alpha$ bands keeping the nuclear region at the centre of the CCD. All the regions of interest lie in the nuclear region of the galaxy. Continuum images show eight unresolved knots, whereas the $H\alpha$ image does not show any of these knots, but has a distribution extending over all knots, with the bright point coinciding with the nucleus. We have selected this region for photometry. The photometric transformations are based on the observations carried out on 1991 Feb 14. The zeropoints are obtained from observations of EG 99.

3. The Photometric Catalogue of H II Regions

The calibrated photometric data on selected H II regions are presented in this section. Table III.4(a) contains the results of our $BVRH\alpha$ photometry with 1-m telescope, while Table III.4(b) contains the results of $BVRIH\alpha H\beta$ [O III] λ 5007 photometry with VBT. The descriptions of the items in the table are as follows.

(1) ID : H II region numbers as identified by us on the accompanying charts (Figs III.1–9). Regions having large photometric errors are not included in the catalogue even if they are numbered.

(2)-(3) X, Y : The X and Y pixel coordinates on the CCD frames.

(4)-(5) RA, DEC : Approximate position of the H II region, along R.A. and declination in seconds of arc, with respect to the galactic nucleus. For NGC 2366 the giant H II complex NGC 2363 is taken as the reference. These are obtained by

tranforming X and Y assuming that the RA-DEC axis is aligned with X-Y axis. Since the alignment during observations is only approximate ($\leq 5°$), RA and DEC values away from the centre are less accurate, compared to those near the centre of the CCD. Thus the positions should be considered accurate only for identification purposes. E, W, N, and S preceeding the numbers indicate respectively whether the H II region is to the East, West, North or South of the Nucleus of the galaxy.

(6) DIA : Diameter of the aperture chosen for magnitude extractions in seconds of arc.

(7)–(9) $V, B - V, V - R$: V Magnitude, $B - V$ and $V - R$ colours of H II regions after subtracting assumed background. The rms errors on the measured magnitudes is in the range 0.05–0.10, as estimated from measurements on multiple frames.

(10) $\log F\alpha$: Observed Hα+ [N II] flux in units of erg cm^{-2}s^{-1}. The magnitudes can be taken to be accurate to 0.1 dex.

(11) W(Hα) : Hα+ [N II] emission equivalent widths in Å. R magnitude is used as an estimate for the continuum at Hα. (See eqn II.17 for an exact definition). The measurement errors are ≤ 20 Å.

(12) Qual. : An index of photometric quality. See the discussion below for definition.

(13) Other Id. : Identification from other authors when available. Notes to the table, list the relevent references.

Table III.4(b) contains the results of our $BVRIH\alpha H\beta$ [O III]λ 5007 photometry. All these data are obtained with the VBT. Description of columns (1)–(8) are same as above. Results of I band photometry are given in column (9) as $V - I$ colours. Column (10) contains Hα+ [N II] fluxes. $\frac{I(H\alpha)}{I(H\beta)}$ and $\frac{I([O III]\lambda\ 5007)}{I(H\beta)}$ ratios are given in columns (11) and (12) respectively in log units. Hα, Hβ and [O III]λ 5007 fluxes are not corrected for the contribution from the continuum within the band. However, the expected continuum within the narrow bands is

negligibly small. The last column lists other identifications.

The regions in the catalogue are given a photometric quality index based on the errors on the derived $B - V$ and $V - R$ colours due to the uncertainty in the background estimation, following the methods discussed in section II.3. We assume that the background values are underestimated by a maximum amount of 10%. The photometric quality is 1 if the computed errors on $B - V$ and $V - R$ is ≤ 0.1 mag. Similarly regions having errors between 0.1–0.2 are given an index 2, those between 0.2–0.3 are given an index 3. Index 4 means that the estimated errors in one of the colours is greater than 0.3 mag. Correction for this uncertainty has the effect of making the colours systematically bluer than the catalogue values. The actual errors on the colours and magnitudes are less than this because of the following reasons.

(a). 10% uncertainty in background measurements is an upper estimate.

(b). The underestimated backgrounds might well be compensated by weak emissions from the extended haloes outside the chosen apertures.

The rms errors on the measured magnitudes are estimated based on measurements on multiple frames. First the magnitudes of each region in different measurements (for a given filter) are compared with the one having the best photometric quality (or reference frame) and a mean value of zero point shifts between the frames are found out. These zero point shifts are applied on all the frames to bring all of them to the system of reference frame. Shifted magnitudes are combined with the reference magnitudes to obtain the mean magnitude and rms errors on these magnitudes. Typical errors are in the range 0.05–0.10 mag. Since $B - V$ and $V - R$ colours are obtained by independent BVR measurements the errors on colours will be slightly more. We estimate the errors on the colours to be less than 0.15 mag.

The observed $B-V$ and $V-R$ colours are plotted against observed V magnitudes and H$\alpha+$ [N II] fluxes in Figs III.10. These plots are useful in checking any

Table III.4(a) Photometric catalogue of H II regions.

Id	X	Y	RA	DEC	DIA	V	$B-V$	$V-R$	$\log F\alpha$	W(Hα)	Qual.	Other Id.
1	2	3	4	5	6	7	8	9	10	11	12	13

NGC 1365

Id	X	Y	RA	DEC	DIA	V	$B-V$	$V-R$	$\log F\alpha$	W(Hα)	Qual.	Other Id.
1	365	346	W047	N115	8.6	16.75	0.18	0.16	−12.90	216	1	RW-B
2	337	351	W049	N105	15.0	15.77	0.17	0.30	−12.47	208	1	RW-C,L7
3	296	390	W062	N090	9.3	16.95	0.25	0.24	−12.95	216	1	RW-D,L15
4	266	377	W058	N080	11.4	16.32	0.25	0.23	−12.91	130	1	RW-E
5	234	397	W065	N068	12.9	16.24	0.34	0.18	−13.20	67	1	RW-F
6	203	429	W076	N057	12.9	16.22	0.28	0.20	−13.03	94	1	RW-F
7	144	441	W081	N036	7.9	18.47	0.25	0.44	−13.33	297	4	
8	111	452	W085	N024	12.1	16.93	0.24	0.34	−12.82	257	3	L28
9	325	285	W025	N101	10.7	17.36	0.16	0.28	−12.70	534	3	
10	343	252	W013	N107	10.0	17.30	0.27	0.24	−12.95	294	1	
11	65	479	W094	N008	7.1	17.58	0.10	0.61	−12.90	303	3	L6
12	15	472	W092	S010	7.1	17.31	0.41	0.49	−13.06	183	2	
13	89	168	E017	N017	8.6	16.18	0.31	0.63	−12.43	246	1	L4
14	73	211	E001	N011	8.6	14.84	0.57	0.52	−12.39	87	1	L12
15	30	234	W007	S005	7.9	14.21	0.59	0.58	−12.21	69	1	L3
16	43	215	W000	S000	5.0	15.01	1.51	1.05	−12.35	67	1	Nuc

NGC 1566

Id	X	Y	RA	DEC	DIA	V	$B-V$	$V-R$	$\log F\alpha$	W(Hα)	Qual.	Other Id.
1	341	294	W016	N074	5.0				−12.98	283	4	RW-A
2	324	304	W019	N068	9.3	15.94	−0.11	0.74	−12.12	354	4	RW-B,HP-I
3	305	310	W021	N061	7.9	16.17	0.12	0.59	−12.47	229	3	RW-C,HP-II
4	210	367	W042	N028	11.4	15.87	0.20	0.38	−12.80	98	4	RW-D,HP-IV
5	136	369	W042	N001	14.3	15.62	0.16	0.55	−12.25	233	4	RW-E,HP-VI
11	105	126	E044	S010	17.9	15.74	−0.20	0.44	−12.73	97	4	HP-V
12	53	127	E044	S029	14.3	16.05	−0.01	0.53	−12.58	166	2	HP-III

NGC 2366

Id	X	Y	RA	DEC	DIA	V	$B-V$	$V-R$	$\log F\alpha$	W(Hα)	Qual.	Other Id.
1	102	278			25.0	13.76	0.14	0.39	−11.24		1	NGC 2363, HK72
2	122	228			19.8	15.60	−0.03	0.70	−12.23		1	HK54
3	108	263			53.6	13.52	0.11	0.60	−11.16		1	1+2

NGC 2903

Id	X	Y	RA	DEC	DIA	V	$B-V$	$V-R$	$\log F\alpha$	W(Hα)	Qual.	Other Id.
1	125	370	W011	S078	8.6	17.30	0.39	0.88	−12.68	301	2	MRS(−003−070)
2	114	231	E039	S082	11.4	16.71	0.03	0.56	−12.66	249	2	MRS(+047−072)
3	96	255	E030	S088	6.4				−12.98		4	MRS(+039−078)
4	152	305	E012	S068	8.6				−12.86		4	
5	126	404	W023	S077	7.1	16.99	0.38	0.54	−13.04	137	1	
6	315	358	W006	S010	6.4	15.27	0.48	0.44	−14.68	-1	1	Oka-e
7	327	342	W001	S006	5.0	14.82	0.51	0.54	−12.88	27	1	Oka-c
8	335	348	W003	S003	3.6	15.90	0.75	0.74	−13.25	26	1	TPP-n

Table III.4(a) Continued.

Id	X	Y	RA	DEC	DIA	V	$B - V$	$V - R$	$\log F\alpha$	W(Hα)	Qual.	Other Id.
1	2	3	4	5	6	7	8	9	10	11	12	13
9	347	349	W003	N001	5.7	14.95	0.58	0.64	−12.42	79	1	Oka-d
10	359	337	E001	N006	6.4	14.70	0.42	0.49	−12.74	35	1	Oka-a
11	343	340	E000	N000	5.0	15.10	0.65	0.69	−12.51	71	1	Oka-b
12	441	274	E023	N035	6.4	17.72	−0.20	0.62	−12.87	367	4	MRS(+024+047)
13	516	349	W004	N061	9.3	16.71	0.17	0.79	−12.48	298	2	MRS(−003+069)
14	621	394	W020	N099	7.1				−13.52		4	MRS(−021+105)
15	593	392	W019	N089	7.1	17.99	0.08	0.41	−13.31	205	4	
16	484	384	W016	N050	8.6	18.19	0.11	0.84	−12.99	346	4	
17	542	123	E077	N071	7.9	18.16	0.12	0.49	−13.31	225	4	
18	506	246	E033	N058	5.7	17.25	0.09	0.49	−13.38	83	2	

NGC 2997-NE

Id	X	Y	RA	DEC	DIA	V	$B - V$	$V - R$	$\log F\alpha$	W(Hα)	Qual.	Other Id.
1	268	123	E080	N059	6.4	17.49	0.28	0.81	−12.79	299	2	RW-B
2	255	133	E076	N055	5.0	18.07	0.23	0.40	−13.27	250	2	RW-C
3	267	162	E066	N059	7.1				−13.23		4	RW-D
4	277	186	E057	N062	5.0			1.00	−13.57		4	RW-E,WR13
5	290	214	E047	N067	5.7			0.82	−13.62		4	RW-F
6	296	237	E039	N069	10.7			0.89	−13.60		4	RW-G
7	294	249	E035	N069	4.3	18.74	0.13	0.35	−13.71	173	3	RW-G
8	287	261	E030	N066	5.0	18.75	0.02	0.24	−13.71	194	4	
9	299	275	E025	N070	7.1				−13.66		4	RW-H
10	302	293	E019	N071	7.9	17.45	0.08	0.31	−13.27	154	3	RW-I,WR20
11	303	314	E011	N072	6.4				−13.35	357	4	RW-J
12	295	330	E006	N069	5.0	18.47	0.20	0.44	−13.47	217	3	RW-K
13	310	352	W002	N074	4.3	18.88	0.09	0.24	−13.82	168	4	RW-L,WR23
14	304	360	W005	N072	3.6	19.13	0.19	0.36	−14.19	82	3	
15	304	373	W010	N072	5.0				−13.56		4	
16	279	410	W023	N063	7.9				−13.47		4	
17	260	427	W029	N056	6.4	18.29	0.53	0.39	−13.66	126	4	
18	202	497	W054	N036	5.7				−13.62		4	
19	150	492	W052	N017	5.7				−13.91		4	
20	98	501	W055	S001	9.3	18.54	−0.16	0.74	−13.51	159	4	
21	332	521	W062	N082	3.6				−13.87		4	
22	332	532	W066	N082	3.6	18.80	0.33	−0.10	−14.49	47	4	
23	292	442	W034	N068	5.7				−13.50		4	
24	362	342	E001	N093	10.0	18.17	0.16	0.25	−13.70	116	4	
25	352	242	E037	N089	8.6	19.17	0.24	0.75	−13.71	179	4	
26	261	300	E016	N057	7.9				−13.59		4	
27	203	282	E023	N036	3.6				−14.51		4	
28	214	285	E022	N040	3.6				−14.34		4	

Table III.4(a) Continued.

Id	X	Y	RA	DEC	DIA	V	B − V	V − R	log Fα	W(Hα)	Qual.	Other Id.
1	2	3	4	5	6	7	8	9	10	11	12	13
29	322	174	E061	N079	4.3				−13.95		4	
30	304	142	E073	N072	6.4	18.11	0.36	0.36	−13.65	110	4	
31	298	125	E079	N070	5.7	18.67	0.41	0.57	−13.41	266	4	
32	279	111	E084	N063	7.1	18.13	0.29	0.32	−13.68	109	4	
33	247	56	E104	N052	7.1				−13.55		2	
34	163	48	E106	N022	4.3	17.65	0.32	0.54	−13.40	107	4	
35	172	77	E096	N025	6.4				−13.94		4	
36	212	134	E076	N039	5.7				−14.03		2	

NGC 2997-NE(Groups)

Id	X	Y	RA	DEC	DIA	V	B − V	V − R	log Fα	W(Hα)	Qual.	Other Id.
1	269	124	E079	N060	17.9	15.72	0.38	0.53	−12.29	240	2	1+2+32
2	294	250	E034	N069	14.3	16.97	0.07	0.56	−12.94	165	4	6+7+8
3	294	277	E025	N069	8.6	18.05	0.20	0.46	−13.34	199	4	9
4	300	324	E008	N071	12.9	17.52	0.18	0.77	−12.82	296	4	10+11+12
5	303	362	W006	N072	14.3	17.70	0.30	0.49	−12.97	319	4	13+14+15
6	337	525	W064	N084	10.7	18.14	0.14	0.11	−13.41	253	4	21+22
7	209	284	E022	N038	18.6	16.96	0.03	0.30	−13.09	148	4	27+28
8	168	49	E106	N024	14.3	16.49	0.19	0.61	−13.01	86	4	34+35
9	300	133	E076	N071	12.9	16.80	0.37	0.44	−12.94	156	4	30+31

NGC 2997-SW

Id	X	Y	RA	DEC	DIA	V	B − V	V − R	log Fα	W(Hα)	Qual.	Other Id.
1	145	55	E042	S065	9.3	17.25	0.54	0.61	−13.17	121	3	WR15
3	128	204	W011	S071	8.6	17.28	0.40	0.73	−12.76	295	3	WR24
5	148	366	W069	S064	13.6	16.35	0.33	0.52	−12.87	117	2	WR31
8	270	437	W095	S020	9.3	17.45	−0.06	0.47	−13.27	131	4	WR33
9	246	490	W113	S029	7.1				−14.12		4	WR37
11	320	460	W103	S002	7.1	18.78	0.14	0.60	−13.53	223	4	
12	230	432	W093	S035	9.3	17.55	0.39	0.52	−13.19	167	4	
14	187	459	W103	S050	7.9	17.84	0.22	0.41	−13.43	138	4	
15	180	417	W087	S053	8.6	17.39	0.18	0.42	−13.29	125	2	
16	101	443	W097	S081	5.0	17.86	0.31	0.33	−14.04	37	1	
17	166	354	W065	S058	6.4	18.52	0.20	0.66	−13.52	169	4	
18	151	302	W046	S063	17.9	16.04	0.23	0.41	−13.26	39	3	
19	157	265	W033	S061	8.6	18.50	0.84	0.50	−13.36	275	4	
20	159	236	W023	S060	5.0				−13.30		4	
22	155	214	W015	S061	6.4	17.77	0.38	0.55	−13.45	109	1	

NGC 3351

Id	X	Y	RA	DEC	DIA	V	B − V	V − R	log Fα	W(Hα)	Qual.	Other Id.
1	337	235	E023	N066	7.1	17.59	−0.04	0.38	−13.53	88	4	MRS(+014−067)
2	134	302	W001	S006	6.4	14.61	0.55	0.60	−12.57	42	1	MRS(−004−006)
3	137	288	E004	S005	4.3	15.54	0.55	0.50	−13.48	13	1	AN-a3
4	152	282	E006	N000	7.1	14.45	0.45	0.47	−12.73	28	1	AN-a1

Table III.4(a) Continued.

Id	X	Y	RA	DEC	DIA	V	$B-V$	$V-R$	$\log F\alpha$	W(Hα)	Qual.	Other Id.
1	2	3	4	5	6	7	8	9	10	11	12	13
5	166	295	E001	N005	5.0	15.42	0.69	0.61	−12.81	51	1	AN-c1
6	159	307	W003	N003	5.7	14.39	0.63	0.51	−12.86	19	1	AN-d
7	151	299	E000	N000	3.6	15.42	0.94	0.67	−14.71	1	1	AN-e(Nuc)

NGC 4303

Id	X	Y	RA	DEC	DIA	V	$B-V$	$V-R$	$\log F\alpha$	W(Hα)	Qual.	Other Id.
1	57	348	W030	S039	4.3	18.44	0.34	0.69	−13.32	232	2	
2	56	360	W034	S039	4.3	17.86	0.06	0.40	−13.51	117	2	
3	46	334	W025	S043	7.1	16.96	0.25	0.44	−12.88	211	2	HK175
4	47	309	W016	S042	9.3	15.90	0.21	0.48	−12.42	219	1	HK155
5	47	243	E007	S042	6.4	17.60	0.63	0.53	−13.25	149	2	
6	71	206	E021	S034	6.4	17.26	0.30	0.48	−13.01	196	2	
7	52	183	E029	S041	7.1	17.64	0.45	0.64	−13.11	191	4	HK76
8	98	144	E043	S024	10.7	16.66	0.04	0.51	−13.22	68	2	
9	180	138	E045	N005	8.6	16.48	0.25	0.45	−12.88	134	1	HK49
10	206	98	E059	N014	7.9	17.62	0.68	0.60	−13.32	119	4	
11	183	88	E063	N006	8.6	17.03	0.09	0.12	−14.80	-4	2	
12	230	50	E076	N023	6.4	18.35	0.07	0.67	−13.33	217	4	
13	259	255	E003	N033	4.3	18.52	0.03	0.50	−13.70	125	4	
14	241	320	W020	N027	4.3	19.35	0.50	0.87	−13.64	222	4	
15	279	294	W011	N040	5.0	18.85	0.02	0.64	−13.69	152	4	
16	281	313	W017	N041	5.0	18.21	0.16	0.25	−13.84	86	2	
17	263	305	W015	N035	8.6	17.55	0.42	0.48	−13.78	43	2	
18	257	321	W020	N032	4.3	18.65	0.53	0.20	−14.30	48	3	
19	304	299	W012	N049	5.0	18.39	1.18 :	0.73	−13.28	239	3	HK157
20	320	292	W010	N055	5.7	17.64	0.63	0.41	−13.42	116	2	
21	294	263	E000	N046	5.7	18.49	0.16	0.85	−13.22	266	4	HK135
22	312	211	E019	N052	6.4	18.18	0.34	1.04	−13.00	277	4	
23	328	209	E020	N058	6.4	16.99	0.34	0.33	−13.38	75	2	
24	351	193	E025	N066	6.4	16.48	0.20	0.35	−12.97	119	1	HK91
25	353	168	E034	N067	5.0	18.98	0.17	0.91	−13.38	275	4	
26	333	181	E030	N060	8.6	16.19	0.14	0.30	−13.20	56	1	
27	143	205	E021	S008	6.4	19.07	0.60	0.59	−13.49	309	4	HK95
28	222	344	W029	N020	7.9				−13.84	207	4	
29	314	272	W003	N053	5.7	16.79	0.49	0.38	−13.46	50	1	
30	285	220	E016	N042	7.9	17.15	0.39	0.41	−13.46	68	1	
31	359	139	E045	N069	9.3				−13.63		4	
32	296	141	E044	N046	7.9				−13.45		4	
33	294	160	E037	N046	5.0				−13.44		4	
34	282	128	E049	N041	5.7				−13.53		4	
35	211	158	E038	N016	8.6	17.02	0.38	0.45	−13.18	109	2	

Table III.4(a) Continued.

Id	X	Y	RA	DEC	DIA	V	B − V	V − R	log Fα	W(Hα)	Qual.	Other Id.
1	2	3	4	5	6	7	8	9	10	11	12	13
36	139	140	E044	S010	5.7	18.29	0.68	0.50	−13.66	112	4	
37	92	168	E034	S026	8.6	17.92	0.46	0.26	−13.63	107	4	
38	48	284	W007	S042	7.9	17.21	0.77	0.50	−13.31	95	2	
39	75	396	W047	S032	5.7	17.76	0.50	0.37	−13.98	38	1	
40	101	382	W042	S023	7.1				−13.28		4	
NGC 4303(Groups)												
1	237	475	W075	N025	28.6	15.19	0.63	0.12	−12.44	152	4	
2	154	403	W050	S004	21.4	16.16	0.31	0.23	−13.07	79	4	39+40
3	50	349	W030	S041	16.4	16.68	−0.36	0.44	−12.41	474	4	1+2+3
4	45	293	W010	S043	17.9	15.37	0.35	0.49	−12.38	146	2	4+38
5	62	256	E003	S037	9.3	16.29	0.60	0.27	−13.68	21	1	5
6	38	241	E008	S046	10.7	17.25	0.35	0.50	−12.95	218	4	
7	91	145	E042	S027	9.3	16.86	−0.03	0.61	−13.17	84	2	8
8	137	128	E049	S010	21.4	15.08	0.38	0.49	−12.82	41	2	36
9	180	136	E046	N005	8.6	16.49	0.24	0.46	−12.87	136	1	9
10	194	92	E061	N010	17.9	15.86	0.30	0.34	−12.81	97	3	10+11
11	210	154	E039	N016	10.7	16.74	0.42	0.43	−13.06	116	2	35
12	287	143	E043	N043	17.1				−12.77		4	32+33+34
13	351	192	E026	N066	6.4	16.05	0.27	0.38	−12.85	104	1	24
14	334	183	E029	N060	6.4	16.14	0.36	0.25	−13.45	31	1	26
15	321	208	E020	N055	11.4	15.24	0.50	0.31	−12.78	61	1	22+23
16	313	295	W011	N052	12.1	15.80	0.38	0.44	−12.75	97	1	19+20
NGC 4449												
.1	273	55	E080	N047	16.4	15.58	0.26	0.51	−12.33	201	1	
2	311	109	E061	N061	10.7	17.23	0.05	0.66	−12.59	446	1	
3	231	205	E026	N032	15.7	15.10	0.07	0.29	−12.71	66	1	
4	159	210	E025	N006	11.4	15.39	0.11	0.45	−12.53	113	1	
5	160	244	E012	N007	15.0	14.44	0.20	0.40	−12.46	57	1	
6	190	253	E009	N017	10.0	14.98	0.12	0.33	−12.73	54	1	
7	109	230	E017	S011	15.7	15.40	0.23	0.53	−12.51	110	1	
8	41	230	E017	S036	15.0	15.65	0.19	0.55	−12.34	203	1	HK16
9	75	328	W017	S024	20.0	13.41	0.02	0.30	−11.79	114	1	HK27
10	298	250	E010	N056	20.0	14.88	0.12	0.32	−12.76	46	1	
11	342	274	E002	N072	15.7	16.02	0.03	0.46	−12.44	247	1	
12	140	278	E000	S000	12.1	13.59	0.22	0.38	−12.20	49	1	Nuc
NGC 5253												
1	191	257	E000	S000	9.3	13.31	0.33	0.37	−11.24	337	1	Nuc
2	164	265	W003	S010	9.3	13.96	0.16	0.38	−11.84	154	1	HS

See Table III.4(b) for index to cross identification.

89

Table III.4(b) $BVRIH\alpha H\beta[OIII]$ Photometry[†].

Id	X	Y	RA	DEC	DIA	V	$B-V$	$V-R$	$V-I$	$\log F\alpha$	$\log \frac{F\alpha}{F\beta}$	$\log \frac{F_{[OIII]}}{F\beta}$	Other Id.
1	2	3	4	5	6	7	8	9	10	11	12	13	14
NGC 4449													
1	55	248	E077	N051	18.9	15.09	0.10	0.64	0.74	−12.32	0.72	0.67	
2	91	224	E057	N064	11.1	16.42	−0.05	0.73	0.55	−12.65	0.81	0.80	
3	151	279	E024	N033	16.6	14.81	0.13	0.35	0.62	−12.56	0.52	0.62	
4	156	330	E021	N005	6.7	16.50	0.11	0.68	0.73	−12.83	0.76	0.65	
5	172	323	E012	N009	11.1	14.41	0.19	0.40	0.78	−12.44	0.49	0.59	
6	183	307	E006	N018	13.3	14.33	0.20	0.39	0.70	−12.37	0.52	0.61	
7	164	355	E017	S009	15.5	15.21	0.24	0.53	0.70	−12.56	0.63	0.61	
8	163	400	E017	S034	20.0	15.26	0.06	0.64	0.63	−12.30	0.70	0.69	HK16
9	229	379	W019	S022	22.2	13.19	0.08	0.40	0.56	−11.75	0.60	0.65	HK27
10	181	236	E007	N057	21.1	14.77	0.21	0.36	0.75	−12.64	0.45	0.58	
11	198	210	W002	N072	15.5	15.60	−0.08	0.52	0.45	−12.48	0.74	0.92	
12	194	339	E000	N000	11.1	13.52	0.24	0.41	0.82	−12.09	0.52	0.62	Nuc
13	227	210	W018	N072	21.1	15.79	−0.03	0.62	0.47	−12.52	0.72	0.67	
14	152	190	E023	N083	16.6	14.91	0.01	0.49	0.52	−12.30	0.65	0.69	
15	134	172	E033	N093	11.1	15.39	−0.25	0.83	0.21	−12.07	0.83	0.89	CM39
16	114	175	E044	N091	11.1	16.36	−0.13	0.93	0.45	−12.47	0.84	0.68	
18	286	467	W051	S071	16.6	16.69	−0.09	0.39	0.20	−13.09	0.63	0.62	
19	126	220	E038	N066	21.1	15.73	0.25	0.36	0.70	−13.13	0.30	0.60	
20	13	276	E100	N035	10.0	17.41	−0.10	0.65	0.50	−13.11	0.73	0.82	
NGC 4449 (Groups)													
1	55	248	E077	N051	55.5	13.24	0.25	0.55	0.86	−11.79	0.63	0.64	
2	130	195	E036	N080	44.4	13.30	0.06	0.60	0.51	−11.57	0.73	0.73	
3	203	231	W005	N060	50.0	13.04	0.20	0.48	0.79	−11.76	0.57	0.63	
4	159	306	E019	N018	38.9	12.26	0.25	0.39	0.72	−11.60	0.49	0.59	
5	150	378	E024	S022	44.4	14.22	0.07	0.58	0.61	−11.99	1.21	1.16	
6	215	386	W012	S026	38.9	12.33	0.17	0.40	0.69	−11.52	0.55	0.63	
7	194	339	E000	N000	7.8	13.75	0.28	0.40	0.83	−12.24	0.48	0.60	
8	194	339	E000	N000	25.5	12.13	0.31	0.41	0.83	−11.60	0.47	0.58	
9	194	339	E000	N000	40.0	11.46	0.32	0.41	0.83	−11.34	0.47	0.58	

Table III.4(b) Continued.

Id	X	Y	RA	DEC	DIA	V	$B-V$	$V-R$	$V-I$	$\log F\alpha$	$log\frac{F\alpha}{F\beta}$	$\log \frac{F_{[OIII]}}{F\beta}$	Other Id.
1	2	3	4	5	6	7	8	9	10	11	12	13	14

NGC 4656

Id	X	Y	RA	DEC	DIA	V	$B-V$	$V-R$	$V-I$	$\log F\alpha$	$log\frac{F\alpha}{F\beta}$	$\log \frac{F_{[OIII]}}{F\beta}$	Other Id.
1	332	431	E000	N000	20.0	14.50	−0.12	0.38	0.63	−12.08	0.73	1.14	Nuc
2	306	439	E014	S004	13.3	15.26	0.11	0.44	1.00	−12.64	0.62	0.92	
3	289	415	E024	N009	16.6	15.10	0.13	0.41	1.09	−12.80	0.49	0.72	
4	253	367	E044	N036	8.9	17.38	−0.01	0.43	0.79	−13.38	0.65	0.94	
5	140	218	E107	N118	22.2	15.62	−0.17	0.42	0.57	−12.50	0.65	0.90	
6	109	191	E124	N133	33.3	14.21	−0.05	0.33	0.64	−12.15	0.58	0.85	
7	93	182	E133	N138	12.2	16.25	−0.12	0.37	0.58	−12.83	0.68	0.92	
8	57	198	E153	N129	34.4	14.48	0.06	0.23	0.62	−12.39	0.50	0.62	
9	170	141	E090	N161	22.2	16.66	−0.13	0.27	0.59	−13.04	0.60	1.03	

† Photomerty is based on VBT observations.

Notes :

The notations used for Identification in the last column are :

CM   : Crillon and Monnet (1969)

HK   : Hodge and Kennicutt (1983)

HP   : Hawley and Phillips (1980)

AN   : Alloin and Nieto (1982)

Oka : Oka *et al.* (1974)

TPP : Prabhu (1980b)

L   : Lindblad, P.O. (see Alloin *et al.* 1981)

MRS : McCall, Rybski, and Shields (1985)

RW : Roy and Walsh (1986, 1987, 1988)

WR : Walsh and Roy (1989a,b)

    See column 1 for the identification of numbers not preceded by alphabets.

systematic dependence of colours on the magnitudes or fluxes. H II regions in different galaxies are given different symbols. The absence of any clear dependence of colour with magnitude or Hα+[N II] fluxes indicates that there are no systematic errors in our photometry. The background subtracted $V - R$ colours in galaxies NGC 2903, 2997 are close to the background colours. The background colours as estimated from the regions around H II regions agree well with the colours obtained by azimathally averaging over concentric annuli.

4. Nuclear Growth Profiles and Comparison with Earlier Photometry

Growth profiles around the nuclei of programme galaxies are constructed for all galaxies observed with 1-m telescope. Concentric circular apertures are chosen for this purpose upto the maximum possible radius. Sky regions are chosen away from the main body of the galaxy. Aperture growth profiles around nuclei of galaxies are not sensitive to the choice of sky regions. Surface brightness profiles are also constructed by azimuthaly averaging the counts in successive annular apertures. The photometric results are represented as $V, B - V, V - R, \log H\alpha + [N II]$ and W(Hα) profiles. These results are displayed in Figs III.11–18. NGC 2366 and NGC 4656 are not included for this study as the former does not have a well defined nucleus around which growth curve can be constructed and the centre of the latter lies at the edge of the CCD. Each figure contains 6 (a–f) plots, inclusive of both growth and surface brightness profiles. The azimuthally averaged surface brightness profiles have a width of 1 pixel. The results are also presented in tabular form at selected radii in Tables III.5. Column 1 contains the radii of the circular aperture in arcsec. Next 5 columns contain the photometric results, for the entire region inside the given aperture. The quantities in the last 5 columns are azimuthally averaged colour and surface brightness values at the indicated radii. We draw the following conclusions from these profiles.

(1) Disk $B - V$ colour lies between 0.6–0.7 mag for majority of the sample galaxies. The colour is redder ($\sim$ 1 mag) in NGC 2997 and bluer in irregulars NGC 4449 and 5253 (0.3 and 0.4 respectively).

(2) Disk $V - R$ colour is $\sim$ 0.6 mag for all the programme galaxies except for NGC 4449 and 5253, which have bluer (0.35 and 0.45) $V - R$ colours.

(3) The Hα equivalent width within an aperture of 1 arcmin is less than 25Å for most of the spirals in the sample. For NGC 1365, 2997 and 4449 the values are around 70, 50 and 45 Å respectively.

(4) At the position of the nuclear rings in NGC 2997 and 3351, the colours are bluer and Hα equivalent widths slightly higher than the immediate surroundings.

(5) The Hα equivalent width is highest in the nuclear region of NGC 5253 reaching values of 350 Å decreasing rapidly outwards.

In Table III.6, we compare our BV photometry with multi-aperture photoelectric photometry of other observers taken from the *UBV galaxy catalogue* of Longo and de Vaucouleurs (1983). The difference between our photometry and that of Wegner (1979), Dottori (1979) and Alcaino (1976) is shown as a function of aperture size in Figs III.19, 20 and 21 respectively. The agreement between our photometry and catalogue data is very good. The disagreement for radius $\leq$ 10 arcsec is due to errors in centering the galaxy in photoelectric photometry and the effect of seeing. For the three southern galaxies (NGC 1566, 2997 and 5253) in the sample for which, photometry from Wegner (1979) is available the agreement is the best. For NGC 1365, photometry of Alcaino (1976) is the closest. Photometry of Tifft (1969, 1961) agrees well for NGC 2903, 4303 and 4449. The catalogue magnitudes and colours agree well for NGC 2366.
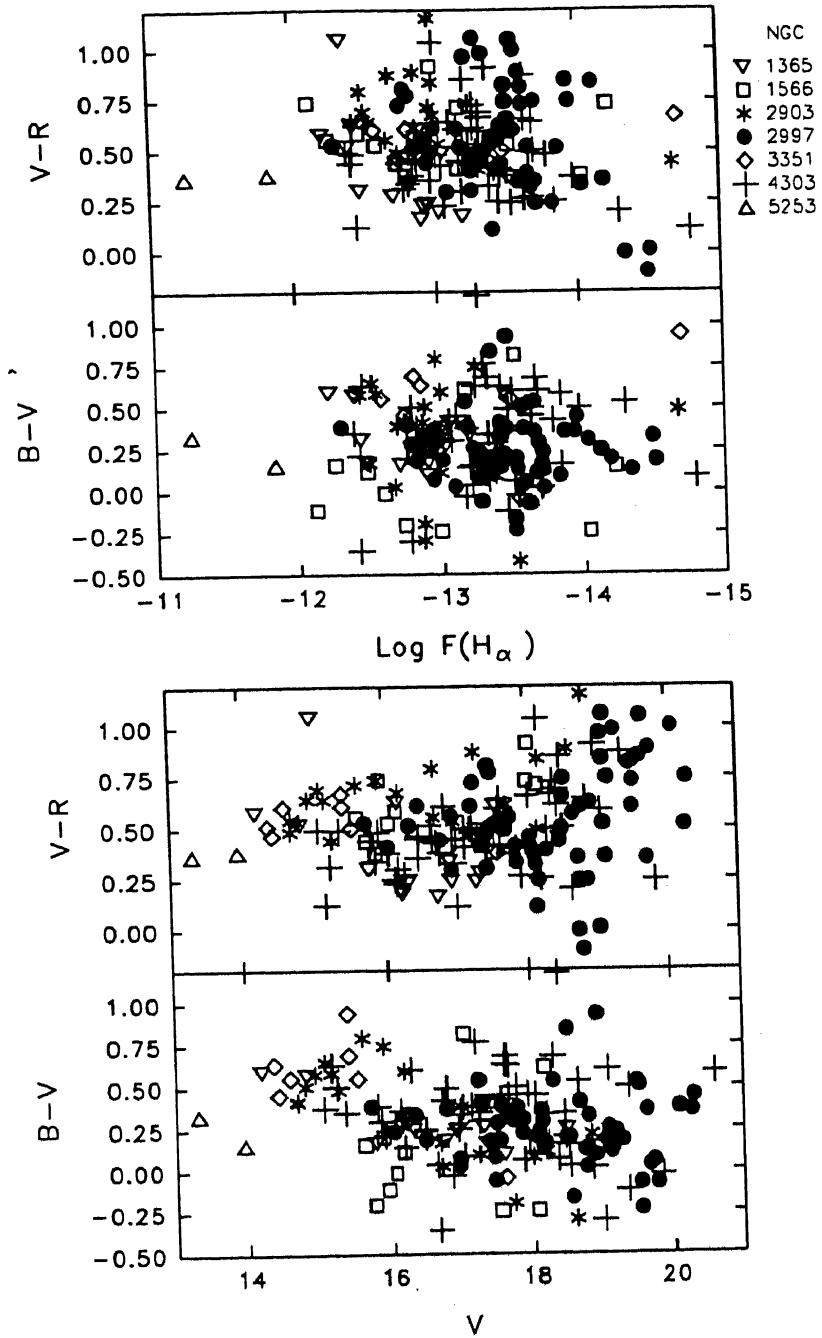
Figure III.10 Observed $B-V$ and $V-R$ colours are plotted against observed $H\alpha+[N\,II]$ flux and V band magnitude.

Table III.5 Aperture photometry of Galaxies[†].

Rad arcsec	V	$B-V$	$V-R$	$\log F\alpha$ erg cm^{-2}s^{-1}	W(Hα) Å	μ_V	μ_{B-V}	μ_{V-R}	μ_α	$\mu_{W(H\alpha)}$
				NGC 1365						
1.07	15.83	1.24	1.11	−12.65	67.50	17.32	1.23	1.09	−13.26	67.20
2.14	14.69	1.16	1.00	−12.23	68.80	17.91	1.06	0.85	−13.57	70.50
3.93	13.84	1.03	0.87	−11.93	70.20	18.50	0.86	0.72	−13.82	77.00
5.00	13.49	0.97	0.83	−11.80	72.80	18.65	0.79	0.70	−13.84	86.20
6.43	13.11	0.89	0.78	−11.65	75.00	18.69	0.68	0.65	−13.93	77.10
7.85	12.77	0.82	0.75	−11.56	69.60	18.73	0.66	0.62	−14.18	46.10
10.00	12.40	0.79	0.71	−11.49	61.30	19.11	0.76	0.63	−14.46	33.90
12.50	12.10	0.78	0.69	−11.43	53.60	19.37	0.74	0.58	−14.74	23.50
				NGC 1566						
1.07	15.65	0.61	0.82	−14.69	0.00	17.11	0.63	0.81	−15.40	0.00
2.14	14.39	0.69	0.76	−14.69	0.00	17.51	0.78	0.70	−15.40	0.00
3.93	13.49	0.84	0.68	−14.69	0.00	18.15	1.08	0.57	−14.16	29.50
5.00	13.17	0.91	0.65	−13.26	2.20	18.44	1.10	0.57	−14.27	29.80
6.43	12.87	0.95	0.64	−12.58	8.20	18.78	1.08	0.60	−14.43	27.60
7.85	12.63	0.97	0.63	−12.32	11.90	19.04	1.10	0.60	−14.52	28.30
10.00	12.37	1.00	0.62	−12.10	15.60	19.32	1.14	0.58	−14.61	30.90
12.50	12.11	1.01	0.61	−11.95	17.60	19.49	0.95	0.64	−15.13	10.30
15.71	11.85	1.01	0.61	−11.83	18.50	19.84	1.08	0.56	−14.76	35.60
19.99	11.61	1.01	0.60	−11.64	22.90	20.19	0.97	0.58	−14.83	41.10
24.99	11.38	0.98	0.60	−11.47	27.60	20.38	0.80	0.57	−14.77	56.10
31.77	11.12	0.92	0.59	−11.25	36.20	20.68	0.63	0.58	−14.70	86.70
35.70	11.00	0.89	0.59	−11.15	40.60	20.75	0.63	0.56	−14.81	72.60
				NGC 2903						
1.07	15.98	0.53	0.57	−13.48	18.90	17.45	0.53	0.56	−14.04	20.30
2.14	14.71	0.55	0.56	−12.90	22.70	17.78	0.59	0.57	−14.10	24.00
3.93	13.68	0.62	0.59	−12.49	21.90	18.15	0.69	0.62	−14.31	19.90
5.00	13.28	0.64	0.59	−12.33	21.80	18.28	0.69	0.60	−14.30	23.00
6.43	12.86	0.65	0.59	−12.15	22.70	18.40	0.68	0.59	−14.29	26.80
7.85	12.53	0.66	0.59	−11.98	24.70	18.59	0.66	0.59	−14.32	30.10
10.00	12.19	0.66	0.59	−11.83	25.40	18.93	0.68	0.59	−14.53	25.60
12.50	11.90	0.67	0.59	−11.73	24.50	19.26	0.72	0.60	−14.84	16.40
15.71	11.65	0.69	0.59	−11.65	23.20	19.61	0.81	0.60	−14.96	17.60
19.99	11.38	0.71	0.59	−11.56	22.10	19.81	0.78	0.58	−15.03	18.00
24.99	11.11	0.72	0.59	−11.47	21.50	19.94	0.71	0.55	−15.08	18.90
31.77	10.81	0.71	0.58	−11.36	21.40	20.21	0.65	0.55	−15.14	20.90
39.98	10.54	0.73	0.57	−11.25	21.50	20.39	0.76	0.54	−15.20	21.40

Table III.5 Continued.

Rad arcsec	V	$B-V$	$V-R$	$\log F\alpha$ erg cm^{-2}s^{-1}	W(Hα) Å	μ_V	μ_{B-V}	μ_{V-R}	μ_α	$\mu_{W(H\alpha)}$
49.98	10.26	0.73	0.56	-11.12	22.90	20.70	0.78	0.55	-15.17	30.90
63.19	9.98	0.74	0.56	-10.96	25.40	20.93	0.76	0.54	-15.19	36.50
79.25	9.72	0.73	0.55	-10.79	29.60	21.18	0.67	0.49	-15.22	44.80
82.11	9.68	0.73	0.55	-10.77	30.10	21.31	0.69	0.48	-15.27	46.10
NGC 2997										
1.07	16.21	1.28	0.41	-13.63	19.50	17.73	1.23	0.47	-14.27	17.30
2.14	15.07	1.15	0.54	-13.23	15.10	18.26	1.04	0.64	-14.54	12.60
3.93	14.16	1.02	0.61	-12.67	22.50	18.75	0.85	0.62	-14.21	43.60
5.00	13.80	0.95	0.60	-12.37	32.00	18.91	0.78	0.56	-14.15	60.70
6.43	13.45	0.89	0.58	-12.16	38.70	19.25	0.74	0.55	-14.37	51.00
7.85	13.22	0.87	0.58	-12.05	40.20	19.69	0.82	0.58	-14.63	40.70
10.00	13.01	0.88	0.59	-11.97	39.70	20.31	1.03	0.61	-14.90	37.30
12.50	12.83	0.91	0.58	-11.90	39.70	20.64	1.09	0.55	-14.97	46.00
15.71	12.64	0.94	0.57	-11.80	41.80	20.89	1.08	0.48	-15.01	55.70
19.99	12.43	0.96	0.55	-11.69	45.60	21.12	1.04	0.41	-15.06	66.10
23.21	12.29	0.97	0.53	-11.62	48.10	21.21	1.03	0.35	-15.08	73.20
NGC 3351										
1.07	16.17	0.98	0.65	-14.99	-0.70	17.63	0.97	0.66	-15.70	-0.50
2.14	14.83	0.94	0.66	-13.59	4.70	17.83	0.88	0.66	-14.47	9.70
3.93	13.61	0.81	0.63	-12.69	12.50	17.82	0.69	0.58	-14.21	19.20
5.00	13.07	0.75	0.60	-12.39	15.80	17.81	0.63	0.53	-14.15	22.70
6.43	12.61	0.70	0.58	-12.12	19.40	18.16	0.62	0.57	-14.19	27.90
7.85	12.33	0.69	0.59	-11.96	21.70	18.68	0.74	0.63	-14.35	29.00
10.00	12.09	0.72	0.60	-11.86	21.60	19.24	0.90	0.66	-14.83	15.80
12.50	11.90	0.75	0.61	-11.81	20.10	19.61	0.95	0.67	-15.11	11.70
15.71	11.71	0.77	0.62	-11.76	18.60	19.99	0.89	0.68	-15.26	11.40
19.99	11.51	0.78	0.63	-11.70	17.60	20.28	0.79	0.65	-15.40	11.20
24.99	11.33	0.78	0.63	-11.65	16.60	20.63	0.73	0.66	-15.53	11.30
31.77	11.14	0.77	0.64	-11.58	16.60	21.02	0.73	0.66	-15.46	18.90
39.98	10.96	0.76	0.64	-11.49	17.10	21.31	0.69	0.69	-15.49	22.70
48.20	10.81	0.75	0.65	-11.40	18.10	21.48	0.66	0.70	-15.45	28.60

Table III.5 Continued.

Rad arcsec	V	$B-V$	$V-R$	$\log F\alpha$ erg cm^{-2}s^{-1}	W(Hα) Å	μ_V	μ_{B-V}	μ_{V-R}	μ_α	$\mu_{W(H\alpha)}$
				NGC 4303						
1.07	15.43	0.70	0.67	-13.47	10.60	16.88	0.70	0.67	-14.04	10.90
2.14	14.12	0.70	0.66	-12.89	12.00	17.18	0.70	0.65	-14.07	13.50
3.93	13.22	0.69	0.64	-12.45	14.80	18.00	0.70	0.60	-14.30	18.00
5.00	12.96	0.70	0.63	-12.35	14.90	18.52	0.76	0.60	-14.65	12.90
6.43	12.75	0.72	0.63	-12.30	13.80	19.12	0.84	0.61	-15.20	6.30
7.85	12.61	0.74	0.63	-12.28	12.80	19.56	0.88	0.64	-15.46	5.00
10.00	12.45	0.76	0.63	-12.26	11.50	19.90	0.90	0.65	-15.83	2.90
12.50	12.28	0.78	0.63	-12.22	10.90	20.10	0.86	0.63	-15.47	8.10
15.71	12.09	0.78	0.63	-12.19	9.70	20.26	0.79	0.60	-15.89	3.70
19.99	11.86	0.77	0.62	-12.13	9.10	20.43	0.66	0.57	-15.61	8.50
24.99	11.63	0.75	0.61	-12.04	9.20	20.68	0.62	0.56	-15.62	10.50
31.77	11.39	0.72	0.60	-11.93	9.50	20.87	0.57	0.56	-15.58	13.60
39.98	11.10	0.67	0.59	-11.70	12.60	20.86	0.47	0.55	-15.19	33.70
49.98	10.75	0.58	0.58	-11.32	22.20	20.84	0.36	0.53	-15.05	45.90
				NGC 4449						
1.07	15.75	0.41	0.54	-13.88	6.60	17.22	0.39	0.51	-14.30	9.80
2.14	14.54	0.34	0.46	-12.92	20.70	17.70	0.26	0.37	-13.95	38.30
3.93	13.71	0.27	0.39	-12.35	37.70	18.47	0.19	0.34	-14.08	59.70
5.00	13.41	0.26	0.38	-12.19	42.50	18.74	0.25	0.35	-14.19	58.40
6.43	13.11	0.25	0.37	-12.05	44.50	18.97	0.25	0.34	-14.37	48.90
7.85	12.85	0.26	0.37	-11.95	44.40	19.10	0.28	0.36	-14.49	40.70
10.00	12.52	0.27	0.37	-11.83	43.00	19.20	0.29	0.36	-14.57	37.10
12.50	12.19	0.28	0.37	-11.72	41.40	19.35	0.31	0.37	-14.65	35.10
15.71	11.86	0.29	0.37	-11.59	40.60	19.51	0.31	0.37	-14.66	39.40
19.99	11.50	0.29	0.37	-11.44	41.80	19.65	0.30	0.37	-14.62	49.60
24.99	11.18	0.29	0.37	-11.28	44.70	19.90	0.29	0.38	-14.70	51.90
31.77	10.86	0.29	0.37	-11.14	46.00	20.16	0.29	0.36	-14.88	44.80
39.98	10.58	0.30	0.37	-11.01	48.00	20.53	0.34	0.37	-14.97	50.50
46.41	10.41	0.31	0.37	-10.94	47.70	20.62	0.47	0.46	-15.21	28.90

Table III.5 Continued.

Rad arcsec	V	$B-V$	$V-R$	$\log F\alpha$ erg cm^{-2}s^{-1}	$W(H\alpha)$ Å	μ_V	μ_{B-V}	μ_{V-R}	μ_α	$\mu_{W(H\alpha)}$
				NGC 5253						
1.07	15.69	0.50	0.40	-12.17	350.60	17.16	0.49	0.39	-12.75	358.40
2.14	14.42	0.44	0.38	-11.66	355.40	17.49	0.38	0.37	-12.90	351.40
3.93	13.44	0.37	0.37	-11.31	324.10	18.02	0.30	0.37	-13.22	273.20
5.00	13.10	0.34	0.37	-11.20	302.80	18.33	0.26	0.38	-13.41	230.90
6.43	12.77	0.32	0.37	-11.12	274.40	18.56	0.25	0.38	-13.63	171.80
7.85	12.50	0.30	0.38	-11.05	245.10	18.74	0.25	0.39	-13.80	134.60
10.00	12.21	0.29	0.38	-10.99	217.20	19.13	0.27	0.41	-13.99	121.90
12.50	11.96	0.29	0.39	-10.93	194.70	19.38	0.31	0.39	-14.17	103.70
15.71	11.71	0.30	0.39	-10.88	173.90	19.75	0.29	0.40	-14.42	82.20
19.99	11.48	0.31	0.39	-10.84	153.70	20.19	0.37	0.42	-14.76	55.50
24.99	11.29	0.32	0.40	-10.82	136.00	20.58	0.38	0.44	-15.02	42.60
31.77	11.12	0.33	0.41	-10.80	121.40	21.16	0.45	0.46	-15.29	38.30
39.98	10.97	0.35	0.41	-10.78	109.40	21.62	0.45	0.47	-15.72	21.70
49.98	10.85	0.37	0.42	-10.77	98.00	22.12	0.65	0.51	-16.68	3.60
60.69	10.75	0.39	0.43	-10.77	89.10	22.59	0.73	0.57	-15.97	26.90

† Quantities (μ) in columns 7–11 are azimuthally averaged surface brightnesses at the given radii. The width of the averaging annulus is 1 pixel.

Notes to Table III.6 : The codes used for original references are the same as that of Longo and de Vaucouleurs (1983) and are reproduced below

ALC-76 Alcaino (1976)

CWH-75 Chincarini and Walker (1975) (see Longo and de Vaucouleurs 1983)

DOT-79 Dottori (1979)

GHJ-82 Griersmith, Hyland and Jones (1982)

NEF-70 Neff (1970)

TIF-61 Tifft (1961)

TIF-69 Tifft (1969)

VVL-72 Vorontsov-Velyaminov, Lyuti, Zaitseva (1973)

WEG-79 Wegner (1979)

ZAL-73 Zasov, Lyuti (1973)

Table III.6 Comparison with multi-aperture
photoelectric photometry.

Galaxy NGC	Rad arcsec	Photoelectric V	B − V	P.E. − Ours ΔV	ΔB − V	Reference
1365	2.74	14.75	0.87	−0.41	0.24	ALC-76
	5.46	13.48	0.84	−0.12	0.10	ALC-76
	10.40	12.32	0.73	0.03	0.06	ALC-76
	3.14	14.77	0.71	−0.65	0.37	DOT-79
	5.89	12.95	0.68	0.26	0.23	DOT-79
	11.94	12.02	0.77	0.14	0.01	DOT-79
1566	7.71	12.61	0.93	0.04	0.04	WEG-79
	8.26	12.67	0.88	−0.10	0.10	WEG-79
	8.26	12.68	0.95	−0.11	0.03	WEG-79
	15.04	11.83	0.95	0.07	0.06	WEG-79
	17.67	11.79	0.90	−0.06	0.11	WEG-79
	3.14	13.76	0.96	0.04	−0.17	DOT-79
	5.99	12.67	0.89	0.27	0.04	DOT-79
	11.94	11.98	0.92	0.19	0.01	DOT-79
	30.00	11.16	0.79	0.02	0.15	DOT-79
	3.96	13.42	0.85	0.06	−0.01	GHJ-82
	7.54	12.64	0.88	0.04	0.09	GHJ-82
	7.54	12.70	0.89	−0.02	0.08	GHJ-82
	7.71	12.56	0.88	0.09	0.09	GHJ-82
	15.04	11.89	0.89	0.01	0.12	GHJ-82
	15.04	11.89	0.90	0.01	0.11	GHJ-82
	15.04	11.91	0.92	−0.01	0.09	GHJ-82
2903	4.98	13.15	0.66	0.14	−0.02	TIF-69
	8.07	12.37	0.64	0.12	0.02	TIF-69
	10.90	12.00	0.66	0.07	0.01	TIF-69
	13.10	11.77	0.66	0.08	0.01	TIF-69
	18.08	11.44	0.70	0.05	0.01	TIF-69
	19.37	11.32	0.72	0.09	−0.01	TIF-69
	30.70	10.80	0.74	0.05	−0.02	TIF-69
	32.15	10.70	0.74	0.10	−0.03	TIF-69
	54.59	10.14	0.72	0.02	0.02	TIF-69
	5.46	12.95	0.58	0.18	0.07	CWH-75
	8.46	12.37	0.59	−0.05	0.07	CWH-75
	14.03	11.69	0.62	0.08	0.06	CWH-75
	29.32	10.82	0.67	0.09	0.05	CWH-75
	64.14	9.92	0.68	0.05	0.06	CWH-75

Table III.6 Continued.

Galaxy NGC	Rad arcsec	Photoelectric V	B − V	P.E. − Ours ΔV	ΔB − V	Reference
2997	8.26	13.19	0.86	−0.03	0.01	WEG-79
	17.67	12.53	0.91	0.01	0.04	WEG-79
	3.14	14.81	0.69	−0.32	0.38	DOT-79
	5.99	13.48	0.74	0.06	0.16	DOT-79
	11.94	12.71	0.82	0.15	0.08	DOT-79
3351	4.98	14.08	0.75	1.00	0.00	VVL-72
	13.40	11.87	0.77	−0.03	−0.01	VVL-72
	18.08	11.58	0.82	0.01	−0.04	TIF-61
	24.95	11.45	0.85	−0.12	−0.07	ZAL-73
	30.70	11.14	0.86	0.03	−0.09	TIF-61
	33.66	11.01	0.88	0.09	−0.11	ZAL-73
4303	4.98	12.88	0.78	0.09	0.06	TIF-69
	8.07	12.50	0.81	0.11	0.06	TIF-69
	13.10	12.16	0.81	0.10	0.09	TIF-69
	19.37	11.75	0.81	0.14	0.07	TIF-69
	32.15	11.18	0.75	0.15	0.07	TIF-69
4449	10.90	12.40	0.31	−0.03	−0.04	TIF-61
	11.94	12.30	0.31	−0.02	−0.04	GDU-59
	45.11	10.45	0.37	−0.01	−0.07	NEF-70
5253	5.21	13.16	0.22	−0.13	0.11	WEG-79
	7.71	12.71	0.25	−0.19	0.05	WEG-79
	8.26	12.59	0.23	−0.13	0.07	WEG-79
	15.04	11.76	0.29	−0.01	0.01	WEG-79
	17.67	11.67	0.28	−0.07	0.02	WEG-79
	3.14	13.36	0.85	0.41	−0.46	DOT-79
	5.99	12.53	0.54	0.32	−0.22	DOT-79
	11.94	11.69	0.60	0.31	−0.31	DOT-79
	30.00	11.00	0.51	0.16	−0.18	DOT-79
	2.74	14.85	−0.21	−0.85	0.62	ALC-76
	5.46	13.59	−0.17	−0.61	0.50	ALC-76
	10.40	12.43	0.03	−0.29	0.26	ALC-76
	22.24	11.57	0.18	−0.18	0.13	ALC-76
	44.37	11.02	0.30	−0.11	0.06	ALC-76

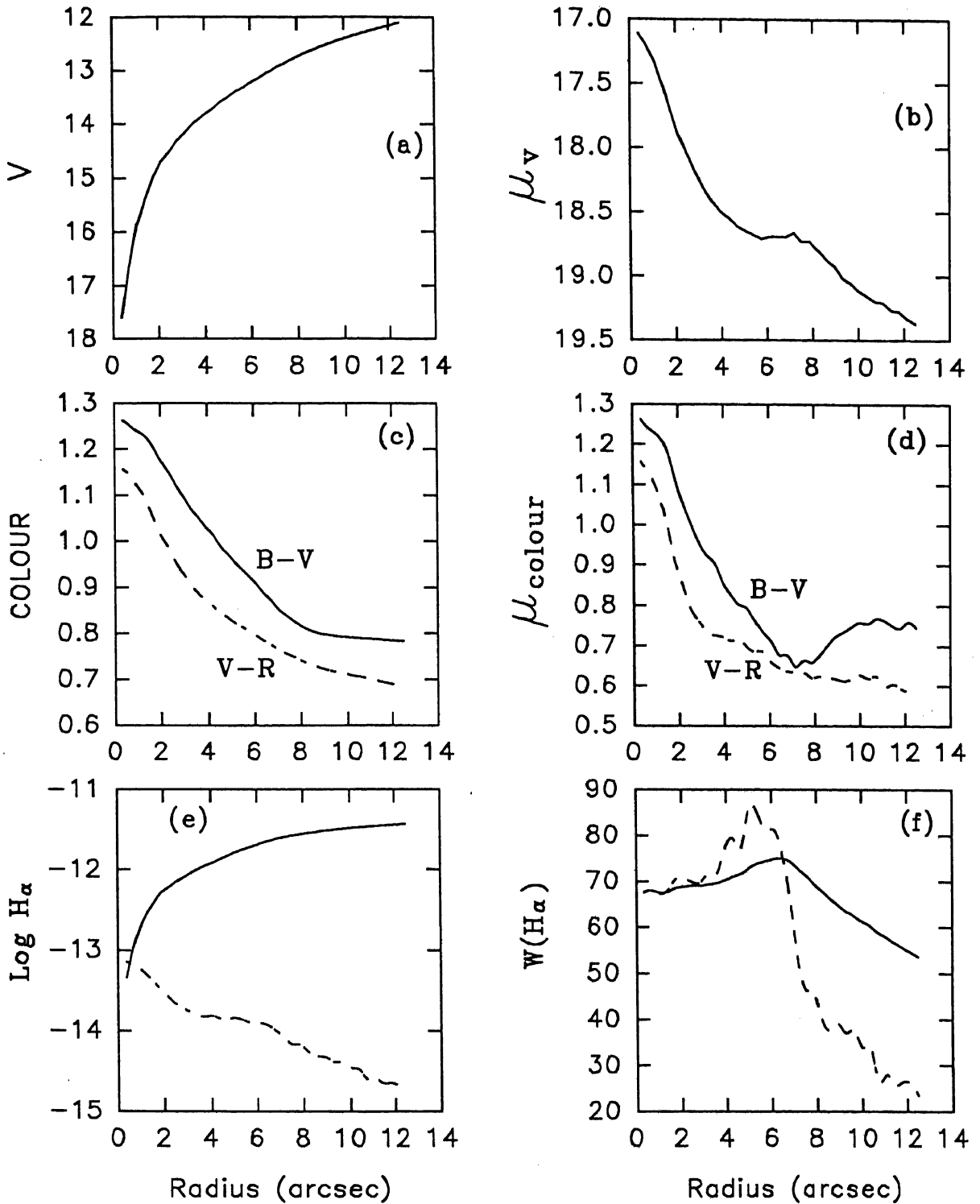See page 98 for notes to the references.

NGC 1365

Figure III.11 Azimuthally averaged growth and surface brightness profiles of NGC 1365. (a) V band growth profile, (b) surface brightness profile in V, (c) growth profiles in colours, (d) profile of local colours, (e) growth (solid line) and local (dashed line) profiles of $H\alpha + [NII]$ flux, (f) growth and local $H\alpha + [NII]$ equivalent width.
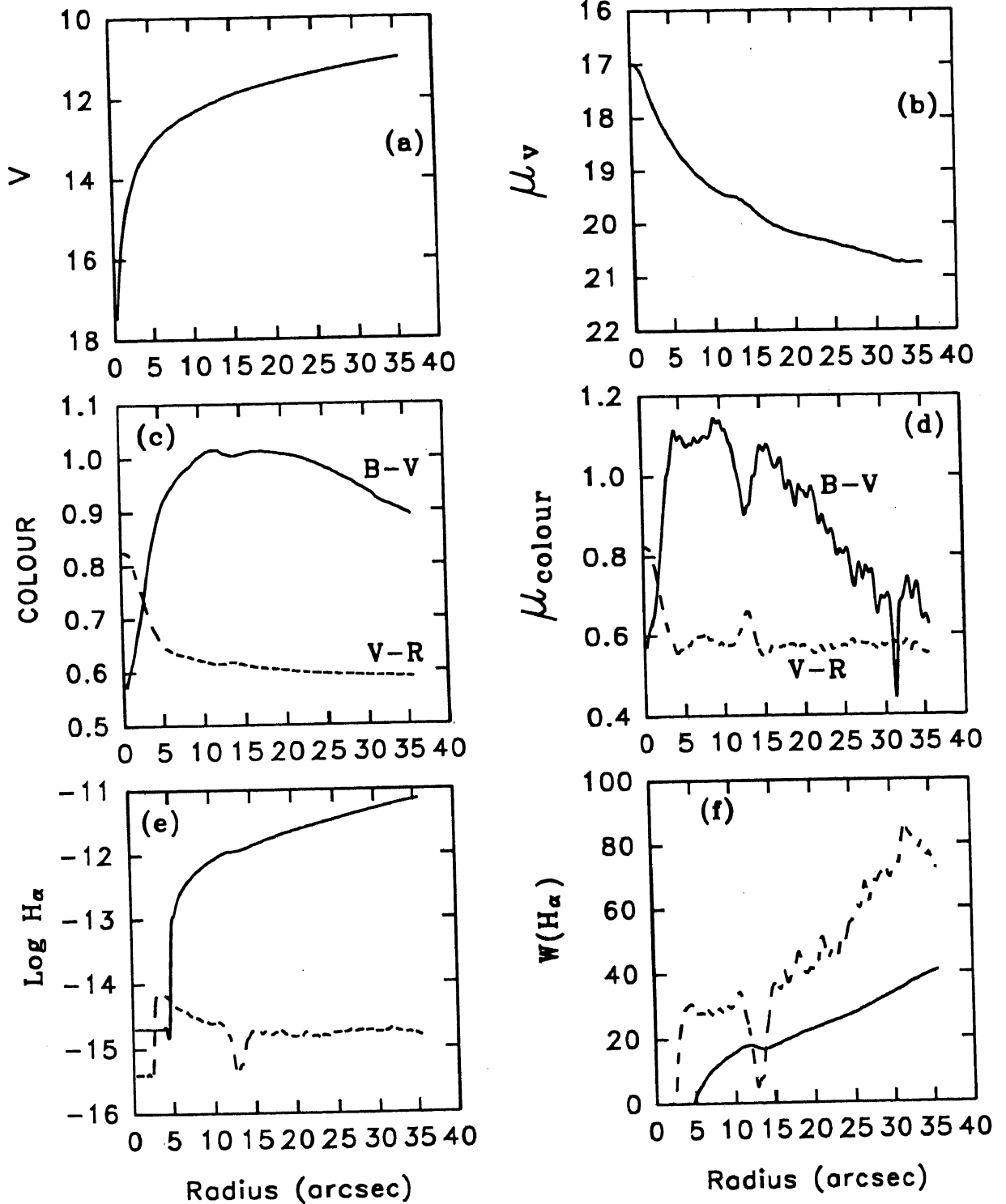
NGC 1566

Figure III.12 Azimuthally averaged growth and surface brightness profiles of NGC 1566. See Fig. III.11 for details.

NGC 2903
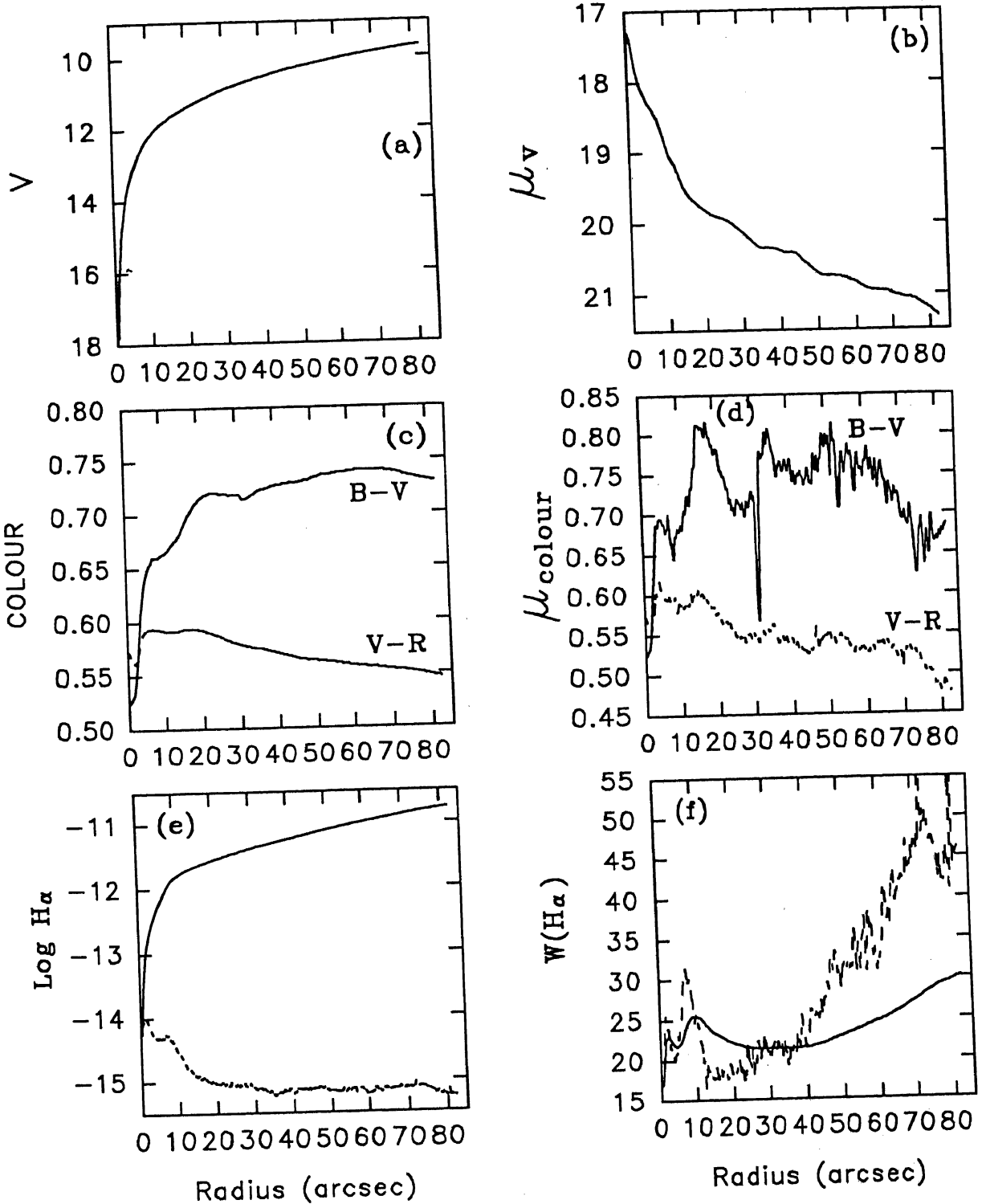
Figure III.13 Azimuthally averaged growth and surface brightness profiles of NGC 2903. See Fig. III.11 for details.
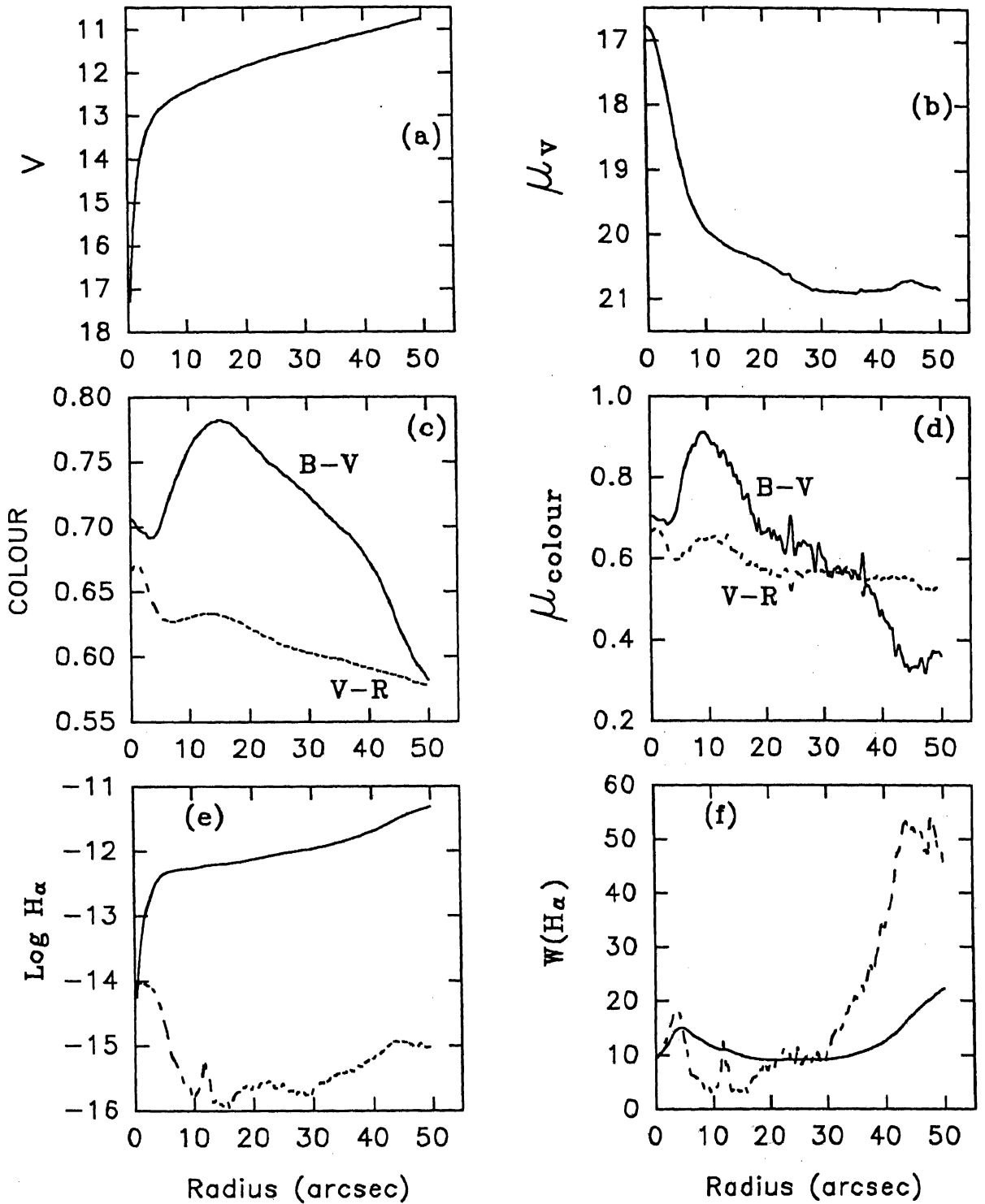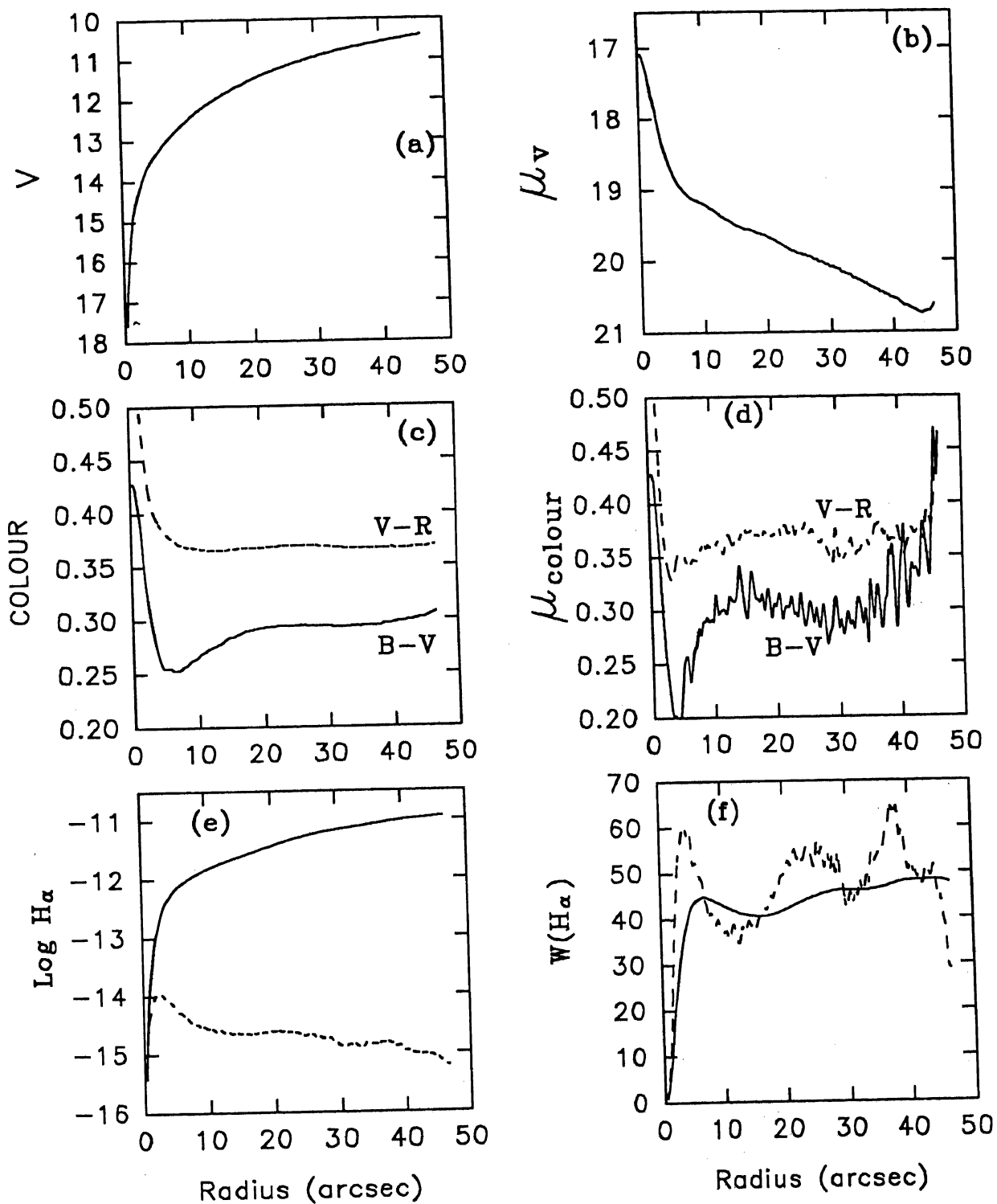
NGC 2997
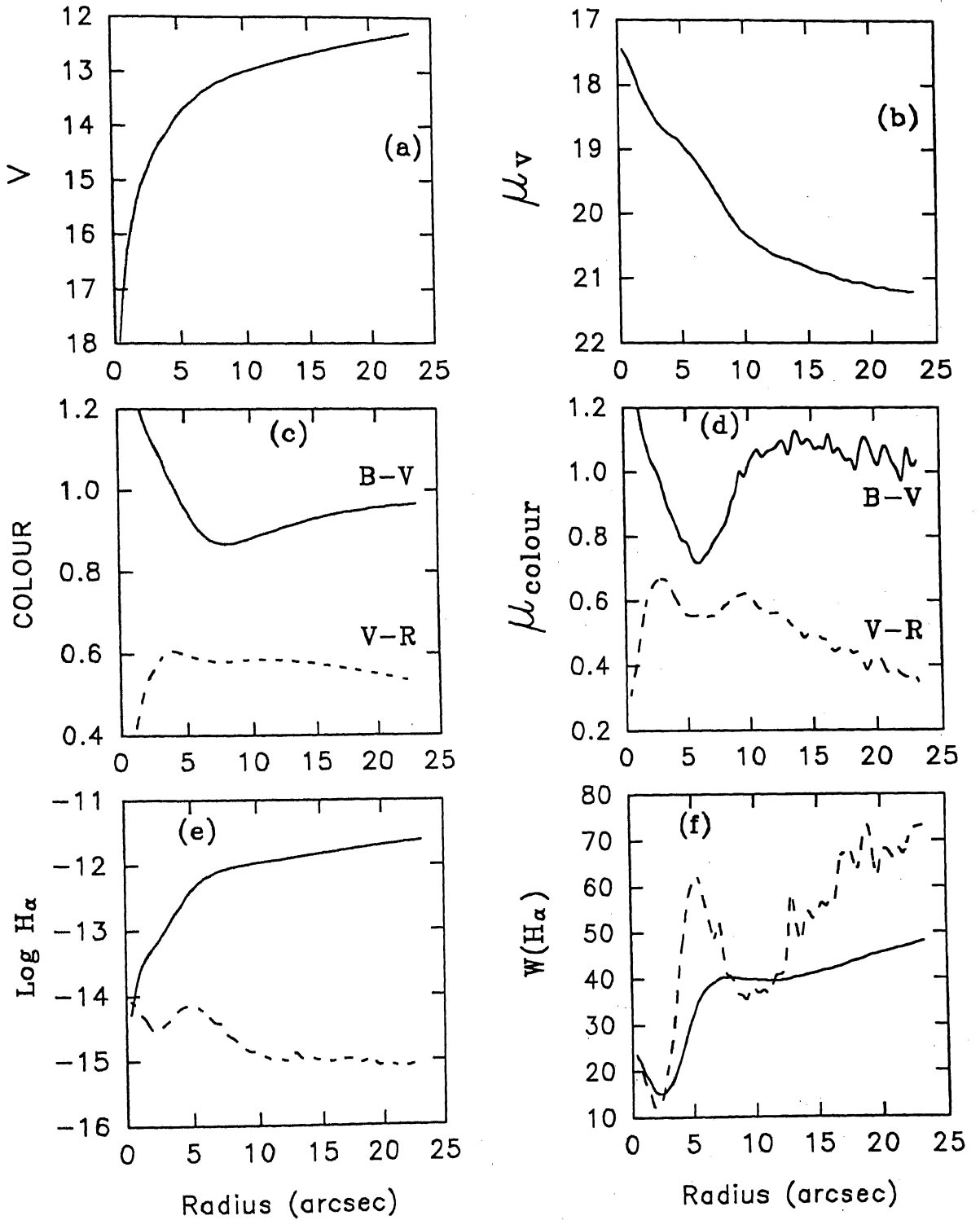
Figure III.14 Azimuthally averaged growth and surface brightness profiles of NGC 2997. See Fig. III.11 for details.

NGC 3351
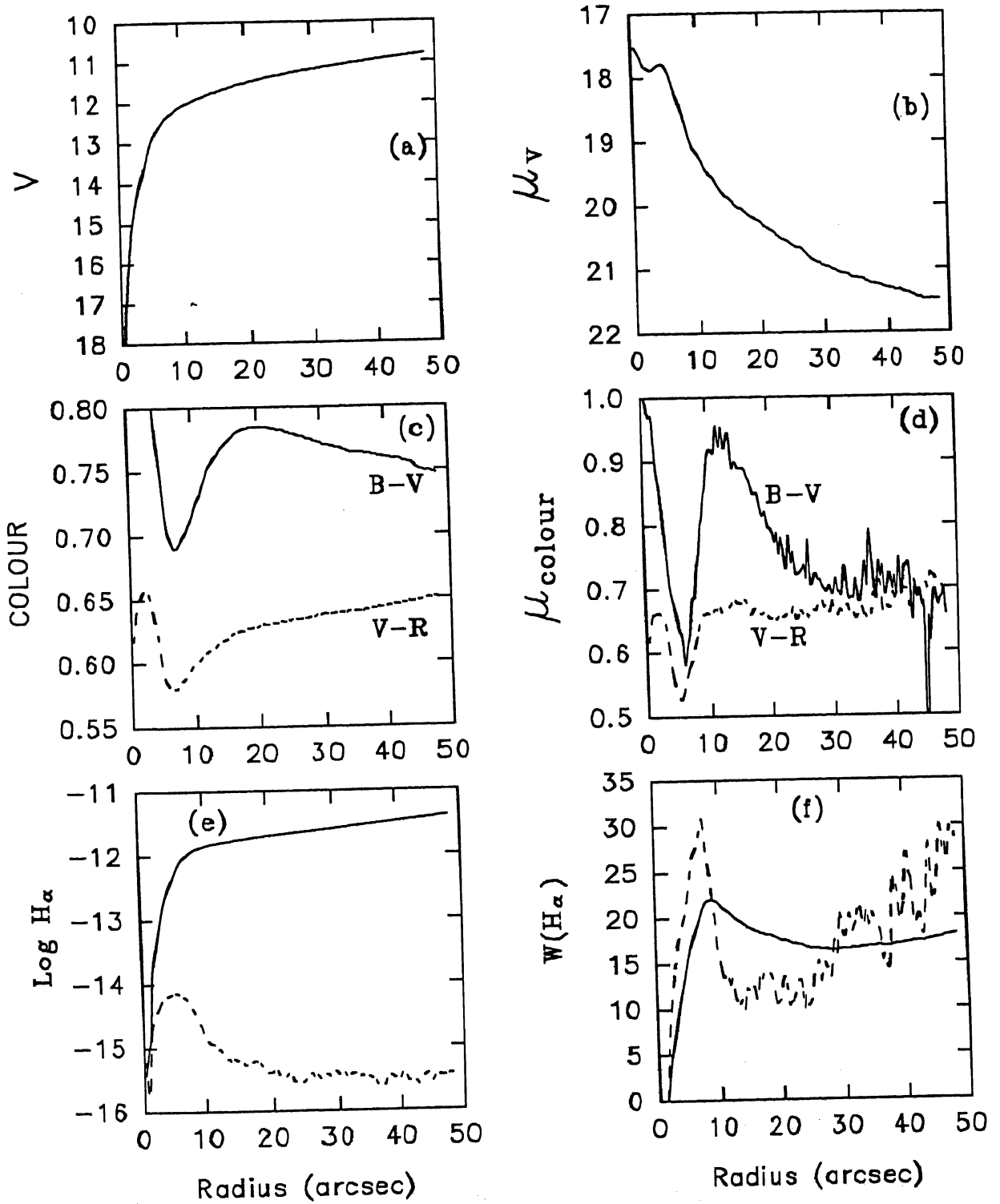
Figure III.15 Azimuthally averaged growth and surface brightness profiles of NGC 3351. See Fig. III.11 for details.

NGC 4303

Figure III.16 Azimuthally averaged growth and surface brightness profiles of NGC 4303. See Fig. III.11 for details.

NGC 4449

Figure III.17 Azimuthally averaged growth and surface brightness profiles of NGC 4449. See Fig. III.11 for details.
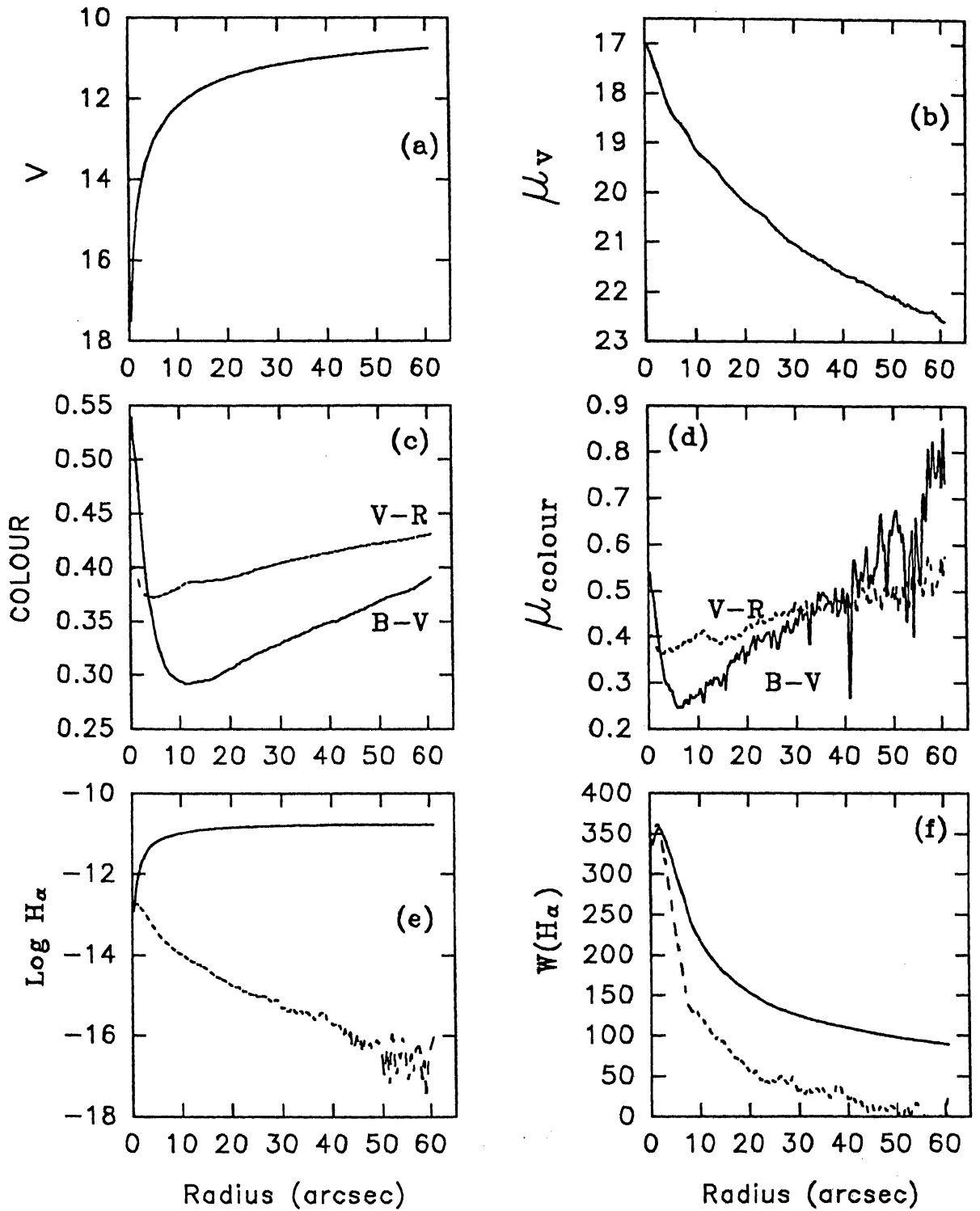
NGC 5253

Figure III.18 Azimuthally averaged growth and surface brightness profiles of NGC 5253. See Fig. III.11 for details.
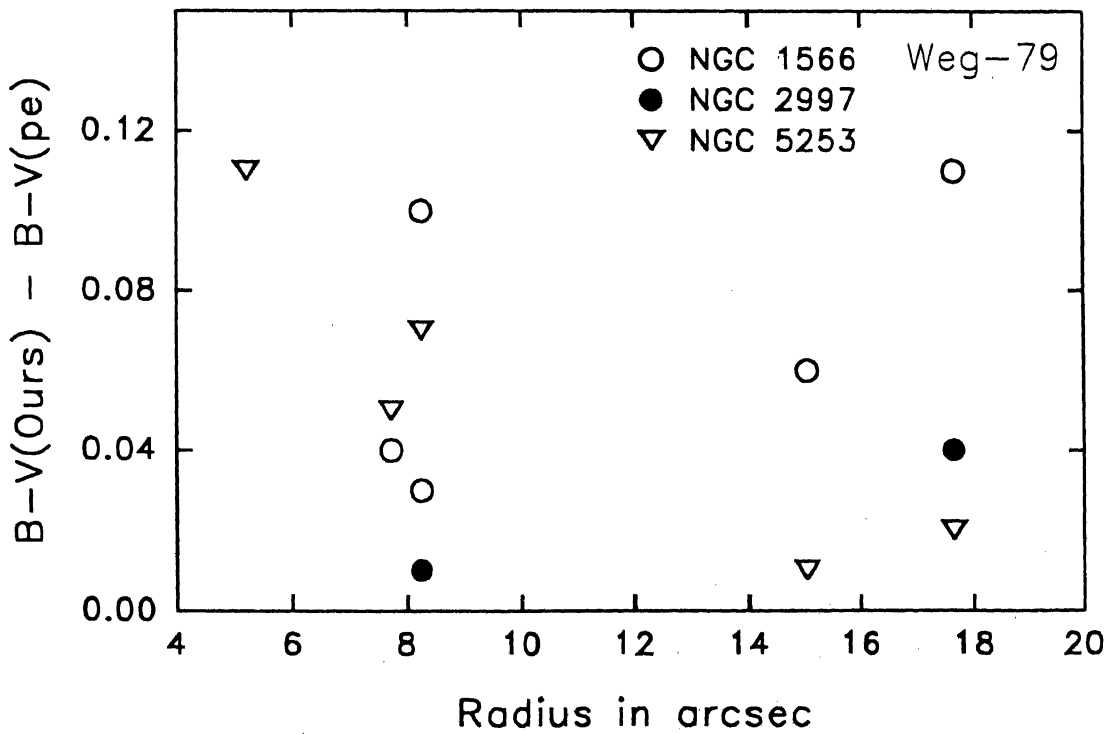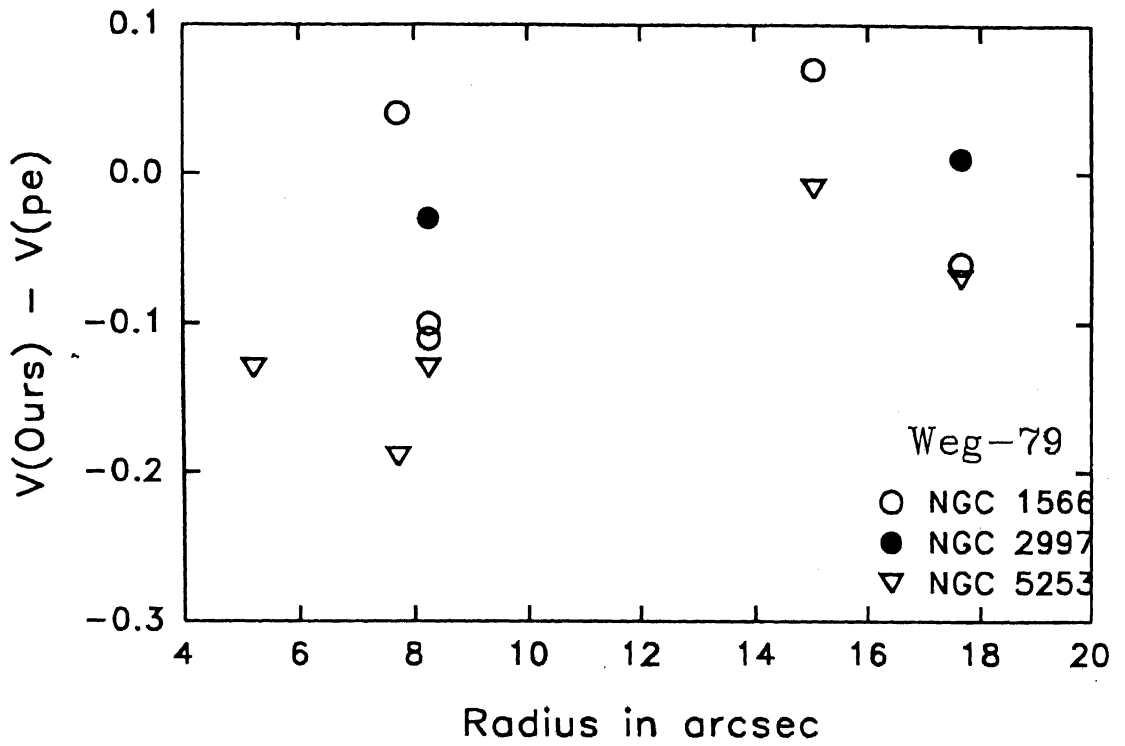
Figure III.19 Comparison of synthetic aperture photometry of galaxies with the photoelectric data of Wegner (1979).
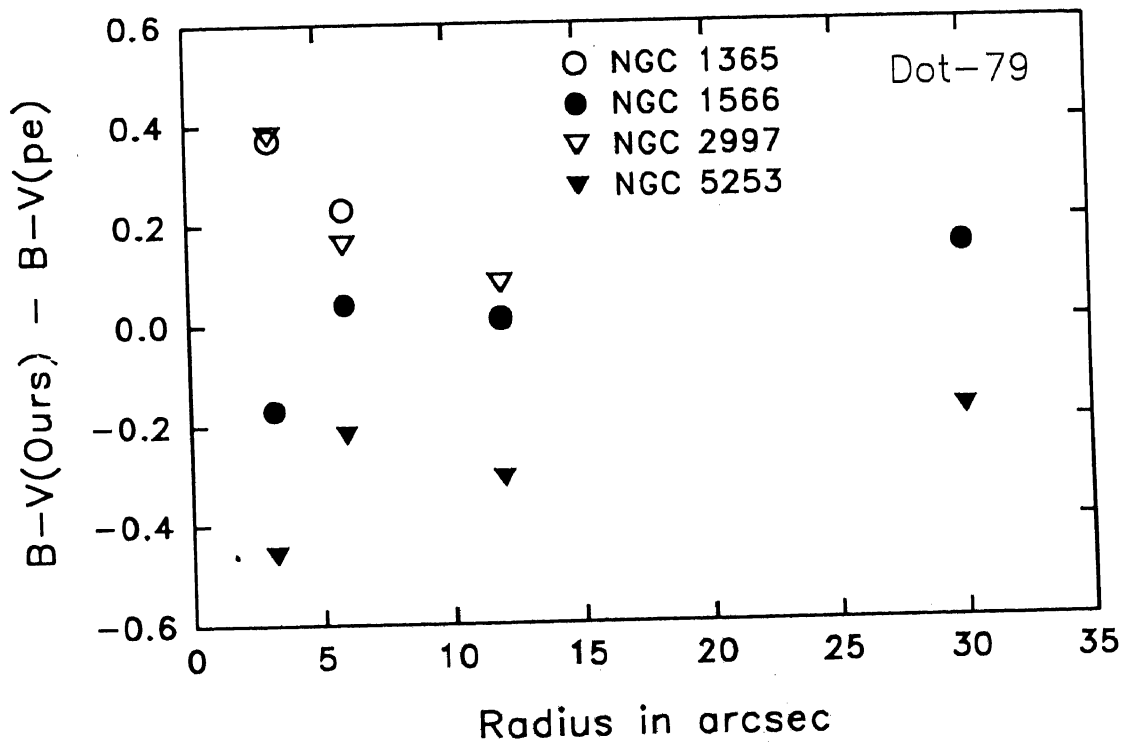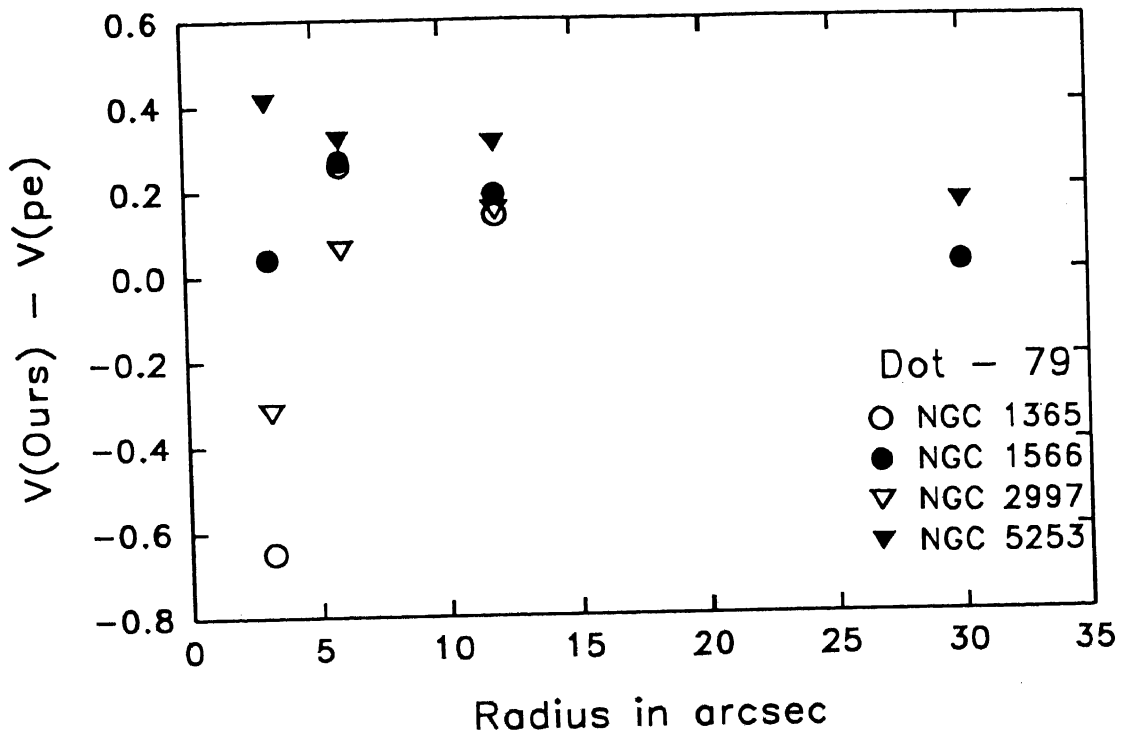
Figure III.20 Comparison of synthetic aperture photometry of galaxies with the photoelectric data of Dottori (1979).
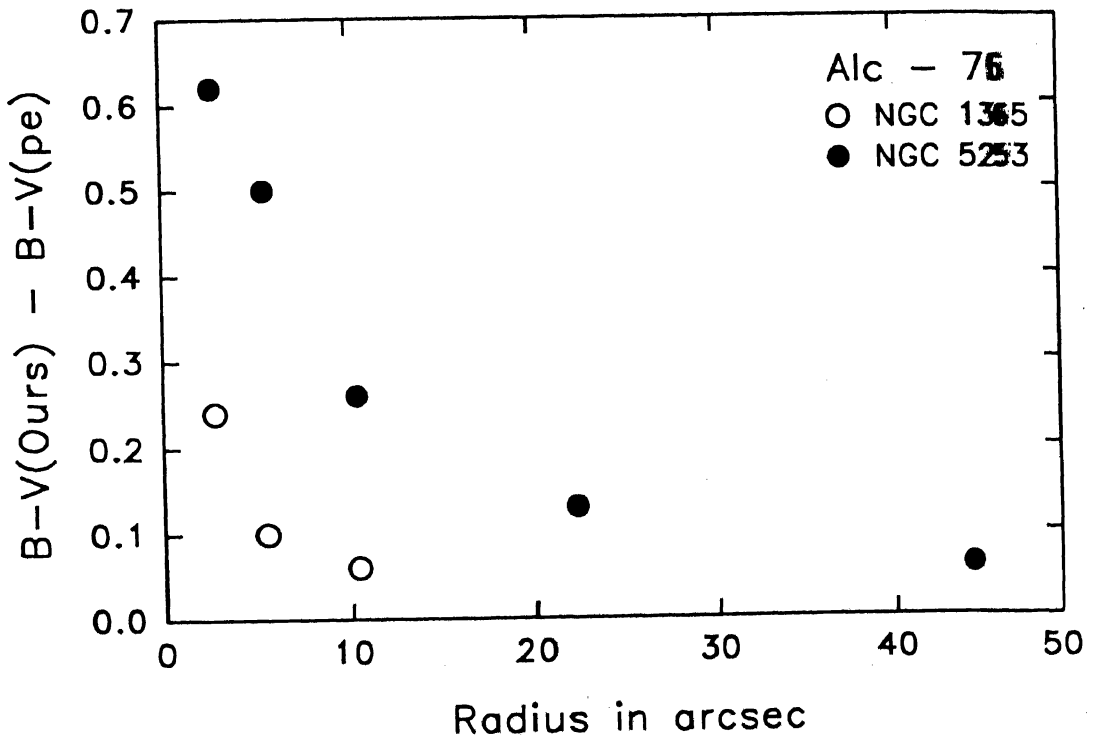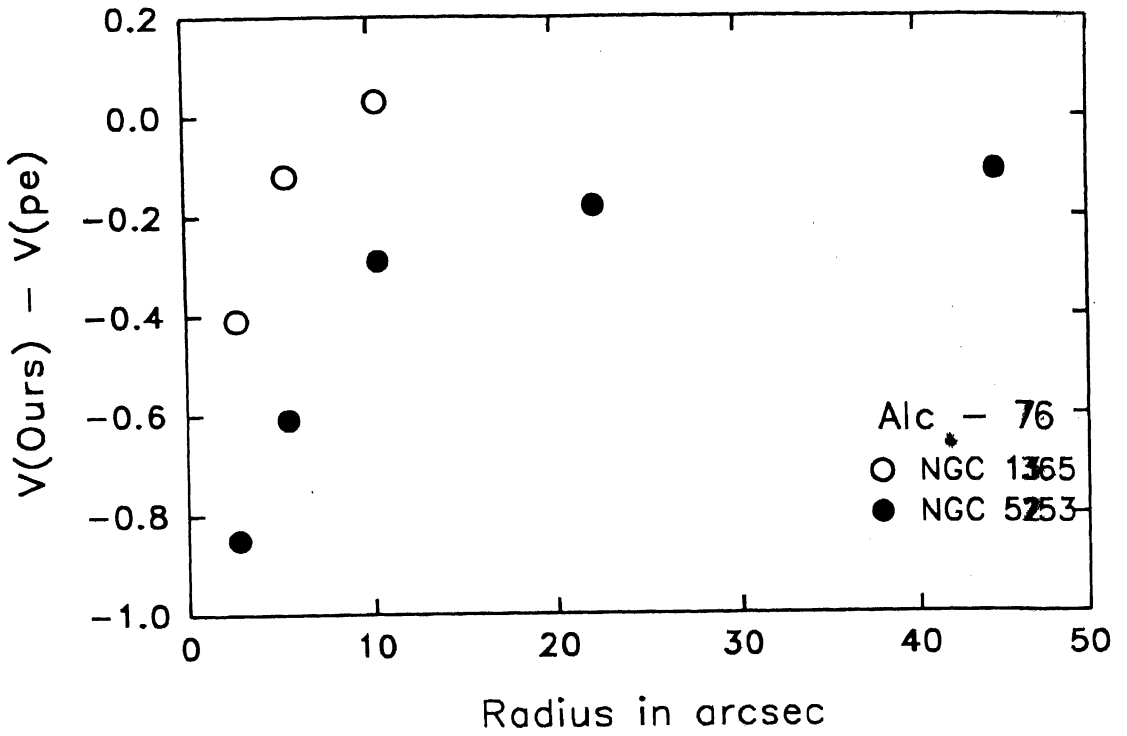
Figure III.21 Comparison of synthetic aperture photometry of galaxies with the photoelectric data of Alcaino (1976).

IV. EVOLUTIONARY POPULATION SYNTHESIS MODEL

Giant extragalactic H II complexes and H II galaxies are the only regions outside our own Galaxy that show clear evidences of recent star formation. Hence these are the ideal testing grounds for the theories of star formation and evolution under varying physical and chemical environments. Such a study would involve a comparison of synthesized properties of star-forming regions with observables. The observables like the emission or absorption lines, or the continuum emission, which are signatures of individual stars, gas excited by them and dust heated by them, are spread over the entire range of electromagnetic spectrum from radio to X-rays. Often observations at different wavelength bands give complimentary information. In a recent paper Mas-Hesse and Kunth (1991) have modelled starburst regions, synthesizing a variety of observables.

In this work, a model of star-forming region is constructed with a view to synthesizing observable parameters in the optical wavelength region. Most of such efforts hitherto were concentrated on synthesizing Hα or Hβ equivalent widths and optical colours, suitable for comparison with spectroscopically derived parameters. The computations in the present work are meant to be compared with the observables in the optical band obtained through CCD imaging. The most important of these parameters is the ratio of equivalent Hβ luminosity to blue band luminosity.

A giant star-forming complex consists of a star cluster and an associated nebulosity arround it. Ionizing photons from hot OB stars in the star cluster are the source of ionization in the nebula. Most of the emission lines from the complex are produced in the gaseous nebula, while the continuum has contribution from both stars and gas. In the model, the contributions from cluster and nebula to any band are computed separately. Pure cluster continua are derived from observables by subtracting the gaseous contribution. Computations of the cluster-related and

gas-related quantities are explained below in sections 1 and 2 respectively.

1. Model Clusters

A complete description of a star cluster can be done by the following set of parameters :

1. IMF of stars defined by

        (a) Slope (α)

        (b) Upper cut-off (m_u)

        (c) Lower cut-off (m_l)

2. Age (t)

3. Metallicity (Z)

4. Total Mass (M_T)

The range of the above parameters used in the present computations are $m_l = 1.0, m_u = 30\text{–}120$, $\alpha = 0.5 - 3.5$, $t = 0 - 14$ Myr, $Z = 0.02, 0.002$. $Z = 0.02$ corresponds to solar metallicity ($Z_\odot$). m_l, m_u and all other mass related quantities appearing now-onwards are measured in solar unit $M_\odot$. Metallicities when expressed in solar units are denoted by z. For given values of parameters, the fluxes at any wavelength can be computed as,

$$L_\lambda(imf; t; z) = A \int_{m_l}^{m_u} l_\lambda(m; t; z) m^{-\alpha} dm \qquad (\text{IV.1})$$

with

$$M_T = A \int_{m_l}^{m_u} m^{1-\alpha} dm \qquad (\text{IV.2})$$

$$l_\lambda(m; t; z) = \pi f_\lambda(m; t; z) 4\pi R^2(m; t; z) \qquad (\text{IV.3})$$

where $f_\lambda(m; t; z)$ is the intensity emitted from a star of mass m at an evolutinary

113

stage t at wavelength λ. R is the radius of the star A, the normalizing constant. z is the abundance of the gas from which the stars are formed.

The luminosity in any given band B with a normalized response curve $R_B(\lambda)$ is computed as,

$$L_B(imf;t;z) = \int_{band} L_\lambda(imf;t;z)R_B(\lambda)d\lambda. \qquad \text{(IV.4)}$$

Lyman continuum luminosity is obtained by integrating the spectrum between 228 Å and 912 Å.

$$N_L(imf;t;z) = \int_{228}^{912} L_\lambda(imf;t;z)\frac{\lambda}{hc}d\lambda. \qquad \text{(IV.5)}$$

These computations require a library of stellar spectra for a wide range of masses at various evolutionary stages for solar and nonsolar abundances. Such a spectrum can be computed theoretically by combining stellar evolutionary models with atmospheric models. Melnick, Terlevich and Eggleton (1985) have constructed such a model for $Z = Z_\odot$ and $0.02\,Z_\odot$ using Kurucz (1979) atmospheric models and their own evolutionary codes. Olofsson (1989) has computed model spectra suitable for BCGs ($Z = 0.002$) using evolutionary models from various authors compiled from literature. After these works homogenous stellar evolutionary data has been published by Maeder (1990). Recently Mas-Hesse and Kunth (1991) have published detailed models suitable for comparison with multiwavelength observations. The latter model differs from others in that the observed stellar properties are used instead of theoretically computed parameters. Our models are very similar to that of Melnick, Terlevich and Eggleton (1985) except that Maeder's new stellar evolutionary data are used along with Kurucz (1979) atmospheres. Evolutionary tracks from Maeder (1990) cover a mass range $15 \leq m \leq 120$ at $Y = 0.28$ and $Z = 0.002, 0.005, 0.02, 0.04$ and follow the star until the end of core carbon burning taking into account the effects of mass loss and convective overshooting. For

stars of lower masses we have used the models of Alcock and Paczynski (1978) $[X = 0.7, \ Z = 0.03, 0.01, 0.003, 0.001, 0.0004]$ and Maeder and Meynet (1989) $[Y = 0.28, \ Z = Z_\odot]$. We use the above evolutionary models to compute $\log g$ and T_{eff} at various evolutionary states for $Z = Z_\odot$ and $Z = 0.1 Z_\odot$ for $1 \le m \le 120$. The spectrum for a given $\log g$ and T_{eff} is computed using Kurucz (1979) solar abundance models, interpolating linearly in $\log g$ when necessary. The effect of abundances on the resultant spectrum for a given $\log g$ and T_{eff} is found to be negligible (Howarth and Lynas-Gray 1989). However T_{eff} for a given mass will be higher at lower metallic abundances. For $T_{\text{eff}} > 50000$ K for which, there are no models available from Kurucz, we have used a blackbody model, which is a good approximation at these high temperatures. Also at $T_{\text{eff}} < 5500$ Kurucz (1979) models are not available and hence computaions are done with the lowest available temperature for that $\log g$. This is not a good aproximation, especially during red supergiant (RSG) phase of the star. Hence the colours $B - V$ and $V - R$ are recomputed in such cases using observed properties of RSGs, as tabulated by Johnson (1966) for solar abundance models.

It can be seen from equations (IV.1–IV.5) that, computations of cluster properties require a knowledge of l_λ at every mass point chosen for integration. Ideally one should obtain this by directly interpolating Maeder's table at every evolutionary stage for intermediate masses. Kurucz spectra should be computed at each of these masses, which are then to be integrated over the chosen IMF. This results in an integrated spectrum of the cluster, which should be integrated over selected wavelength bands to get band fluxes. At the mass intervals chosen by us (0.5–1.0 $M_\odot$), this will demand too much of computer time. However, the same results can be obtained by first integrating the spectra of individual masses over any given band followed by integrating over the IMF. This requires much less computer time, with negligible loss of accuracy.

Table IV.1 Derived stellar quantities.

Mass $M_\odot$	T_{eff} ° K	$\log \frac{L_{bol}}{L_\odot}$	B.C.	$\log \frac{R}{R_\odot}$	V	$B-V$	$V-R$	$\log n_l$ Ph s^{-1}	$\log n_l$ Ph s^{-1} cm^{-2}
$Z = 0.02$, Age $= 0$									
1.0	5500.0	−0.207	−0.163	−0.059	5.431	+0.646	+0.423	22.158	−0.509
1.3	6546.4	0.401	−0.039	0.091	3.787	+0.416	+0.288	24.590	1.624
1.6	7042.8	0.696	−0.013	0.175	3.022	+0.331	+0.232	25.541	2.407
1.7	7808.5	0.898	−0.003	0.186	2.507	+0.227	+0.152	33.999	10.841
1.9	8522.5	1.076	−0.035	0.200	2.094	+0.107	+0.071	34.582	11.398
2.1	9264.5	1.248	−0.137	0.213	1.768	+0.023	+0.028	36.152	12.942
2.3	10006.5	1.407	−0.277	0.225	1.510	−0.015	+0.006	37.277	14.042
2.5	10874.9	1.579	−0.456	0.239	1.257	−0.061	−0.010	38.300	15.037
2.8	11628.0	1.732	−0.607	0.257	1.028	−0.089	−0.017	38.923	15.624
3.0	12494.9	1.896	−0.775	0.277	0.786	−0.110	−0.024	39.533	16.196
3.3	13245.9	2.035	−0.919	0.296	0.581	−0.114	−0.031	40.129	16.752
3.6	14121.4	2.189	−1.079	0.317	0.357	−0.129	−0.037	40.716	17.297
4.0	15147.9	2.357	−1.258	0.340	0.116	−0.145	−0.044	41.358	17.893
4.4	16019.2	2.495	−1.403	0.361	−0.085	−0.158	−0.049	41.880	18.374
4.8	17011.8	2.644	−1.559	0.383	−0.302	−0.171	−0.055	42.435	18.885
5.2	17980.0	2.784	−1.703	0.405	−0.507	−0.184	−0.060	42.906	19.312
5.8	18915.4	2.914	−1.835	0.426	−0.701	−0.195	−0.065	43.274	19.638
6.3	19997.1	3.057	−1.975	0.449	−0.918	−0.207	−0.071	43.701	20.019
6.9	21254.3	3.214	−2.128	0.475	−1.157	−0.219	−0.077	44.109	20.376
7.6	22298.7	3.343	−2.244	0.497	−1.363	−0.229	−0.082	44.453	20.674
8.3	23435.3	3.477	−2.365	0.521	−1.579	−0.238	−0.086	44.805	20.978
9.1	24692.3	3.619	−2.487	0.547	−1.811	−0.247	−0.091	45.191	21.312
10.0	25783.0	3.737	−2.591	0.568	−2.002	−0.254	−0.094	45.503	21.582
11.0	27034.3	3.866	−2.702	0.592	−2.214	−0.262	−0.098	45.854	21.886
12.0	28467.4	4.007	−2.818	0.617	−2.450	−0.272	−0.102	46.260	22.241
13.2	29657.3	4.117	−2.906	0.637	−2.637	−0.279	−0.106	46.598	22.540
14.5	31019.4	4.238	−3.008	0.658	−2.837	−0.285	−0.108	46.931	22.830
15.8	32272.2	4.349	−3.098	0.679	−3.025	−0.290	−0.109	47.225	23.082
17.4	33475.8	4.456	−3.178	0.701	−3.212	−0.294	−0.110	47.514	23.328
19.1	34847.2	4.573	−3.262	0.725	−3.421	−0.299	−0.111	47.847	23.614
20.9	36191.6	4.684	−3.369	0.747	−3.591	−0.301	−0.110	48.046	23.767
22.9	37456.2	4.786	−3.469	0.768	−3.746	−0.303	−0.110	48.221	23.900
25.1	38859.7	4.896	−3.575	0.791	−3.915	−0.305	−0.109	48.423	24.056
27.5	39781.2	4.973	−3.641	0.809	−4.041	−0.306	−0.108	48.571	24.167
30.2	40816.7	5.057	−3.721	0.829	−4.172	−0.308	−0.109	48.687	24.243

Table IV.1 Continued.

Mass $M_\odot$	T_{eff} ° K	$\log \frac{L_{bol}}{L_\odot}$	B.C.	$\log \frac{R}{R_\odot}$	V	$B - V$	$V - R$	$\log n_l$ Ph s^{-1}	$\log n_l$ Ph s^{-1} cm^{-2}
33.1	41983.1	5.150	−3.811	0.851	−4.314	−0.311	−0.110	48.801	24.314
36.3	43300.5	5.252	−3.909	0.875	−4.470	−0.313	−0.111	48.931	24.397
39.8	44792.4	5.363	−4.015	0.901	−4.643	−0.316	−0.113	49.081	24.494
43.7	45654.7	5.435	−4.077	0.921	−4.760	−0.317	−0.113	49.165	24.539
47.9	46571.4	5.511	−4.142	0.941	−4.884	−0.318	−0.114	49.251	24.584
52.5	47597.6	5.594	−4.213	0.964	−5.021	−0.319	−0.114	49.347	24.634
57.5	48748.9	5.685	−4.290	0.989	−5.172	−0.321	−0.115	49.454	24.692
63.1	49684.3	5.763	−4.352	1.012	−5.306	−0.321	−0.115	49.548	24.740
69.2	50413.9	5.830	−4.191	1.032	−5.634	−0.309	−0.104	49.662	24.813
75.9	51226.2	5.903	−4.238	1.055	−5.771	−0.310	−0.105	49.740	24.846
83.2	52131.8	5.984	−4.289	1.080	−5.920	−0.312	−0.106	49.826	24.881
91.2	52789.0	6.048	−4.327	1.101	−6.043	−0.313	−0.106	49.893	24.906
100.0	53403.7	6.110	−4.361	1.122	−6.165	−0.314	−0.107	49.959	24.929
109.6	54085.9	6.179	−4.398	1.146	−6.298	−0.315	−0.107	50.030	24.955
$Z = 0.002$, Age = 0									
2.1	12808.3	1.532	−0.836	0.074	1.755	−0.107	−0.027	39.385	16.454
2.3	13367.5	1.664	−0.943	0.102	1.533	−0.112	−0.032	39.831	16.842
2.5	14008.8	1.808	−1.058	0.134	1.288	−0.124	−0.037	40.288	17.236
2.8	14747.4	1.967	−1.190	0.168	1.024	−0.136	−0.041	40.783	17.662
3.0	15579.8	2.135	−1.332	0.205	0.746	−0.148	−0.047	41.318	18.124
3.3	16230.8	2.244	−1.438	0.224	0.578	−0.157	−0.051	41.704	18.472
3.6	16975.8	2.364	−1.555	0.245	0.394	−0.168	−0.055	42.127	18.853
4.0	17832.2	2.496	−1.684	0.268	0.193	−0.179	−0.060	42.551	19.230
4.4	18820.8	2.641	−1.825	0.294	−0.027	−0.190	−0.065	42.960	19.588
4.8	19968.0	2.800	−1.975	0.322	−0.274	−0.204	−0.071	43.421	19.993
5.2	21018.3	2.939	−2.105	0.347	−0.492	−0.214	−0.076	43.768	20.291
5.8	21949.7	3.059	−2.212	0.369	−0.685	−0.223	−0.080	44.076	20.554
6.3	23018.3	3.190	−2.327	0.393	−0.899	−0.233	−0.085	44.415	20.844
6.9	24249.9	3.335	−2.452	0.420	−1.134	−0.242	−0.089	44.790	21.165
7.6	25234.9	3.447	−2.546	0.442	−1.322	−0.249	−0.093	45.086	21.418
8.3	26291.0	3.564	−2.645	0.465	−1.514	−0.256	−0.096	45.384	21.670
9.1	27499.9	3.691	−2.750	0.489	−1.728	−0.264	−0.100	45.727	21.964
10.0	28889.4	3.831	−2.859	0.516	−1.969	−0.273	−0.104	46.127	22.310
11.0	29978.1	3.916	−2.940	0.527	−2.101	−0.280	−0.107	46.415	22.577
12.0	31219.1	4.010	−3.034	0.538	−2.241	−0.285	−0.109	46.682	22.821

Table IV.1 Continued.

Mass $M_\odot$	T_{eff} °K	$\log \frac{L_{bol}}{L_\odot}$	B.C.	$\log \frac{R}{R_\odot}$	V	$B-V$	$V-R$	$\log n_l$ Ph s^{-1}	$\log n_l$ Ph s^{-1} cm^{-2}
13.2	32638.9	4.112	−3.133	0.551	−2.398	−0.291	−0.111	46.991	23.105
14.5	34270.0	4.225	−3.236	0.565	−2.575	−0.298	−0.113	47.354	23.440
15.8	35476.6	4.331	−3.318	0.588	−2.760	−0.302	−0.114	47.606	23.646
17.4	36361.9	4.436	−3.388	0.619	−2.952	−0.303	−0.113	47.768	23.746
19.1	37357.9	4.550	−3.463	0.653	−3.162	−0.304	−0.112	47.950	23.860
20.9	38671.7	4.659	−3.560	0.677	−3.337	−0.306	−0.111	48.149	24.011
22.9	40396.3	4.757	−3.684	0.688	−3.458	−0.309	−0.111	48.361	24.201
25.1	42312.4	4.863	−3.834	0.701	−3.573	−0.312	−0.112	48.508	24.322
27.5	43251.4	4.940	−3.904	0.720	−3.695	−0.314	−0.112	48.609	24.384
30.2	44304.8	5.024	−3.980	0.741	−3.829	−0.315	−0.113	48.724	24.457
33.1	45489.5	5.116	−4.065	0.765	−3.975	−0.317	−0.113	48.845 .	24.531
36.3	46824.9	5.217	−4.160	0.790	−4.133	−0.318	−0.114	48.961	24.596
39.8	48334.3	5.328	−4.263	0.818	−4.307	−0.320	−0.114	49.091	24.671
43.7	49279.7	5.400	−4.325	0.837	−4.424	−0.321	−0.115	49.178	24.719
47.9	50293.6	5.476	−4.184	0.857	−4.755	−0.309	−0.104	49.307	24.808
52.5	51429.2	5.559	−4.249	0.879	−4.897	−0.311	−0.105	49.397	24.854
57.5	52703.8	5.650	−4.322	0.904	−5.053	−0.313	−0.106	49.495	24.903
63.1	53745.7	5.728	−4.380	0.926	−5.191	−0.314	−0.107	49.578	24.942
69.2	54565.5	5.796	−4.425	0.947	−5.316	−0.316	−0.108	49.650	24.972
75.9	55478.7	5.870	−4.474	0.969	−5.452	−0.317	−0.109	49.728	25.005
83.2	56497.6	5.952	−4.528	0.994	−5.601	−0.318	−0.109	49.813	25.040
91.2	57196.1	6.017	−4.565	1.016	−5.728	−0.319	−0.110	49.881	25.064
100.0	57828.6	6.081	−4.598	1.039	−5.854	−0.320	−0.110	49 946	25.085
109.6	58530.2	6.151	−4.634	1.063	−5.993	−0.321	−0.111	50.018	25.108

Table IV.2(a) Results of the cluster model without evolution.

No	M_u $M_\odot$	Slope	$\log(\phi)$ erg s^{-1} M$_\odot^{-1}$	$\log\frac{M}{L_v}$ $\frac{M_\odot}{L_\odot}$	$\log\frac{M}{L}$ $\frac{M_\odot}{L_\odot}$	$\log(\frac{\phi}{L_B})$	$B-V$	$V-R$	$W(\mathrm{H}\beta)$ Å	$W(\mathrm{H}\alpha)$ Å
$M_l = 1\,\mathrm{M_\odot}, Z = 0.02$, Age $= 0$
1	30	0.50	34.39	−1.04	−3.28	−0.64	−0.29	−0.11	270.4	1821.4
2	30	1.00	34.27	−0.98	−3.19	−0.69	−0.29	−0.10	243.1	1670.2
3	30	1.50	34.09	−0.87	−3.05	−0.77	−0.28	−0.10	209.9	1475.2
4	30	2.00	33.82	−0.72	−2.83	−0.87	−0.26	−0.09	170.1	1222.5
5	30	2.50	33.46	−0.50	−2.53	−1.01	−0.23	−0.07	125.2	913.6
6	30	3.00	33.00	−0.27	−2.17	−1.21	−0.18	−0.04	80.1	581.9
7	30	3.50	32.49	−0.05	−1.79	−1.48	−0.11	0.00	43.0	302.3
8	60	0.50	35.08	−1.20	−3.70	−0.12	−0.31	−0.11	615.0	3235.2
9	60	1.00	34.98	−1.15	−3.61	−0.17	−0.31	−0.11	576.1	3106.0
10	60	1.50	34.80	−1.05	−3.46	−0.24	−0.30	−0.11	521.5	2910.7
11	60	2.00	34.52	−0.87	−3.21	−0.34	−0.28	−0.10	444.1	2601.8
12	60	2.50	34.09	−0.62	−2.85	−0.50	−0.25	−0.08	340.0	2118.8
13	60	3.00	33.56	−0.33	−2.40	−0.73	−0.20	−0.05	218.4	1443.1
14	60	3.50	32.95	−0.08	−1.93	−1.05	−0.13	−0.01	110.7	747.4
15	120	0.50	35.49	−1.38	−3.99	0.10	−0.31	−0.11	789.6	3725.3
16	120	1.00	35.40	−1.33	−3.91	0.07	−0.31	−0.11	762.8	3655.7
17	120	1.50	35.23	−1.22	−3.77	0.01	−0.31	−0.11	717.8	3531.8
18	120	2.00	34.93	−1.02	−3.49	−0.08	−0.30	−0.10	639.9	3295.7
19	120	2.50	34.44	−0.71	−3.06	−0.25	−0.27	−0.09	511.6	2838.5
20	120	3.00	33.83	−0.37	−2.54	−0.50	−0.21	−0.06	333.2	2036.8
21	120	3.50	33.15	−0.09	−2.00	−0.87	−0.13	−0.01	161.7	1057.3
$M_l = 1\,\mathrm{M_\odot}, Z = 0.002$, Age $= 0$
1	30	0.50	34.50	−0.92	−3.25	−0.41	−0.30	−0.11	401.4	2447.6
2	30	1.00	34.39	−0.87	−3.17	−0.47	−0.30	−0.11	363.8	2278.3
3	30	1.50	34.21	−0.77	−3.03	−0.55	−0.29	−0.10	316.0	2046.7
4	30	2.00	33.95	−0.63	−2.82	−0.66	−0.27	−0.10	256.5	1731.0
5	30	2.50	33.60	−0.44	−2.54	−0.82	−0.25	−0.09	188.5	1329.5
6	30	3.00	33.15	−0.22	−2.20	−1.03	−0.23	−0.08	120.6	884.6
7	30	3.50	32.66	−0.01	−1.84	−1.30	−0.19	−0.06	65.8	493.8
8	60	0.50	35.12	−1.11	−3.66	0.01	−0.31	−0.11	719.4	3542.0
9	60	1.00	35.02	−1.05	−3.58	−0.03	−0.31	−0.11	683.3	3438.4
10	60	1.50	34.85	−0.95	−3.43	−0.10	−0.30	−0.11	628.2	3269.4
11	60	2.00	34.56	−0.78	−3.19	−0.21	−0.29	−0.10	543.2	2980.2
12	60	2.50	34.15	−0.54	−2.83	−0.38	−0.27	−0.09	420.9	2495.2
13	60	3.00	33.62	−0.27	−2 40	−0.62	−0.24	−0.08	272.5	1777.4
14	60	3.50	33.03	−0.03	−1.96	−0.95	−0.20	−0.06	140.5	994.8

Table IV.2(a) Continued.

No	M_u $M_\odot$	Slope	$\log(\phi)$ erg s^{-1} M$_\odot^{-1}$	$\log \frac{M}{L_v}$ $\frac{M_\odot}{L_\odot}$	$\log \frac{M}{L}$ $\frac{M_\odot}{L_\odot}$	$\log(\frac{\phi}{L_B})$	$B-V$	$V-R$	$W(H\beta)$ Å	$W(H\alpha)$ Å
15	120	0.50	35.48	−1.27	−3.96	0.21	−0.32	−0.11	871.0	3925.1
16	120	1.00	35.40	−1.22	−3.88	0.18	−0.32	−0.11	846.6	3867.3
17	120	1.50	35.24	−1.12	−3.74	0.12	−0.31	−0.11	804.2	3762.2
18	120	2.00	34.94	−0.92	−3.46	0.03	−0.30	−0.11	726.5	3552.7
19	120	2.50	34.47	−0.63	−3.04	−0.15	−0.28	−0.10	589.4	3124.1
20	120	3.00	33.86	−0.31	−2.53	−0.42	−0.25	−0.08	389.1	2333.8
21	120	3.50	33.20^	−0.04	−2.02	−0.79	−0.21	−0.06	192.9	1312.3

Table IV.2(b) Results of the cluster model with evolution.

Age Myr	$\log(\phi)$ erg s^{-1} M$_\odot^{-1}$	$\log \frac{M}{L_v}$ $\frac{M_\odot}{L_\odot}$	$\log \frac{M}{L}$ $\frac{M_\odot}{L_\odot}$	$\log(\frac{\phi}{L_B})$	$B-V$	$V-R$	$W(H\beta)$ Å	$W(H\alpha)$ Å
$M_l = 1\,\mathrm{M_\odot}$, $M_u = 30\,\mathrm{M_\odot}$, $\alpha = 3.5$, $Z = 0.02$								
0.0	32.51	−0.05	−1.80	−1.46	−0.12	−0.01	44.5	315.8
0.5	32.51	−0.06	−1.80	−1.46	−0.12	−0.01	44.5	315.6
1.0	32.51	−0.06	−1.81	−1.47	−0.13	−0.01	44.3	314.9
1.5	32.52	−0.06	−1.82	−1.47	−0.13	−0.01	44.4	315.8
2.0	32.53	−0.07	−1.83	−1.46	−0.13	−0.01	45.1	321.7
2.5	32.51	−0.07	−1.82	−1.48	−0.12	−0.01	42.8	302.9
3.0	32.51	−0.07	−1.83	−1.48	−0.12	−0.01	42.9	304.5
3.5	32.52	−0.08	−1.84	−1.48	−0.13	−0.01	42.7	303.7
4.0	32.52	−0.08	−1.85	−1.49	−0.13	−0.01	42.3	301.4
4.5	32.49	−0.09	−1.86	−1.53	−0.13	−0.01	38.5	275.5
5.0	32.41	−0.10	−1.88	−1.62	−0.14	−0.02	31.3	226.2
5.5	32.31	−0.12	−1.89	−1.74	−0.14	−0.02	24.1	176.2
6.0	32.18	−0.17	−1.91	−1.90	−0.11	0.14	17.1	126.6
6.5	32.07	−0.44	−1.95	−2.17	0.19	0.37	9.4	64.3
7.0	32.14	−0.33	−1.95	−1.99	0.20	0.46	14.9	111.0
7.5	31.89	−0.25	−1.91	−2.20	0.11	0.50	8.5	63.3
8.0	31.71	−0.24	−1.88	−2.35	0.12	0.50	5.9	43.8
8.6	31.57	−0.25	−1.84	−2.51	0.11	0.45	4.1	28.7
9.2	31.45	−0.22	−1.78	−2.58	0.18	0.48	3.4	22.0
9.8	31.38	−0.32	−1.81	−2.67	0.33	0.57	3.1	22.9
11.0	31.26	−0.41	−1.78	−2.89	0.31	0.39	1.3	5.9
12.0	31.21	−0.22	−1.72	−2.74	0.34	0.72	2.7	18.9
13.0	31.21	−0.32	−1.66	−2.98	0.00	0.12	1.2	8.2
14.0	31.17	−0.02	−1.58	−2.73	−0.01	0.24	2.5	17.4

Table IV.2(b) Continued.

Age Myr	$\log(\phi)$ erg s^{-1} M$_\odot^{-1}$	$\log \frac{M}{L_v}$ $\frac{M_\odot}{L_\odot}$	$\log \frac{M}{L}$ $\frac{M_\odot}{L_\odot}$	$\log(\frac{\phi}{L_B})$	$B-V$	$V-R$	$W(H\beta)$ Å	$W(H\alpha)$ Å
$M_l = 1\,\mathrm{M_\odot}, M_u = 60\,\mathrm{M_\odot}, \alpha = 2.5, Z = 0.02$								
0.0	34.08	−0.62	−2.84	−0.52	−0.26	−0.09	331.4	2079.5
0.5	34.09	−0.63	−2.85	−0.52	−0.26	−0.09	330.7	2077.8
1.0	34.11	−0.65	−2.88	−0.52	−0.26	−0.09	328.0	2067.3
1.5	34.13	−0.68	−2.90	−0.53	−0.26	−0.09	323.9	2049.9
2.0	34.14	−0.72	−2.93	−0.55	−0.26	−0.09	310.6	1987.9
2.5	34.14	−0.75	−2.95	−0.59	−0.26	−0.09	292.5	1898.0
3.0	34.08	−0.82	−2.98	−0.71	−0.26	−0.09	231.4	1576.4
3.5	33.95	−1.01	−3.01	−1.02	−0.23	−0.07	122.7	893.3
3.6	33.93	−1.07	−3.02	−1.10	−0.22	−0.06	103.1	755.6
4.1	33.93	−0.99	−3.00	−1.03	−0.25	−0.08	121.7	897.8
4.5	33.84	−0.89	−2.94	−1.02	−0.25	−0.08	123.8	918.6
5.0	33.64	−0.83	−2.86	−1.17	−0.25	−0.08	90.9	694.2
5.6	33.31	−1.19	−2.83	−1.79	−0.09	0.01	20.8	144.2
6.0	33.31	−1.18	−2.81	−1.67	0.17	0.36	32.5	250.3
6.5	33.16	−1.32	−2.79	−1.91	0.31	0.48	17.4	114.9
7.0	33.05	−1.10	−2.74	−1.75	0.43	0.68	29.0	233.9
7.5	32.73	−0.94	−2.68	−1.97	0.29	0.79	15.0	121.5
8.0	32.50	−0.89	−2.61	−2.13	0.31	0.80	10.1	81.8
8.4	32.37	−0.94	−2.59	−2.26	0.46	0.91	8.0	64.0
9.0	32.29	−1.13	−2.56	−2.51	0.51	0.57	6.1	48.3
9.4	32.16	−0.87	−2.45	−2.42	0.39	0.71	4.9	31.5
10.0	32.09	−0.99	−2.48	−2.53	0.60	0.75	5.1	41.4
11.0	31.97	−1.08	−2.43	−2.79	0.49	0.50	1.4	5.6
12.0	31.91	−0.77	−2.34	−2.45	0.71	1.03	6.3	49.5
13.0	31.91	−0.93	−2.24	−2.88	0.02	0.17	1.5	9.8
14.0	31.85	−0.36	−2.10	−2.37	0.03	0.49	6.1	47.7
$M_l = 1\,\mathrm{M_\odot}, M_u = 120\,\mathrm{M_\odot}, \alpha = 1.0, Z = 0.02$								
0.0	35.39	−1.33	−3.90	0.06	−0.31	−0.11	758.5	3643.5
0.5	35.41	−1.38	−3.93	0.03	−0.31	−0.11	734.4	3579.0
1.0	35.39	−1.40	−3.96	−0.01	−0.32	−0.11	704.3	3503.2
1.5	35.39	−1.51	−4.00	−0.11	−0.31	−0.11	619.8	3250.5
2.0	35.38	−1.62	−4.03	−0.23	−0.31	−0.11	529.4	2942.3
2.5	35.23	−1.72	−3.99	−0.47	−0.29	−0.10	361.5	2250.5
3.0	35.15	−1.86	−4.00	−0.69	−0.27	−0.09	243.3	1645.3
3.5	34.92	−1.69	−3.75	−0.73	−0.23	−0.07	221.2	1477.2
4.0	34.62	−1.46	−3.51	−0.81	−0.25	−0.08	190.7	1324.3
4.4	34.28	−1.34	−3.37	−1.04	−0.26	−0.09	120.7	902.8
5.0	33.95	−1.09	−3.14	−1.11	−0.27	−0.09	103.2	789.2

Table IV.2(b) Continued.

Age Myr	$\log(\phi)$ erg s^{-1} M$_\odot^{-1}$	$\log\frac{M}{L_v}$ $\frac{M_\odot}{L_\odot}$	$\log\frac{M}{L}$ $\frac{M_\odot}{L_\odot}$	$\log(\frac{\phi}{L_B})$	$B-V$	$V-R$	$W(\mathrm{H}\beta)$ Å	$W(\mathrm{H}\alpha)$ Å
5.4	33.74	−1.34	−3.09	−1.54	−0.18	−0.05	38.5	288.7
6.0	33.61	−1.48	−3.03	−1.64	0.27	0.43	36.3	275.9
6.5	33.42	−1.61	−2.97	−1.90	0.39	0.51	17.4	110.1
7.0	33.25	−1.31	−2.88	−1.67	0.63	0.78	39.0	317.7
7.5	32.83	−1.05	−2.76	−1.90	0.49	0.95	17.5	144.3
8.0	32.52	−0.96	−2.65	−2.10	0.54	0.98	10.9	90.7
8.4	32.35	−1.00	−2.61	−2.24	0.69	1.05	8.4	68.4
9.0	32.26	−1.21	−2.55	−2.56	0.65	0.63	6.1	49.1
9.4	32.08	−0.86	−2.39	−2.41	0.59	0.84	4.9	28.8
10.0	32.00	−1.00	−2.43	−2.54	0.83	0.86	5.8	47.9
11.0	31.83	−1.06	−2.34	−2.85	0.61	0.57	1.1	4.2
12.0	31.76	−0.66	−2.19	−2.33	1.11	1.19	11.4	94.7
13.0	31.76	−0.82	−2.04	−2.91	0.05	0.20	1.4	8.7
14.0	31.69	0.01	−1.82	−2.09	0.21	0.83	12.5	103.3

$M_l = 1\,\mathrm{M}_\odot, M_u = 30\,\mathrm{M}_\odot, \alpha = 1.0, Z = 0.002$

Age Myr	$\log(\phi)$	$\log\frac{M}{L_v}$	$\log\frac{M}{L}$	$\log(\frac{\phi}{L_B})$	$B-V$	$V-R$	$W(\mathrm{H}\beta)$	$W(\mathrm{H}\alpha)$
0.0	32.64	0.01	−1.84	−1.30	−0.20	−0.06	65.8	496.6
0.5	32.65	0.00	−1.85	−1.30	−0.20	−0.06	66.5	501.2
1.0	32.66	0.00	−1.85	−1.29	−0.20	−0.06	67.3	507.3
1.5	32.67	0.00	−1.86	−1.29	−0.20	−0.06	68.3	514.6
2.0	32.68	−0.01	−1.87	−1.28	−0.20	−0.06	69.0	520.5
2.5	32.66	0.01	−1.86	−1.28	−0.20	−0.07	69.0	523.1
3.0	32.67	0.01	−1.86	−1.27	−0.21	−0.07	70.6	534.2
3.5	32.69	0.00	−1.87	−1.26	−0.21	−0.07	72.0	545.0
4.0	32.70	0.00	−1.88	−1.26	−0.21	−0.07	72.7	549.9
4.5	32.69	−0.01	−1.89	−1.27	−0.21	−0.07	71.4	541.1
5.0	32.69	−0.01	−1.90	−1.28	−0.21	−0.07	69.6	528.7
5.5	32.69	−0.03	−1.91	−1.30	−0.21	−0.07	67.3	512.8
6.0	32.66	−0.04	−1.93	−1.34	−0.21	−0.07	61.0	467.9
6.5	32.54	−0.08	−1.95	−1.49	−0.21	−0.07	43.5	339.0
7.0	32.41	−0.17	−1.97	−1.72	−0.20	−0.06	26.2	204.1
7.5	32.28	−0.35	−2.00	−1.97	−0.09	0.04	14.0	94.7
8.0	32.16	−0.37	−1.97	−2.11	−0.07	0.05	10.2	67.3
8.6	32.05	−0.38	−1.93	−2.23	−0.09	0.02	7.7	53.1
9.0	32.01	−0.37	−1.91	−2.27	−0.10	0.01	7.1	49.7

Table IV.2(b) Continued.

Age Myr	$\log(\phi)$ erg s^{-1} M$_\odot^{-1}$	$\log \frac{M}{L_v}$ $\frac{M_\odot}{L_\odot}$	$\log \frac{M}{L}$ $\frac{M_\odot}{L_\odot}$	$\log(\frac{\phi}{L_B})$	$B-V$	$V-R$	$W(H\beta)$ Å	$W(H\alpha)$ Å
9.4	31.98	−0.44	−1.88	−2.34	−0.01	0.07	5.7	36.5
10.0	31.89	−0.28	−1.84	−2.29	−0.04	0.07	6.7	42.5
11.0	31.76	−0.47	−1.86	−2.51	0.17	0.22	3.6	17.8
12.0	31.74	−0.53	−1.82	−2.63	0.10	0.16	2.9	15.7
13.0	31.66	−0.61	−1.82	−2.72	0.25	0.26	2.1	9.9
14.0	31.66	−0.41	−1.74	−2.60	0.03	0.11	3.1	18.4

$M_l = 1\,\mathrm{M}_\odot, M_u = 60\,\mathrm{M}_\odot, \alpha = 2.5, Z = 0.002$

Age Myr	$\log(\phi)$ erg s^{-1} M$_\odot^{-1}$	$\log \frac{M}{L_v}$ $\frac{M_\odot}{L_\odot}$	$\log \frac{M}{L}$ $\frac{M_\odot}{L_\odot}$	$\log(\frac{\phi}{L_B})$	$B-V$	$V-R$	$W(H\beta)$ Å	$W(H\alpha)$ Å
0.0	34.13	−0.54	−2.82	−0.39	−0.27	−0.10	410.3	2451.6
0.5	34.14	−0.55	−2.84	−0.39	−0.27	−0.10	408.8	2446.6
1.0	34.16	−0.57	−2.86	−0.40	−0.27	−0.10	406.4	2437.8
1.5	34.17	−0.59	−2.88	−0.40	−0.28	−0.10	402.8	2425.7
2.0	34.19	−0.62	−2.91	−0.41	−0.28	−0.10	398.8	2410.0
2.5	34.20	−0.64	−2.92	−0.42	−0.28	−0.10	393.2	2388.4
3.0	34.21	−0.67	−2.95	−0.45	−0.28	−0.10	374.1	2305.4
3.5	34.21	−0.74	−2.98	−0.52	−0.28	−0.10	334.2	2120.3
4.0	34.12	−1.13	−3.02	−0.95	−0.19	−0.05	138.6	965.8
4.5	33.97	−1.32	−3.06	−1.28	−0.15	−0.02	67.9	476.8
5.0	33.84	−1.46	−3.02	−1.52	−0.08	0.03	38.3	252.8
5.5	33.74	−1.45	−2.94	−1.61	−0.07	0.02	31.0	209.4
6.1	33.59	−1.27	−2.88	−1.58	−0.08	0.03	33.7	224.5
6.5	33.44	−1.14	−2.85	−1.62	−0.10	0.04	31.6	210.3
6.9	33.29	−1.20	−2.83	−1.83	−0.13	−0.01	19.5	139.9
7.4	33.13	−1.18	−2.78	−1.96	−0.10	0.01	14.4	100.2
8.0	32.96	−1.19	−2.73	−2.11	−0.01	0.10	10.0	60.3
8.4	32.92	−1.19	−2.66	−2.09	0.12	0.19	9.6	50.1
9.2	32.75	−1.31	−2.61	−2.38	0.12	0.18	5.0	26.4
9.6	32.66	−1.25	−2.59	−2.36	0.27	0.27	4.9	22.2
11.0	32.46	−1.22	−2.50	−2.51	0.29	0.28	3.4	15.1
12.0	32.44	−1.27	−2.44	−2.64	0.17	0.20	2.7	13.7
13.0	32.35	−1.35	−2.42	−2.74	0.33	0.30	2.0	8.4
14.0	32.35	−1.08	−2.30	−2.57	0.10	0.16	3.3	18.1

Table IV.2(b) Continued.

Age Myr	$\log(\phi)$ erg s^{-1} M$_\odot^{-1}$	$\log \frac{M}{L_v}$ $\frac{M_\odot}{L_\odot}$	$\log \frac{M}{L}$ $\frac{M_\odot}{L_\odot}$	$\log(\frac{\phi}{L_B})$	$B-V$	$V-R$	$W(\mathrm{H}\beta)$ Å	$W(\mathrm{H}\alpha)$ Å
$M_l = 1\,\mathrm{M}_\odot, M_u = 120\,\mathrm{M}_\odot, \alpha = 1.0, Z = 0.002$
0.0	35.39	-1.22	-3.87	0.17	-0.32	-0.11	842.5	3856.8
0.5	35.41	-1.27	-3.90	0.15	-0.31	-0.11	822.2	3806.8
1.0	35.44	-1.33	-3.94	0.12	-0.31	-0.11	798.5	3746.4
1.5	35.47	-1.40	-3.97	0.07	-0.31	-0.11	764.8	3659.2
2.0	35.43	-1.46	-4.01	-0.02	-0.32	-0.11	690.4	3465.0
2.5	35.33	-1.54	-3.97	-0.21	-0.31	-0.11	547.6	3004.0
3.0	35.08	-2.01	-4.02	-0.89	-0.24	-0.08	161.6	1146.8
3.5	35.23	-2.05	-4.02	-0.77	-0.20	-0.04	202.5	1334.0
4.0	34.62	-2.17	-3.80	-1.48	-0.15	-0.03	43.8	319.2
4.5	34.38	-1.99	-3.58	-1.53	-0.13	0.00	38.5	268.7
5.0	34.17	-2.07	-3.46	-1.79	-0.04	0.06	20.7	133.1
5.5	34.02	-1.97	-3.29	-1.84	-0.04	0.04	18.3	121.3
6.1	33.81	-1.69	-3.16	-1.77	-0.05	0.06	21.9	141.1
6.5	33.61	-1.49	-3.08	-1.77	-0.05	0.07	22.0	139.3
7.1	33.42	-1.50	-3.00	-1.96	-0.02	0.09	14.0	86.9
7.6	33.16	-1.41	-2.90	-2.13	-0.03	0.08	9.4	59.5
8.0	32.98	-1.39	-2.82	-2.27	0.04	0.14	6.7	38.1
8.4	32.93	-1.36	-2.70	-2.22	0.19	0.23	6.9	33.6
9.2	32.71	-1.43	-2.62	-2.52	0.17	0.21	3.5	17.5
9.6	32.59	-1.34	-2.58	-2.49	0.34	0.30	3.5	14.8
11.0	32.34	-1.25	-2.42	-2.64	0.36	0.31	2.4	10.1
12.0	32.31	-1.27	-2.32	-2.76	0.21	0.23	2.0	9.8
13.0	32.19	-1.32	-2.27	-2.85	0.38	0.32	1.5	6.1
14.0	32.19	-1.00	-2.08	-2.63	0.14	0.18	2.8	14.7

To further reduce the computer time, the band fluxes at each of the mass points used in the integral are obtained in two stages. First Maeder's tables are interpolated at each of the 51 evolutionary stages to obtain tracks for about 60 stellar masses, roughly at equal intervals of $\log(m)$. Kurucz spectra are obtained at each of these mass points, and are integrated over filter bandpasses to synthesize observables. Thus a set of basic stellar quantities are obtained for the 60 mass points, which are further interpolated to get the band fluxes at every chosen mass point for the integration over the IMF. The basic stellar quantities and computed luminosities for the selected stellar masses at zero age are given in Table IV.1 for Z=0.02 and 0.002, as an example. Last two columns in the table are computed Lyman continuum luminosity and surface flux respectively. Because of the presence of short term evolutionary stages such as the red supergiants and Wolf-Rayet stars in Maeder's models, it is necessary to have atleast around 60 mass points in the first interpolation, to have continuity of the computed quantities near fast evolutionary stages. On the other hand, if the stellar masses in a cluster are not continuously distributed, we expect the cluster quantities to be heavily affected by short term peaks.

1.1 Model Results and Dependence on Input Parameters

For any given IMF, age and metallicity, the observables are computed for a total mass M_T of the cluster. The quantities synthesized are :

(i) Lyman continuum photon luminosity N_L ($\mathrm{ph\,s^{-1}}$ in terms of equivalent Hβ luminosity ($\mathrm{erg\,s^{-1}}$) defined as (Melnick, Terlevich and Eggleton 1985),

$$\phi = 4.78 \times 10^{-13} N_L. \qquad (\mathrm{IV.6})$$

(ii) $\log(\frac{\phi}{L_B})$ — the ratio of equivalent Hβ luminosity to blue band luminosity.

(iii) $B - V$ and $V - R$ colours.

(iv) Hα and Hβ equivalent widths for an assumed gas temperature of 10000 K.
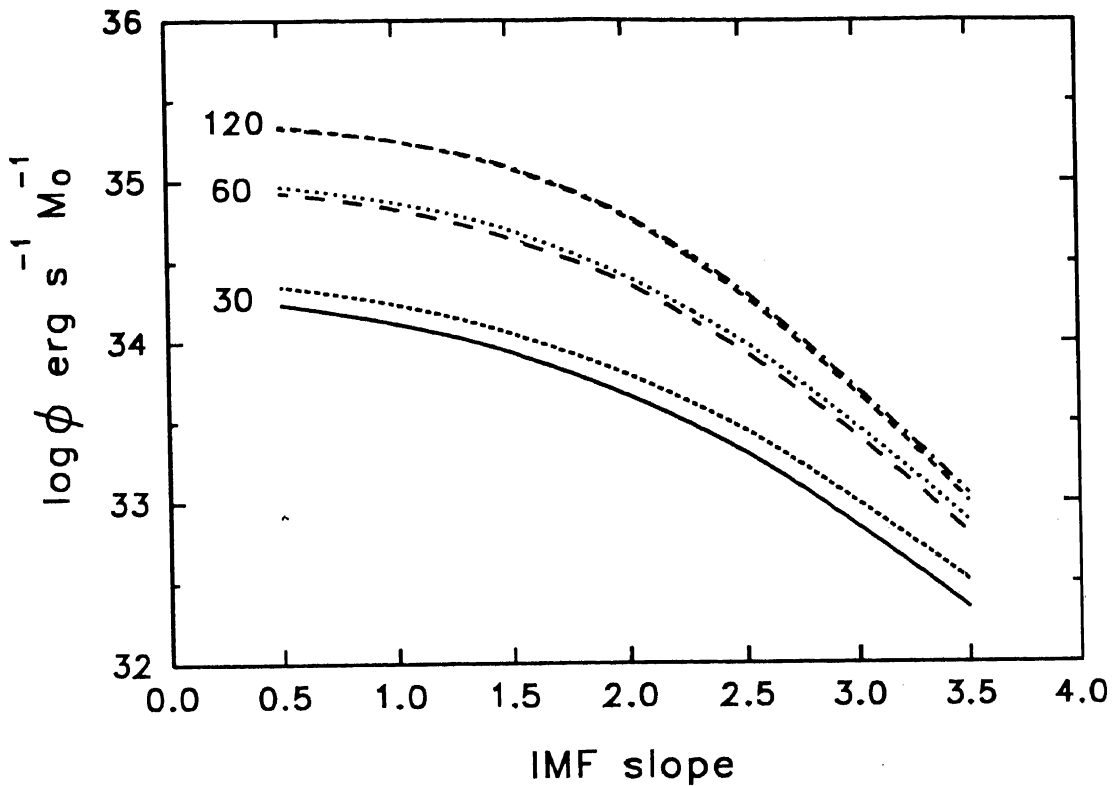
Figure IV.1 Variation of $\log(\phi)$ with IMF slope(α), at zero age for three values of upper mass cut-offs ($m_u = 30, 60, 120$) and two metallicities ($Z = 0.02$ and 0.002). Solid line, long dash and medium dash lines correspond to $Z = 0.02$ and short dash, dot, and dash-dot lines correspond to $Z = 0.002$.

(v) $\log(\frac{M}{L_V})$ and $\log(\frac{M}{L})$ — mass to light ratios of the cluster for the visible and bolometric luminosity respectively, expressed in solar units.

In addition spectra at all the 342 Kurucz wavelengths are computed for 3 IMFs at evolutionary stages 0, 3, 6 and 10 Myr.

The magnitudes are converted into luminosities in optical bands using Bessell's (1990) zeropoints. $\frac{\phi}{L_B}$ introduced here resembles Hβ equivalent width, but is relatively easier to obtain through imaging observations. The computed values of the above quantities for a zero age cluster are given in Table IV.2(a), for all the IMFs chosen at both Z=0.002 and 0.02. Dependance of these quantities with age of the cluster is also studied. For this purpose we have selected three IMFs and evolved the cluster upto 14 Myr. The IMFs chosen are the ones having the least number
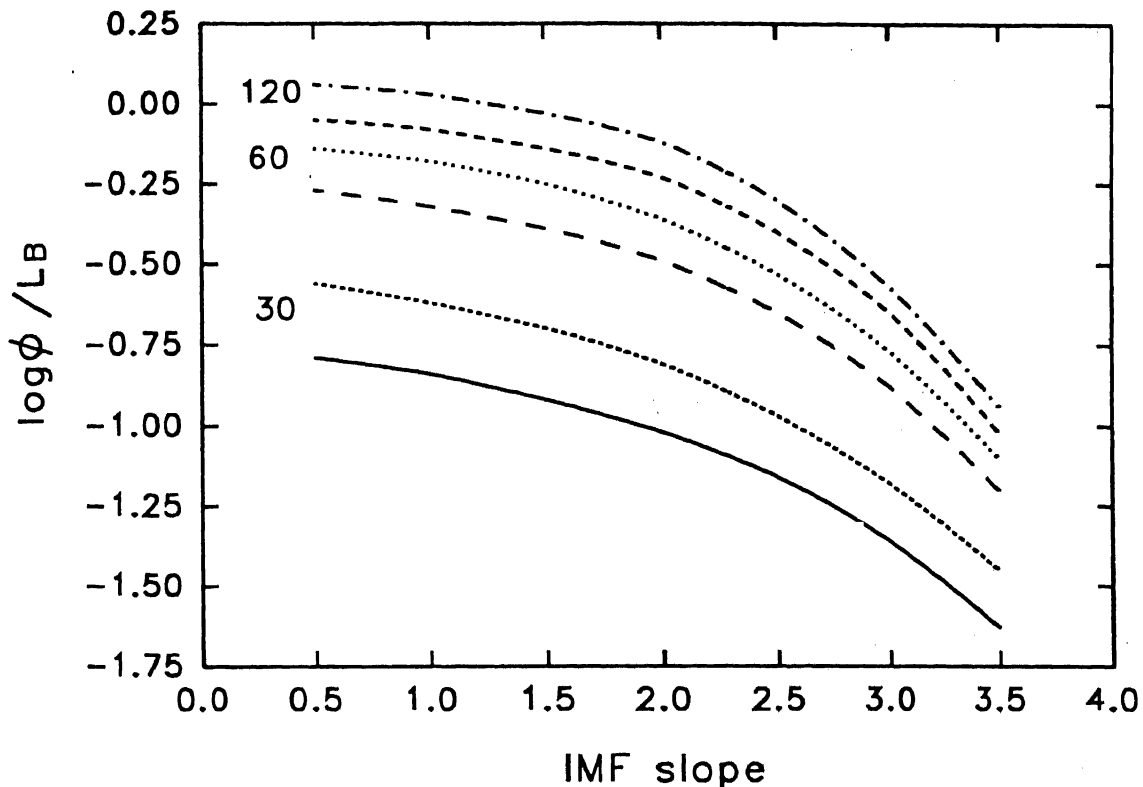
Figure IV.2 Variation of $\log(\frac{\phi}{L_B})$ with IMF slope(α). See the caption of Fig. IV.1 for rest of the details.

of massive stars (IMF1: $m_u = 30, \alpha = 3.5$), maximum number of massive stars (IMF3: $m_u = 120, \alpha = 1.0$), and an intermediate one (IMF2: $m_u = 60, \alpha = 2.5$), which is close to Salpeter IMF ($\alpha = 2.35$). Cluster quantities for evolution upto 14 Myr are given in Table IV.2(b). A lower cut-off mass of 1 $M_\odot$ is assumed in all the models. According to Maeder (1990), only stars more massive than 32 $M_\odot$ can become Wolf-Rayet stars. As Wolf-Rayet star features are often found in giant H II complexes, we do not disuss the effects of decreasing m_u below 30.

Figures IV.1–IV.3 show the variation of $\log(\phi)$, $\log(\frac{\phi}{L_B})$ and $B - V$ with IMF slope for upper cut-off masses 30, 60 and 120 $M_\odot$, at solar and 0.1 solar abundances. Computations are done at 0.5 intervals of α between 0.5 and 3.5. For every m_u, models at lower metallicities have higher $\log(\phi)$ and $\log(\frac{\phi}{L_B})$ and bluer $B - V$ colours. In the models hitherto we have assumed that all the ionizing photons are used up by the gas. In reality some of the ionizing photons might be absorbed by
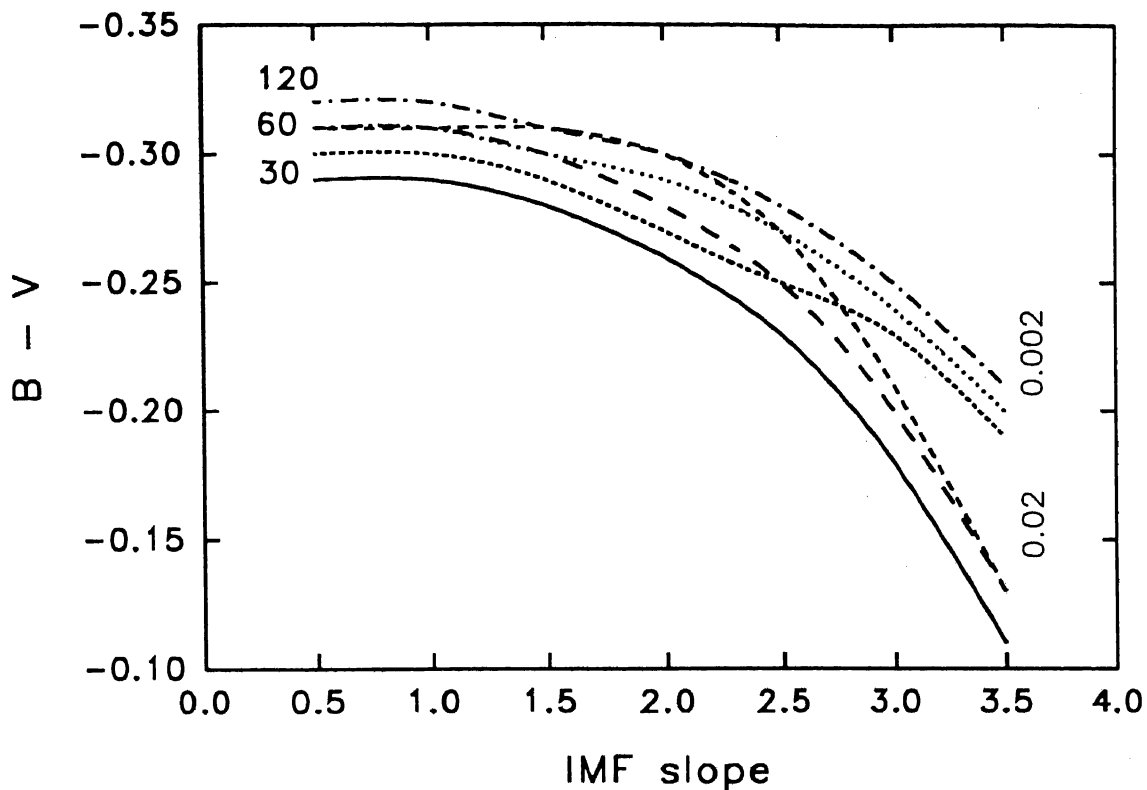
Figure IV.3 Variation of $B - V$ colour with IMF slope(α). See the caption of Fig. IV.1 for rest of the details.

the dust particles and hence may not be available for ionization. We have taken the missing fraction to be 30% following normal conventions (Mas-Hesse and Kunth 1991) and decreased all the $\log(\phi)$ related quantities by 0.15 dex. Thus values in the tables are values assuming there is no absorption of ionizing photons by dust while the plots correct for this effect, by assuming that 30% of the ionizing photons are absorbed by dust. The effect of evolution on $\log(\phi)$ and $\log(\frac{\phi}{L_B})$ is shown in Figs IV.4–IV.5 for the three IMFs and two abundances upto 14 Myr. Fig. IV.6 shows the $B - V$ evolution for IMF2 for the two chosen metallicities. The behaviour for the other two IMFs is similar and is not shown here for the sake of clarity. All the stars in the cluster are assumed to be formed over a very short time (instantaneous burst). For all the IMFs considered only stars younger than 3–4 Myr contribute to the total Lyman continuum luminosity. $\log(\frac{\phi}{L_B})$ evolves slightly slower than $\log(\phi)$ because of slight increase of blue luminosity of the cluster during evolution.
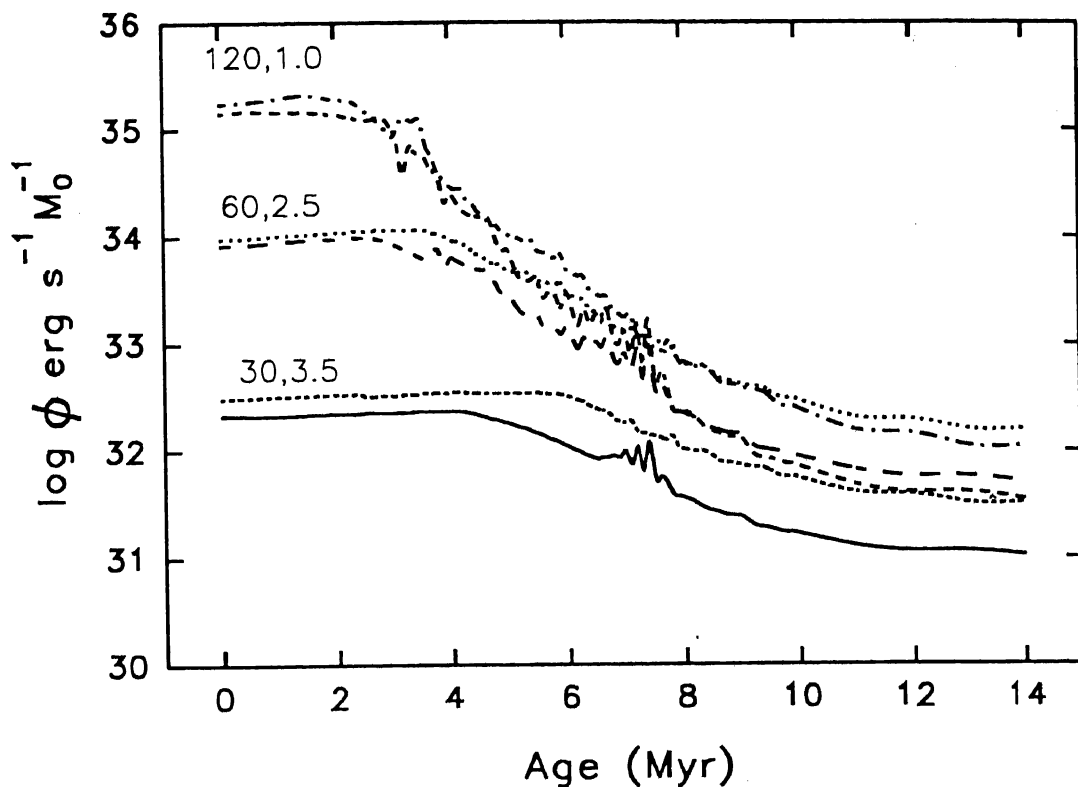
Figure IV.4 Evolution of $\log(\phi)$ upto 14 Myr, for three IMFs (m_u =30, α = 3.5; m_u =60, α =2.5; m_u =120, α =1.0), at two metallicities (Z =0.02 and 0.002). See the caption for Fig. IV.1 for the explanation of line types.

Computations are performed at 0.1 Myr interval upto 8 Myr and 0.2 Myr interval beyond that. These age resolutions are small enough to include effects of short term evolutionary stages such as red supergiants and Wolf-Rayet stars. The appearance of short-term bumps in our diagrams are because of the presence of these stages. The effect is more severe for solar abundance models because of the higher mass loss rates. The exact number of bumps somewhat depends on the mass resolution in the computations. Thus the position and strength of the bumps should not be taken seriously and the presence of these bumps only underlines the uncertainty in the derived quantities once the cluster starts evolving, especially for clusters with small number of massive stars. Models with different IMFs become indistinguishable after 4 Myr, especially at $Z = 0.02$. All the observables computed here are affected by the presence of red supergiants which start appearing at 6 Myr. $\log(\frac{\phi}{L_B})$ decreases faster and $B - V$ and $V - R$ colours become redder at this stage. The affect is less
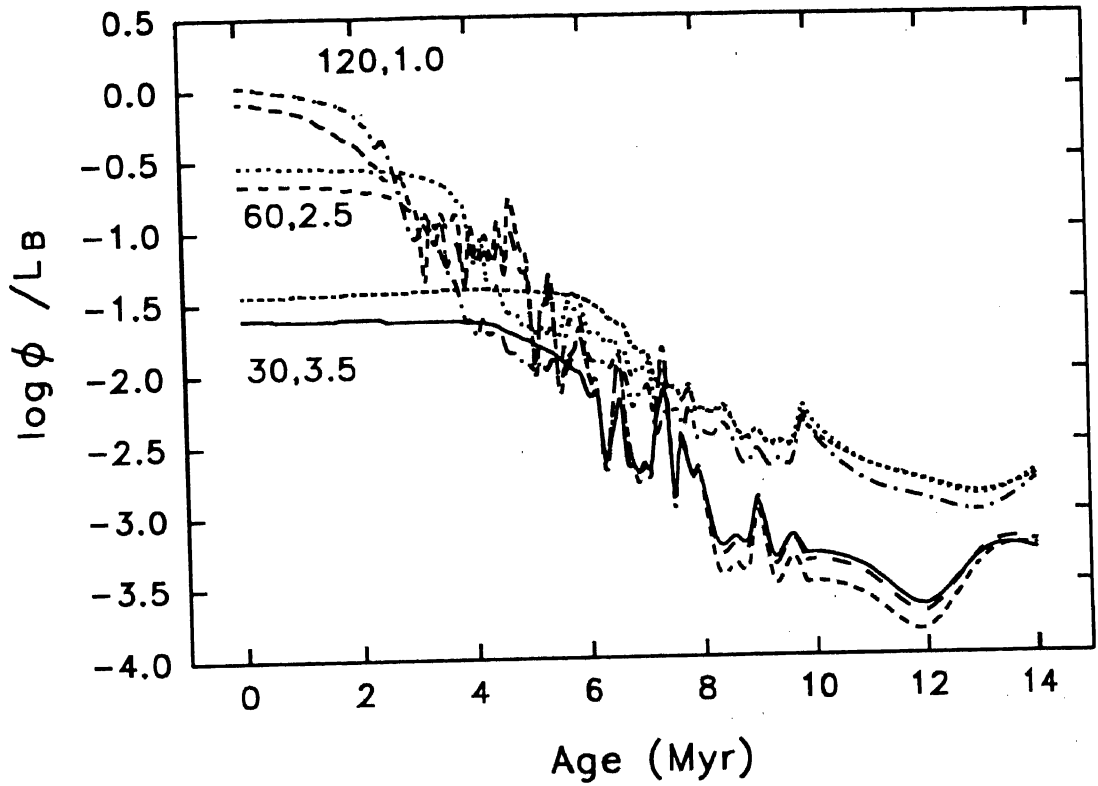
Figure IV.5 Evolution of $\log(\frac{\phi}{L_B})$. See Fig. IV.4 for details.
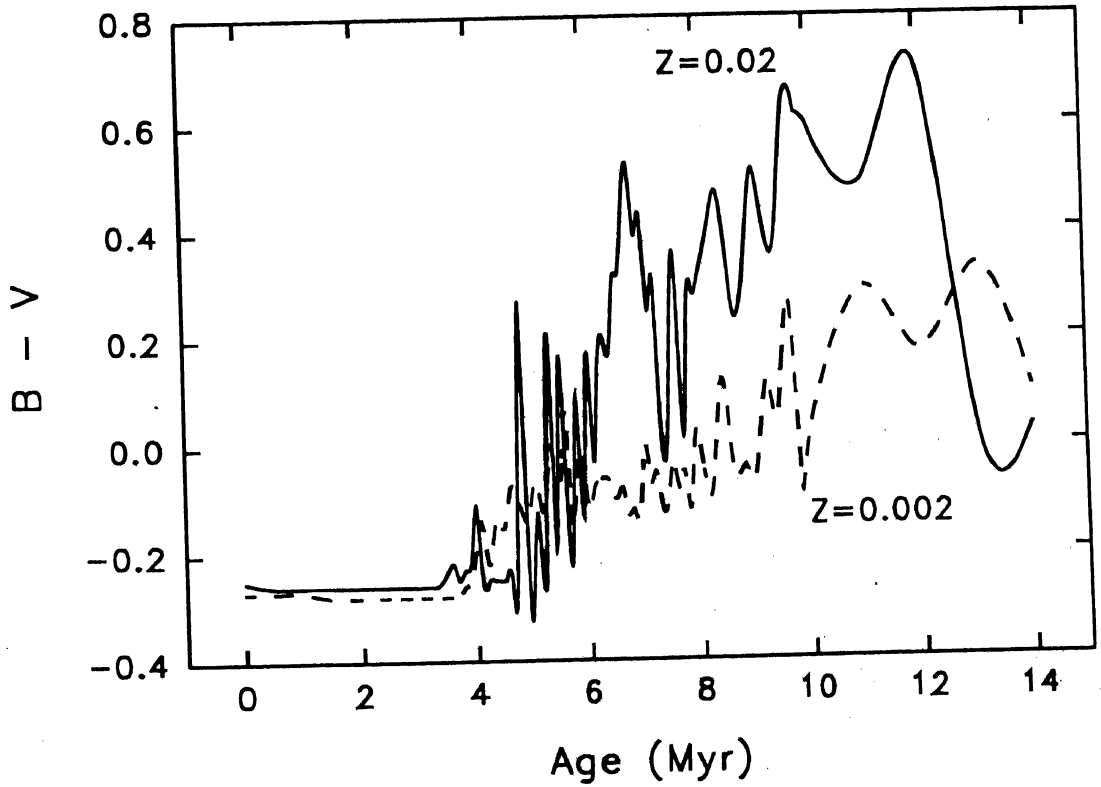
Figure IV.6 Evolution of $B - V$ colour. For the sake of clarity, only one IMF ($m_u = 60$, $\alpha = 2.5$) is shown for $Z = 0.02$ (thick line) and $Z = 0.002$.

severe at lower metallicities.

It is seen that increasing α, decreasing m_u and increasing age, all have the effect of decreasing $\log(\phi)$ and $\log(\frac{\phi}{L_B})$. This is because of a relative decrease of ionizing stars in the cluster. Although at lower abundances the above quantities are slightly higher, it is only a second order effect. Figure IV.7 shows the $\log(\frac{\phi}{L_B})$ vs $B - V$ plot for the three IMFs described above for evolutions upto 14 Myr. The large scatter in $B - V$ is due to the appearance of Red Super Giants after 6 Myr. It can be noticed that the spread is more for IMFs containing more massive stars (IMF3 > IMF2 > IMF1). $V - R$ is shown against $B - V$ in Fig. IV.8 for the same parameters as for the previous figure. Moving diagonally from bottom-left corner to top-right, there is constant decrease of massive stars in the cluster. The presence of scatter in this diagram shows that $V - R$ changes are not strictly correlated with $B - V$ changes. This is because the Red Super Giant phase affects $V - R$ more than $B - V$. Being distance independent both the above figures are important for diagnostics.

1.2 Spectral Evolution of the Cluster

The integrated spectrum of the pure star cluster is computed according to equation (IV.1) at the 342 Kurucz wavelength points. These spectra are shown in the wavelength region 228 Å - 10000 Å for the three IMFs chosen, as Figures IV.9–IV.12. For each IMF, spectra are shown at solar (a) and $0.1\,Z_\odot$ (b) abundances. In Fig. IV.9, we compare the spectra for the three IMFs denoted by 1, 2 and 3 corresponding to IMF1, IMF2 and IMF3 respectively. The spectra become quite distinguishable at the far-uv wavelengths. Fig. IV.10 contains the spectra for IMF1 at 0, 3, 6 and 10 Myr. Figs IV.11–IV.12 contain similar spectra for IMF2 and IMF3 respectively.

All the spectra are normalized to the value at λ 5556 Å and hence the differences seen basically imply differences in $\lambda - V$ colours. The spectral changes during evo-
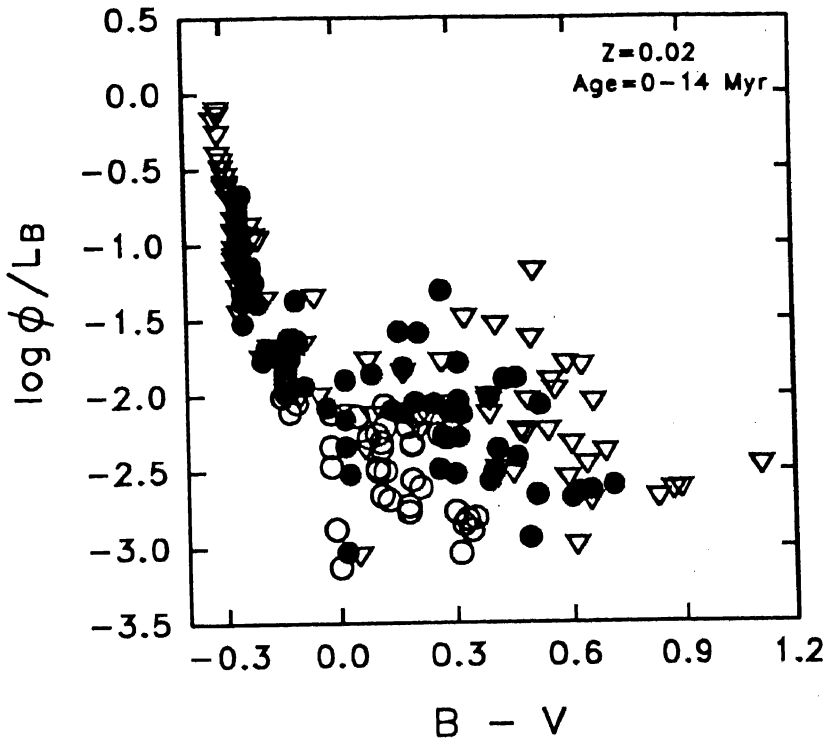
Figure IV.7 Locus of points in $\log(\frac{\phi}{L_B})$ vs $B-V$ diagram as the cluster evolves upto 14 Myr, for the three IMFs. The open circles, filled circles and inverted triangles correspond respectively to IMFs with $m_u =30$, $\alpha = 3.5$; $m_u =60$, $\alpha =2.5$ and $m_u =120$, $\alpha =1.0$.
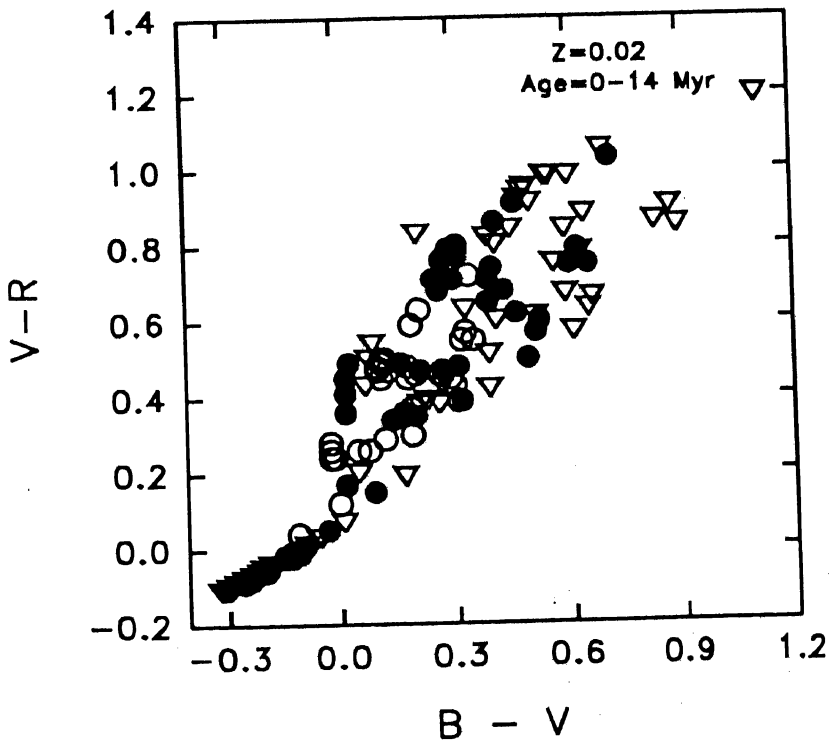
Figure IV.8 Same as Fig. IV.7 but $V-R$ is plotted against $B-V$ colour.
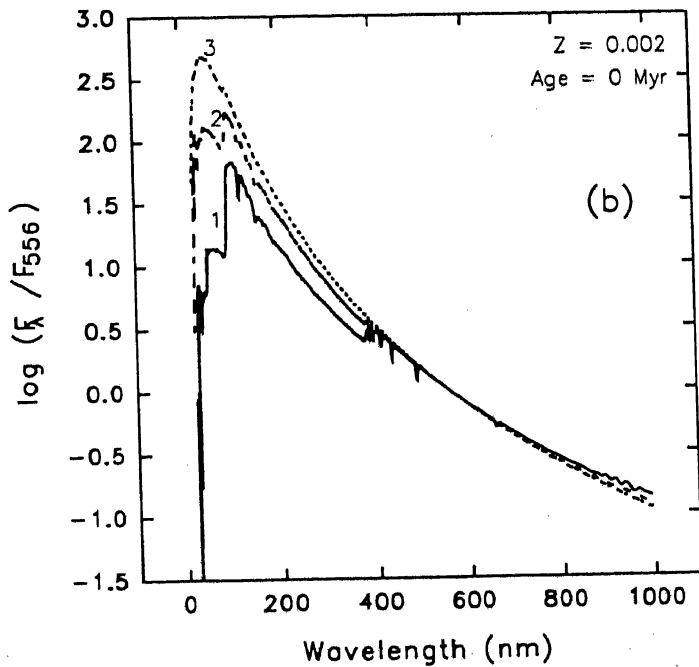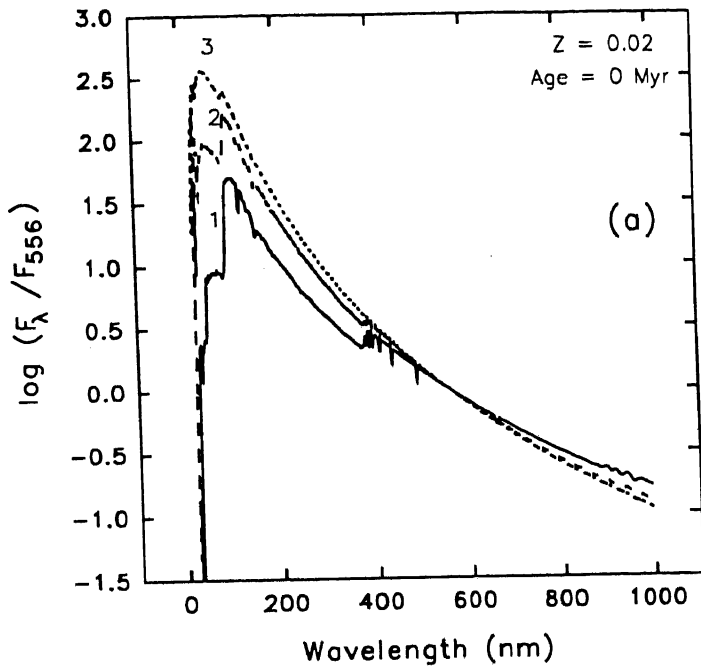
Figure IV.9 Integrated spectra of star clusters for IMFs with $m_u = 30$, $\alpha = 3.5$; $m_u = 60$, $\alpha = 2.5$ and $m_u = 120$, $\alpha = 1.0$ denoted respectively as 1, 2 and 3 on the plots. The spectra are normalized at $\lambda = 5556\text{Å}$. In this figure and in all the subsequent figures, models for solar abundances are denoted by (a) and 0.1 solar abundances by (b).
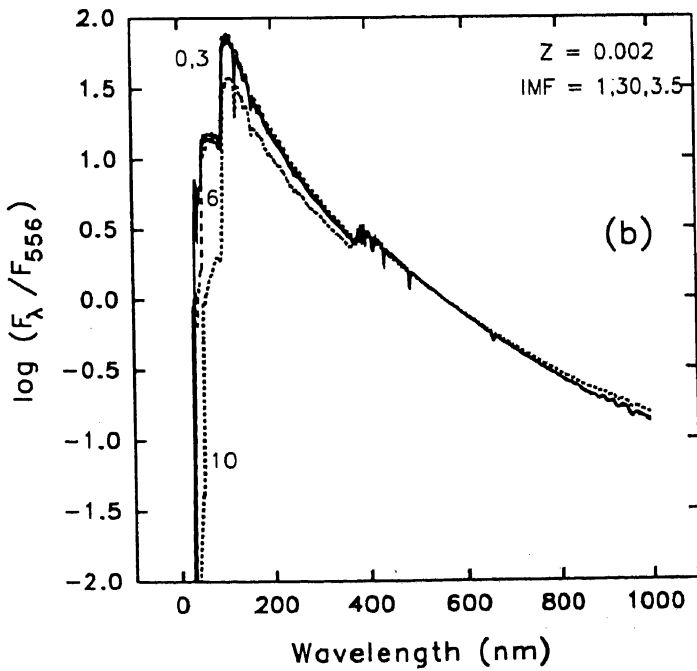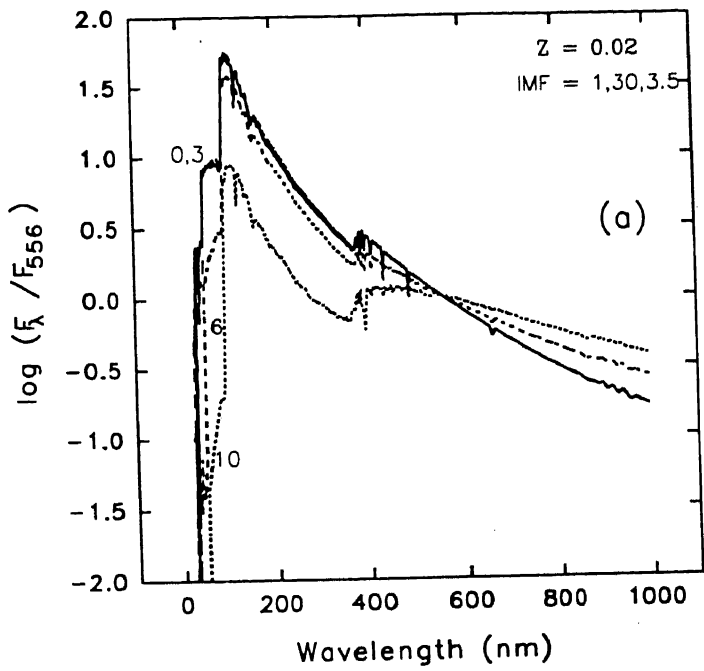
Figure IV.10 Integrated spectra of a star cluster at ages 0, 3, 6 and 10 Myr for IMF with $m_u = 30$ and $\alpha = 3.5$ for $Z = 0.02$ (a) and $Z = 0.002$ (b).
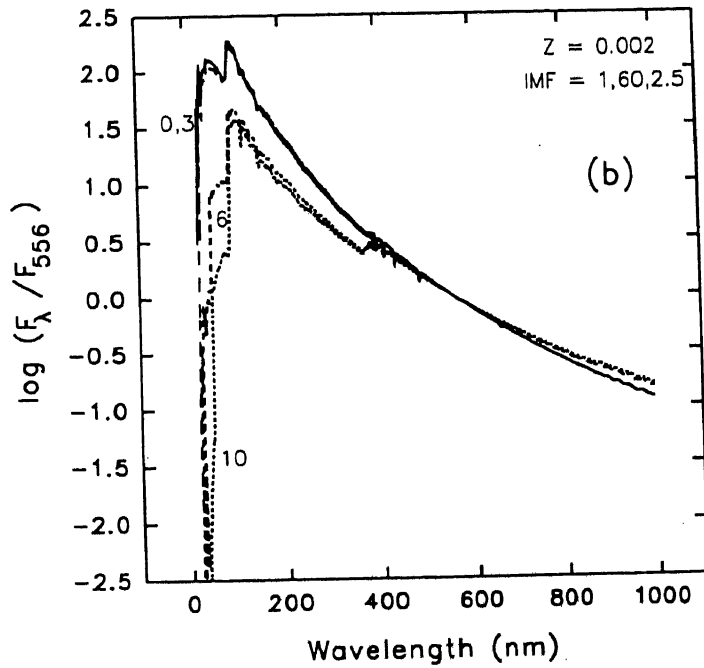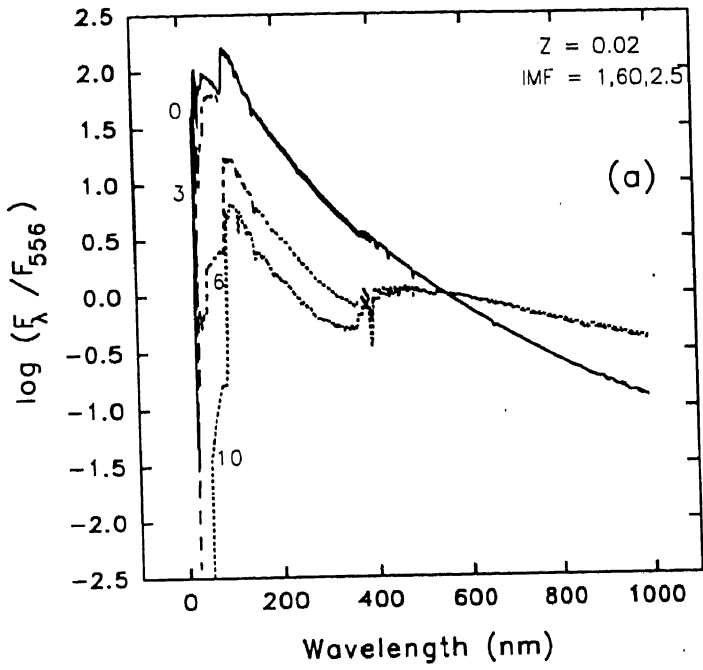
Figure IV.11 Integrated spectra of a star cluster at ages 0, 3, 6 and 10 Myr for IMF with $m_u = 60$ and $\alpha = 2.5$ for $Z = 0.02$ (**a**) and $Z = 0.002$ (**b**).
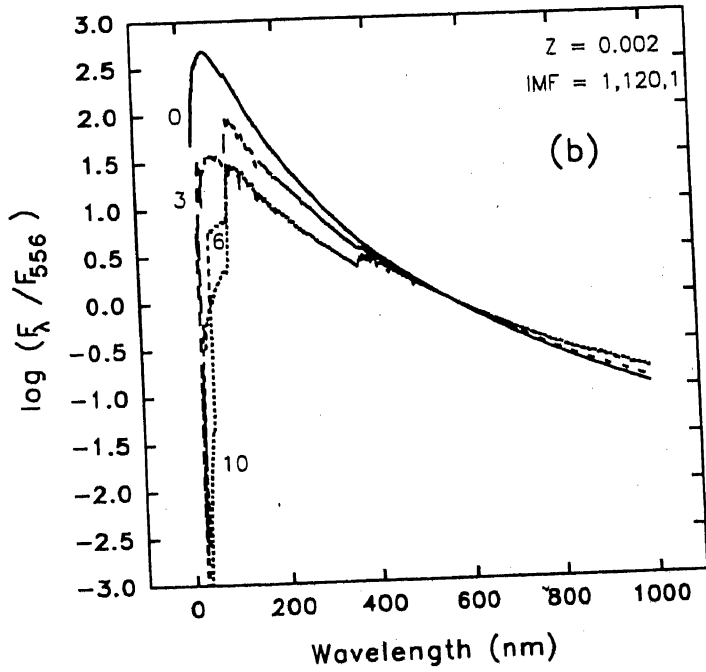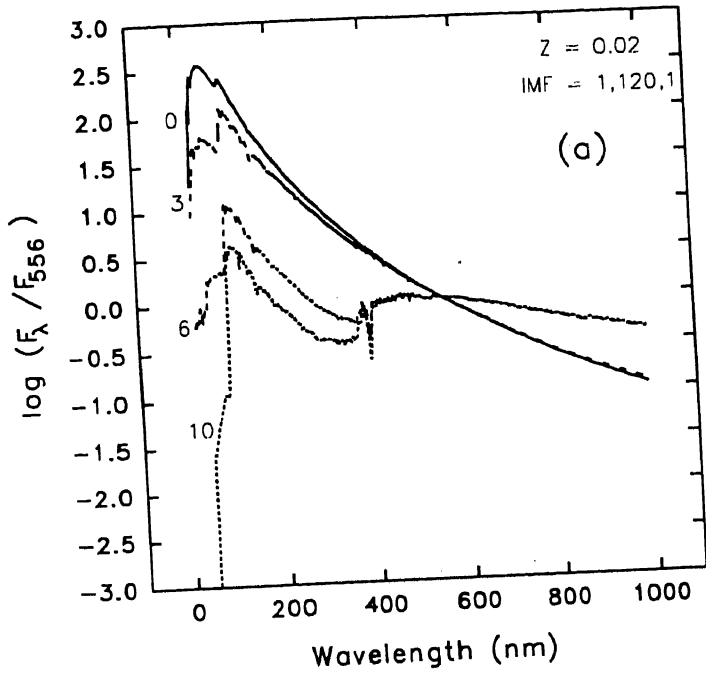
Figure IV.12 Integrated spectra of a star cluster at ages 0, 3, 6 and 10 Myr for IMF with m_u =120 and α =1.0 for Z =0.02 (a) and Z =0.002 (b).
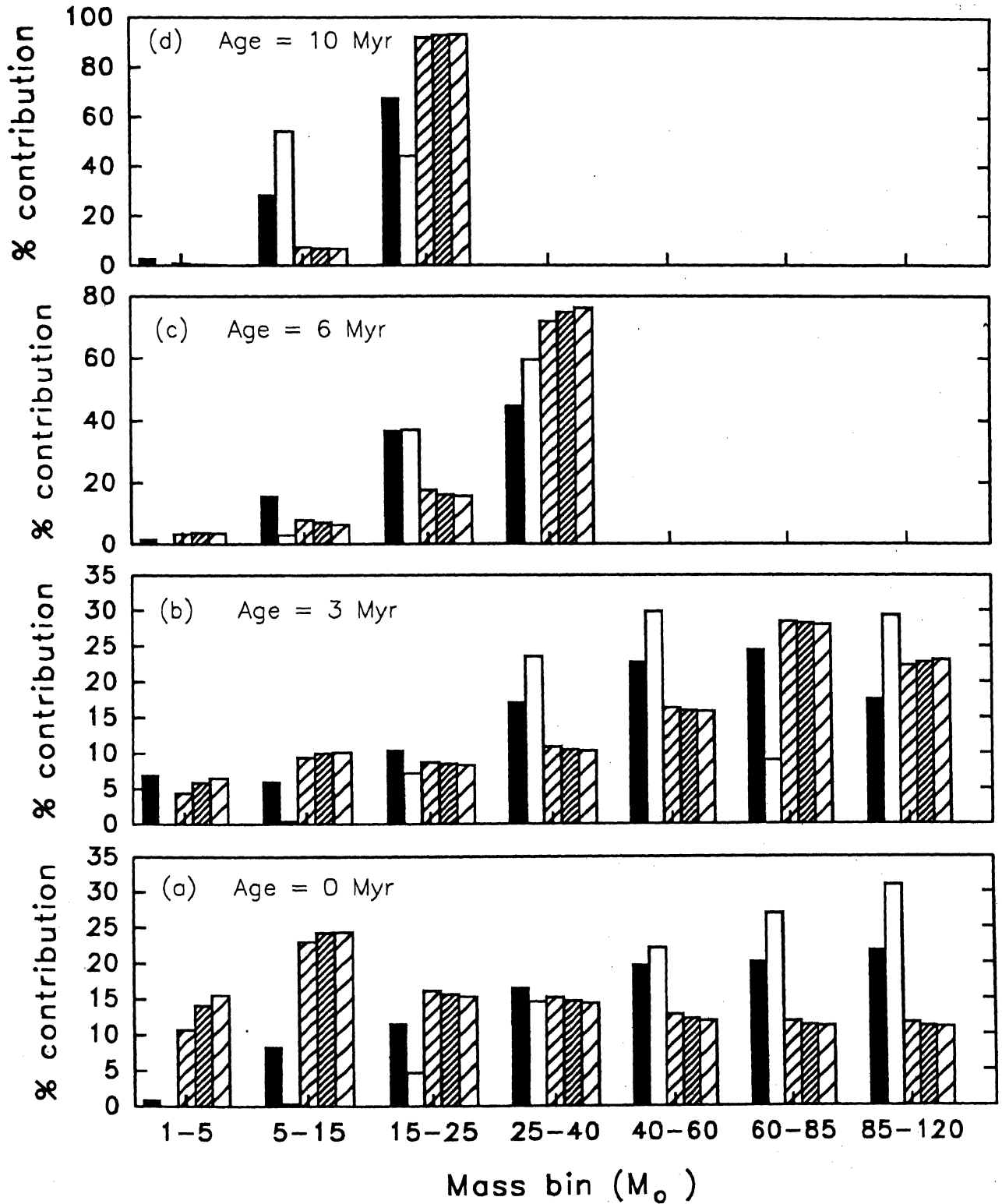
Figure IV.13 Contribution of different mass bins to the Bolometric (solid bars), Lyman continuum (empty bars), Blue band (larger hatching), Visual band (closer hatching) and Red band (medium hatching) luminosities. % contribution at four ages are given in (a), (b), (c) and (d). The IMF chosen is the one having m_u =120 and α =2.5.

lution are more pronounced for solar abundance models. These spectra are purely of stellar origin and do not include the gaseous part; hence they cannot be directly compared with the observed spectra, unless the gas contribution is negligible. Contributions from different mass bins to Bolometric, Lyman continuum, Blue band, Visual band and Red band luminosities as the cluster evolves, are shown as bar diagrams in Fig. IV.13. The IMF chosen is the one with $m_u = 120, \alpha = 2.5$ at solar abundance. At zero age (Fig. IV.13(a)), the main contribution to the Bolometric (solid bars) and Lyman continuum (empty bars) luminosity comes from stars more massive than $40 M_\odot$, while the stars in the mass range 5–15 dominate the optical luminosity (hatched bars). At 3 Myr (b), stars more massive than $25 M_\odot$ dominate all the bands. Notice that at this age, maximum amount of optical luminosity comes from 60–$85 M_\odot$ stars, which contribute little to Lyman continuum luminosity. This is because of the decrease in the effective temperatures of the hot stars as they move away from main sequence towards Blue/Red supergiant branch. The stars in the mass range 85–$120 M_\odot$ have already started their evolution towards left in the H-R diagram after reaching minimum effective temperatures. Beyond this age (Figs c and d), the surviving most massive stars dominate the contribution to all the bands.

1.3 Continuous Star Formation

In the above computations it is assumed that the entire mass is converted into stars in a short time scale. We now investigate the effect of stars being formed continuously. The evolution of $\log(\frac{\phi}{L_B})$ with this model is computed assuming a Constant Star Formation Rate (CSFR) over the period of star formation. Under these assumptions, the Lyman continuum photons will reach an asymptotic value in 3–4 Myr, because dying stars are replaced by new stars. However the stars contributing to blue luminosity live longer and hence there will be accumulation of these stars
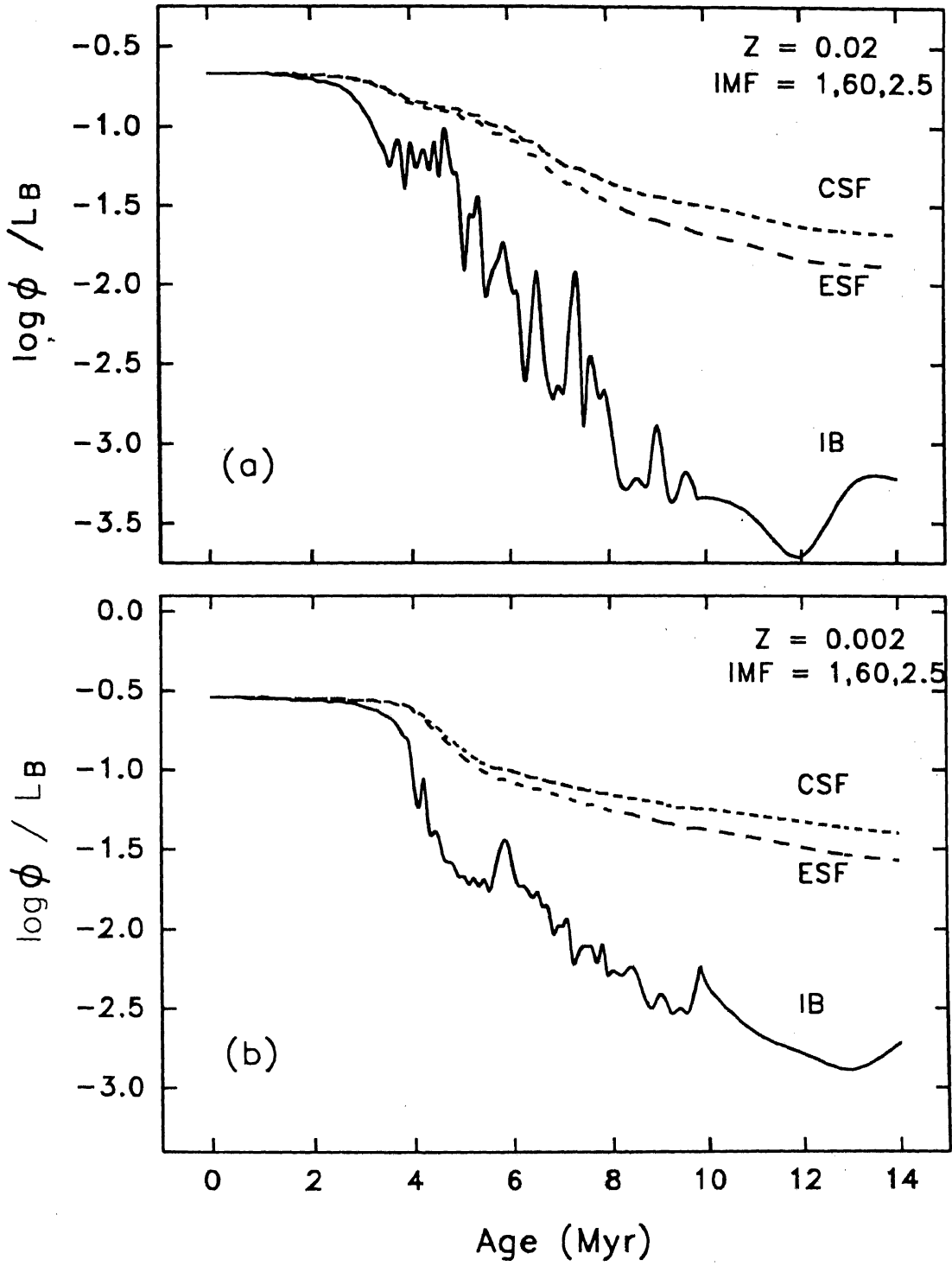
Figure IV.14 Effect of continuous star formation on $\frac{\phi}{L_B}$ for solar (a) and $0.1\,Z_\odot$ (b) models for one of the sample IMFs. The solid line, long dash and medium dash lines correspond to instantaneous star formation, exponentially decreasing star formation ($t_0 = 10$ Myr) and a constant star formation respectively.

with age. Thus compared to an instantaneous burst model, we expect more blue luminosity and hence lower values $\frac{\phi}{L_B}$ at any given age. On the other hand, if the star formation was higher at earlier epochs, and is decreasing exponentially with time with an e-folding time scale of 10 Myr, the results will be intermediate to Instantaneous burst model and CSFR. These effects are shown in Figure IV.14 for one of the IMFs, both at solar (a) and 0.1 $Z_\odot$ (b) abundances. The solid line, long dash and medium dash lines correspond to instantaneous star formation, exponentially decreasing star formation and a constant star formation respectively.

1.4 Statistical Effects on the Derived Quantities

Following the normal approach, we have assumed the stellar masses to be continuous, and have integrated the above equations with a mass step of 0.5 for $m \leq 20$ and 1 for higher masses. The actual observables are expected to asymptotically approach the values derived from the above integrations, as the cluster mass increases. The observed values will be different if the total mass of the cluster is small, because of statistical fluctuations in the stellar masses and numbers. We investigate here the minimum mass required for any IMF, such that statistical fluctuations in star formation does not affect the observable quantities. Two kinds of statistical effects are considered.

Case (i) : Statistical fluctuations in stellar numbers: The entire mass range between 1–120 is binned into equal $\log(m)$ intervals and all the stars in a given bin are assigned the same mass. The relative number of stars in each bin are constrained by the IMF slope. We define the cluster mass $M_{\min}$ when the bin containing the most massive and hence the least number of stars, has only one star. The number of stars in each mass bin are computed for various total masses, each mass being a multiple of $M_{\min}$. The actual number of stars in each mass bin $N(m; imf)$ are computed from a routine which selects the number of stars based on Poissonian statistics,

around the expected number. This gives naturally integral number of stars in each mass bin. The observational quantities are computed using the equations of the following kind instead of Equation (IV.1).

$$L_\lambda(imf; t; z) = \left(\frac{1}{M_T}\right) \sum_{Sp.T.} l_\lambda(m; t; z) N(m; imf) \qquad (IV.7)$$

For a given total mass of the cluster $M_T = n \times M_{min}$, where n is a factor greater than 1 and represents the number of stars in the most massive stellar bin. The observables are computed for 100 trials of $N(m; imf)$. These trials are used to estimate the mean and rms values for all the observables considered in this work. The above exercise is carried out for values of $n = 1, 2, 3, 4, 5, 10, 50$ and 100 for two IMFs. The results are summarised for two of the IMFs in Table IV.3(a). The quantities related to massive stars such as $\log(\phi), H\beta$ equivalent width (not included in the table) are affected more because of statistical fluctuations in stellar numbers. When the mass of the cluster is such that it contains only one O3 type ($M = 120 M_\odot$) star, the rms errors are $\sim 8.5\%$ in Lyman continuum flux and $\sim 3\text{--}4$ % in optical flux. Colours are not affected due to statistical fluctuations, which is expected as the lower mass stars, which are plenty in number, contribute to optical colours. For masses of the cluster $> 50 \times M_{min}$, the rms errors are less than 0.01 dex and the mean values converge to those obtained using continuous mass distribution (last rows in tables denoted by Int).

Case (ii) : Statistical fluctuations in stellar masses : Stellar masses are binned and M_{min} is defined in a manner similar to case (i). The relative number of stars in each bin are constrained by the IMF slope, and are truncated to integral values. Instead of assigning a single mass to the entire bin, here we assume statistical fluctuations of stellar masses within a bin. The actual masses of individual stars in each bin are selected randomly, so as to lie within the mass limits for that bin. Thus in this case, we neglect the Poisson noise on the numbers in each bin, but consider only the random selection of stellar masses. Once the masses of all the stars for a given IMF

141

Table IV.3(a) Effect of statistical fluctuations
in the number of stars.

n	$\log(\phi)$	$\log(\frac{\phi}{L_B})$	$B-V$
IMF : 1,120,1.0	$M_{\min}=910M_\odot$		
1	35.399 ± 0.085	0.178 ± 0.045	-0.318 ± 0.004
2	35.396 ± 0.065	0.177 ± 0.034	-0.318 ± 0.004
3	35.397 ± 0.040	0.179 ± 0.020	-0.319 ± 0.003
4	35.405 ± 0.034	0.183 ± 0.017	-0.319 ± 0.003
5	35.399 ± 0.033	0.178 ± 0.016	-0.318 ± 0.004
10	35.401 ± 0.028	0.181 ± 0.015	-0.320 ± 0.002
50	35.406 ± 0.013	0.184 ± 0.007	-0.320 ± 0.000
100	35.409 ± 0.009	0.186 ± 0.005	-0.320 ± 0.000
Int	35.400	0.180	-0.320
IMF : 1,120,2.5	$M_{\min}=16115M_\odot$		
1	34.474 ± 0.085	-0.143 ± 0.055	-0.280 ± 0.005
2	34.476 ± 0.061	-0.135 ± 0.040	-0.280 ± 0.002
3	34.469 ± 0.051	-0.140 ± 0.031	-0.280 ± 0.002
4	34.467 ± 0.044	-0.141 ± 0.028	-0.280 ± 0.002
5	34.460 ± 0.043	-0.146 ± 0.028	-0.280 ± 0.000
10	34.466 ± 0.026	-0.141 ± 0.016	-0.280 ± 0.000
50	34.467 ± 0.011	-0.140 ± 0.008	-0.280 ± 0.000
100	34.466 ± 0.008	-0.142 ± 0.006	-0.280 ± 0.000
Int	34.470	-0.150	-0.280

Table IV.3(b) Effect of statistical fluctuations
in the mass of stars.

n	$\log(\phi)$	$\log(\frac{\phi}{L_B})$	$B-V$
IMF : 1,120,1.0	$M_{\min}=910M_\odot$		
1	35.403 ± 0.021	0.181 ± 0.010	-0.320 ± 0.000
2	35.400 ± 0.017	0.180 ± 0.009	-0.320 ± 0.000
3	35.407 ± 0.013	0.184 ± 0.007	-0.320 ± 0.000
4	35.403 ± 0.012	0.182 ± 0.007	-0.320 ± 0.000
5	35.408 ± 0.009	0.184 ± 0.006	-0.320 ± 0.000
10	35.404 ± 0.007	0.182 ± 0.005	-0.320 ± 0.000
50	35.407 ± 0.004	0.180 ± 0.002	-0.320 ± 0.000
100	35.409 ± 0.003	0.180 ± 0.001	-0.320 ± 0.000
Int	35.400	0.180	-0.320
IMF : 1,120,2.5	$M_{\min}=16115M_\odot$		
1	34.487 ± 0.027	-0.132 ± 0.019	-0.280 ± 0.000
2	34.484 ± 0.017	-0.134 ± 0.011	-0.280 ± 0.000
3	34.488 ± 0.013	-0.131 ± 0.009	-0.280 ± 0.000
4	34.485 ± 0.011	-0.133 ± 0.008	-0.280 ± 0.000
Int	34.470	-0.150	-0.280

are established, the obervables are computed by summing over all these masses. Rest of the analysis is very similar to case (i) and the Table IV.3(b) contains the results. In this case, when there is just one O3 star, the maximum errors on the derived quantities are 2% only.

Thus the observed quantities of GEHRs, which typically contain more than several thousands of solar masses in stars, are not affected by statistical fluctuations.

2. Computations of Nebular Flux

Ultraviolet photons from hot stars in the cluster ionize the surrouding gas leaving hydrogen, helium, oxygen, nitrogen, carbon and other astrophysically abundant elements in different ionized states. Most of these ionizing photons are used up by hydrogen, and at equilibrium, every ionization is followed by recombinations to one of the levels in the hydrogen atom (Osterbrock 1989). Energy input to the nebula in the form of kinetic energy of the electrons is lost due to collisions and radiative recombinations, leaving the nebula at a fixed temperature, once the thermal equilibrium is reached. This heated gas along with the ions at various excited states gives rise to a spectrum, characteristic of H II regions. The basic physics governing the emission mechanism from these regions is well understood and hence theoretical spectrum of such a region can be synthesized from only a few input parameters such as temperature, density, abundance of elements and absolute flux in one of the Balmer lines. In the next two subsections, we describe these emission mechanisms briefly.

2.1 Estimation of the Gaseous Continuum

The main emission mechanisms contributing to continuum emission from a gas are free-free, free-bound, and two-photon ($2q$) emissions from Hydrogen and Helium. The net emission coefficient γ_{eff} can be expressed as a sum of these emission coef-

ficients, weighted by the relative abundance of the particular ionized state.

$$\gamma_{\text{eff}} = \gamma(\text{H I}) + \gamma(2\text{q}) + \frac{n(\text{He}^+)}{n(\text{H})}\gamma(\text{HeI}) + \frac{n(\text{He}^{++})}{n(\text{H})}\gamma(\text{HeII}) \qquad (\text{IV.8})$$

In our computations we assume a helium abundance of 10% by number all of which is in the singly ionized state. Individual γ's computed and tabulated by Brown and Mathews (1970) are used here. The continuum intensity in erg cm^{-2}s^{-1}Å^{-1} at a wavelength λ is related to γ_{eff} as ,

$$I_\lambda = \gamma_{\text{eff}}\left(\frac{c}{\lambda^2}\right)\left(\frac{1}{\text{E}_{\text{H}\beta}\alpha_{\text{H}\beta}^{\text{eff}}(\text{H}^0, T_e)}\right) I_{\text{H}\beta}. \qquad (\text{IV.9})$$

$\text{E}_{\text{H}\beta}$ is the energy of the Hβ photon, $\alpha_{\text{H}\beta}^{\text{eff}}(\text{H}^0, T_e)$ is the Hβ recombination coefficient and $I_{\text{H}\beta}$ is the Hβ line flux in erg cm^{-2}s^{-1} .

2.2 Estimation of the Gaseous Emission line Strengths

Osterbrock (1974, 1989) has compiled the emission line stregths of various lines of hydrogen and helium relative to Hβ line strength for typical densities and temperatures of H II regions. The strength of emission lines from other elements, however are dependant on the relative abundance of the elements and the ionization and temperature structure of the nebula and hence need detailed modelling. Such models are constructed by Dopita and Evans (1986), Rubin (1985), McCall, Rybsky and Shields (1985) among others. From observations of a large sample of extragalactic H II regions McCall, Rybsky and Shields (1985) have shown that the majority of the emission line ratios can be parametrised by a single parameter, namely $\frac{\text{I}([\text{O II}]\lambda\,3726)+\text{I}([\text{O III}]\lambda\,5007)}{\text{I}(\text{H}\beta)}$. The basic physics behind this can be summarized as follows. The cooling of the nebula is mainly controlled by the radiative losses in oxygen ions, which constitute more than 45% (Lequeux et al. 1979) of metallic mass. This gives rise to an anti-correlation between oxygen abundance and nebular temperature. On the other hand most of the oxygen in GEHRs is in singly ([O II])

and doubly ([O III]) ionized states, both of which have bright emission lines in the optical region ([O II] λ 3726, [O III] λ 5007). Oxygen abundances can be quite accurately estimated using one or both of these lines. The observed correlations of line ratios of other elements with oxygen abundance suggests that the relative abundances of other elements such as C, N and S do not vary much from region to region. Photoionization models are successful in reproducing the observed correlation between line ratios and oxygen abundance, which can be used to predict the line ratios from a knowledge of oxygen abundance alone.

Our interest here is to estimate the line contribution to BVR band fluxes. The computations of McCall, Rybsky and Shields (1985) are used for this purpose. We considered only the bright lines of N, O and S apart from hydrogen lines in our calculations. Their tables 15 and 12 help us to estimate the oxygen abundance from the strengths of [O II] λ 3726 and [O III] λ 5007 lines, which in turn is used to estimate the strength of various lines from other elements.

3. Comparison with Other Models

Currently a number of models exist, which synthesize the cluster parameters at one or the other wavelength band. Among these, the most suitable model for comparison with our results is from Mas-Hesse and Kunth (1991). We compare our results with their Tables 6(a), 6(e), 7(a) and 7(b). The quantities compared are the total monochromatic luminosities from the cluster+gas and % contribution of the gas to the total luminosities at 2 Myr for solar and 0.1 solar abundances. Hβ luminosities and equivalent widths are also compared. The IMF chosen for comparison is the one with $m_l = 2$, $m_u = 120$ and $\alpha = 2.0$. In their model, Mas-Hesse and Kunth (1991) have assumed that only 70% of the available lyman continuum photons are used up for ionization. We have taken this into account in our comparison. The results of the comparisons are given in Figs IV.15–IV.16. Figs IV.15(a) and (b)

145
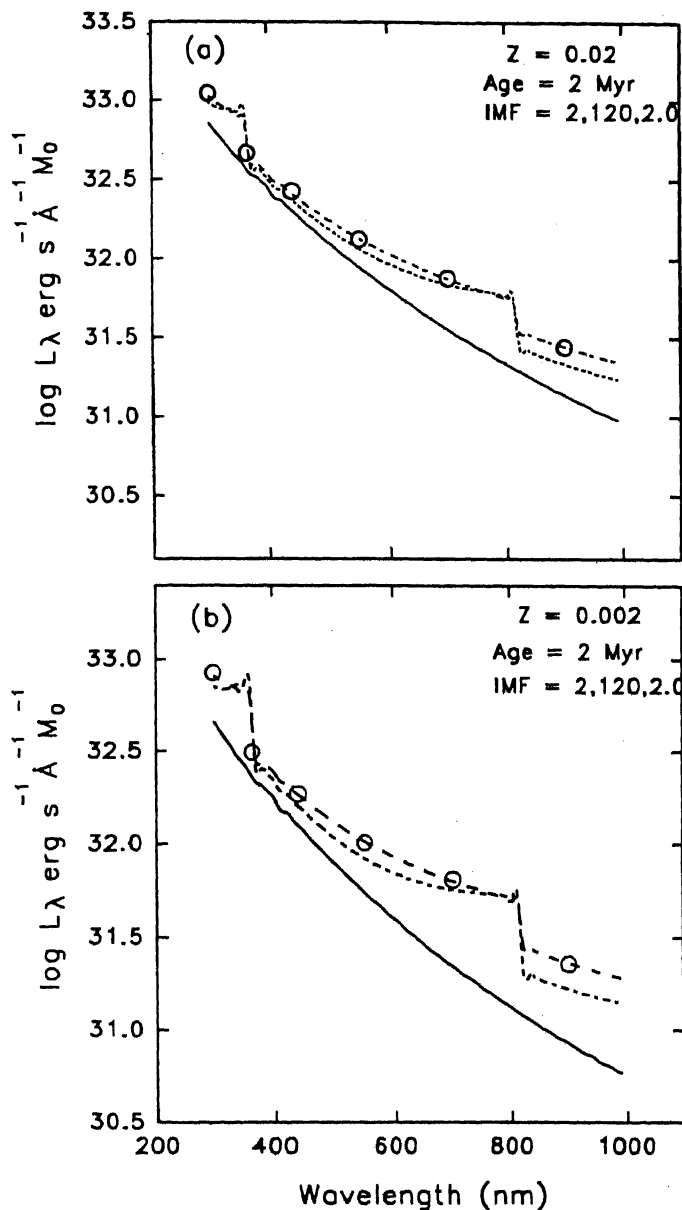
Figure IV.15 Comparison of our spectra with monochromatic luminosities from Mas-Hesse and Kunth (1991), for an IMF, with $m_l = 2$, $m_u = 120$ and $\alpha = 2.5$ at 2 Myr, at $Z_\odot$ **(a)** and $0.1 Z_\odot$ **(b)** abundances. Solid line is the pure cluster spectrum, while the long dashed and medium dashed lines are after adding the continuum gas spectra at 10000 K and 5000 K respectively. The circles represent the values from Table 6(a) and (e) of Mas-Hesse and Kunth (1991).

show the total cluster spectrum between 3000Å and 10000Å at solar and 0.1 solar abundances. Thick line shows the pure cluster spectrum, whereas the long-dashed and medium-dashed lines show the total cluster spectrum after adding the contribution from gaseous continuum at 10000° and 5000° K respectively. The circles represent the values from Mas-Hesse and Kunth (1991) Table 6(a) and (e). The addition of the gaseous continuum at 10000° K agrees within 0.05 dex at all the wavelengths. In Figs IV.16(a) and (b), the fractional contribution of the gas to the total continuum is compared with Mas-Hesse and Kunth values. The thick line corresponds to the gas at 10000 K and dotted line at 5000 K. As before, the circles are from Mas-Hesse and Kunth.

Again agreement is quite good confirming that there is no zeropoint or any other shifts between our and Mas-Hesse and Kunth's computations for cluster as well as nebular quantities. It should be remembered that our spectra and luminosities are based on Kurucz (1979) models for each stellar mass, whereas Mas-Hesse and Kunth used observed spectra for each spectral type. Also Mas-Hesse and Kunth used Maeder's earlier models (Maeder and Meynet 1987, 1989). Thus the good agreement suggests that model spectra from Kurucz are as good as typical observed spectra and that Maeder's different models do not change the integrated cluster properties significantly, at least for the first 2 Myr.

4. Summary

A GEHR in the model is assumed to be a gaseous nebula with an embedded star cluster. The star cluster is defined completely by (i) IMF (m_l, m_u, α), (ii) age (t) (iii) metallicity (Z) and (iv) total mass (M_T). The parameter space studied are $m_l = 1, m_u = 30, 60, 120, \alpha = 0.5$-$3.5, t = 0$-$14$ Myr, $Z = 0.002, 0.02$ and $M_T = 1$. Two kinds of star formation events are considered. In the first one all the stars in the cluster are assumed to have formed over a short time scale (Instantaneous
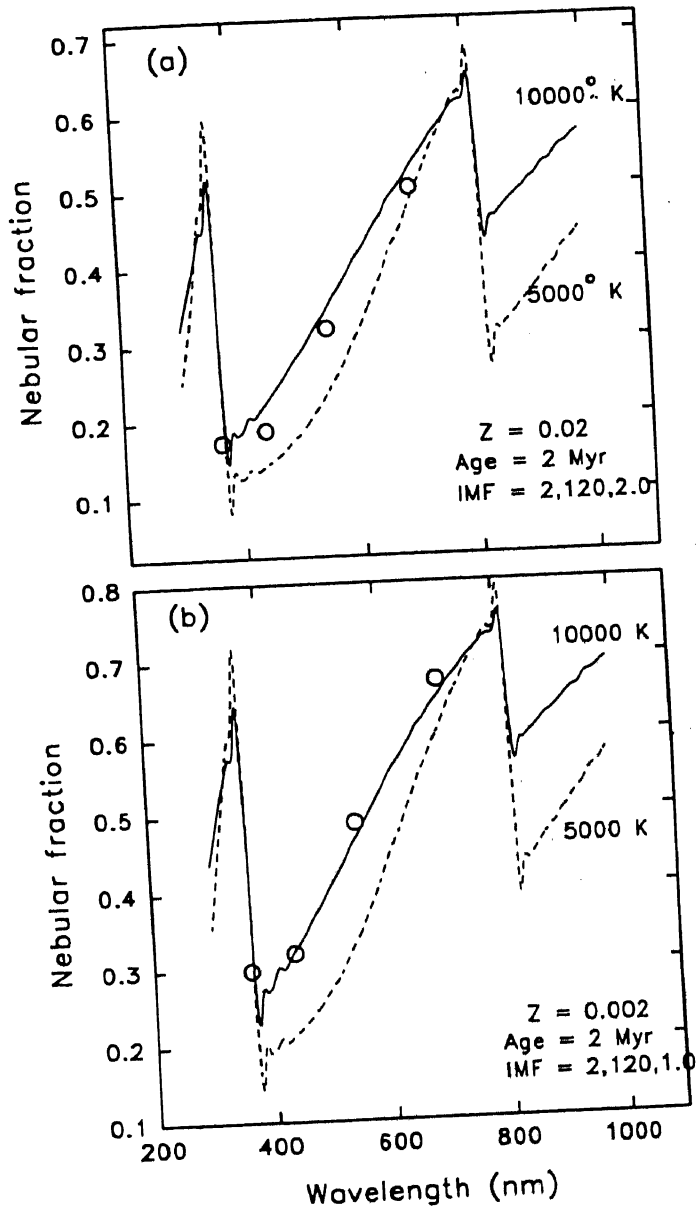
Figure IV.16 Fractional nebular contribution to the total continuum for the same cluster parameters as for Fig. IV.15. The thick line corresponds to the gas at 10000 K and dotted line at 5000 K. Circles are from Table 7(a) and (b) of Mas-Hesse and Kunth.

Burst), while in the second case the cluster stars are assumed to have formed over a period of time, either at a constant or an exponentially decreasing rate. Maeder's (1990) evolutionary models which include the effects of mass loss and convective core overshooting are used along with Kurucz (1979) atmosphere to synthesize the model spectrum and luminosities over BVR bands and Lyman continuum. The results are presented in Table IV.2 and Figs IV.1–IV.14. The ratio of Lyman continuum to Blue band luminosity $\frac{\phi}{L_B}$ is found to be sensitive to IMF changes for ages less than 4 Myr. Beyond this age, the computed quantities are highly affected because of the short-term evolutionary effects due to RSG/WR phases of massive stars. The effect is more at solar and higher abundances. The appearence of RSGs at around 6 Myr makes the $B - V$ and $V - R$ colours redder. The derived quantities are more sensitive to changes in IMF parameters and ages compared to changes in metallicities, before the massive stars in the cluster start evolving. The effect on the derived parameters due to any statistical fluctuations in the number and masses of the individual stars are also discussed. For GEHRs with $\log L(H\alpha) > 39.00$ erg s^{-1}, the statistical effects are found to be negligible. Gaseous continuum in the optical region is computed using the tables of Brown and Mathews (1970). Cluster+gas continuum spectrum is compared with that of Mas-Hesse and Kunth (1990) for one of the IMFs. The agreement is found to be within 0.05 dex.

V. PHYSICAL PROPERTIES OF GEHRs

The parameters involving star formation are derived by comparing the observational data in selected bands with the models described in the last chapter. The number of parameters needed to fully define an H II region are large compared to the number of observables and hence it is essential to fix a few of the parameters at values assumed to be typical, and vary only those which are more sensitive to observables. The number of free parameters can be reduced by choosing diagnostic diagrams involving dimensionless ratios such as colours and equivalent widths. This eliminates the errors due to our insufficient knowledge regarding the total mass of stars involved in the star formation event resulting from the uncertainties in absolute photometry, uncertainty in the distance estimate to individual galaxies *etc.* Among the various parameters, the observed quantities in the optical region are more sensitive to age, slope(α) and upper cut-off mass (m_u) of the Initial Mass Function (IMF). The evolutionary change in the observational quantities is neglegible for the first three million years and hence for young systems, α and m_u are the only free parameters. On the other hand IMF differences become insignificant for clusters older than ~ 4 Myr. Thus IMF can be determined only for younger clusters. For older systems the derived ages are independent of IMF parameters.

We use our $BVRH\alpha$ photometry to form $B - V$, $V - R$ colours and $\log(\frac{\phi}{L_B})$, the ratio of equivalent Hβ to B band luminosity. $\log(\frac{\phi}{L_B})$ vs $B - V$ serves as the main diagnostic diagram in our analysis. The lower cut-off of the IMF, which least affects the above diagnostic diagram is fixed at $m_l = 1$ (as in the previous chapter all masses are expressed in terms of solar mass $M_\odot$). However derived masses are very sensitive to the choice of m_l and increase by an order an magnitude for $m_l = \cdot 1$ Most of the observed regions have metallicities close to solar or a few times more, and hence only solar models are used in our comparisons. Thus we have three

parameters, namely upper cut-off mass (m_u), slope (α) of the IMF and age to be determined.

1. Treatment of Observational Data

About one fourth of the regions (45 out of 180) in our catalogue (Table III.4) have published spectroscopic data. Such regions are selected for a more detailed analysis. Out of these some regions are dropped if the photometric quality index is 4 (background uncertainties leading to errors in excess of 0.3 mag in $B - V$ and $V - R$ colours). The selection criterion of rms error on an individual measurement is < 0.15 mag in colours and 0.05 dex in $\log(\frac{\phi}{L_B})$ left us with 5 regions in NGC 1365, 3 in NGC 2903, 14 in NGC 2997, 2 in NGC 3351, 3 in NGC 4303 in addition to the giant H II complex NGC 2363 in NGC 2366 and the starburst nucleus of NGC 5253. Measurements using bigger apertures, which include more than one emitting knot, are also included around seven regions in NGC 2997.

The spectroscopic data involving [O III] and Balmer lines are used to estimate the abundance of oxygen, electron temperature (T_e) and visual extinction (A_v) (McCall, Rybsky and Shields 1985). All the observed quantities have to be corrected for the interstellar extinction before comparing with the models. Total extinction towards extragalactic H II regions consists of three parts — (i) extinction from the interstellar medium (ISM) of our galaxy (A_v(gal)), (ii) extinction from the ISM of the parent galaxy outside the H II region and (iii) extinction due to the dust mixed with the gas within the H II region. A_v(gal) values for the programme galaxies are given in Table III.1. The extinction derived from Balmer decrement contains contribution from all the components. Large spread in the extinction values for regions within a single galaxy implies non-uniform distribution of dust within the parent galaxy, either within or outside the H II region. There have been some studies investigating the relative contribution of the dust mixed with

151

the ionized gas, known as 'internal extinction', to the total extinction from the parent galaxy (Lequeux *et al.* 1981). These studies show the internal extinction to be non-negligible at least for some regions. The extinction values as derived using radio thermal continuum (see Appendix A) is statistically known to be higher than that derived from Balmer decrement (Israel and Kennicutt 1980). Caplan and Deharveng (1986) have studied the effect of different dust configurations, including the dust internal to the H II regions to explain the observed discrepancy between the radio and optically derived extinction values. Internal reddening is found to be significant for some regions in LMC. Since the presence of internal dust complicates the extinction corrections (Mathis 1983), it is conventional to neglect the effects of internal dust and use the extinction values derived from Balmer decrement in most of the applications. We follow this method for gaseous emission and propose a better prescription for clusters embedded in GEHRs.

The Hα band fluxes have contribution also from [N II] 6548, 6583 Å. The observed fluxes in this band are corrected for interstellar extinction using A_v values derived from Balmer decrement and galactic extinction curve (Seaton 1979). Hα fluxes are computed from the observed Hα+ [N II] fluxes using the spectroscopically derived [N II]/Hα ratios. Lyman continuum luminosities are derived from Hα luminosities using Equation I.1, which assumes an ionization bounded case B nebula (Osterbrock 1989). Equivalent Hβ luminosity (ϕ) is computed from this using Equation IV.6.

The treatment of broad band magnitudes is slightly different. First an estimation of the contribution of the gas (line + continuum) within each band is made based on the extinction corrected Hα luminosity, following the methods described in the previous chapter. The resultant quantities represent pure cluster quantities but for the correction for interstellar extinction. We denote these quantities by a subscript *, and refer as 'undereddened', while the observed quantities are denoted

by the subscript 'obs' (*e.g.* $(B-V)_{obs}$, $(B-V)_*$ *etc.*). The resultant quantities are corrected for galactic and total extinction using $A_v(gal)$ and $A_v(Bal)$ and denoted by suffixes 1 and 2 respectively. The process is summarised below.

$$(B-V)_{obs}- \text{ gas subt } \longrightarrow (B-V)_*,$$

$$(B-V)_*- A_v(gal) \longrightarrow (B-V)_1,$$

$$(B-V)_*- A_v(Bal) \longrightarrow (B-V)_2,$$

Table V.1 contains the results on individual H II regions. Galaxy identification is given in column 1. Column 2 contains identification numbers for GEHRs following Chapter III. Oxygen abundances in column 3 are derived from $([O\,II]+[O\,III])/H\beta$ ratio using the semi-emperical calibration of McCall, Rybsky and Shields (1985). These authors also provide relation between oxygen abundance and electron temperature, which is used to derive T_e given in column 5. Column 4 lists the visual extinction based on Balmer decrement. Oxygen abundance and visual extinction are based on the sources of spectroscopic data listed in Table III.1. V magnitude, $(B-V)_*$ and $(V-R)_*$ colours in columns 6–8 are undereddened pure cluster quantities. Lyman continuum luminosity is given in column 9. Column 10 contains $\log(\frac{\phi}{L_B})_*$ values.

2. Comparison with Models

We have plotted in Fig. V.1 the values of $\log(\frac{\phi}{L_B})_1$ against $(B-V)_1$, which are corrected only for galactic extinction. H II regions from different galaxies are shown by different symbols, as indicated at the right. Small and large aperture measurments are distinguished in the case of NGC 2997. Maximum errors on the plotted quantities are indicated by the cross at the top-left corner of the diagram. The effect of cluster evolution on the observed quantities is denoted by the solid curve, with the reddest point on the curve corresponding to 7 Myr.

Table V.1 Derived properties of H II regions.

NGC	No	$12 + \log \frac{O}{H}$	A_v	T_e	V_*	$(B-V)_*$	$(V-R)_*$	$\log(N_L)$	$\log(\frac{\phi}{L_B})_*$
1	2	3	4	5	6	7	8	9	10
1365	1	9.13	0.91	6000	16.88	0.11	0.11	51.15	-1.24
	2	9.20	1.07	5626	15.90	0.10	0.28	51.63	-1.15
	3	9.11	0.86	6083	17.10	0.17	0.20	51.10	-1.18
	4	9.20	1.10	5627	16.39	0.20	0.21	51.19	-1.36
	5	9.13	0.96	6014	16.28	0.32	0.17	50.83	-1.71
2366	1	8.06	0.45	12180	14.53	-0.31	0.12	51.96	-0.67
2903	1	9.29	1.97	5153	17.54	0.25	0.93	51.68	-0.38
	2	9.26	0.29	5317	16.97	-0.11	0.61	51.23	-1.21
	13	9.37	2.39	4671	16.91	0.02	0.81	51.23	-0.33
2997-NE	1	9.18	2.13	5726	17.75	0.11	0.85	51.65	-0.39
	2	9.29	1.58	5129	18.21	0.16	0.36	51.00	-0.84
	7	9.25	1.90	5369	18.83	0.06	0.32	50.66	-0.97
	9	9.29	1.30	5124	19.25	0.02	0.52	50.66	-0.99
	10	9.32	1.33	5000	17.53	0.03	0.28	50.93	-1.23
	12	9.30	1.60	5100	18.59	0.11	0.42	50.80	-0.90
	13	9.22	1.81	5510	18.96	0.04	0.21	50.50	-1.09
	14	9.22	1.81	5510	19.17	0.16	0.34	50.14	-1.31
	15	9.22	1.81	5510	19.79	0.36	0.58	50.66	-0.35
	24	9.17	1.40	5771	18.24	0.13	0.22	50.52	-1.32
	34	9.21	2.43	5537	17.71	0.28	0.53	51.16	-0.83
	G1	9.19	2.24	5637	15.88	0.28	0.50	52.22	-0.50
	G2	9.25	2.00	5362	17.08	-0.01	0.55	51.50	-0.86
	G3	9.30	1.38	5090	18.18	0.13	0.44	50.89	-0.98
	G4	9.31	1.81	5033	17.77	0.02	0.81	51.55	-0.52
	G5	9.19	2.09	5650	17.92	0.16	0.43	51.49	-0.46
	G6	9.34	2.37	4830	18.23	0.09	0.02	51.14	-0.72
	G8	9.21	2.43	5537	16.55	0.15	0.62	51.56	-0.95
2997-SW	1	9.34	1.63	4821	17.32	0.50	0.59	51.11	-0.95
	3	9.29	2.15	5136	17.49	0.27	0.70	51.71	-0.36
	5	9.30	2.04	5084	16.42	0.30	0.48	51.59	-0.91
3351	1	9.50	1.75	3921	17.60	-0.05	0.38	50.74	-1.27
	2	9.42	1.97	4374	14.63	0.54	0.61	51.65	-1.31
4303	4	9.21	0.43	5526	16.12	0.11	0.52	52.06	-1.18
	9	9.35	0.86	4795	16.57	0.21	0.46	51.74	-1.29
	24	9.33	0.43	4927	16.56	0.16	0.36	51.52	-1.53
5253	1	8.37	0.95	10410	13.75	0.11	0.13	51.56	-0.69

Table V.1 Continued.

NGC	No	$(B-V)_3$	$(V-R)_3$	$\log(\frac{\phi}{L_B})_3$	$\log(M_T)^\dagger$
1	2	11	12	13	14
1365	1	−0.11	−0.06	−1.59	5.32
	2	−0.15	0.09	−1.55	5.80
	3	−0.04	0.04	−1.51	5.27
	4	−0.05	0.02	−1.77	5.36
	5	0.09	0.00	−2.08	5.00
2366	1	−0.44	0.02	−0.89	5.35
2903	1	−0.13	0.63	−1.00	5.07
	2	−0.19	0.55	−1.35	5.40
	13	−0.41	0.48	−1.02	5.47
2997-NE	1	−0.34	0.50	−1.12	5.04
	2	−0.21	0.07	−1.44	5.17
	7	−0.36	0.00	−1.65	4.83
	9	−0.30	0.27	−1.51	4.66
	10	−0.30	0.03	−1.76	5.10
	12	−0.26	0.13	−1.51	4.97
	13	−0.37	−0.11	−1.75	4.67
	14	−0.25	0.02	−1.97	4.31
	15	−0.05	0.26	−1.01	4.16
	24	−0.21	−0.04	−1.87	4.69
	34	−0.20	0.16	−1.62	5.33
	G1	−0.18	0.14	−1.25	5.61
	G2	−0.44	0.21	−1.56	5.67
	G3	−0.21	0.18	−1.53	5.06
	G4	−0.39	0.49	−1.18	4.94
	G5	−0.29	0.09	−1.18	4.88
	G6	−0.39	−0.35	−1.50	5.31
	G8	−0.33	0.25	−1.74	5.73
2997-SW	1	0.12	0.30	−1.57	5.28
	3	−0.18	0.35	−1.10	5.88
	5	−0.14	0.14	−1.62	5.76
3351	1	−0.40	0.11	−1.84	4.91
	2	0.16	0.32	−1.92	5.82
4303	4	0.00	0.43	−1.37	6.23
	9	0.00	0.30	−1.62	5.91
	24	0.05	0.27	−1.72	5.69
5253	1	−0.11	−0.04	−1.05	4.95

$\dagger$ For an IMF with $M_l = 1\,M_\odot$, $M_u = 120\,M_\odot$, $\alpha = 2.5$, and age = 0. or 4 Myr. See text for details.

superposed on the. line are spaced at every 0.5 Myr. The IMF chosen is close to Salpeter's IMF and has $m_l = 1, m_u = 60$ and $\alpha = 2.5$ for solar metallicity. For m_u other than 60, the evolutionary track is similar to the one shown, except that the starting (age $= 0$) $\frac{\phi}{L_B}$ value is different. For $m_u > 60$ it starts at a higher value than shown and the converse is true for lower masses. At $\alpha = 2.5$, the colour reddens by 0.04 mag as the upper cut-off is decreased from 120 to 30, whereas $\log(\frac{\phi}{L_B})$ decreases by 0.75 dex for the same range of masses. As the more massive stars die, the evolution follows that of a cluster with a lower m_u. The arrow on the right side of the figure is the reddening vector, with the length corresponding to 1 mag visual extinction. It can be noticed that the evolutionary track forms an envelope around the observed points even before correcting for reddening in the parent galaxy. It is possible to bring the observed points over the theoretical line by dereddening by A_v ranging from 0 to 1.4 mag. The giant H II complex NGC 2363 is the only region which is bluer than the model in Fig. V.1. Also this is the only region in the sample whose metallicity is much lower than solar ($\sim 0.1\,Z_\odot$). Models are themselves bluer by 0.05 magnitudes at this metallicity. One expects lesser amount of dust at this metallicity and hence the expected extinction is also low. Since this region is different from the rest of our sample we exclude it from the general discussion.

In Fig. V.2, the observed quantities are plotted after dereddening by A_v, as derived from Balmer decrement (quantities with suffix 2). All the above models are retained. The most striking feature in this figure is that the $B - V$ colour for the majority of regions is bluer than the bluest models. Fig. V.1 shows that there are many regions close to the model, which require very little extinction correction, whereas the computed extinction values from Balmer decrement have a median value close to 1.5 mag, with only 4 regions having values less than 0.75 mag. This
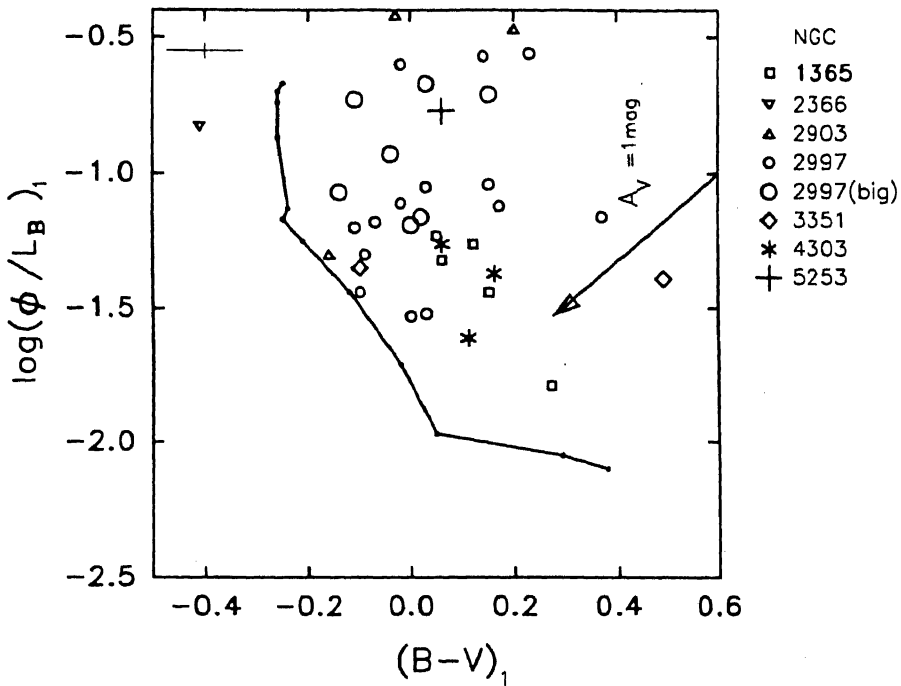
Figure V.1 Observed regions in $\log(\frac{\phi}{L_B})_1$ vs $(B - V)_1$ plane. Corrections are made only for galactic extinction. Maximum rms errors are shown by the cross at the top left corner. The arrow indicates extinction correction corresponding to $A_v = 1$. The evolution of a cluster with $m_u = 60$ and $\alpha = 2.5$ is shown by the thick line. The dots on the line are spaced 0.5 Myr apart with the dot at the bottom right being at 7 Myr.

figure indicates that by dereddening the cluster related quantities by extinction derived from Balmer decrement, we are overcorrecting for extinction.

The dereddened $(B-V)_2$ colours are plotted against the visual extinction A_v derived from Balmer decrement after correcting for the galactic extinction in Fig. V.3. A trend of blue $(B-V)_2$ colours having higher extinction is clearly seen in the figure. In fact the blue $(B - V)_2$ colours are mostly restricted to regions having $A_v > 1.5$ mag. The figure corroborates our assertion that the cluster stars on an average experience lesser extinction than the surrounding ionized gas. Such a situation is possible if the gas around the cluster is clumpy and the line emission from each of the clumps undergoes extinction by the dust in the neutral component in its periphery. The radiation from the cluster can partially escape unobscured through
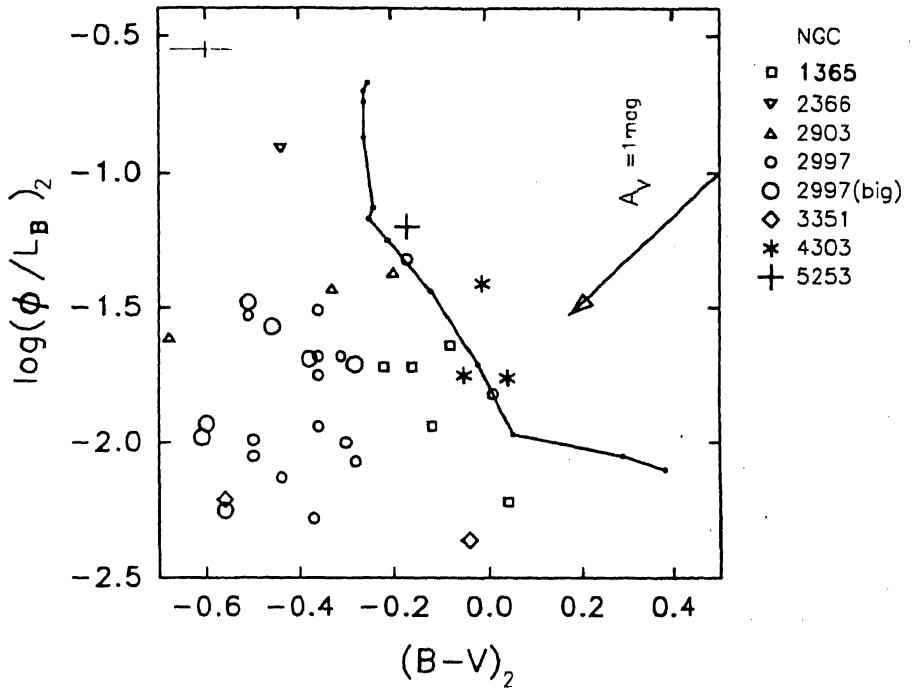
Figure V.2 Observed regions in $\log(\frac{\phi}{L_B})_2$ vs $(B-V)_2$ plane. Extinction corrections are made based on Balmer decrement. Other details are as in Fig. V.1.

the regions between the clumps. We will hence formulate a different prescription to estimate the extinction of the star cluster which should be more accurate atleast statistically.

2.1 Estimation of Extinction towards Embedded Stars

The observed range of colours is much more than the range that can be produced due to IMF variations. For an assumed slope of the IMF, the colour reddens by 0.05 mag for m_u changing from 120-30. Thus as a first approximation we can neglect the dependence of IMF on colours for clusters younger than 4 Myr. We assume $B - V = -0.25$ as typical value for the young clusters in our sample, which corresponds to $\alpha = 2.5$. However it is safe to assume that the regions having high $\frac{\phi}{L_B}$ are young regions. We hence make independent estimates of extinction (A_{vc}) towards the embedded clusters, by assuming that GEHRs have lower extinction
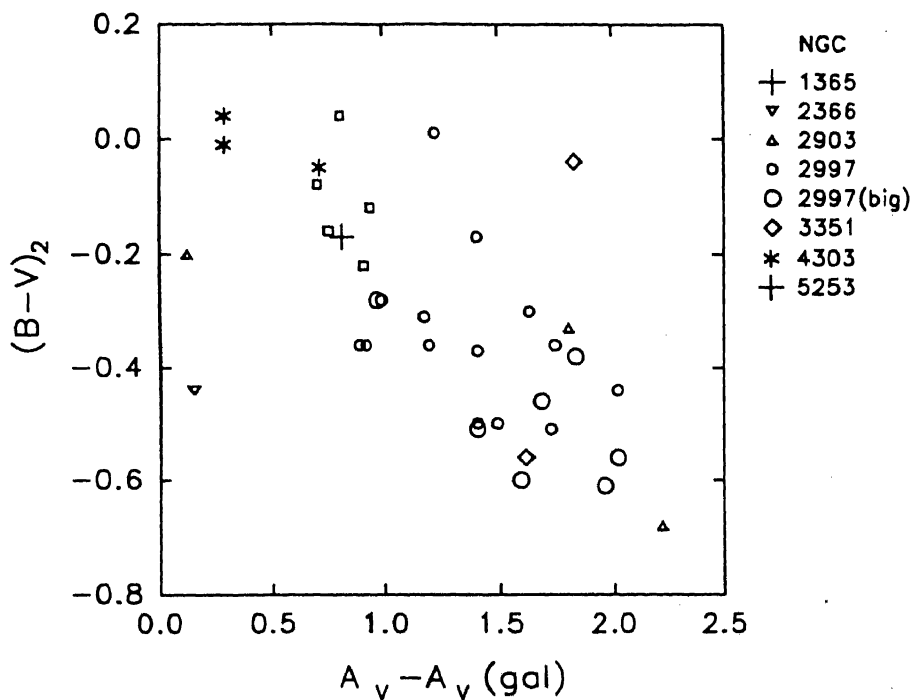
Figure V.3 The corrected $B-V$ colours plotted against A_v corrected for galactic extinction.

towards the embedded stars compared to the gas. Dust distribution in a clumpy manner, along with different spatial distribution of stars and gas within the emitting volume, is the most probable source of differential extinction. The prescription is formulated by the equation

$$I = I_0[g + (1 - g)\exp(-\tau)] , \qquad (V.1)$$

where τ is the internal extinction suffered by the gas and g is the fraction of the stellar continuum that does not suffer any internal extinction. The above equation means that a fraction $(1 - g)$ is experiencing "normal" extinction whereas the remaining fraction g escapes without encountering any clump of dust. The effective extinction sufferred by the cluster is defined as,

$$10^{-0.4A_{vc}} = g10^{-0.4A_v(\text{gal})} + (1 - g)10^{-0.4A_v}. \qquad (V.2)$$

g can be solved from this equation to get,

$$g = \frac{10^{-0.4A_{vc}} - 10^{-0.4A_v}}{1 - 10^{-0.4A_v}}. \qquad (V.3)$$

In this formulation we have assumed the entire extragalactic extinction to be internal, in the absence of a clear understanding of the relative contribution of the extinction outside the H II complex in the parent galaxy. If there is an additional foreground absorption A_g in the parent galaxy, the cluster and the gas would both undergo this extinction and the value 1 in the denominator of Equation V.3 will have to be replaced by $10^{-0.4A_g}$. This will have the effect of increasing the derived value of g. However, Equation V.1 also would be modified by having the same factor multiplying the first g and hence the effect on the derived values of A_{vc} would be small.

Assuming that the bluest regions with the highest values of $\log \frac{\phi}{L_B}$ to be younger than 3 Myr, the values of A_{vc} and g are estimated. Out of the eight regions with $(B - V)_1 < 0.00$, one is rejected as it is 3σ away from the mean. The resultant mean value is $g = 0.46 \pm 0.05$. We assume this value of g to be typical for the whole sample of GEHRs. Using this average value, A_{vc} is recomputed for all the regions using the above equation. The cluster quantities are dereddened using these values of A_{vc} and the resulting quantities are identified by suffix 3.

$$(B - V)_* - A_{vc}(\text{star}) \longrightarrow (B - V)_3$$

The resultant values are plotted in Fig. V.4 and listed in Table V.1. It is apparent that the blueward envelope would agree with the theoretical model only if the model is shifted down by 0.5 dex along the $\log(\frac{\phi}{L_B})$ axis. This can be understood in terms of reduced availability of ionizing photons to the gas as discussed in the following.

2.2 Destruction and Escape of Ionizing Photons

Four regions in NGC 2997 exhibit the redward evolution of the model beyond 4 Myr, but require reduction of $\frac{\phi}{L_B}$ by 0.5 dex to match the model. In an attempt to understand this shift, we express the discrepancy in $\log(\frac{\phi}{L_B})$ between observations

160
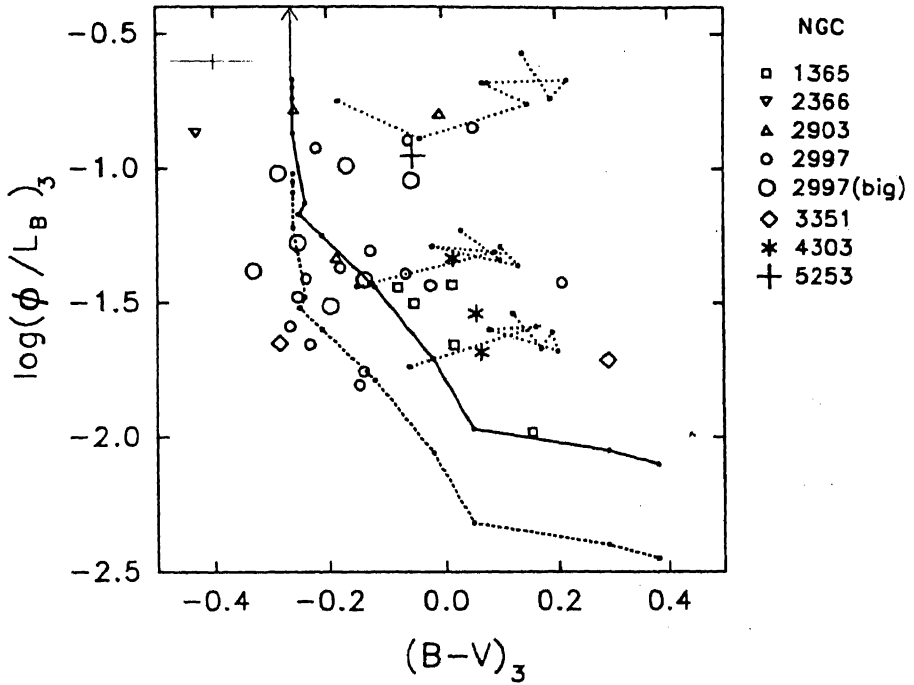
Figure V.4 Observed regions in $\log(\frac{\phi}{L_B})_3$ vs $(B - V)_3$ plane. Extinction corrections are made for A_{vc} with $g = 0.46$. The dashed line is the model represented by thick line, but with an escape fraction of 0.55. A model with $m_u = 120$ and no escape of Lyman photons begins at the tip of the arrow. Sequences with dotted lines correspond to composite models with the younger population at 0 (top), 3.5 (middle) and 5 (bottom) Myr superposed on an older population. The leftmost point on these curves represents older population at 5, 6, 6 Myr respectively. Further points are placed at increments of 1 Myr.

and the highest value in the model by a parameter f defined as,

$$\log(\frac{\phi}{L_B})_{\mathrm{obs}} = \log(\frac{\phi}{L_B})_{\mathrm{mod}} + \log f, \qquad (\mathrm{V}.4)$$

where f is a fraction between 0 and 1. Values of f for the four regions in NGC 2997 have an average of 0.07 ± 0.02. For the instantaneous star formation model considered here, changes in $\frac{\phi}{L_B}$ are controlled by changes in ϕ. Thus, physically, f represents the fraction of the total available Lyman continuum photons compared to the theoretically expected one for zero age cluster. Three obvious causes for this are the reduction in the output as the cluster evolves, the destruction of photons by dust, and escape through lower density regions or escaping detection due to total

161

absorption of Hα photons by dust clouds. Thus f can be factorized as,

$$f = (1 - \eta_{\text{dust}})(1 - \eta_{\text{evol}})(1 - \eta_{\text{esc}}), \qquad (V.5)$$

where η_{dust} is the fractional Lyman continuum photons that are absorbed by dust, η_{evol} is the fractional decrease in the Lyman continuum photons as the cluster evolves and η_{esc} is the fraction of Lyman continuum photons that are escaping from the nebula without being used up in ionization, or escaping detection due to total absorption of Hα photons. $\eta_{\text{evol}} = 0$ at zero age and increases to 0.7 and 0.8 at ages 4 and 5 Myr respectively. Dust competes with the gas absorbing a fraction of the ionizing photons. Smith, Biermann and Mezger (1978) and Mezger (1978) have estimated this fraction to be between 0.7 and 0.2 for giant galactic H II regions. Belfort, Mochkovitch and Dennefeld (1987) have assumed a useful mean value of $\eta_{\text{dust}} = 0.30$, a the value also used by many others. (see $e.g.$ Mas-Hesse and Kunth 1991). With the assumption of η_{dust} and η_{evol}, we can use our observations to estimate η_{esc}. For the four H II regions in NGC 2997, assuming their age to be 4.5 Myr as indicated by our estimate of colours,

$$f = 0.70 \times 0.25 \times (1 - \eta_{\text{esc}}) = 0.17 \times (1 - \eta_{\text{esc}}).$$

This yields an escaping fraction of Lyman continuum photons amounting to 60%. The escaping Lyman photons will ionize the low density medium surrounding the H II complexes. The detection of these low density ionized extensions requires very sensitive Hα observations such as carried out by Hunter and Gallagher (1992).

The proposed shift of the model would move it below the highest observed values of $\frac{\phi}{L_B}$. There are two possible explanations for this. First, such a large escape fraction may not be representative of the youngest regions. Larger escape for older regions could be understood in terms of the blister model proposed to explain the observed properties of majority of galactic H II regions (Tenorio-Tagle

162

1979, 1982). According to this model, the matter would stream out of the initial H II region as the blister bursts out and forms a low density conical extension through a 'champagne flow'. The radiation ionizing this region is not accounted for since its contrast with the background would be very low, and can hence be treated as escaping. If the champagne flow starts at ~ 3 Myr, the escaping fraction would be smaller at earlier epochs and larger at later epochs as observed. Alternatively, the regions with high $\frac{\phi}{L_B}$ may harbour more massive stars. Adding a larger number of massive stars would stretch the theoretical model to higher values of $\log(\frac{\phi}{L_B})$. As these stars die away after a few Myr the evolution would follow that of a cluster with a lower value of m_u. The regions with high $\frac{\phi}{L_B}$ are hence the only evidences for a high upper mass cutoff in the IMF. We will pursue this alternative further in the following section. If we consider the total absorption of some Hα photons by dense clouds leading to the Lyman photons escaping detection we will have a third explanation which we will pursue in a later section in the context of discrepancy between the Balmer and radio extinction estimates.

2.3 Effect of Multiple Star Bursts

Evolution of an instantaneous starburst, with escape of a fraction of Lyman continuum photons and reduced reddening towards stars compared to the gas is found to explain the blueward envelope of regions in the $\log(\frac{\phi}{L_B})$, $(B - V)$ diagram. However, there is considerable spread of $(B - V)$ colours at any given $\frac{\phi}{L_B}$ which cannot be explained by an instantaneous burst model. A look at similar diagrams using $(V - R)$ colour in place of $(B - V)$ colours shows that the spread is certainly not due to errors in our estimate of reddening to the cluster. We show in Figs V.5 – V.7 such diagrams. There are many regions in Fig. V.6 which are redder than the model even after correcting for extinction following Balmer line ratio, where as the Balmer correction makes $B - V$ much bluer than the models.
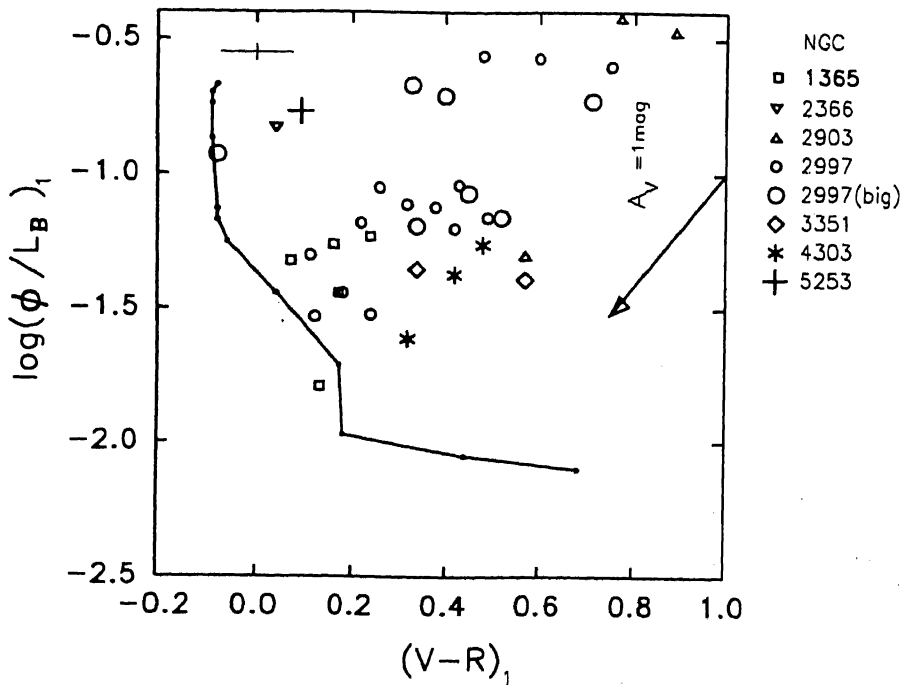
Figure V.5 Observed regions in $\log(\frac{\phi}{L_B})_1$ vs $(V - R)_1$ plane. See Fig. V.1 for other details.

The observed spread in colours can be easily explained as the effect of having more than one burst with different ages in an individual GEHR. Evidence for two starbursts separated by ~ 10 Myr exist for 30 Dor already (McGregor and Hyland 1981). When two starbursts with ages differing by more than 3 Myr coexist, the contribution to ϕ is mainly due to the younger starburst whereas at B, V, R wavelengths the older burst contributes increasingly. The effect of older starburst would be more dramatic when the stars with 25–40 $M_\odot$ in the older cluster become red supergiants. The composite of two starbursts of equal strength with the younger one at 0, 3.5 and 5 Myr is shown in Figs V.4 and V.7 as three sequences by dotted lines. It was found necessary to include the stars up to 120 $M_\odot$ in the case of the younger cluster at zero age in order to explain the regions with high $\frac{\phi}{L_B}$. This supports the second explanation advocated in the last section for the low estimate of f. The sequences shown in the figure are higher than the observed
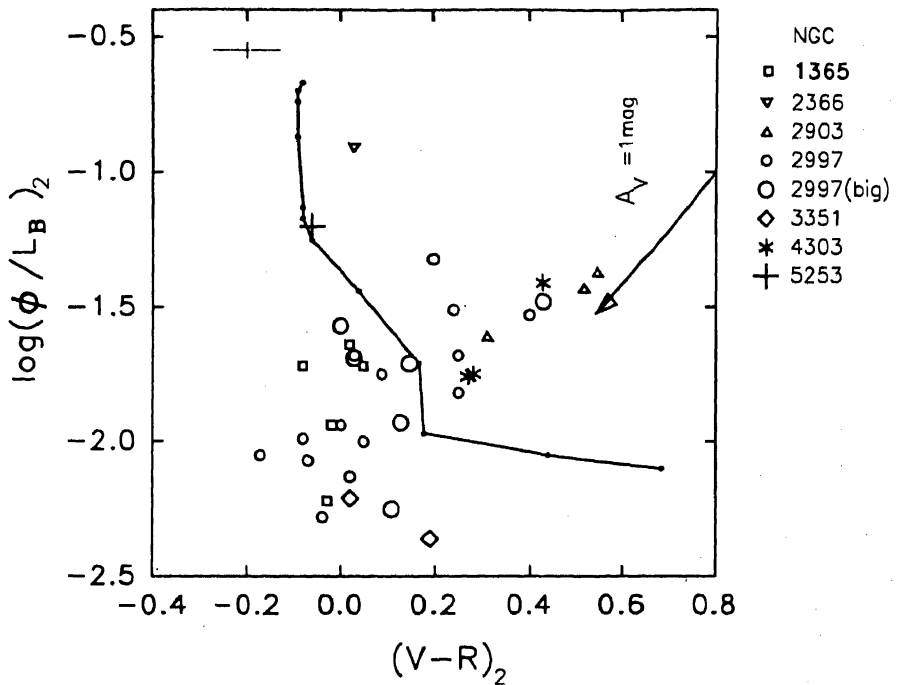
Figure V.6 Observed regions in $\log(\frac{\phi}{L_B})_2$ vs $(V - R)_2$ plane. See Fig. V.2 for other details.

points indicating that either the upper mass cutoff should be reduced slightly or some escape of Lyman continuum photons does exist. We will assume the latter explanation because of other evidences for escape of Lyman photons and absorption of $H\alpha$ photons.

The first of the red supergiants in the cluster start appearing at 5 Myr. When the older cluster evolves from 6 to 7 Myr the region evolves to the red quickly. This can be identified with the epoch when 25 $M_\odot$ stars become supergiants. At later epoch when these stars become bluer again lower mass stars begin to turn into supergiants and the region will have minor excursions in the red region. The effect is apparent better in $V - R$ colours compared to the $B - V$ colours because of enhanced contribution of RSGs to these bands. It is significant that the reddest regions observed require a population 10 ± 3 Myr older than the current burst, a value similar to the one found in the case of 30 Doradus.
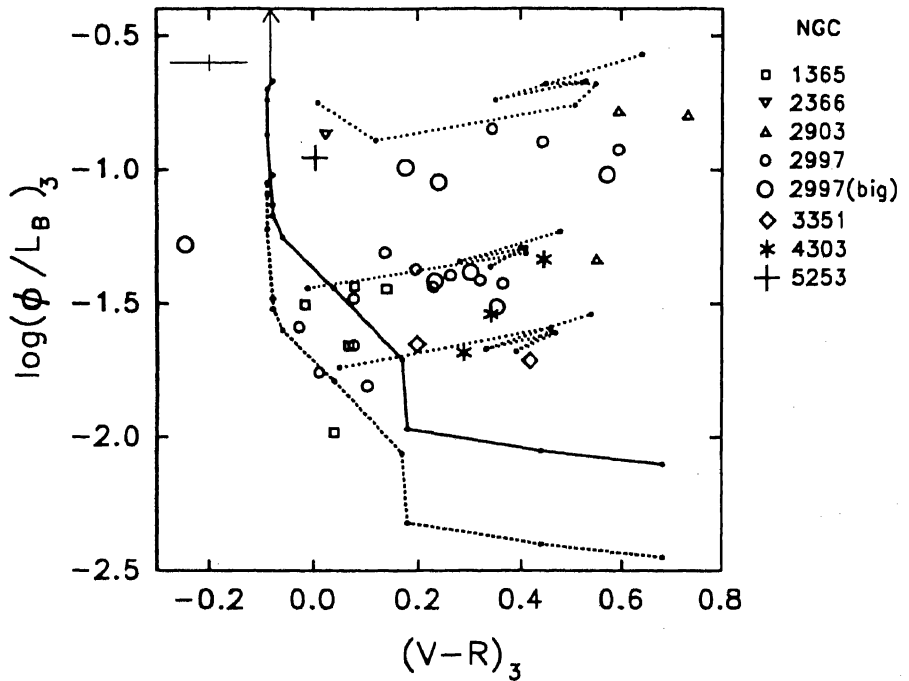
Figure V.7 Observed regions in $\log(\frac{\phi}{L_B})_3$ vs $(V - R)_3$ plane. See Fig. V.4 for other details.

Some of large aperture measurements for NGC 2997 contain a cluster with very low Hα flux as well as a nearby H II region with hardly detectable continuum from cluster. These apertures thus contain two resolved regions of different age and support our contention that other small aperture measurements pertain to two clusters that are not resolved.

The clusters evolve rapidly to lower $\frac{\phi}{L_B}$ values in our diagrams after 3 Myr. The effect of stars with masses > 60 M$_\odot$ is also very low by this epoch. The sequences shown in the figures for the younger cluster at 3.5 and 5 Myr shows that two populations may coexist in a majority of regions. There are, however, a few evolved regions such as the four regions in NGC 2997 that were used for the determination of η_{esc} which do not have strong evidence for an older cluster. Such examples are lacking at zero age.

The zero-age points for a single burst with upper cutoff at 120 M$_\odot$ is at the tip of

the vertical arrows in Figs V.4 and V.7.

2.4 Masses of Young Clusters

For an assumed IMF, the masses of the star forming complexes can be estimated based on the Lyman continuum luminosity of the regions. Corrections for decrease in ionizing luminosity due to evolution, destruction by dust and escape of photons (as parametrised bt f) has to be done to obtain the total ionizing luminosity emitted from the cluster. Total mass (M_T) is thus given by,

$$\log(M_T) = \log(\phi)_{obs} - \log f - \log(\phi)_{imf},$$

where $(\phi)_{imf}$ is the model derived luminosity per unit mass. Since we have made only a statistical estimate for η_{esc} in Equation V.4, we will ignore it at present and comment on its effect on the derived mass distribution. Further, we group the observed regions as young (zero age) and old (~ 4 Myr) clusters based on Figs V.4 and V.7 so that a mean value of η_{evol} can be used for each group. We will ignore the large aperture measurements in the case of NGC 2997 since they generally include many individual regions. We assume further that the estimate of ϕ pertains only to the younger of the cluster in the case of coexistence of different clusters as indicated in the previous section. The masses derived with these assumptions and an IMF with $\alpha = 2.5$ and $m_u = 120$ are given in the last column of Table V.1. Their histogram distribution is given in Fig. V.8 where the younger clusters are distinguished. The mean value is

$$\log(M_T) = 5.2 \pm 0.5$$

for the entire sample ($n = 29$). The youngest regions also have a similar distribution (denoted by the hatched area). If 50% of the Lyman photons are escaping then the mass estimate will have to be doubled.

167
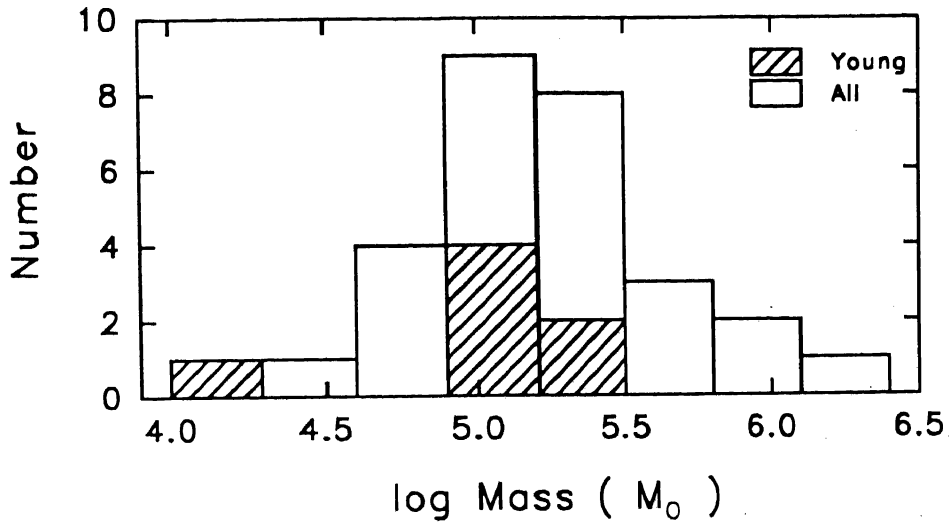
Figure V.8 Histogram of masses of GEHRs. The hatched area denotes youngest regions.

The above estimates indicate that the mean mass of clusters is $\sim 2 \times 10^5$ $M_\odot$. The high mass end of galactic Giant Molecular Clouds (GMC) reaches values upto 10^6 $M_\odot$ (Solomon *et al.* 1987). If we assume the star forming parent clouds in GEHRs to be having properties similar to the GMCs in our galaxy, the inferred star formation efficiencies are about 20%. From high resolution CO observations of molecular clouds in the arm of M 51, Vogel, Kulkarni and Scoville (1988) derive masses upto 3×10^7 $M_\odot$, referred as Giant Molecular Associations (GMAs). If such clouds are common in external galaxies, only a small fraction of GMA mass would be converted into stars in each episode of star formation.

2.5 Comments on Selected GEHRs

NGC 2366 is left out in most of the above discussions because of its low metallicity. This region was of special interest in many previous investigations (Peimbert, Peña, Torres-Peimbert 1986, Kennicutt, Balick and Heckman 1980). This is one of the regions with the smallest Balmer decrement values. The present study suggests

that the stars in this complex do not experience any extinction in the parent galaxy. The absence of 2200 Å absorption feature in the IUE spectrum (Rosa, Joubert and Benvenuti 1985) may support this view. $\frac{\phi}{L_B}$ and colours agree well with IMF slope of 2.5 and $m_u = 60$ $M_\odot$ with $\eta_{esc} = 0.2$. Alternatively, the IMF could be extended to 120 $M_\odot$ with an escape fraction of 0.65. In the latter case the inferred mass of the cluster is 2×10^5 $M_\odot$. There is no evidence for an older cluster in the region.

The starburst nucleus of NGC 5253 has also been studied well using multiwave-length observations (Walsh and Roy 1989a, Gonzalez-Riestra, Rego and Zamorano 1987, Moorwood and Glass 1982). Colours dereddened using Balmer decrement are normal for this region, indicating that gaseous extinction is in agreement with the cluster extinction. The escape fraction is also not significant. A young cluster of IMF slope 2.5 and $m_u = 120$ $M_\odot$ together with a similar cluster of age 4–5 Myr agrees with observations. The inferred mass with no escape fraction is $10^5 M_\odot$.

Among the GEHRs in spirals the most interesting complex is the one lying at the tip of the North-East arm of NGC 2997. The complex contains three knots (denoted by 1, 2, 32 in Fig. III.4(a)) of similar brightness in continuum light while the knot 32 is totally absent in line emission. Knots 1 and 2 are treated as independent regions and are included in our plots. A bigger aperture is also chosen enclosing all the emitting knots. The bigger aperture measurement require multiple population as expected. It is significant that several of the smaller aperture measurements in NGC 2997 also indicate the presence of an earlier burst.

2.6 The Larger Sample

The results obtained above are based on the GEHRs for which spectroscopy was available from literature. Our catalogue contains photometry of many more regions for which there is no spectroscopic information on oxygen abundance and visual extinction from Balmer decrement. We made an attempt to see the results on

this larger sample taking average extinction and abundance values for the galaxies. For the regions with spectroscopic data, the most commonly occurring value of extinction and oxygen abundance is assumed to be typical for that galaxy. A g value of 0.5 is used in computing A_{vc} and the analysis is done similar to the methods described above. The sample contains 65 regions from galaxies NGC 1365, 2997, 4303 and 4449, with NGC 4303 dominating the sample. The regions of previous analysis in these galaxies are included but are treated with average extinction. Spectrophotometry of CM 39 in NGC 4449 by Lequeux *et al.* (1979) is used as typical values for other regions in that galaxy. The sample however does not include CM 39.

The regions are shown in $\log(\frac{\phi}{L_B})_3$ vs $(B-V)_3$ plane in Fig. V.9, and $\log(\frac{\phi}{L_B})_3$ vs $(V-R)_3$ plane in Fig. V.10. The diagrams resemble the earlier sample of spectroscopically studied GEHRs. The effect of reddening estimate being not very accurate for an individual region is seen through some regions being bluer than the model. This may partially explain the paucity of young objects in the sample. However the main cause of the latter is probably the escape of Lyman continuum photons from a majority of regions.

2.7 Summary of Results

From the discussions above we draw the following conclusions regarding the GEHRs in our sample.

(1) Dereddened and gas subtracted $B-V$ colours are found to correlate with the visual extiction estimated from the Balmer decrement. Regions having the bluest colours are the ones which have larger A_v values, which suggests that the colours are overcorrected for reddening. A model is proposed in which only half the light from the cluster is reddened as much as the gaseous emission and the remaining half emerges unattenuated from the GEHR. This prescription makes the observations
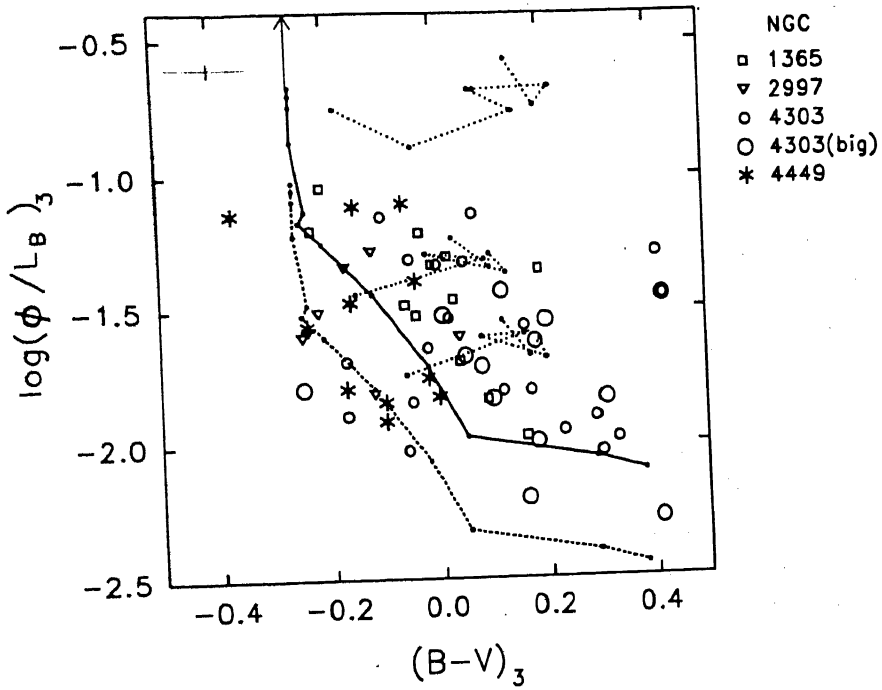
Figure V.9 The larger sample in $\log(\frac{\phi}{L_B})_3$ vs $(B-V)_3$ plane. See Fig. V.4 for details.
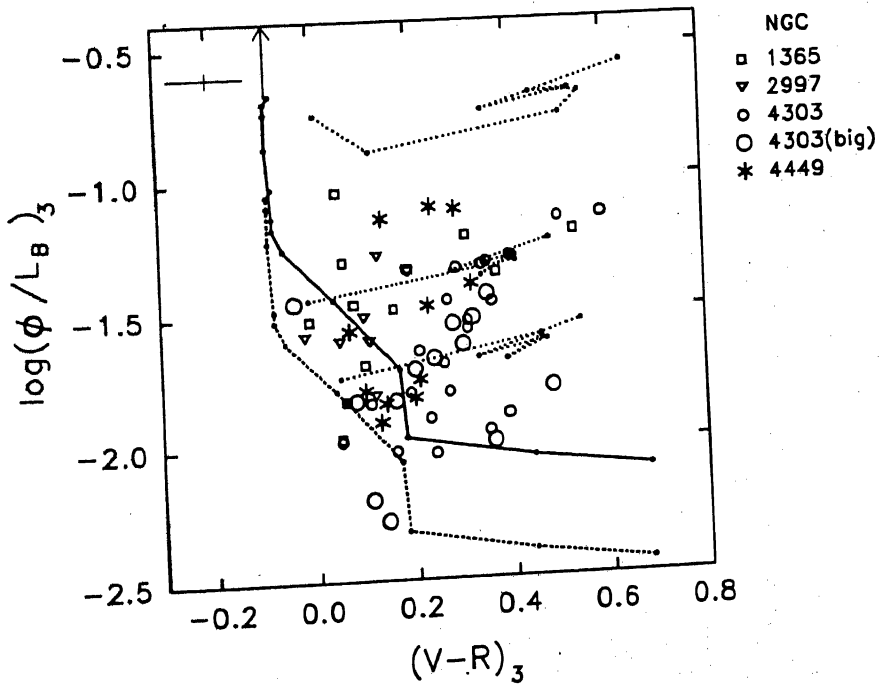

Figure V.10 The larger sample in $\log(\frac{\phi}{L_B})_3$ vs $(V-R)_3$ plane. See Fig. V.7 for details.

agree with the theoretical models of the cluster light.

(2) A parameter f which is the fraction of detectable Lyman continuum photons is introduced to quantify the discrepancy between model and observed values of $\log(\frac{\phi}{L_B})$. There is evidence that at least in some cases only half the ionizing radiation is detected. The reason for non-detection could be escape of ionizing photons from the densest part of gas into lower density regions, and/or total absorption of some of the Balmer line photons by intervening clouds.

(3). The $V - R$ colours indicate the presence of a red supergiant population. Adding such a population to a young population, responsible for the ionization, explains all the three observables satisfactorily. The observations indicate that the older population is often > 5 Myr older than the younger component, with occasional evidence for a population which is > 7 Myr older.

(4) The evaluation of IMF parameters namely m_u and α, which are greatly needed in understanding star-formation processes in different environments, is hampered by the uncertainties in f and g and by the existence of an older population. The present observations do not compel us to choose IMF slope far away from the Salpeter's value of 2.35.

(5) The masses converted to stars in each burst is $2 \times 10^5 \, M_\odot$, within a factor of three.

We will discuss in Section 4 these results in the context of earlier work on GEHRs.

3. Multi-band Structure of GEHRs

Structural properties of GEHRs in many nearby galaxies have been analysed by Kennicutt (1984), based on Hα images. Accordingly they are classified as "classical", "high-surface brightness", "diffuse", "multiple core complex" and shell or ring-like H II regions. It is interesting to compare the structures in different bands

especially between bands indicative of emission lines and stellar continua. Such a study would show the distribution of ionizing stars within the nebula directly. Compared to the regions studied by Kennicutt (1984), the regions in the present sample are smaller in angular size and hence cannot be studied with the same detail. However, differences in structure in different bands can be studied by the superposition of digital images. While Hα images trace the distribution of the ionized gas, the broad-band images in BVR trace the stellar continuum. Thus the structural information of H II complexes in continnum bands gives the position of the embedded stars within the nebula. According to the classical Strömgren model for H II region, the ionizing stars occupy a small portion in the centre of the nebula. It is interesting to see how good is this simple picture for GEHRs. In the following we study this aspect based on our images.

One can easily compare or distinguish features on images by superposition or blinking of aligned images. We have used both these options on the COMTAL display device. Three images can be superposed into one composite colour image, by assigning Blue, Green and Red for the three components. We have formed such colour composites by the superposition of B, V and Hα images respectively. The resultant images are reproduced in Figs V.11 – 14 in the form of photographs of four of the programme galaxies. In spite of some loss of information in the reproduction process, most interesting regions can still be traced on the photographs.

Three of the galaxies in the sample (NGC 2997, 4303 and 4449) show many regions which have significant structural differences compared to the expected alignment errors. Particularly interesting cases are Nos 24, 5, 6, 7, 9, 35, 21, 14/18, 19/20 in NGC 4303, 1/2/32, 6/7, 13/14/15, 21/22, 34 in NGC 2997-NE and 8, 10, 11, 13, 14 in NGC 4449. (See Figs III.1–9 for identification numbers of the regions.) Notice the relative brightness differences in the red and blue/green peaks of neighbouring knots around the above regions. At the position of some of the bright

Figure V.11 Colour image of NGC 2903. B, V and Hα images are mixed as blue, green and red components. The inset is the nuclear region at improved contrast.
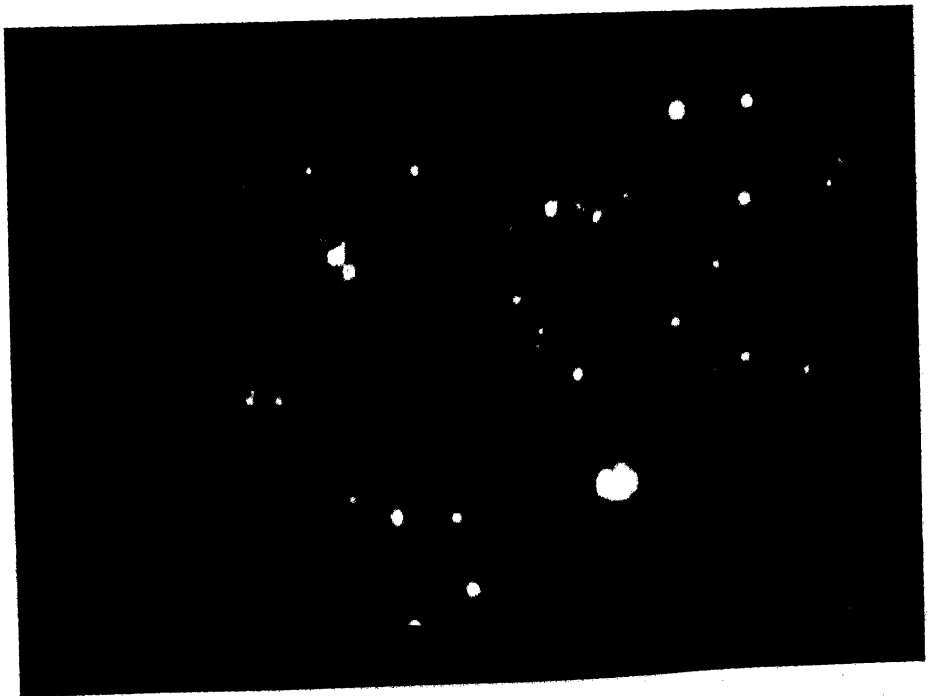

Figure V.12 Colour image of North-East portion of NGC 2997. B, V and Hα images are mixed as blue, green and red components. The inset is the nuclear region at improved contrast.

Figure V.13 Colour image of NGC 4303. B, V and Hα images are mixed as blue, green and red components.

Figure V.14 Colour image of NGC 4449. B, V and Hα images are mixed as blue, green and red components.

Hα knots, the stellar continuum is weak or absent and vice versa. Neighbouring knots in some cases are numbered separately. We have measured the positions of regions showing signs of structural differences in NGC 2997 and 4303 on Hα and B frames. The separation between the peaks of nebular and stellar continuum knot is 42 ± 20 pc for 5 regions in NGC 2997 and 100 ± 37 pc for 13 regions in NGC 4303 respectively. It is obvious that the lower limit to the separations is due to the lack of resolution (~ 18 and 34 pc at the distances of NGC 2997 and 4303). The upper limit to the separation comes from the typical separation of star forming complexes (chain of H II regions) in spiral arms. The mean separation is 450 ± 100 and 1200 ± 475 for the two galaxies that we have considered. It is interesting to note that the separation between the neighbouring knots with striking brightness differences are around one tenth of the mean separation between distinct H II complexes. Also the separation between the nebular and continuum knots that we have obtained are typical sizes of Giant Molecular Clouds. This separation is also of the same order as the one between the old and young populations in 30 Dor (Hyland et al. 1992).

In order to explain the photometric properties of H II complexes, we required a population older than 6 Myr superposed on a younger population for majority of the sample regions. We are tempted to believe that in some cases we have actually resolved these two populations as Hα and continuum knots. If the younger population has formed due to some trigger due to the older population, we estimate the speed of propagation as $40 - 100$ pc in ~ 10 Myr, or 4–10 km s^{-1}. This value is reasonable for a trigger in terms of mass-loss stellar wind from the older population.

4. Discussion

The most widely used diagnostic for star-formation so far is the spectroscopically derived Hβ equivalent width. There are some studies where ultraviolet (UV) fluxes

are compared with optical fluxes. Thermal radio emission has also been used as a probe for the ionizing radiation. In addition, the near-infrared observations of individual stars have been made in the cluster NGC 2070 in 30 Dor in LMC. We re-examine these results in the context of our results in the following.

4.1 Hβ equivalent widths

Viallefond (1987) from his compilations, finds that the Hβ equivalent widths and the effective temperatures of the cluster (defined by the ratio of helium ionizing to hydrogen ionizing photons) cannot be simultaneously explained. He finds the observed Hβ equivalent widths to be lower by a factor of 3–4 compared to models with Salpeter IMF without evolution. This is essentially the same discrepancy that we have found in $\log(\frac{\phi}{L_B})$ in our data. Viallefond discusses the following possible reasons causing this discrepancy.

(1) Hβ equivalent widths are underestimated due to aperture size effects and improper background subtraction.

(2) The stellar atmosphere and evolutionary models may not be proper for the sample used, which contain objects at much lower metallicities.

With our uniform data obtained through imaging, the uncertainties due to aperture effects are eliminated. Most of our sample regions have solar or higher metallicities, and hence solar abundance models should be applicable. The good agreement between our model based on Kurucz atmospheres and that of Mas-Hesse and Kunth (1991) based on observed stellar spectra, clearly indicates that there are no significant differences between observational data and models. Thus the errors in observations or models are not likely to explain the discrepancy.

A spectrophotometric catalogue of H II galaxies containing 425 objects is published recently by Terlevich et al. (1991). It is known since the time of Sargent and Searle (1970) that H II galaxies are ionized by massive clusters of coeval OB

177

stars. These galaxies are presently experiencing a high level of star formation activity closely resembling "starburst" galaxies on the higher scale and GEHRs on the lower scale. Observable properties are dominated by young stellar component with little or no evidence for any underlying population (Campbell and Terlevich 1984; Melnick, Terlevich and Moles 1985). Among other quantities, Terlevich *et al.* publish Hα and Hβ equivalent widths in their catalogue. Like Giant extragalactic H II regions these galaxies are also supposed to be simpler systems dominated by a young star forming complex. Thus the evolutionary population synthesis model discussed in Chapter IV is valid for these systems as well. We compare median Hα and Hβ equivalent widths of this sample with our model at $Z = 0.002$ metallicity, to check whether this sample also shows the discrepancy that we have found. The computed median Hα and Hβ equivalent widths for the sample regions are $172\,\text{Å}$ and $33\,\text{Å}$ respectively. These values compare very well with models which produce $\log(\frac{\phi}{L_B})$ values close to our median value of -1.75. For the IMF with $m_u = 60$ and $\alpha = 2.5$ at $Z = 0.002$, the model corresponds to evolution beyond 6.5 Myr (see Table IV.2b). In this large sample there are only three galaxies which have Hβ equivalent widths $> 350\,\text{Å}$, the expected value for a cluster younger than 3 Myr. The median values of Hα and Hβ equivalent widths correspond to f values of 7.1% and 8.0%. This value compares well with the value of 8.0% for the 3–5 Myr objects in our sample. Thus an escape of a fraction of ionizing photons and an addition of a 10 Myr old population to a younger population of 0–5 Myr can explain the observed equivalent widths in this sample as well. It should be remembered that our 2-population model is different from the contnuous star formation models often invoked to explain the low equivalent widths. Continuous star formation will produce too much of oxygen for a normal IMF, and hence cannot explain the observed low Hβ equivalent widths in metal poor regions (Lequeux and Viallefond 1980, Viallefond and Thuan 1983). In our 2-population model, the enriched elements fom the

older population are yet to mix with the gas surrounding the younger population, because of possible spatial separation between the young and the old populations.

4.2 The Cluster Extinction

UV Continuum Observations

Young and massive stars emit most of their energy at UV wavelengths. Thus UV continuum serves as a very good tracer of massive star formation. Such data has become available only recently through rocket and satellite observations. Rosa, Joubert and Benvenuti (1985) have published UV spectra of GEHRs based on *International Ultraviolet Explorer* (IUE) observations. It is found that often the 2200 Å absorption feature is weak or absent, although optical extinction combined with galactic extinction law predicts much stronger bump. From the observed bumps in 5 objects Rosa, Joubert and Benvenuti (1985) infer $E(B - V)$ to be not larger than 0.5 for GEHRs. It should be noted that the $E(B - V)$ value obtained from this method measures the "true" stellar extinction, while that derived from Balmer decrement measures the extinction towards gaseous component.

Viallefond and Thuan (1983) have conducted a multiwavelength study of I Zw 36 in which they compare fluxes at UV wavelengths with optical flux. They use the nebular C III]λ 1909 Å line in combination with Balmer lines to to determine the internal extinction in 4 H II complexes. This method suffers from the uncertainties in C/O ratio in these objects. They derive UV(1608Å) − optical(4862Å) colour indices by correcting the stellar continuum by the derived extinction values for all the 4 objects. Comparing with the models, they conclude that the models do not produce enough UV flux relative to optical flux. This again supports the view that correcting optical continuum using A_V(Balmer) may overestimate the optical flux from the star cluster.

M 83 was one of the targets for rocket UV imaging by Bohlin *et al.* (1990). The

UV images of the galaxy are obtained at 1540 and 2360 Å and aperture photometry is perfomed on 18 H II regions to get m_{fuv} and m_{nuv} respectively. They have performed $V, B - V$ photometry based on the images of Talbot, Jensen and Dufour (1979). By fitting a straight line to the underreddened $m_{\text{nuv}} - V$ and $m_{\text{fuv}} - V$ colours, they find that the reddening curve towards stars in this galaxy is the same as that for our galaxy. The colour excesses $E(B - V)$ are derived by comparing the underreddened $m_{\text{nuv}} - V$ colours with a model with Salpeter slope and $m_u = 120$ and $m_l = 1.8$. Mean value of colour excess so derived is 0.25 with a small scatter (rms of 0.05). Dufour *et al.* (1980) present optical spectrophotometry of six H II regions in this galaxy apart from the nucleus. The derived $E(B - V)$ values from Balmer decrement have a median value of 0.75. These observations are again consistent with our argument that the reddening towards stellar component is less than that for nebular component. Dereddening the colours with the $E(B - V)$ values of Bohlin *et al.* fits well with the models with evolution within 2 Myr. This is in sharp contrast against the conclusions of Viallefond and Thuan (1983), who find a higher amount of UV flux compared to visual flux from extinction corrections based on nebular lines. Thus the solution to the problem lies in estimating reddening separately towards stars and using these values for stellar continua instead of the values derived from nebular lines. The predicted Lyman continuum luminosity is around 3 times that computed from observed Hα luminosity for M 83 H II regions, implying f values less than 0.31.

Thermal Radio Emission

Several groups have compared the extinction derived from radio 5 GHz thermal continuum $A_v(\text{radio})$ (using Equation A12) with that derived from Balmer decrement $A_v(\text{Balmer})$ (Equation A10) (Israel and Kennicutt 1980, Viallefond, Goss and Allen 1982, Caplan and Deharveng 1986). General conclusion from these studies is that $A_v(\text{radio})$ is around 1 mag greater than $A_v(\text{Balmer})$. Practically it is often

difficult to match the apertures for radio and optical measurements, which might explain a part of the uncertainty in the above conclusions. However it is believed that the observed higher values of A_v(radio) is real and may be related to the distribution of dust between the source and the observer. Caplan and Deharveng (1986) investigated various dust configurations to explain radio and optical extinctions in a sample of H II regions in LMC. From these they conclude that uniform extinction cannot explain LMC data. Some of the extinction is due to clumped dust, well outside of the emission zone, and the rest is caused by dust located closer to or mixed with the ionized gas, where scattering effects are important. Measurement of extinction directly from resolved stars indicates that there is interstellar dust, quite irregularly distributed.

A Generalized Model for Extinction

The observations thus indicate that the extinction of gaseous emission is higher in the optical compared to the radio; the extinction of the cluster is lower both in the optical and UV compared to the gaseous emission in the optical.

In the normal way of extinction correction it is assumed that the absorbing particles are uniformly distributed in a layer, which is situated far away from the source. Thus all the photons emitted from the source pass through the same amount of optical thickness. This assumption breaks down if the absorbing particles are mixed with the emitting source. In such a case some of the scattered radiation enters the line of sight, thus in effect increasing the total amount of light in any direction (Mathis 1983). Even if one neglects scattering, the effect of dust mixed with the gas is to decrease the effective amount of extinction at shorter wavelengths (Thronson *et al.* 1990). The ratio of observed to intrinsic intensities under such circumstances can be written as

$$\frac{1 - \exp{(-\tau_\lambda)}}{\tau_\lambda},$$

181

instead of the usually used form $\exp(-\tau_\lambda)$ (see eqn. A1) for the uniform absorbing layer. The above equation effectively gives a different wavelength dependence for the extinction, thus at least qualitatively explaining the UV, optical and radio observations. However, for explaining the lower extinction for stars one would need to postulate that the stars are situated closer to the surface layers of the gas cloud.

Dust particles with selective absorption cross section in the range 504–912 Å has been invoked by Viallefond (1987), in order to explain the missing fraction of ionizing photons. However the existence of such small particles within the H II complex is yet to be confirmed. We suggest that a clumpy distribution of emitting clouds with internal dust, and a partial escape of stellar continuum inclusive of some ionizing radiation through the gaps between the clumps, explains observations through all the bands through a single model.

4.3 The 30 Doradus Complex in LMC

The Tarantula or 30 Dor nebula in the LMC is the closest example of a GEHR. Its relatively nearby location has helped its observation in a greater detail. The near infrared observations revealed the existence of two populations of stars (red and blue) in this complex (McGregor and Hyland 1981). More recently Hyland *et al.* (1992) have surveyed the region to deeper limits ($K = 13$) and the early results are confirmed. The red population is explained to be corresponding to the red supergiant phase of stars with mass $> 20\,M_\odot$ formed about 20 Myr ago. The older population is spatially separated from the younger one by distances of the order of tens of pc. Hyland *et al.* suggest that the younger cluster has formed due to the collision of the parent cloud with the mass loss wind of the older cluster stars. The present work has brought out the evidence for such supergiants in a majority of extragalactic H II regions.

It was normally believed that the ionizing stars in H II regions are situated in the central regions of the nebula, following the Strömgren picture of H II regions. However observationally many well studied H II regions can be explained only in terms of young clusters situated at the edge of the molecular clouds (Israel 1978). Statistical studies of the locations and velocities of ionized and molecular gas have led some authors to suggest that most H II regions are "blisters" at the edges of the molecular clouds (Israel 1978; Fich, Treffers and Blitz 1982). Tenorio-Tagle (1979) and Yorke, Bodenheimer and Tenorio-Tagle (1982), Icke, Gatley and Israel (1980) have shown that such configuration naturally arise from the evolution of H II regions in non-uniform media. If a star forms close to the edge of a molecular cloud, the ionized volume may expand to a point where the ionization front bursts out from the boundary into the surrounding more rarified interstellar medium. The pressure imbalance then leads to a "champagne flow", where ionized gas within the cavity is forced out through the "nozzle" and rapidly expands into an extended low-density nebula. The supply of dense ionized gas is continuously replenished as the ionization front pushed deeper into the molecular cloud. In a sample of LMC H II regions McCall, Hill and English (1990) have found many H II regions which fit into the above model. Lot of ionizing photons can also escape the star forming region through the nozzle. Thus the observed low Lyman continuum photons can be explained in terms of escape of these photons from the nebula. However, the spatial resolution is not sufficiently high and the mapping of Hα not sufficiently deep for us to obtain a conclusive evidence on the conformity of GEHRs with the blister model.

VI. CONCLUSIONS AND FUTURE PROSPECTS

We have compared the $BVRH\alpha$ photometry of a sample of Giant extragalactic H II regions with an Evolutionary Population Synthesis Model after correcting for extinction by dust. The basic diagnostic diagrams used are the ratio of Lyman continuum luminosity to blue band luminosity denoted by $\log(\frac{\phi}{L_B})$, plotted against the $B-V$ and $V-R$ colours. The results of the study are summarized below.

(1) The stellar component is experiencing a *lower* amount of extinction as compared to the gaseous component.

(2) There is evidence for a significant amount of *escape* of Lyman continuum photons from at least some of the nebulae.

(3) A majority of the regions have experienced more than one burst of star formation over the last 10 Myr.

(4) About $10^5\,M_\odot$ of gas is converted to stars during each burst of star formation. The evaluation of IMF slope and upper mass cutoff are difficult unless an accurate allowance is made for the first three effects. We will discuss these results in the following in the context of future studies aiming to model the regions better.

1. Improvements in the Optical Data

Our photometric data was essentially restricted to $BVRH\alpha$ bands. The detection of red supergiant population shows the importance of including I band also in the photometry. We have used published slit-spectroscopic information on Balmer decrement and [O III]/Hβ ratio because of difficulties of reaching useful signal levels at the 1-m telescope with which a major fraction of the data was obtained. Aperture photometry in these bands is desirable so that quantities that are representative of the entire cluster can be obtained. Since these lines fall in the middle of the effective wavelengths of B and V bands, either a specially designed broadband filter or a

prescription involving both the B and V bands need to be used for subtracting in-band continuum. Additionally, slit spectroscopic or area spectroscopic observations will be useful in estimating fluctuations of these quantities within a region.

We have highlighted the importance of background subtraction in Chapter III. The galaxy background has been carefully estimated in the present study by choosing an appropriate nearby region where the contribution from the GEHR is negligible. A continuum model of the entire galaxy may provide a better estimate of the background. One essentially needs to use multi-band observaions to separate GEHRs from the galaxy background of older stars.

Improving the sensitivity in the optical region will also contribute significantly to our understanding of these regions. As an example, the measurements of low ionization regions near GEHRs can help detection of 'champagne flows' and also help in more complete census of ionizing photons. Secondly, non-detection of some of the regions in the continuum forced us to enlarge the aperture to include a nearby continuum source. A deeper measure of these regions can help studying these regions individually, and also to check the models as well as extinction of the youngest regions that possibly have evidence for the high upper mass cutoff.

We found a population older than 6 Myr to be coexisting with the younger population in a majority of GEHRs. This stage is characterized by the appearance of red supergiants. Spectroscopically red supergiannts can be traced by the near infrared Ca III triplet absorption features. Spectroscopic observations of this feature will be useful for a more direct estimate of the number of supergiants present.

There has been considerable interest generated recently in the early evolution of a starburst when Wolf-Rayet stars form from the stars with initial masses above $\sim 40\, M_\odot$. The effect of these would be to harden the ionizing radiation, but there is considerable uncertainty in the model atmospheres. The H II regions with Wolf-

Rayet stars, known as 'warmers', have higher exitation spectra characterised by the higher intensities of [O III] and [N II] lines as well as by the presence of He II 4686 Å line. Spectroscopic information on these lines as well as photometry in the He II line will be useful in estimating the contribution of Wolf-Rayet stars.

2. Multiwavelength Observations

We have discussed in Chapter V the pointers to the effects of non-uniform extinction based on radio, optical and UV observations. If gaseous and stellar emission from each GEHR is observed over the largest possible range of wavelengths, it will be easier to model the distribution of dust better and correct the flux from gas and dust separately. The near-IR emission is affected much less by dust compared to the optical and UV radiation. The effect of red supergiants is also much more enhanced in this region. The availability of infrared imaging CCDs has made it possible to carry out near-IR photometry of these regions in the same way as done here in the optical region. Infrared spectroscopy will help in measuring the absorption features such as CO bands due to red supergiants.

High resolution CO maps of regions around GEHRs will help to trace the position of ionized region with respect to the molecular cloud. This is very similar to the methods employed by Israel (1978) for galactic H II regions and is a direct test for blister geometry. Far IR mapping would help similarly in mapping the geometry of the dust distribution. Different bands in this region isolate dust heated to different temperatures. Radio radiation, being totally transparent to dust, will help mapping the structure of entire gaseous emission. It would be important to use several bands so that thermal continuum can be isolated. The nonthermal component of radiation will also be useful in estimating the number of supernovae explosions in the cluster which can provide crosschecks on the IMF model.

186

3. Observations at Increased Resolution

Increased resolution in different bands will provide better maps of individual GEHRs and help in modelling the structure better. Maximum Entropy Image Reconstruction techniques, image stabilization techniques, and intriniscally good site will all be useful in obtaining such information from groundbased optical telescope. However, there is considerable scope here for the use of space telescopes in the optical as well.

APPENDIX

A. Interstellar Extinction

Dust particles present in the Inter-stellar medium (ISM) between the observer and the source of light, scatter and absorb a part of light. The process known as the *Interstellar Extinction* results in the reduction in the amount of light reaching the observer according to the equation,

$$F_\lambda = I_\lambda \exp(-\tau_\lambda), \qquad (A1)$$

where I_λ is the intensity of light that would have reached the observer in the absence of interstellar extinction, F_λ is the intensity actually observed, and τ_λ is a quantity called *optical depth*, which quantifies the extinction. It is conventional to express the above equation in terms of A_v, the extinction in magnitudes within the visual band, and E_λ, a function defining the shape of the extinction curve. Thus,

$$F_\lambda = I_\lambda 10^{-0.4 A_v E_\lambda}, \qquad (A2)$$

with

$$E_\lambda = \frac{X(1/\lambda)}{R_v}. \qquad (A3)$$

λ is the wavelength in microns and X is the extinction curve, which is an average over different directions in the Galaxy, and is given by Seaton (1979). R_v measures the total-to-selective extinction and is given by the expression,

$$R_v = \frac{A_v}{E(B-V)}. \qquad (A4)$$

$E(B-V)$ is the amount of reddening $B-V$ colour experiences and is often referred to as colour excess. Average value of $R_v = 3.1$ (Cardelli, Clayton and Mathis 1989), which corresponds to $E_\lambda = 1.322, 1.000, 0.748,$ and 0.484 for $B, V, R,$ and I filters respectively with Seaton's (1979) curve. When studying the emission line objects

it is conventional to represent the extinction in terms of that at Hβ namely $C_{\mathrm{H}\beta}$, defined as,

$$F_{\mathrm{H}\beta} = I_{\mathrm{H}\beta}10^{-C_{\mathrm{H}\beta}}. \tag{A5}$$

Combining equations A2 and A5,

$$C_{\mathrm{H}\beta} = 0.4A_v E_{\mathrm{H}\beta}. \tag{A6}$$

From Seaton's curve $E_{\mathrm{H}\beta} = 1.19$ and hence,

$$A_v = 2.1 C_{\mathrm{H}\beta}. \tag{A7}$$

With the above definition of $C_{\mathrm{H}\beta}$, the intrinsic ratios of emission lines can be determined from observed ratios using the equation,

$$\log \frac{I_\lambda}{I_{\mathrm{H}\beta}} = \log \frac{F_\lambda}{F_{\mathrm{H}\beta}} + C_{\mathrm{H}\beta}f(\lambda), \tag{A8}$$

where

$$f(\lambda) = \frac{X(1/\lambda)}{X_\beta} - 1 \tag{A9}$$

The values of X, E and f at wavelengths corresponding to the most commonly observed emission lines in H II regions are given in Table A.1. It is clear from the above equations, that the accuracy of extinction corrections depends on the accuracy of $C_{\mathrm{H}\beta}$ measurements. The most accurate way of determining the value of $C_{\mathrm{H}\beta}$ observationally is by choosing emission lines, whose ratios can be estimated theoretically. Hydrogen recombination line ratios such as $\frac{I_{\mathrm{H}\alpha}}{I_{\mathrm{H}\beta}}$, $\frac{I_{\mathrm{H}\gamma}}{I_{\mathrm{H}\beta}}$, $\frac{I_{\mathrm{Br}\alpha}}{I_{\mathrm{H}\beta}}$ etc. and free-free radio thermal emission to Hβ ratio $\frac{I_\nu}{I_{\mathrm{H}\beta}}$ are weakly dependent on the physical conditions such as temperature and density and hence are best suited for this purpose. Osterbrock (1974, 1989) has compiled the values of these ratios as a function of temperature and density, which can be approximated by the following equations,

$$\frac{I_{\mathrm{H}\alpha}}{I_{\mathrm{H}\beta}} = 2.860 \left(\frac{T_e}{10^4}\right)^{-0.07}, \tag{A10}$$

$$\frac{I_{H\gamma}}{I_{H\beta}} = 0.469 \left(\frac{T_e}{10^4}\right)^{+0.025} , \qquad (A11)$$

$$\frac{I_\nu}{I_{H\beta}} = 3.321 \times 10^9 \left(\frac{T_e}{10^4}\right)^{+0.52} \left(\frac{\nu}{10^9}\right)^{-0.01} \text{Hz} . \qquad (A12)$$

Thus $C_{H\beta}$ value can be obtained by observing in one or more of these ratios and using Equation A8. $C_{H\beta}$ obtained using Balmer line ratios are referred to as $C_{H\beta}$(Balmer) and that obtained combining with radio thermal flux is denoted by $C_{H\beta}$(radio).

Table A.1 Reddening curve at selected wavelengths. [†]

Ident	Wavelength Å	X	E	f
B	4400	4.105	1.324	0.115
V	5500	3.184	1.027	−0.135
R	7000	2.298	0.741	−0.376
I	9000	1.475	0.476	−0.599
[O II]	3727	4.619	1.490	0.255
H δ	4102	4.310	1.390	0.171
H γ	4340	4.156	1.341	0.129
[O III]	4363	4.138	1.335	0.124
He II	4686	3.835	1.237	0.042
H β	4861	3.681	1.188	0.000
[O III]	4959	3.595	1.160	−0.024
[O III]	5007	3.554	1.147	−0.035
[O I]	6300	2.632	0.849	−0.285
[N II]	6548	2.498	0.806	−0.321
H α	6563	2.491	0.803	−0.323
[N II]	6584	2.480	0.800	−0.326
[S II]	6717	2.417	0.780	−0.344
[S II]	6731	2.410	0.778	−0.345

[†] Based on galactic extinction curve (Seaton 1979) and $R_v = 3.1$

References

Alcaino, G.: 1976, *Astr. Astrophys. Suppl.,* **26**, 261.

Alcaino, G.: 1974, *Astr. Astrophys. Suppl.,* **13**, 305.

Alcock, C., Paczynski, B.:1978, *Astrophys. J.,* **223**, 244.

Alloin, D., Edmunds, M.G., Lindblad, P.O., Pagel, B.E.J.: 1981, *Astr. Astrophys.,* **101**, 377.

Alloin, D., Nieto, J.-L.: 1982, *Astr. Astrophys. Suppl.,* **50**, 491.

Beck, S.C., Beckwith, S., Gatley, I.: 1984, *Astrophys. J.,* **279**, 563.

Belfort, P., Mochkovitch, R., Dennefeld, M..: 1987, *Astr. Astrophys.,* **176**, 1.

Bessell, M.S.: 1990, *Publ. astr. Soc. Pacific,* **102**, 1181.

Bessell, M.S.: 1979.., *Publ. astr. Soc. Pacific,* **91**, 589.

Bessell, M.S.: 1976, *Publ. astr. Soc. Pacific,* **88**, 557.

Bhat, P.N., Singh, K.P., Prabhu, T.P., Kembhavi, A.K.: 1992, *J. Astrophys. Astr.,* **13**, 293.

Bica, E., Alloin, D., Schmidt, A.: 1990, *Mon. Not. R. astr. Soc.,* **242**, 241.

Blitz, L., Israel, F.P., Neugebauer, G., Gatley, I., Lee, T.J., Beattie, D.H.: 1981, *Astrophys. J.,* **249**, 76.

Bohlin, R.C., Cornett, R.H., Hill, J.K., Stecher, T.P.: 1990, *Astrophys. J.,* **363**, 154.

Bottinelli, L., Gougenheim, L., Paturel, G., de Vaucouleurs, G.: 1984, *Astr. Astrophys. Suppl.,* **56**, 381.

Brown, R.L., Mathews, W.G.: 1970, *Astrophys. J.,* **160**, 939.

Buat, V., Donas, J., Deharveng, J.M.: 1987, *Astr. Astrophys.,* **185**, 33.

Buta, R.: 1988, *Astrophys. J. Suppl.*, **66**, 233.

Campbell, A.W., Terlevich, R.J.: 1984, *Mon. Not. R. astr. Soc.*, **211**, 15.

Campbell, A.W., Terlevich, R.J., Melnick, J.: 1986, *Mon. Not. R. astr. Soc.*, **223**, 811.

Caplan, J., Deharveng, L.: 1986, *Astr. Astrophys.*, **155**, 297.

Cardelli, J.A., Clayton, G.C., Mathis, J.S.: 1989, *Astrophys. J.*, **345**, 245.

Cepa, J., Beckman, J.E.: 1990, *Astr. Astrophys. Suppl.*, **83**, 211.

Cepa, J., Beckman, J.E.: 1989, *Astr. Astrophys. Suppl.*, **79**, 41.

Chevalier, C., Ilovaisky, S.A. 1991, *Astr. Astrophys. Suppl.*, **90**, 225.

Crillon, R., Monnet, G.: 1969, *Astr. Astrophys.*, **1**, 449.

De Gioia-Eastwood, K.: 1985, *Astrophys. J.*, **288**, 175.

de Vaucouleurs, G.: 1979, *Astr. J.*, **84**, 1270.

de Vaucouleurs, G., de Vaucouleurs, A., Corwin, H.G.: 1976 *Second Reference Catalogue of Bright Galaxies*, Texas.

Devereux, N.A., Kenney, J.D.P., Young, J.: 1992, *Astr. J.*, **103**, 784.

Dinerstein, H.L.: 1990, in *The Interstellar Medium in External Galaxies*, ed. Thronson, H.A., Shull, J.M., (Dordrecht: Kluwer).

Djorgovski, S.: 1984, in *Proc. Workshop Improvements to Photometry*, eds. Borucki, W.J., Young, A. NASA CP-2350, p. 152.

Dopita, M.A., Evans, I.N.: 1986, *Astrophys. J.*, **307**, 431.

Dottori, H.A.: 1979, *Astr. Astrophys. Suppl.*, **37**, 519.

Dufour, R.J., Talbot, R.J., Jensen, E.B., Shields, G.A.: 1980, *Astrophys. J.*, **236**, 119.

Edmunds, M.G., Pagel, B.E.J.: 1984, *Mon. Not. R. astr. Soc.*, **211**, 507.

Elmegreen, D.M., Elmegreen, B.G.: 1984, *Astrophys. J. Suppl.*, **54**, 127.

Fanelli, M.N., O'Connell, R.W., Thuan, T.X.: 1988 *Astrophys. J.*, **334, 665**.

Fernie, J.D. 1974, *Publ. astr. Soc. Pacific*, **86,** 837.

Fich, M., Treffers, R.R., Blitz, L.: 1982, In *Regions of Recent Star Formation*, ed. Roger, R.S., Dewdney, P.E. (Reidel, Dordrecht) **93**, 201.

Gallagher, J.S., Hunter, D.A., Tutukov, A.V.: 1984, *Astrophys. J.*, **284**, 544.

Gondhalekar, P.M.: 1983, *Adv. Space Res.* **2**, 163.

Gonzalez-Riestra, R., Rego, M., Zamorano, J.: 1987, *Astr. Astrophys.*, **186**, 64.

Griersmith, D., Hyland, A.R., Jones, T.J.: 1982, *Astr. J.*, **87**, 1106.

Hamuy, M., Maza, J.: 1989, *Astr. J.*, 97, 720.

Hardie, R.H. 1977, in *Astronomical Techniques*, ed. Hiltner W.A., University of Chicago Press, London.

Hawley, S.A., Phillips, M.M.: 1980, *Astrophys. J.*, **235**, 783.

Hippelein, H.H.: 1986, *Astr. Astrophys.*, **160**, 374.

Hodge, P.W.: 1969, *Astrophys. J. Suppl.*, **18**, 73.

Hodge, P., Jaderlund, E., Meakes, M.: 1990, *Publ. astr. Soc. Pacific*, **102**, 1263.

Hodge, P.W., Kennicutt, R.C.: 1983, *Astr. J.*, **88**, 296.

Horne, K.: 1988, in *New Directions in Spectrophotometry*, eds. Philip, A.G.D., Hayes, D.S., Adleman, S.J., Davis, L. Press Schenectady p. 285.

Howarth, I.D., Lynas-Gray, A.E.: 1989, *Mon. Not. R. astr. Soc.*, **240**, 513.

Howell, S.B. 1989, *Publ. astr. Soc. Pacific*, **101**, 616.

Huchra, J.P.: 1977, *Astrophys. J.*, **217**, 928.

Hunter, D.A.: 1982, *Astrophys. J.*, **260**, 81.

Hunter, D.A., Gallagher, J.S.: 1992, *Astrophys. J. (Lett.),* **391**, L9.

Hunter, D.A., Gallagher, J.S.: 1990, *Astrophys. J.,* **362**, 480.

Hunter, D.A., Gallagher, J.S., Rautenkranz, D.: 1982, *Astrophys. J. Suppl.,* **49**, 53.

Hyland, A.R., Straw, S., Jones, T.J., Gatley, I.: 1992, *Mon. Not. R. astr. Soc.,* **257**, 391.

Icke, V., Gatley, I., Israel, F.P.: 1980, *Astrophys. J.,* **236**, 808.

Israel, F.P.: 1980, *Astr. Astrophys.,* **90**, 246.

Israel, F.P.: 1978, *Astr. Astrophys.,* **70**, 769.

Israel, F.P., Kennicutt, R.C.: 1980, *Astophys. Lett.,* **21**, 1.

Jensen, E.B., Talbot, R.J., Dufour, R.J.: 1981, *Astrophys. J.,* **243**, 716.

Johnson, H.L, 1966, *Ann. Rev. Astr. Astrophys.,* **4**, 193.

Joner, M.D., Taylor, B.J. 1990, *Publ. astr. Soc. Pacific,* **102,** 1004.

Jones, J.E.,Jones, B.J.T.: 1980, *Mon. Not. R. astr. Soc.,* bf 191, 685.

Kennicutt, R.C.: 1988, *Astrophys. J.,* **334**, 144.

Kennicutt, R.C.: 1984, *Astrophys. J.,* **287**, 116.

Kennicutt, R.C.: 1983a, *Astrophys. J.,* **272**, 54.

Kennicutt, R.C.: 1983b, *Astr. J.,* **88**, 483.

Kennicutt, R.C.: 1981, *Astrophys. J.,* **247**, 9.

Kennicutt, R.C.: 1979, *Astrophys. J.,* **228**, 394.

Kennicutt, R.C., Balick, B., Heckman, T.: 1980, *Publ. astr. Soc. Pacific,* **92**, 134.

Kennicutt, R.C., Chu, Y.: 1988, *Astr. J.,* **95**, 720.

Kennicutt, R.C., Edgar, B.K., Hodge, P.W.: 1989, *Astrophys. J.,* **337**, 761.

Kennicutt, R.C., Kent, S.M.: 1983, *Astr. J.,* **88**, 1094.

Kilkenny, D., Menzies, J.W.: 1990, *South African Astron. Obs. Circ.* **13**, 25.

Kurucz, R.L.: 1979, *Astrophys. J. Suppl.*, **40**, 1.

Larson, R.B.: 1986, *Mon. Not. R. astr. Soc.*, **218**, 409.

Larson, R.B., Tinsley, B.M.: 1978, *Astrophys. J.*, **219**, 46.

Leitherer, C.: 1990, *Astrophys. J. Suppl.*, **73**, 1.

Lequeux, J., Maucherat-Joubert, M., Deharveng, J.M., Kunth, D.: 1981, *Astr. Astrophys.*, **103**, 305.

Lequeux, J., Viallefond, F.: 1980, *Astr. Astrophys.*, **91**, 269.

Lequeux, J., Peimbert, M., Rayo, J.F., Serrano, A., Torres-Peimbert, S.: 1979, *Astr. Astrophys.*, **80**, 155.

Longo, G., de Vaucouleurs, A.: 1983, Monographs in Astronomy No. 3, Texas.

Mackay, C.D.: 1986, *Ann. Rev. Astr. Astrophys.*, **24**, 255.

Maeder, A.: 1990, *Astr. Astrophys. Suppl.*, **84**, 139.

Maeder, A., Meynet, G.: 1989, *Astr. Astrophys.*, **210**, 155.

Maeder, A., Meynet, G.: 1988, *Astr. Astrophys. Suppl.*, **76**, 411.

Maeder, A., Meynet, G.: 1987, *Astr. Astrophys.*, **182**, 243.

Mas-Hesse, M., Kunth, D.: 1991 *Astr. Astrophys. Suppl.*, **88**, 399.

Massey, P., Parker, J.W., Garmany, C.D.: 1989, *Astr. J.*, **98**, 1305.

Mathis, J.S.: 1983, *Astrophys. J.*, **267**, 119.

Mayya, Y.D. : 1991, *J. Astrophys. Astr.*, **12**, 319.

McCall, M.L., English, J.,Shelton, I. 1989, *J. R. astr. Soc. Canada,* **83**, 179.

McCall, M.L., Hill, R., English, J.: 1990 *Astr. J.*, **100**, 193.

McCall, M.L., Rybski, P.M., Shields, G.A.: 1985, *Astrophys. J. Suppl.*, **57**, 1.

McGregor, P.J., Hyland, A.R.: 1981, *Astrophys. J.*, **250**, 116.

McLean, I.S., 1989, in *Electronic and Computer-Aided Astronomy*, Ellis Horwood, Chichester.

Melnick, J.: 1985, *Astr. Astrophys.*, **153**, 235.

Melnick, J.: 1977, *Astrophys. J.*, **213**, 15.

Melnick, J., Terlevich, R., Eggleton, P.P.: 1985, *Mon. Not. R. astr. Soc.*, **216**, 255.

Melnick, J., Terlevich, R., Moles, M.: 1985, *Rev. Mexicana Astron. Astrof.* **11**, 91.

Mezger, P.G.: 1978, *Astr. Astrophys.*, **70**, 565.

Milliard, B., Marcelin, M.: 1981, *Astr. Astrophys.*, **95**, 59.

Moorwood, A.F.M., Glass, I.S.: 1982, *Astr. Astrophys.*, **115**, 84.

Neff, J.S.: 1970, *Mon. Not. R. astr. Soc.*, **149**, 45.

Newberry, M.V.: 1991, *Publ. astr. Soc. Pacific,* **103**, 122.

O'Dell, C.R., Castañeda, H.O.: 1984a, *Astrophys. J.*, **283**, 158.

O'Dell, C.R., Castañeda, H.O.: 1984b, *Astrophys. J.*, **287**, 116.

Oka, S., Wakamatsu, K., Sakka, K., Nishida, M., Jugaku, J.: 1974, *Publ. astr. Soc. Japan*, **26**, 289.

Olofsson, K.: 1989, *Astr. Astrophys. Suppl.*, **80**, 317.

Osterbrock, D.E.: 1989, *Astrophysics of Gaseous Nebulae and Active Galactic Nuclei*, Univ. Science Books, California.

Osterbrock, D.E.: 1974, *Astrophysics of Gaseous Nebulae*, Freeman, San Francisco.

Pagel, B.E.J., Edmunds, M.G., Blackwell, D.E., Chun, M.S., Smith, G.: 1979, *Mon. Not. R. astr. Soc.*, **189**, 95.

Pagel, B.E.J., Edmunds, M.G.: 1981, *Ann. Rev. Astr. Astrophys.*, **19**, 77.

Peimbert, M., Peña, M., Torres-Peimbert, S.: 1986, *Astr. Astrophys.*, **158**, 266.

Pence, W.D., Taylor, K., Atherton, P. : 1990 *Astrophys. J.*, **357**, 415.

Peterson, C.J.: 1978, *Astrophys. J.*, **226**,75

Peterson, C., Rubin, V.C., Ford, W.K., Thonnard, N.: 1976, *Astrophys. J.*, **208**, 662.

Prabhu, T.P.: 1980a, *J. Astrophys. Astr.*, **1**, 129.

Prabhu, T.P.: 1980b, *Astrophys. Space Sci.*, **68**, 519.

Prabhu, T.P., Mayya, Y.D., Anupama, G.C.: 1992, *J. Astrophys. Astr.*, **13**, 129.

Rieke, G.H., Lebofsky, M.J., Thompson, R.I., Low, F.J., Tokunaga, A.T.: 1980, *Astrophys. J.*, **238**, 24.

Rosa, M., Joubert, M., Benvenuti, P.: 1985, *Astr. Astrophys. Suppl.*, **57**, 361.

Roy, J.-R., Arsenault, R., Joncas, G.: 1986, *Astrophys. J.*, **300**, 624.

Roy, J.-R., Belly, J., Walsh, J.R.: 1989, *Astr. J.*, **97**, 1010.

Roy, J.-R., Boulesteix, J., Joncas, G., Grundseth, B.: 1991, *Astrophys. J.*, **367**, 141.

Roy, J.-R., Walsh, J.R.: 1986, *Mon. Not. R. astr. Soc.*, **223**, 39.

Roy, J.-R., Walsh, J.R.: 1987, *Mon. Not. R. astr. Soc.*, **228**, 883.

Roy, J.-R., Walsh, J.R.: 1988, *Mon. Not. R. astr. Soc.*, **234**, 977.

Rubin, R.H.: 1985, *Astrophys. J. Suppl.*, **57**, 349.

Rubin, V.C., Ford, W.K., Peterson, C.: 1975, *Astrophys. J.*, **199**, 39.

Sabbadin, F., Bianchini, A.: 1979, *Publ. astr. Soc. Pacific*, **91**, 280.

Sagar, R, Pati, A.K. 1989, *Bull. astr. Soc. India*, **17**, 6.

Salpeter, E.E.: 1955, *Astrophys. J.*, **121**, 161.

Sandage, A.R., Tammann.: 1981, *A Revised Shapley-Ames Catalog of Bright Galaxies* (Carnegie Inst., Washington).

Sandage, A.R., Tammann, G.A.: 1976, *Astrophys. J.*, **210**, 7.

Sandage, A.R., Tammann.: 1975, *Astrophys. J.*, **196**, 313.

Sandage, A.R., Tammann.: 1974, *Astrophys. J.*, **190**, 525.

Sargent, W.L.W., Searle, L.: 1970, *Astrophys. J. (Lett.)*, **162**, L155.

Schild, R.E. 1983, *Publ. astr. Soc. Pacific*, **95**, 1021.

Searle, L., Sargent, W.L.W., Bagnuolo, W.G.: 1973, *Astrophys. J.*, **179**, 427.

Seaton, M.J.: 1979, *Mon. Not. R. astr. Soc.*, **187**, 73P.

Sérsic, J.L., Pastoriza, M.: 1967, *Publ. astr. Soc. Pacific*, **79**, 152.

Sérsic, J.L., Pastoriza, M.: 1965, *Publ. astr. Soc. Pacific*, **77**, 287.

Shaver, P.A., McGee, R.A., Danks, A.C., Pottasch, S.R.: 1983, *Mon. Not. R. astr. Soc.*, **204**, 53.

Shields, G.A.: 1990, *Ann. Rev. Astr. Astrophys.*, **28**, 525.

Shields, G.A., Skillman, E.D., Kennicutt, R.C.: 1991, *Astrophys. J.*, **371**, 82.

Simkin, S.M.: 1975, *Astrophys. J.*, **195**, 293.

Simons, D.A., DePoy, D.L., Becklin, E.E., Capps, R.W., Hodapp, K.-W., Hall, D.N.B.: 1988, *Astrophys. J.*, **335**, 126.

Smith, L.F., Biermann, P., Mezger, P.G.: 1978, *Astr. Astrophys.*, **66**, 65.

Solomon, P.M., Rivolo, A.R., Barrett, J., Yahil, A.: 1987, *Astrophys. J.*, **319**, 730.

Stayton, L.C., Angione, R.J., Talbert, F.D.: 1983, *Astr. J.*, **88**, 602.

Strömgren, B.: 1966, *Ann. Rev. Astr. Astrophys.*, **4**, 433.

Talbot, R.J., Jensen, E.B., Dufour, R.J.: 1979, *Astrophys. J.*, **229**, 91.

Tenorio-Tagle, G.: 1982, In *Regions of Recent Star Formation*, ed. Roger, R.S., Dewdney, P.E. (Reidel, Dordrecht) **93**, 1.

Tenorio-Tagle, G.: 1979, *Astr. Astrophys.,* **71**, 59.

Terlevich, R.: 1985, in *Star-forming Dwarf Galaxies*, ed. Kunth, D.,.

Terlevich, R., Melnick, J.: 1985, *Mon. Not. R. astr. Soc.,* **213**, 841.

Terlevich, R., Melnick, J.: 1981, *Mon. Not. R. astr. Soc.,* **195**, 839.

Terlevich, R., Melnick, J., Masegosa, J., Moles, M., Copetti, M.V.F.: 1991, *Astr. Astrophys. Suppl.,* **91**, 285.

Thronson, H., Majewski, S., Descartes, L., Hereld, M.: 1990, *Astrophys. J.,* **364**, 456.

Thuan, T.X., Van, J.T.T. (Gif sur Yvette: Editions Frontiere), p. 395.

Tifft, W.G.: 1969, *Astr. J.,* **74**, 354.

Tifft, W.G.: 1961, *Astr. J.,* **66**, 390.

van Woerden, H., Bosma, A., Mebold, V.: 1975, in *La Dynamique des Galaxies Spirales* ed. Weliachew, L., Editions du Centre National de la Recherche Scientifique, p. 483.

Viallefond, F.: 1987, Ph.D. Thesis, *University of Paris.* .

Viallefond, F.: 1985, in *Star-forming Dwarf Galaxies*, ed. Kunth, D., Thuan, T.X., Van, J.T.T. (Gif sur Yvette: Editions Frontiere), p. 207.

Viallefond, F., Thuan, T.X.: 1984, *Astrophys. J.,* **269**, 444.

Viallefond, F., Goss, W.M., Allen, R.J.: 1982, *Astr. Astrophys.,* **115**, 373.

Vilchez, J.M., Pagel, B.E.J.: 1988, *Mon. Not. R. astr. Soc.,* **231**, 257.

Vogel, S.M., Kulkarni, S.R., Scoville, N., Z.: 1988, *Nature* **334**, 402.

von Hippel, T., Bothun, G.: 1990, *Astr. J.,* **100**, 403.

Vorontsov-Velyaminov, B.A., Lyuti, V.M., Zaitseva, G.: 1973, *Sov. Astron. Jl.* **16**, 71.

Waller, W.H.: 1990 *Publ. astr. Soc. Pacific,* **102**, 1217 .

Walsh, J.R., Roy, J.-R.: 1989a, *Mon. Not. R. astr. Soc.,* **239**, 297.

Walsh, J.R., Roy, J.-R.: 1989b, *Astrophys. J.,* **341**, 722.

Webster, B.L., Smith, M.G.: 1983, *Mon. Not. R. astr. Soc.,* **204**, 743.

Wegner, G.: 1979, *Ast· phys. Space Sci.,* **60**, 15.

Weliachew, L., Sancisi, R., Guelin, M.: 1978, *Astr. Astrophys.,* **65**, 37.

Wevers, B.M.H.R.: 1984, Groningen Univ. Ph.D. Thesis

Winkler, H., Van Wyk, F., Glass, I.S.: 1990, *South African Astron. Obs. Circ.* **14**, 25.

Winter, A.J.B.: 1975, *Mon. Not. R. astr. Soc.,* **172**, 1.

Wynn-Williams, C.G., Becklin, E.E.: 1985, *Astrophys. J.,* **290**, 108.

Yorke, H.W., Bodenheimer, P., Tenorio-Tagle, G.: 1982, In *Regions of Recent Star Formation*, ed. Roger, R.S., Dewdney, P.E. (Reidel, Dordrecht) **93**, 15 .

Zasov, A.V., Lyuti, V.M.: 1973, *Sov. Astron. Jl.* **17**, 169.